MATHEMATICAL MODELING OF NONPREMIXED TURBULENT METHANE-AIR FLAMELESS COMBUSTION IN A STRONG-JET/WEAK-JET BURNER

by

Yong Jin Lee

A thesis submitted to the Department of Chemical Engineering

In conformity with the requirements for

the degree of Doctor of Philosophy

Queen's University

Kingston, Ontario, Canada

September, 2010

Abstract

Flameless combustion technology has been developed over the past twenty years achieving low-NOx emissions and high energy efficiency for industrial applications. In the present work, three aspects of flameless combustion were examined based on a burner employing the Strong-Jet/Weak-Jet (SJ/WJ) configuration.

In the first part of the work, a 3-D SJ/WJ physical model was developed in the Lagrangian perspective for an isothermal pair of free jets. The model was used to predict the WJ trajectory, identify important design/operation factors, and estimate the extent of mixing in the main combustion region (confluence region). The model was also validated with experimental data and showed excellent agreement over a wide range of flow conditions.

In the second part of the work, a simplified chemical kinetic model was developed for the flameless combustion of natural gas. A detailed chemical reaction mechanism (GRI Mech 3.0) was successfully reduced to a skeletal chemical reaction mechanism under flameless combustion conditions by Principal Component Analysis, sensitivity analysis and reaction flow analysis. The skeletal mechanism was further simplified to a set of 2-D manifolds by Trajectory-Generated Low-Dimensional Manifolds (TGLDM) method. The set of 2-D manifolds was tested by the Batch Reactor (BR) and Perfect Stirred Reactor (PSR) models. From the BR model test, it was found that the chemical reaction rates were well represented by the 2-D manifolds. The effect of the physical perturbation, tested by PSR model, could be handled by the perpendicular projection instead of the orthogonal projection because both showed similar discrepancies with the skeletal mechanism.

In the final part of the work, the steady-state Reynolds-Averaged Navier-Stokes (RANS) simulation was conducted for the turbulent flameless combustion in the SJ/WJ furnace, based on

the Probability Density Function (PDF)/Mixing approach. The set of 2-D manifolds and Conditional Source-term Estimate (CSE) method were used for the combustion reaction and the estimation of the mean production/destruction rate, respectively. This CSE-TGLDM model provided good predictions of major species concentrations. However, the gas temperatures and CO concentrations were highly over-predicted.

Acknowledgements

Completing this Ph.D. thesis was such a long journey for me. Many endless aids and supports have been given by many people in the course of the journey. I would like first to thank my supervisor and co-supervisor, Dr. E.W.(Ted) Grandmaison and Dr. M.D. Matovic, for their endless patience, encouragement and support, and also for introducing me to the science of combustion. I would also like to thank my colleague, Yu He, for his kindness and sincerity. It was always delight to work with him. Also, I can't skip my truthful colleague, Tony Mendes, for his warm heart.

I want to express sincere gratitude to my Master supervisor, Dr. Jong In Dong, for the beginning of this journey. I would like to give my special thank to Dr. Hyo Kim for teaching me mathematics and introducing me the science/engineering.

Lastly I could not express enough thank to my wife, Eun Young Kim, and my mother, Kyoung Ja Kim, for their devoted sacrifice. I love my daughter, Seoyeon, in my heart, thank you for giving me such the wonderful pleasure.

Table of Contents

List of Figures

List of Tables

Nomenclatures

$\mathcal{A}$	A functional formulated from the original integration equation in Chapter 2
A	Constant in Chapter 3
a	The absorption coefficient of radiation [1/m] in Chapter 2 or the quadrature coefficient in Chapter 5
$\mathcal{B}$	A functional obtained from *a priori* information (stabilizing functional) in Chapter 2
$\mathbf{B}$	Accumulated matrix of local sensitivity coefficient matrices in Chapter 2
B	Constant in Chapter 3
b	Jet boundary width defined as a length indicating 50% of intermittency [m] in Chapter 2 and 3
b_j	The quadrature coefficients in Chapter 5
C	Constant in Chapter 2 and 3
C_c	Centerline velocity decay constant in Chapter 2 and 3
C_e	Entrainment coefficient in Chapter 2 and 3
c	The quadrature coefficient in Chapter 5
$c_{p,j}$	Specific heat of j species at constant pressure [J/kg K] in Chapter 2, 4 and 5
D	Diffusivity [m^2/s] in Chapter 2
d_{12}	Distance between SJ and WJ nozzles in Chapter 3
d_o	Diameter of a jet nozzle [m] in Chapter 2 and 3
$\vec{e}_k$	Unit vector in the k-coordinate in Chapter 3
$\mathbf{F}$	Accumulated matrix of local reaction rate matrices in Chapter 2
$\vec{F}$	Physical mixing vector due to convection and/or diffusion [1/s] in Chapter 2

$\vec{F}_{i,l}$ External force vector acting on fluid element issued from *i*-th nozzle during δt due to the entrainment effect of *l*-th jet flow in Chapter 3

$F_{i,j}$ Reaction rate of *i*-th species due to *j*-th reaction in Chapter 2

f Production/destruction rate vector function in Chapter 2

f_i Production/destruction rate function of *i*-th dependent variable in a ODE system (*i*-th element of **f**) in Chapter 2

G_o Momentum flow rate at the nozzle exit [N] in Chapter 2

g_k Gravity in the *k*-direction [m/s^2] in Chapter 2

h The specific enthalpy of mixture, defined as $h = \sum Y_i h_i$ [J/kg] in Chapter 2, 4 and 5

h_i The specific enthalpy of *i* species [J/kg] in Chapter 2, 4 and 5

h^o The standard specific enthalpy of mixture, defined as $h^o = \sum Y_i h_i^o$, [J/kg] in Chapter 2, 4 and 5

h_i^o The standard specific enthalpy of formation of *i* species at 1 atm and 298 K [J/kg] in Chapter 2, 4 and 5

Δh The specific sensible enthalpy of mixture, defined as $\Delta h = h - h^o$, [J/kg] in Chapter 2, 4 and 5

Δh_i The specific sensible enthalpy of *i* species, defined as $\Delta h_i = h_i - h_i^o$, [J/kg] in Chapter 2, 4 and 5

$\vec{\vec{I}}$ Unit matix

i' The directional total intensity [W/m^2 sr] in Chapter 2

i'_λ The directional spectral intensity [W/m^3 sr] in Chapter 2

J Jacobian matrix in Chapter 2

$\vec{J}_i$ The diffusion flux vector of *i* species [kg/m^2 s] in Chapter 2

$J_{e,i}$ Mass flow into the fluid element issued from *i*-th nozzle during δt due to the entrainment effect [kg/s] in Chapter 2

k Turbulence kinetic energy [m^2/s^2] or thermal conductivity [W/mK] in Chapter 2

k_j Parameters of a ODE system i.e. reaction rate constant of j-th reaction in Chapter 2

l The number of mass transport equations or ODE in Chapter 2 and 4

N Conserved scalar dissipation rate in CMC (=χ/2) [1/s] in Chapter 2

n Total number of dependent variables (species) in Chapter 2, 4 and 5

n_c The number of cells within the ensemble in Chapter 5

n_{mf} The number of the user-divided mixture fraction points in Chapter 5

n_r Refractive index [-] in Chapter 2

m Total number of parameters (reactions) in ODE system in Chapter 2

m_i Mass of the fluid element issued from i-th nozzle during δt [kg] in Chapter 2 and 3

$\dot{m}$ Mass flow rate [kg/s] in Chapter 2 and 3

$\dot{m}_o$ Mass flow rate at the nozzle exit [kg/s] in Chapter 2 and 3

$\dot{m}_e$ Entrainment mass flow rate at the downstream jet location [kg/s] in Chapter 2 and 3

P Favre-averaged Probability Density Function (PDF) in Chapter 2 and 5

$\vec{\vec{P}}$ Projection matrix projecting a vector onto the manifolds in Chapter 2

Pr The Prandtl number [-] in Chapter 2

p Pressure [atm] in all Chapters

Q_{ext} External heat source in PSR model [J/kg s] in Chapter 4

$\vec{q}_1$ Position vector for the fluid element issued from WJ nozzle in Chapter 3

q_k The heat flux in the k-direction [J/m^2 s] in Chapter 2

q^{in} Inflow rate per unit reactor volume in the PSR model [kg/m^3 s] in Chapter 4

R Gas constant, 8.31447 [J/mol K] in all Chapters

r,θ,z Coordinates of the Cylindrical coordinate system [m,-,m]

Re_{jet} Jet Reynolds number (=$\rho_o u_o d_o/\mu_o$) [-] in Chapter 2 and 3

S The modulus of the mean rate-of-strain tensor (=$\sqrt{2S_{ij}S_{ij}}$, where $S_{ij} = \frac{\partial u_j}{\partial x_i}$) in Chapter 2 or the path length of radiation [1/s] in Chapter 2

$\vec{S}$ Chemical production/destruction rate vector [1/s] in Chapter 2

$\vec{s}$ The directional vector for radiation [m] in Chapter 2

s_i Arc length of the *i* jet trajectory [m] in Chapter 3

s_o Virtual origin of a jet [m] in Chapter 3

Sc Schmidt number [-] in Chapter 2

T Temperature [K] in all Chapters

Tr Trace of matrix

t Time [s] in all Chapters

$u,v,w,...$ Parameters for manifolds in Chapter 2

u_k Velocity component in the *k*-direction [m/s] in all Chapters

u_c Centerline velocity [m/s] in Chapter 2 and 3

u_o Source velocity (=$G_o / \dot{m}_o$) [m/s] in Chapter 2 and 3

$\mathbf{V}$ Right eigenvector matrix in Chapter 2

$\tilde{\mathbf{V}}$ Inverse matrix of $\mathbf{V}$ in Chapter 2

V_i Moving volume for *i*-th fluid element [m^3] in Chapter 3

V_z A representative velocity in the main convection flow direction (jet flow direction) [m/s] in Chapter 5

v_i *i*-th column eigenvector of $\mathbf{V}$ in Chapter 2

$\tilde{\mathrm{v}}_i$ *i*-th row eigenvector of $\tilde{\mathbf{V}}$ in Chapter 2

$\vec{v}_i$ Velocity vector of the fluid element issued from *i*-th nozzle [m/s] in Chapter 3

$v_{i,j}$ *j*-direction velocity component of the on the fluid element issued from *i*-th nozzle [m/s] in Chapter 3

$\langle \vec{v} | \eta \rangle$ Conditional averaged vector of $\vec{v}$ about the mixture faction, η (or written as $\vec{v}(\eta)$) in Chapter 2 and 5

W_j Molecular weight of *j* species [kg/kmol] in all Chapters

$\dot{w}_i$ Molar production/destruction rate of *i* species [kmol/m^3 sec] in Chapter 2, 4 and 5

$\vec{x}$ Position vector [m] in Chapter 2

x_k *k*-coordinate [m] in Chapter 2

x,y,z Coordinates of the Cartesian coordinate system [m,m,m]

$\vec{Y}$ State vector in the composition space in Chapter 2

Y_i Mass fraction of *i* species [-] in Chapter 2, 4 and 5 or dependent variable in Chapter 2

Z_i Mass fraction of *i* element [-] in Chapter 2

Z_{i1} Mass fraction of *i* element in the stream 1 nozzle [-] in Chapter 2

Z_{i2} Mass fraction of *i* element in the stream 2 nozzle [-] in Chapter 2

α Non-negative parameters of β-function in Chapter 2 and 5

β Non-negative parameters of β-function in Chapter 2 and 5

$\beta_{i,j}$ First order sensitivity coefficient of *i* dependent variable with respect of *j* parameter in Chapter 2

δ_{ij} The Kronecker delta in all Chapters

ε Turbulence dissipation rate [m^2/s^3] in Chapter 2 or constant (=1.0×10^{-6}) in Chapter 5

η Mixture fraction in terms of independent variable [-] in Chapter 2 and 5

θ_o Angle from *x*-axis to position vector of the WJ nozzle [rad] in Chapter 3

χ Conserved scalar dissipation in the laminar flamelet model [1/s] in Chapter 2

$\mathbf{\Lambda}$ Diagonal matrix whose diagonal elements are eigenvalues, λ in Chapter 2

λ Wavelength [m] in Chapter 2 or Lagrange multiplier (regularization parameter) in Chapter 2 and 5

λ_i The *i*-th eigenvalue in Chapter 2

μ Viscosity [N s/m^2] in all Chapters

ξ Mixture fraction in terms of dependent variable [-] in Chapter 2 and 5

$\vec{\xi}$ Overall sensitivity vector in Chapter 2

ϖ Solid angle [sr] in Chapter 2

$\dot{\varpi}_i$ Volume production/destruction rate of *i* species [1/s] in Chapter 2

ρ Density [kg/m^3] in all Chapters

$\rho_{i,o}$ Density at the exit of *i*-th nozzle [kg/m^3] in Chapter 2 and 3

ρ_∞ Density of surrounding fluid [kg/m^3] in Chapter 2 and 3

σ Stefan-Boltzmann constant (=5.672×10^{-8}) [W/m^{2}K^4] in Chapter 2 or constant in Chapter 2

$\vec{\varsigma}_j$ The *j*-th orthonormal basis vector in Chapter 2

τ Arbitrary time step [s] in Chapter 5

τ_{ik} Stress tensor in the *i*-direction on a surface whose outward normal is in the *k*-coordinate direction [N/m^2] in Chapter 2

$\vec{\Phi}$ Thermodynamic property vector along with the parameter for the manifolds in Chapter 2

ϕ Angle from *x*-axis vector to the projection vector into *xy* plane of initial injection velocity vector of the WJ [rad] in Chapter 3 or an arbitrary scalar in Chapter 2 and 5

$\langle \phi | \eta \rangle$ Conditional averaged scalar value, ϕ, about mixture faction, η (or written as $\phi(\eta)$) in Chapter 2 and 5

ψ_{12} Momentum flow ratio of the WJ to the SJ [-] in Chapter 3

φ Angle from the projection vector into *xy* plane of initial injection velocity vector of the WJ to initial injection velocity vector of the WJ [rad] in Chapter 3

ω_i^j Mass fraction of the *j* component at the *i*-th jet [-] in Chapter 3

Subscripts

G	The ensemble sharing same conditional averaged value in Chapter 2 and 5
high	High jet Reynolds number in Chapter 2 and 3
i	Jet designator, i.e. i=1, 2 for WJ and SJ respectively in Chapter 3
i,j,k	Coordinate, species, reaction etc. designator in all Chapters
l	Laminar in Chapter 2
low	Low jet Reynolds number in Chapter 2 and 3
o	Initial condition in Chapter 2 and 3
ref	Reference in Chapter 2, 4 and 5
t	Turbulent flow in Chapter 2

Superscripts

con	Convection in Chapter 2
e	Equilibrium state in Chapter 2 and 5
eff	Effective in Chapter 2
in	Inflow in Chapter 4
J	Sequence number in the iteration steps in Chapter 5
j	Species component in gas mixture in Chapter 3
l	Laminar flow in Chapter 2
rad	Radiation in Chapter 2
t	Turbulent flow in Chapter 2
*	Dimensionless variable in Chapter 3
+	Dimensionless variable in Chapter 3
X'	Fluctuation about time-averaged value of X in Chapter 2

X'' Fluctuation about Favre-averaged value of X in Chapter 2 or fluctuation about the conditional mean value of X in terms of mixture fraction η in Chapter 2

Overlines

$\dot{X}$ Flow rate of some quantity, X in all Chapters

$\vec{X}$ Vector, X in all Chapters

$\vec{\vec{X}}$ Matrix, X in all Chapters

$\vec{\vec{X}}^T$ Transpose of the matrix, X

$\tilde{X}$ Favre space-averaging of X in all Chapters

$\overline{X}$ Space or time-averaging of X in all Chapters

Note that the Einstein summation convention is used in all Chapters

Chapter 1
Introduction

1.1 Motivation

Flameless combustion is a recent technology developed for control of nitrogen oxides in the field of combustion engineering. Various names and acronyms have been used to describe this technology including Fuel/Oxidant Direct Injection (FODI) [1], flameless oxidation-FLOX [2], MILD or diluted combustion [3] and High Temperature Air Combustion (HiTAC) [4]. The nitrogen oxides, or NOx, of interest in this subject include NO and NO_2 – N_2O is placed in the category of a Greenhouse Gas and isn't usually categorized as NOx. Flameless combustion provides lower NOx emissions based on in-furnace control of the mixing and reaction mechanisms rather than post treatment methods such as Selective Catalytic Reduction (SCR) [5] or Selective Non-Catalytic Reduction (SNCR) [6] in combustion facilities. Side benefits of flameless combustion include lower peak gas temperatures, uniform heat transfer to furnace loads and compatibility with energy saving strategies such as air preheat and oxy-fuel combustion.

Combustion-generated NOx is formed by three mechanisms [7]: thermal-NOx, prompt-NOx, and fuel-NOx. Thermal-NOx, normally produced from the reaction of oxygen and nitrogen in the combustion air, is considered the dominant mechanism and is closely related to the reaction temperature in the combustion environment. Methods to reduce thermal-NOx formation include lowering the peak combustion temperature, shortening the residence time of combustion air within the high peak temperature region, and lowering the concentration of nitrogen in the

combustion air. With flameless combustion, the reaction product gases are mixed with the fuel and oxidant reactants producing a very diffuse reaction zone – the combustion products (e.g. CO_2, H_2O, CO) are entrained into the reactant feed streams before the main combustion reaction occurs. The diluted reactants cause a small amount of heat release (small temperature variance) and relatively slow combustion reaction (fast energy diffusion). Accordingly, there is a relatively low and uniform gas temperature profile in the furnace environment with a significant reduction in thermal-NOx production.

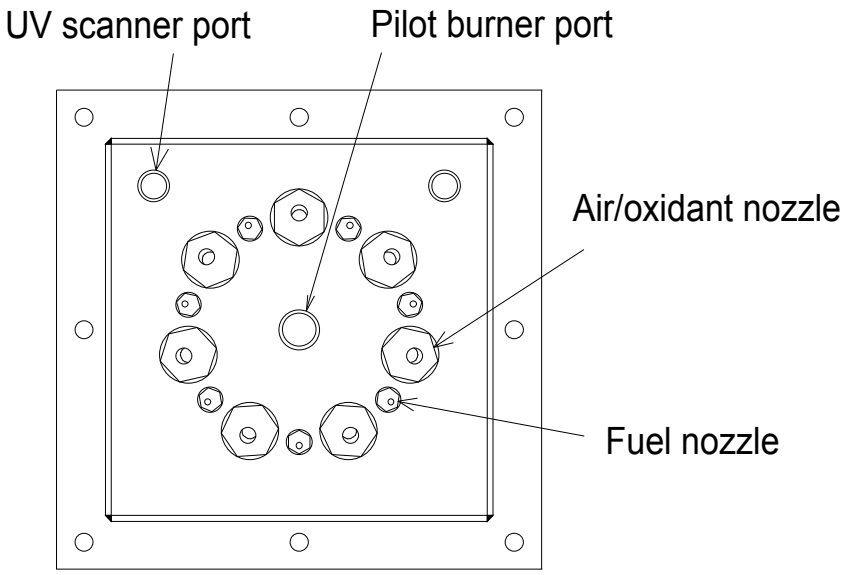

Figure 1.1. A schematic diagram of CGRI burner showing the locations for the air/oxidant and fuel nozzles [8].

The Canadian Gas Research Institute (CGRI) initially developed an ultra-low NOx burner (~310 kW, nonpremixed, natural gas-fired, multiple-jet burner), called the CGRI burner (see Figure 1.1), by adopting the flameless combustion technology. This burner was further studied and improved at the Centre for Advanced Gas Combustion Technology (CAGCT) at Queen's University [1,8,9,

10,11]. A key configuration of the geometry of the CGRI burner, called the 'Strong-Jet/Weak-Jet' (SJ/WJ) configuration, was also studied to understand fundamental characteristics of flameless combustion in the CGRI burner[12,13]. The SJ/WJ system includes a single pair of jets simulating the fuel and oxidant feed streams. The jets have a similar diameter leading to a higher momentum (the Strong Jet) for the oxidant feed and a lower momentum (the Weak Jet) for the fuel feed. The jet feed streams are separated by a specified distance and angle as shown in Figure 1.2.

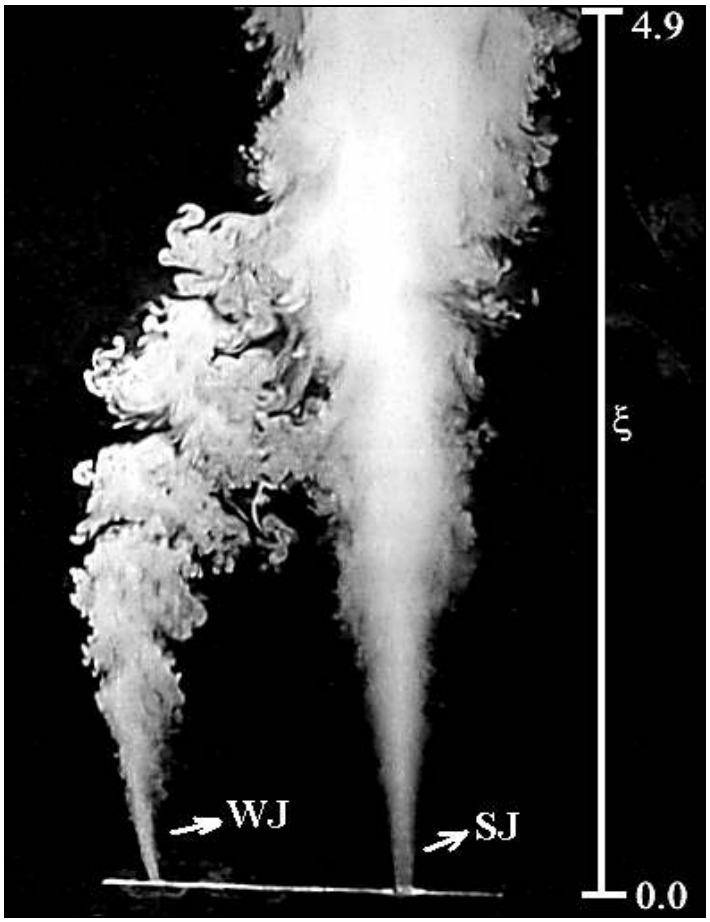

Figure 1.2. Flow visualization photograph of the SJ/WJ interaction under isothermal conditions[12].

Several subjects such as the aerodynamic interaction for the SJ/WJ [12,13], chemical kinetics and reduction of reaction mechanisms for flameless combustion [14], and Computational Fluid Dynamics (CFD) simulation of the flameless combustion in the SJ/WJ furnace [15] were previously studied. Although this previous work made significant contributions in many respects, they have several limitations. This study was, therefore, motivated to improve previous studies and to understand the flameless combustion in the context of SJ/WJ configuration.

1.2 Objectives

The objectives of this present study consist of three parts: (a) a development of 3-D SJ/WJ physical model for an isothermal, free SJ/WJ system, (b) a simplification of a detailed chemical reaction mechanism for flameless combustion, and (c) Reynolds-Averaged Navier-Stokes (RANS) simulation of the turbulent, flameless combustion combined with the simplified chemical kinetics in the SJ/WJ furnace.

A 2-D integral model [13] was previously developed to predict the WJ trajectory for the isothermal, free SJ/WJ system and showed good agreement with experimental data. But, the 2-D integral model has a number of limitations: it can be applied only to a 2-D configuration, i.e. the SJ and the WJ should be coplanar, and the prediction of the WJ behavior is only possible from the nozzle exit to the maximum curved point of the WJ trajectory. Hence, a 3-D SJ/WJ physical model was developed in the present work to overcome the limitations. In addition, important design/operation factors were identified from the 3-D physical model.

The chemical reaction kinetics of flameless combustion is considered to be different from that of typical conventional combustion because of distinct differences in the reaction rates. Accordingly the current reduced chemical kinetic models or those based on few reaction steps, while useful in CFD simulation, have limitations for flameless combustion because they are normally suitable only for typical, conventional combustion systems. Gokulakrishnan [14] attempted to reduce a detailed chemical reaction mechanism for flameless combustion by using Principal Component Analysis (PCA) and sensitivity analysis, but the resulting reduced mechanism contains too many species and reactions to be used in CFD simulation. In this study a significant simplification of a detailed chemical reaction mechanism was made for flameless combustion.

For simplicity many researchers have conducted CFD simulation of flameless combustion with a fast-chemistry assumption [16,17,18,19] and global multi-step reaction mechanisms [2,11,15,17, 18,19,20]. However, some researchers have considered the effects of the detailed chemical kinetics on flameless combustion through the flamelet model [21,22,23,24], the Eddy Dissipation Concept (EDC) [23] and the Conditional Moment Closure (CMC) method [25]. In this work, steady-state RANS simulation of the turbulent flameless combustion in the SJ/WJ furnace was conducted using the Conditional Source-term Estimate (CSE) method [26] associated with the Trajectory-Generated Low-Dimensional Manifolds (TGLDM) method [27] to examine the effects of detailed chemical kinetics.

1.3 Outline of the thesis

This thesis is presented in the form similar to the manuscript format prescribed by the School of Graduate Studies and Research at Queen's University. Chapter 1 presents the motivation and objectives as an introduction to this thesis. Relevant literature for three subjects examined in this work is reviewed in Chapter 2. A 3-D physical model for the SJ/WJ problem is developed in Chapter 3. Chapter 4 covers simplification of a detailed chemical reaction mechanism for the chemical kinetics of flameless combustion. In Chapter 5, steady-state RANS simulation of the flameless combustion in the SJ/WJ furnace is described using the simplified chemical kinetics results from Chapter 4. Finally, conclusions of this work are summarized and future work is recommended in Chapter 6.

Chapter 2
Literature Review

2.1 Introduction

In this chapter, relevant theoretical background is reviewed for three subject areas:

- jet entrainment flow for the SJ/WJ physical model,
- reduction methods for chemical reaction mechanisms, and
- CFD modeling of turbulent combustion.

2.2 Physical model for the Strong-Jet/Weak-Jet system

An appreciation of the primary features of the fuel and oxidant mixing streams is important to understand flameless combustion based on the SJ/WJ technology. Two separate and complex entrainment processes along with merging of the jet streams should be studied. A physical model, describing only basic key features of the system, can be a useful tool to obtain critical information for many engineering applications. This approach can complement CFD simulation and experimental testing in the identification of design/operation controlling factors and the systematic effect analysis of the controlling factors on the system.

Grandmaison *et al.* [13] developed a 2-D integral model to predict the WJ trajectory for the isothermal free SJ/WJ system. Although the 2-D integral model showed good agreement with

experimental data, it was limited to coplanar jets (2-D SJ/WJ configuration) and prediction of the weak jet trajectory up to the point where the jet path has a maximum displacement from the strong jet. In this work an improved 3-D SJ/WJ physical model was developed for the 3-D isothermal free SJ/WJ configuration. The following subsections present a review of the characteristics of a free, circular jet for application in the derivation of the 3-D SJ/WJ physical model.

2.2.1 Entrainment flow

A schematic diagram of a circular (or axisymmetric) free jet is shown in Figure 2.1. On the basis of the self-preservation assumption, supported by experimental data, it is well established that the centerline velocity (u_c) of a circular free jet is inversely proportional to the downstream distance (z), location far enough from the nozzle.

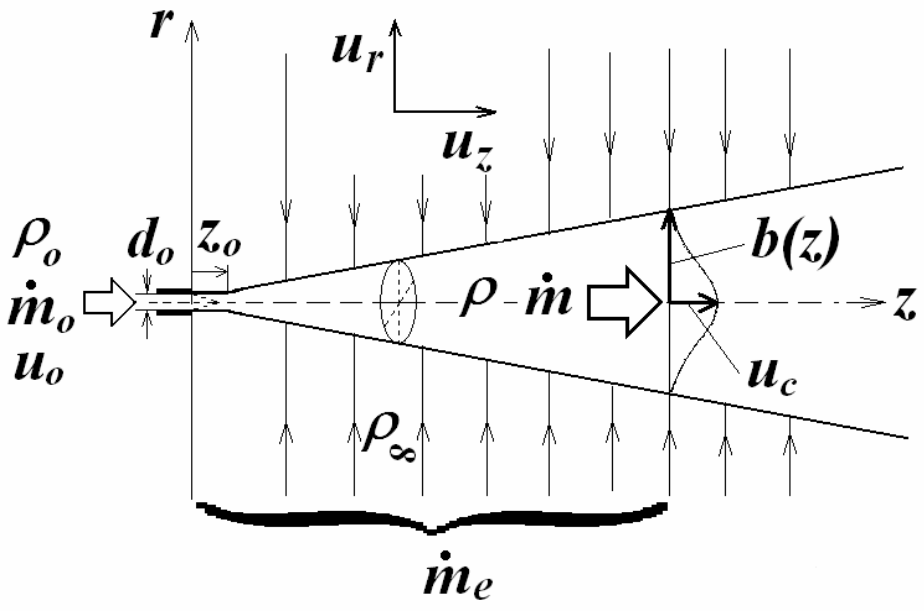

Figure 2.1. A schematic diagram for a circular free jet.

$$\frac{u_0}{u_c} = C_c \frac{(z - z_0)}{d_0} \qquad \text{for} \quad z/d_0 \geq \text{ threshold value} \tag{2.1}$$

The source velocity, u_0, is defined by the ratio of momentum and mass flow rate at the nozzle exit, $u_0 = G_0 / \dot{m}_0$ where G_0 and $\dot{m}_0$ is the momentum and the mass flow rate at the nozzle exit, respectively. The location of virtual origin, z_0, can be ahead or behind the nozzle plane, depending on the boundary layer details at the nozzle. The virtual origin and the centerline velocity decay constant, C_c, are obtained experimentally, using Eq.(2.1). For the high Reynolds number turbulent, free jet, the centerline velocity constant is typically in the range of 0.17 ~ 0.19 as noted by Hussein *et al.* [28]. However, George and Arndt [29] point out that for low Reynolds number, it may not be a constant, but rather a function of the jet source conditions.

A key feature of the circular jet flow is entrainment of ambient fluid, characterized by the mass flow ratio ($\dot{m} / \dot{m}_0$). Ricou and Spalding [30] used a novel experimental method to characterize the entrainment rate of free jets by the relationship:

$$\frac{\dot{m}}{\dot{m}_0} = \begin{cases} C_e \dfrac{(z - z_o)}{d_o} \left(\dfrac{\rho_\infty}{\rho_o} \right)^{\frac{1}{2}} + 1 & \text{for } z > z_o \\ 1 & \text{for } 0 \leq z \leq z_o \end{cases} \tag{2.2}$$

where $\dot{m}$ is mass flow rate at a downstream distance z, expressed as $\dot{m} = \dot{m}_0 + \dot{m}_e$, ρ_∞ and ρ_0 are densities of the ambient fluid and the jet fluid, respectively and C_e is the entrainment coefficient. A value of $C_e = 0.32$ for $\text{Re} \geq 2.5 \times 10^4$ was suggested by Ricou and Spalding [30] and later verified by Hussein *et al.* [28]. However, for low Reynolds number jets, since there is little data in the open literature [31], we introduced an estimate based on the centerline velocity decay constant, $C_{c,low}$, as a function of jet Reynolds number and the ratio of entrainment

coefficient, $C_{e,high}$, and the centerline velocity decay constant, $C_{c,high}$, for the high Reynolds number jet:

$$C_{e,low} = C_{e,high} \frac{C_{c,low}\left(\mathrm{Re}_{jet}\right)}{C_{c,high}} \tag{2.3}$$

In the present work, the linear relation between the centerline velocity decay constant and the jet Reynolds number were obtained from preliminary experimental tests.

2.2.2 Radial entrainment velocity

The radial entrainment velocity of the circular free jet, u_r, plays an important role in deriving the governing equations for the 3-D SJ/WJ physical model. Using the definition of the circular free jet mass flow rate,

$$m = \int_0^r 2\pi\rho u_z(\hat{r}, z)\hat{r}d\hat{r} \quad \text{for } r \gg b(z) \tag{2.4}$$

where ρ is density inside jet flow, u_z is axial velocity of jet flow and r should be located well outside the jet boundary, $b(z)$, where $u_z \approx 0$. By differentiating Eq.(2.4) with respect to z and substituting the continuity equation (axisymmetric case), we can obtain

$$\begin{aligned} \frac{d\dot{m}}{dz} &= \frac{d}{dz}\int_0^r 2\pi\rho u_z \hat{r}d\hat{r} \\ &= 2\pi\rho\int_0^r \frac{\partial}{\partial z}(u_z)\hat{r}d\hat{r} \\ &= 2\pi\rho\int_0^r -\frac{\partial}{\partial r}(\hat{r}u_r)d\hat{r} \\ &= -2\pi\rho r u_r \qquad \text{for } r \geq b(z) \end{aligned} \tag{2.5}$$

From Eq.(2.2) and (2.5), the radial velocity can be expressed as

$$u_r = \begin{cases} -C_1/r & \text{for } z > z_0,\ r \geq b(z) \\ 0 & \text{for } 0 \leq z \leq z_0,\ r \geq b(z) \end{cases} \tag{2.6}$$

where $C_1 = \frac{C_e}{2\pi}\frac{\dot{m}_o}{d_o}\frac{1}{\rho}\left(\frac{\rho_\infty}{\rho_o}\right)^{\frac{1}{2}}$. Due to the entrainment process, the density inside jet flow rapidly becomes equal to the density of the surrounding fluid.

2.3 Reduction methods for detailed chemical reaction mechanisms

An important research topic in the field of combustion is the treatment of elementary chemical reactions for combustion chemistry. The objective is to determine credible reaction mechanisms, parameters and validation of the reaction models for various fuels of industrial interest. Work in this field has led to detailed mechanisms through modeling systems such as GRI-Mech 3.0 [32] which provides reliable information for natural gas combustion. The current version of this mechanism consists of 53 species and 325 reversible reactions. Heavier hydrocarbon fuels involve larger numbers of species and reactions. These mechanisms can lead to more precise predictions of pollutant emissions, and ignition and extinction conditions. But the large number of species creates computational problems when the reaction mechanisms are coupled with the energy and momentum conservation equations in CFD models. Conservation equations must be solved for each species, leading to solution procedures that are impractical in most applications of industrial interest. This has led to the use of and need for reduced chemical reaction mechanisms, describing the essential features of the reaction process with more feasible computational requirements. In this section, several reduction methods will be reviewed.

Global one-step (occasionally two-step), Arrhenius-based reaction mechanisms, developed by fitting experimental and/or numerical data for a certain range of combustion conditions have been widely used for asymptotic studies of hydrocarbon combustion simulation [33,34,35]. For some applications, this approach can provide significant savings in computational time for multi-dimensional combustion simulations. However, the over-simplification of the reaction system leads to poor prediction of important minor species and low confidence in the results for unconventional combustion conditions such as flameless combustion. Some of these drawbacks can be alleviated by using multi-step mechanisms [36,37,38,39] (sometimes called semi-global mechanisms) derived from skeletal chemical reaction mechanisms. With this approach only those species and reactions considered absolutely necessary are included through traditional reduction methods such as the Quasi-Steady State Approximation (QSSA) and Partial Equilibrium Assumption (PEA) [39,40]. However, these methods are generally applicable only to a subset of species and reactions selected with a good understanding of the chemical process making it very difficult to reduce the targeted mechanism into a reliable kinetic model.

Another widely used reduction method is sensitivity analysis [41]. In this procedure, the relative importance of reactions in a targeted mechanism can be assessed by evaluating the derivatives of dependent variables with respect to reaction rate constants. With this information, more important reactions can be more highly ranked relative to less significant ones. Reaction flow analysis [40, 42] is commonly used as a complementary reduction method with sensitivity analysis. Like sensitivity analysis, reaction flow analysis can also identify the order of importance of reactions based on the chemical production/destruction rate of species for each reaction. In addition, it can provide quantitative information about the structure of reaction pathways for a targeted chemical reaction mechanism. Results from these two reduction methods

can be interpreted by Principal Component Analysis (PCA) [43,44,45]. Any reduction size can be obtained based on criteria for the sensitivity analysis and the reaction flow analysis. However, excessive reductions usually lead to unrealistic reduced chemical reaction mechanism. From the author's experience, about 30% reduction in the number of species may be normally expected for a feasible reduced chemical reaction mechanism while more than 60% reduction in the number of reactions can be expected.

Other important reduction methods include Computational Singular Perturbation (CSP) [46,47,48, 49,50], Intrinsic Low-Dimensional Manifolds (ILDM) [51,52,53,54], Trajectory-Generated Low-Dimensional Manifolds (TGLDM) [27] and the Rate-Controlled Constrained-Equilibrium (RCCE) method [55,56,57,58,59].

The CSP method proposed by Lam and Goussis [46,47] analyzes the chemical time-scale of a targeted chemical reaction mechanism and separates it into fast and slow subspaces to remove the stiffness of the ODEs transformed from the targeted chemical reaction mechanism. Although the CSP method can save computational time, the number of dependent variables, i.e. the number of species in the targeted chemical reaction mechanism, remains the same in the reduced system. Accordingly, while the evaluation time for the production/destruction of chemical species (reaction rates) is shortened, we cannot reduce the number of partial differential equation (PDE) in the multi-dimensional combustion simulation (computational times for CFD simulations is more strongly influenced by the number of species rather than the number of reactions).

The ILDM method proposed by Maas and Pope [51] is conceptually similar to the CSP method, but uses a different approach for the reduction process. ILDM identifies a user-defined dimensional slow subspace (manifolds) within the composition space of a targeted chemical reaction mechanism. Properties such as density, temperature and mass fraction are tabulated in a lookup table for the user-defined lower dimension subspace. The most attractive advantage of this manifold approach is that only a small number of dependent variables (the dimension of manifolds) need to be solved in combustion simulation, and other properties can be interpolated from the lookup table. However, with the ILDM method, it is extremely difficult to identify the slow subspace for relatively large chemical reaction mechanisms. In addition, the matrix making the perturbations due to chemical reaction and physical mixing projected into the slow subspace may need to be tabulated, and this requires considerable amount of computer memory.

To avoid these difficulties, Pope and Maas [27] proposed the TGLDM method where the manifolds are defined by a group of reaction trajectories in composition space. The resulting manifolds can be easily constructed because trajectories are easily obtained from an ODE system representing a targeted chemical reaction mechanism. The projection matrix due to chemical reaction might be unnecessary because the reaction rate vector is always in the tangent plane of the manifolds.

The RCCE method transforms a targeted chemical reaction mechanism into a more manageable Differential-Algebraic Equation (DAE) system developed from a set of constraints (a linear combination of species concentration) and using the relationship between the constraints and the so-called constrained equilibrium state obtained by maximizing entropy under the constraints. The constrained equilibrium state has the same meaning as the reaction trajectory in the

composition space. Although several issues in the application of RCCE method such as choosing the constraints, finding initial, boundary conditions are not well settled yet, the basic concepts show promise for future work.

In the following subsections, sensitivity analysis, reaction flow analysis, PCA, ILDM and TGLDM will be described in more detail. Although the ILDM method is not used in this study, it will be reviewed to provide a better understanding of manifold concepts.

2.3.1 Sensitivity analysis

Sensitivity analysis is a method to impartially evaluate the sensitivity of dependent variables in terms of parameters for a dynamic system such as a detailed chemical reaction mechanism. This permits a reduction in the number of reactions allowing us to remove less important reactions from the detailed chemical reaction mechanism.

A dynamic system can be written in parametric form as:

$$\frac{d\vec{Y}}{dt} = \vec{f}(\vec{Y};\vec{k}) \tag{2.7}$$

where t is time, $\vec{Y}$ is a dependent variable vector, $\left[Y_1, Y_2, ..., Y_n\right]^T$, $\vec{f}$ is an arbitrary continuous smooth function vector for the production/destruction rate of the dependent variables, $\left[f_1, f_2, ..., f_n\right]^T$, $\vec{k}$ is a parameter vector, $\left[k_1, k_2, ..., k_m\right]^T$, n is the number of dependent variables (e.g. the number of species in chemical reaction mechanism) and m is the number of parameters

(e.g. the number of reactions in chemical reaction mechanism). A first-order sensitivity coefficient matrix (or simply the sensitivity coefficient matrix), $\beta_{i,j}$, is defined as

$$\beta_{i,j} = \frac{\partial Y_i}{\partial k_j} \tag{2.8}$$

where i = 1,2,…,n, j = 1,2,…,m. The sensitivity equation obtained from differentiating Eq.(2.7) with respect to the parameters can be expressed in the form:

$$\frac{d\beta_{i,j}}{dt} = \frac{\partial f_i}{\partial k_j} + \left(\frac{\partial f_i}{\partial Y_l}\right)\beta_{l,j} \tag{2.9}$$

where $\left(\frac{\partial f_i}{\partial Y_l}\right)$ is the Jacobian matrix. The sensitivity equation, Eq.(2.9), is simultaneously solved with Eq.(2.7). The solution of the sensitivity equation is a set of local $n \times m$ sensitivity coefficient matrices. The set of the local sensitivity coefficient matrices from an initial condition can be manipulated to obtain a total sensitivity coefficient matrix for the PCA process.

2.3.2 Reaction flow analysis

For a reaction mechanism, we can quantitatively evaluate the production/destruction rate of each species associated with each reaction. Hence, less significant reactions, contributing less production/destruction rates can be identified and removed. In addition, with the information obtained from the reaction flow analysis, we can construct a reaction flow structure. For a chemical reaction mechanism, Eq.(2.7) can be reformulated in terms of each reaction rate as

$$\frac{dY_i}{dt} = \sum_{j=1}^{m} F_{i,j} \tag{2.10}$$

where $F_{i,j}$ is the reaction rate of *i*-th species due to *j*-th reaction. Thus, we can obtain a set of the local $n \times m$ reaction rate matrices. Similar to the sensitivity analysis, the set of the local reaction rate matrices can be used to obtain a total reaction rate matrix for the PCA process. Also, we can find total reaction pathways by integrating the local $n \times m$ reaction rate matrix with respect to time.

2.3.3 Principal Component Analysis

PCA is basically a method to reduce the dimension of an information matrix without significant loss of accuracy, based on the orthogonal linear transformation. This can be done by finding a set of orthonormal basis vectors (called Principal Component (PC) and interpreted as coordinates of the system) of the information matrix and only considering the elements within several important basis that correspond to larger magnitude eigenvalues. For the reduction of chemical reaction mechanisms, we can obtain the information matrix from sensitivity analysis and reaction flow analysis.

As mentioned in the previous subsection, the total sensitivity coefficient matrix is obtained from the set of the local sensitivity coefficient matrices by adding each local sensitivity coefficient matrix in the row and multiplying it by its transpose matrix, that is, $\mathbf{B}^{\mathrm{T}}\mathbf{B}$ where

$$\mathbf{B} = \begin{bmatrix} \beta_{i,j}(t_1) \\ \beta_{i,j}(t_2) \\ \vdots \\ \beta_{i,j}(t_f) \end{bmatrix} \tag{2.11}$$

Since the $m \times m$ total sensitivity coefficient matrix, $\mathbf{B}^{\mathrm{T}}\mathbf{B}$, is a real symmetric and positive-semidefinite matrix, the resulting normalized eigenvectors are orthonormal basis and all corresponding eigenvalues are non-negative. For the reduction, instead of using only several important PCs, all the components can be used by considering the eigenvalue as the weighting factor as

$$\vec{\xi} = \sum_{j=1}^{m} abs\left(\vec{\varsigma}_j\right)\lambda_j \tag{2.12}$$

where λ_j is the *j*-th eigenvalue, $\vec{\varsigma}_j$ is the *j*-th orthonormal basis vector having m elements, and therefore, $\vec{\xi}$ is called the overall sensitivity vector. Therefore, by comparing the magnitude of the elements in the overall sensitivity vector, we can identify the relative importance of reactions. Note that the symbol $abs(\vec{v})$ is used here for the application of the absolute value for each element of the vector, not the vector itself.

Finally, the important reactions that remain in a reduced mechanism are determined by choosing a criterion for the overall sensitivity vector, i.e.

$$\frac{\vec{\xi}}{\left|\vec{\xi}\right|} \geq criterion\ value \tag{2.13}$$

Similarly, the set of the local reaction rate matrices can be manipulated to the total reaction matrix, $\mathbf{F}^{\mathrm{T}}\mathbf{F}$ where

$$\mathbf{F} = \begin{bmatrix} F_{i,j}(t_1) \\ F_{i,j}(t_2) \\ \vdots \\ F_{i,j}(t_f) \end{bmatrix} \tag{2.14}$$

Thus, the $m \times m$ total reaction rate matrix and a specified criterion are also used to obtain additional information for the reduction of the chemical reaction mechanism through PCA process.

2.3.4 Intrinsic Low-Dimensional Manifolds

Using ILDM method, we can construct user-defined dimensional manifolds of chemical reaction mechanisms. This is based on the separation of fast time scales and slow time scales by investigating eigenvalues in the Jacobian of the reaction rate vector in terms of the dependent variable.

Like Eq.(2.7) (but with an implicit expression of the parameters), a set of stiff ODEs representing chemical reaction mechanism can be expressed as

$$\frac{d\vec{Y}}{dt} = \vec{f}(\vec{Y}) \tag{2.15}$$

Time scales of the stiff ODEs system are identified by multiplicatively inversing the eigenvalues of the Jacobian, $\mathbf{J} = \frac{\partial f_i}{\partial Y_k}$ where $i = 1, ..., n$ and $k = 1, ..., n$. Eigenvectors corresponding to the eigenvalues indicate the movement directions of the thermodynamic state in the composition

space. Hence, we can identify fast and slow movements in the composition space and ignore fast movements by assuming all the thermodynamic states lie in the slow subspace. The eigenvalues and eigenvectors of the Jacobian can be obtained by the eigen-decomposition

$$\mathbf{J} = \mathbf{V}\Lambda\tilde{\mathbf{V}} \tag{2.16}$$

where $\mathbf{\Lambda}$ is diagonal matrix in the form of 2×2 complex eigenvalue blocks, whose diagonal element is the real part of eigenvalue in the descending order, $\mathbf{V}$ is the right eigenvector matrix consisting of the column-wise eigenvectors of $\mathbf{J}$ in the order of the corresponding eigenvalues, and $\tilde{\mathbf{V}}$ is inverse matrix of $\mathbf{V}$. The eigenvalues and eigenvectors can be separated into m slow and $n-m$ fast coordinates (where m is a user-defined dimension of manifolds plus the number of conserved variables in the ODE system such as element mass fractions, not the number of reactions, Eq.(2.7)):

$$\mathbf{V} = \left(\mathbf{v}_1 \cdots \mathbf{v}_m \mid \mathbf{v}_{m+1} \cdots \mathbf{v}_n\right) = \left(\mathbf{V}_s \mid \mathbf{V}_f\right) \tag{2.17}$$

$$\tilde{\mathbf{V}} = \begin{pmatrix} \tilde{\mathbf{v}}_1 \\ \vdots \\ \tilde{\mathbf{v}}_m \\ \hline \tilde{\mathbf{v}}_{m+1} \\ \vdots \\ \tilde{\mathbf{v}}_n \end{pmatrix} = \begin{pmatrix} \tilde{\mathbf{V}}_s \\ \hline \tilde{\mathbf{V}}_f \end{pmatrix} \tag{2.18}$$

$$\Lambda = \left(\begin{array}{ccc|ccc} \lambda_1 & \cdots & 0 & 0 & \cdots & 0 \\ \vdots & \ddots & \vdots & \vdots & \ddots & \vdots \\ 0 & \cdots & \lambda_m & 0 & \cdots & 0 \\ \hline 0 & \cdots & 0 & \lambda_{m+1} & \cdots & 0 \\ \vdots & \ddots & \vdots & \vdots & \ddots & \vdots \\ 0 & \cdots & 0 & 0 & \cdots & \lambda_n \end{array}\right) \tag{2.19}$$

Note that for simplicity the imaginary part of the eigenvalue is not indicated in Eq.(2.19).

Therefore, if we assume that the fast reactions are quickly equilibrated (exhausted), Eq.(2.15) can be approximated as

$$\tilde{\mathbf{V}}_s \frac{d\mathbf{Y}}{dt} = \tilde{\mathbf{V}}_s \mathbf{f} \tag{2.20-a}$$

$$0 = \tilde{\mathbf{V}}_f \mathbf{f} \tag{2.20-b}$$

The $n-m$ algebraic equations, Eq.(2.20-b), are used to construct the ILDM together with the parameter equations expressing the conserved variables of the ODE systems and user-specified variables.

While the ILDM method appears to have theoretical simplicity, many issues arise in the application of this method to relatively large chemical reaction mechanisms. Since the Jacobian matrix is often ill-conditioned, Schur-decomposition is usually used, instead of eigen-decomposition, to separate fast and slow time scale processes, and later more numerical steps are added to obtain invariant slow and fast subspaces. Also, since the production/destruction rate vector, $\mathbf{f}$, is not in the tangent plane of the ILDM, a projection matrix needs to be tabulated – this projects the reaction rate vector into the manifolds. The greatest difficulty is typically the convergence problem in finding points of the ILDM and this problem increases with larger chemical reaction mechanisms.

2.3.5 Trajectory-Generated Low-Dimensional Manifolds

Because the difficulties in the application of the ILDM method to relatively large size of chemical reaction mechanism are severe, TGLDM method was proposed as alternative method to obtain the low dimensional manifolds in easy way. In the TGLDM method the manifolds are defined by

a group of reaction trajectories in the composition space at an adiabatic, closed system under constant pressure.

For an adiabatic, closed system, mass balance equation for each species can be expressed as

$$\frac{dY_i}{dt} = \frac{\dot{w}_i W_i}{\rho},\ i = 1,...,n \tag{2.21}$$

where t is time, n is the number of species, Y_i is the mass fraction of i species, $\dot{w}_i$ is the molar production/destruction rate of i species, W_i is the molecular weight of i species and ρ is the density of system. And, energy balance equation can be expressed as

$$\sum_{i=1}^{n} Y_i h_i^o + \int_{T_{ref}}^{T} \left(\sum_{i=1}^{n} Y_i c_{p,i} \right) dT - h = 0 \tag{2.22-a}$$

or

$$\frac{dT}{dt} = -\frac{\sum_{i=1}^{n} h_i \dot{w}_i W_i}{\rho \left(\sum_{i=1}^{n} Y_i c_{p,i} \right)} \tag{2.22-b}$$

where T is the temperature of system, T_{ref} is the reference temperature (298 K), h is the specific enthalpy of mixture ($h = \sum_{i=1}^{n} Y_i h_i = \text{constant}$), h_i is the specific enthalpy of i species, h_i^o is the standard specific enthalpy of formation of i species (at 1 atm, 298 K), $c_{p,i}$ is the specific heat of i species at constant pressure. In addition, the ideal gas law is

$$p = \rho R T \left(\sum_{i=1}^{n} \frac{Y_i}{W_i} \right) \tag{2.23}$$

where p is the pressure of system and R is the gas constant (8.31447 J/mol K). For each reaction trajectory, the governing equations are solved with an initial condition obtained from the 'extreme values of major species' concept [27] in which the values of selected major species are obtained by setting other minor species zero, based on the mass balance of participating elements. Then, the solutions from the reasonably-assumed initial conditions are tabulated in a function of user-selected parameters, *u*, *v*, *w*,…, that can be naturally selected from major species. Therefore, we can construct the manifolds mathematically expressed as $\vec{\Phi}(u,v,w,...)$ where $\vec{\Phi}$ is thermodynamic property vector like $\left(\rho, T, Y_1, Y_1, ..., Y_n, \dot{w}_1, \dot{w}_2, ..., \dot{w}_n\right)^T$.

Now, we will discuss an important issue occurring in the application of the manifolds with physical mixing process (convection and/or diffusion). A general mass transport equation can be expressed as

$$\frac{\partial \vec{Y}(\vec{x},t)}{\partial t} = \vec{S}(\vec{Y}(\vec{x},t)) + \vec{F}(\vec{x},t) \tag{2.24}$$

where $\vec{Y}(\vec{x},t)$ is the state vector in the composition space at a certain time and location, *t* and $\vec{x}$, $\vec{S}$ is the chemical production/destruction rate vector and $\vec{F}$ is the physical mixing vector due to convection and/or diffusion. The R.H.S. in Eq.(2.24) is a continuous, smooth vector function. Since every state vector is supposed to lie on manifolds in the TGLDM (and ILDM) method, a linear projection of the time derivative in Eq.(2.24) onto the manifolds can be approximately equated to the time derivative of the manifolds,

$$\frac{\partial \vec{\Phi}}{\partial t} \approx proj\left(\frac{\partial \vec{Y}}{\partial t}\right) \tag{2.25}$$

If we consider 2-D manifolds, $\vec{\Phi}(u,v)$, the time derivative of the manifolds can be

$$\frac{\partial\vec{\Phi}}{\partial t}=\vec{\Phi}_u\frac{\partial u}{\partial t}+\vec{\Phi}_v\frac{\partial v}{\partial t}\approx\vec{\vec{P}}(\vec{S}+\vec{F}) \tag{2.26}$$

where $\vec{\Phi}_u=\frac{\partial\vec{\Phi}}{\partial u}$, $\vec{\Phi}_v=\frac{\partial\vec{\Phi}}{\partial v}$ and $\vec{\vec{P}}$ is the projection matrix projecting a vector onto the manifolds. This projection matrix can be defined in several ways such as geometrically orthogonal projection on the manifold, the ILDM-derived projection [52] or simple perpendicular projection in the direction of parameter space.

A remarkable benefit of TGLDM method is that $\vec{\vec{P}}\vec{S}=\vec{S}$ because the chemical production/destruction rate vector is always in the tangent plane of manifolds. Also, we can select the parameters so that $\vec{\Phi}_u$ and $\vec{\Phi}_v$ are orthonormal relation such as $u=Y_{CO2}$, $v=Y_{H2O}$. Therefore, by algebraically manipulating Eq.(2.26), transport equations for the parameters (u,v) can be obtained as

$$\frac{\partial u}{\partial t}=S_u+(\vec{\Phi}_u^T\vec{\vec{P}})\vec{F} \tag{2.27-a}$$

$$\frac{\partial v}{\partial t}=S_v+(\vec{\Phi}_v^T\vec{\vec{P}})\vec{F} \tag{2.27-b}$$

where S_u and S_v are the chemical production/destruction rate of u and v, respectively, obtained from the chemical production/destruction rate vector, $\vec{S}$.

While the chemical production/destruction rate term in the parameter transport equation does not include any projection matrix, the physical mixing term still does. Since the projection matrix in the application of TGLDM to CFD simulation usually demands huge computation resources

(computational time and data storage space), practically we assume the simple perpendicular projection that is to project the physical mixing force, $\vec{F}$, onto the manifolds in the perpendicular direction of the parameter space. Hence, Eq.(2.27) can be greatly simplified into

$$\frac{\partial u}{\partial t} = S_u + F_u \tag{2.28-a}$$

$$\frac{\partial v}{\partial t} = S_v + F_v \tag{2.28-b}$$

where F_u and F_v is the physical mixing of *u* and *v*, respectively, caused by only each parameter. In conclusion, mass transport equations for all species like Eq.(2.24) can be represented by only few parameter transport equations like Eq.(2.28).

2.4 Modeling of turbulent combustion

In Reynolds-Averaged Navier-Stokes (RANS) or Large Eddy Simulation (LES) of nonpremixed turbulent combustion, one of essential issues is to adequately estimate the mean (time-averaged) chemical production/destruction rate term in the Favre-averaged (or filtered) species mass balance equations. Since chemical reaction rate is normally expressed as a highly nonlinear function of temperature and mass fractions such as the Arrhenius expression, its Favre-averaged (or filtered) value cannot be simply described by the averaged temperature and mass fractions [60, 61]. The Probability Density Function (PDF)/Mixing or Eddy Dissipation Concept (EDC) approach is widely used to deal with this mean production/destruction rate estimation problem. In this section, several methods classified in the PDF/Mixing approach will be reviewed with the governing RANS simulation equations for nonpremixed turbulent reacting flow.

2.4.1 Favre-averaged governing equations for turbulent reacting flow

The RANS turbulence model is predominantly used for steady-state, nonpremixed, turbulent reacting flow. Under several assumptions of no gravity effect, Fick's law, Fourier's law, single diffusivity, single Schmidt number, unity Lewis number, and gradient closure hypothesis, the steady-state Favre-averaged governing equations can be expressed in the form described below. (Note that Favre-averaged and time-averaged values are expressed with a tilda and bar, over the respective symbols such as $\phi = \overline{\phi} + \phi' = \tilde{\phi} + \phi''$ where $\tilde{\phi}$ is defined as $\overline{\rho\phi}/\overline{\rho}$.)

Continuity equation

$$\frac{\partial}{\partial x_k}\left(\overline{\rho}\tilde{u}_k\right) = 0 \tag{2.29}$$

where x_k is spatial variable in the *k*-coordinate, $\overline{\rho}$ is time-averaged density and $\tilde{u}_k$ is Favre-averaged velocity in the *k*-direction.

Momentum equation

$$\frac{\partial}{\partial x_k}\left(\overline{\rho}\tilde{u}_k\tilde{u}_i\right) = -\frac{\partial \overline{p}}{\partial x_i} + \frac{\partial}{\partial x_k}\left(\overline{\tau_{ik}^l} - \overline{\rho u_k'' u_i''}\right) \tag{2.30}$$

where $\overline{p}$ is time-averaged static pressure, τ_{ik}^l is stress tensor for laminar flow in the *i*-coordinate direction on a surface whose outward normal is in the *k*-coordinate direction, u_i'' is Favre-averaged velocity fluctuation in the *i*-coordinate direction, and $-\overline{\rho u_k'' u_i''}$ is the Reynolds stress tensor. These two tensors can be modeled by the Newtonian fluid [62] and Boussinesq hypothesis [60], respectively, as

$$\tau_{ik}^{l} = \mu_l \left(\frac{\partial u_i}{\partial x_k} + \frac{\partial u_k}{\partial x_i} \right) - \frac{2}{3} \mu_l \frac{\partial u_j}{\partial x_j} \delta_{ik} \tag{2.31}$$

$$-\overline{\rho u_k'' u_i''} = -\overline{\rho u_i'' u_k''} = \overline{\tau_{ik}^{t}} = \mu_t \left(\frac{\partial \tilde{u}_i}{\partial x_k} + \frac{\partial \tilde{u}_k}{\partial x_i} \right) - \frac{2}{3} \left(\overline{\rho} \tilde{k} + \mu_t \frac{\partial \tilde{u}_j}{\partial x_j} \right) \delta_{ik} \tag{2.32}$$

where μ_l and μ_t are the laminar and turbulent viscosity, respectively, $\tilde{k}$ is turbulence kinetic energy, and δ_{ik} is Kronecker delta.

Standard k-ε model

$$\mu_t = C_\mu \overline{\rho} \frac{\tilde{k}^2}{\tilde{\varepsilon}} \tag{2.33}$$

$$\frac{\partial}{\partial x_k} \left(\overline{\rho} \tilde{u}_k \tilde{k} \right) = \frac{\partial}{\partial x_k} \left[\left(\mu_l + \frac{\mu_t}{\sigma_k} \right) \frac{\partial \tilde{k}}{\partial x_k} \right] - \overline{\rho u_i'' u_k''} \frac{\partial \tilde{u}_i}{\partial x_k} - \frac{\mu_t}{\overline{\rho}^2} \frac{\partial \overline{\rho}}{\partial x_k} \frac{\partial \overline{p}}{\partial x_k} - \overline{\rho} \tilde{\varepsilon} \tag{2.34}$$

$$\frac{\partial}{\partial x_k} \left(\overline{\rho} \tilde{u}_k \tilde{\varepsilon} \right) = \frac{\partial}{\partial x_k} \left[\left(\mu_l + \frac{\mu_t}{\sigma_\varepsilon} \right) \frac{\partial \tilde{\varepsilon}}{\partial x_k} \right] - C_{\varepsilon 1} \frac{\tilde{\varepsilon}}{\tilde{k}} \left(\overline{\rho u_i'' u_k''} \frac{\partial \tilde{u}_i}{\partial x_k} + \frac{\mu_t}{\overline{\rho}^2} \frac{\partial \overline{\rho}}{\partial x_k} \frac{\partial \overline{p}}{\partial x_k} \right) - C_{\varepsilon 2} \overline{\rho} \frac{\tilde{\varepsilon}^2}{\tilde{k}} \tag{2.35}$$

where $\tilde{k}$ is the Favre-averaged turbulence kinetic energy ($=\frac{1}{2} \frac{\overline{\rho u_i'' u_i''}}{\overline{\rho}}$), $\tilde{\varepsilon}$ is the Favre-averaged turbulence dissipation rate ($=-\frac{1}{\overline{\rho}} \overline{u_i'' \frac{\partial \tau_{ik}}{\partial x_k}}$), $C_\mu = 0.09$, $C_{\varepsilon 1} = 1.44$, $C_{\varepsilon 2} = 1.92$, $\sigma_k = 1.0$ and $\sigma_\varepsilon = 1.30$ [63]. The second term on the right side of Eq.(2.34) and (2.35) can be modeled by

$$-\overline{\rho u_i'' u_k''} \frac{\partial \tilde{u}_i}{\partial x_k} = \mu_t S^2 \tag{2.36}$$

where S is the modulus of the mean rate-of-strain tensor ($=\sqrt{2 S_{ij} S_{ij}}$), and the third term,

$$-\frac{\mu_t}{\overline{\rho}^2} \frac{\partial \overline{\rho}}{\partial x_k} \frac{\partial \overline{p}}{\partial x_k} = -g_k \frac{\mu_t}{\overline{\rho} \, \mathrm{Pr}_t} \frac{\partial \overline{\rho}}{\partial x_k} \tag{2.37}$$

where Pr_t is the turbulent Prandtl number (= 0.85) and g_k is gravity in the k-direction, can be negligible under the assumption of no gravity effect [64].

Energy equation

The chemical heat release term can be expressed explicitly or implicitly in the energy equation:

$$\frac{\partial}{\partial x_k}\left(\bar{\rho}\tilde{u}_k\left(\widetilde{\Delta h}+\frac{\tilde{u}_i\tilde{u}_i}{2}\right)\right)=\frac{\partial}{\partial x_k}\left(-\overline{q_k^{con}}+\overline{q_k^{rad}}-\sum_j^n\overline{h_j\vec{J}_j}+\overline{\tau_{ik}^{eff}u_i}\right)-\sum_j^n h_j^o\bar{\dot{w}}_j W_j \qquad (2.38\text{-a})$$

$$\text{with } \Delta h=\int_{T_{ref}}^{T}\left(\sum_j^n Y_j c_{p,j}\right)dT$$

or

$$\frac{\partial}{\partial x_k}\left(\bar{\rho}\tilde{u}_k\tilde{h}\right)=\frac{\partial}{\partial x_k}\left(\frac{\mu_l+\mu_t}{\mathrm{Pr}_t}\frac{\partial\tilde{h}}{\partial x_k}+\overline{q_k^{rad}}\right) \qquad (2.38\text{-b})$$

$$\text{with } h=\Delta h+h^o=\int_{T_{ref}}^{T}\left(\sum_j^n Y_j c_{p,j}\right)dT+\sum_j^n Y_j h_j^o$$

where n is the involved species number, T is the temperature, T_{ref} is the reference temperature (298 K), Δh is the specific sensible enthalpy of mixture, h is the specific enthalpy of mixture, h_j is the specific enthalpy of j species, h^o is the standard specific enthalpy of mixture (at 1 atm, 298 K), h_j^o is the standard specific enthalpy of formation of j species (at 1 atm, 298 K), q_k^{con} is the heat flux due to conduction in the k-direction, q_k^{rad} is the heat flux due to radiation in the k-direction, $\vec{J}_j$ is the diffusion flux vector of j species that can be expressed by Fick's law, $\overline{\tau_{ik}^{eff}u_i}$ is the viscous dissipation heat that is often negligible, $\bar{\dot{w}}_j$ is the mean (time-averaged) molar production/destruction rate of j species, W_j is the molecular weight of j species, Y_j is the

mass fraction of j species, $c_{p,j}$ is the specific heat of j species at constant pressure, and Pr_t is turbulent Prandtl number (= 0.85). Eq.(2.38-a) is the explicit form and Eq.(2.38-b) is the implicit form.

The conduction heat flux term can be modeled by Fourier's law of heat conduction:

$$\overline{q_k^{con}} = -(k_l + k_t)\frac{\partial \tilde{T}}{\partial x_k} \tag{2.39}$$

where k_l and k_t is the thermal conductivity for laminar and turbulence, respectively. The radiation heat flux, q_k^{rad}, is expressed in vector form [65] as

$$\vec{q}^{rad}(\vec{x}) = \int_0^{4\pi} \vec{s} \int_0^{\infty} i'_\lambda(\vec{x},\vec{s})\, d\lambda d\varpi = \int_0^{4\pi} i'(\vec{x},\vec{s})\vec{s}\, d\varpi \tag{2.40}$$

where i'_λ is the directional spectral intensity, i' is the directional total intensity, $\vec{x}$ is the position vector, $\vec{s}$ is the directional vector, λ is the wavelength, ϖ is the solid angle. Thus, we need to know the directional spectral intensity passing in some direction ($\vec{s}$) at a certain point ($\vec{x}$) to calculate the radiation heat flux. However, since using the direction spectral intensity requires significant computational resources, by assuming gray medium and surface, the directional total intensity is used instead. In order to obtain the directional total intensity the radiative transfer equation (RTE) is derived by a radiation balance. With the additional assumption of negligible scatter effects, we can significantly simplify the RTE to the form,

$$\frac{di'(\vec{x},\vec{s})}{dS} = -ai'(\vec{x},\vec{s}) + an_r^2\frac{\sigma T^4}{\pi} \tag{2.41}$$

where S is path length, a is absorption coefficient, n_r is refractive index and σ is Stefan-Boltzmann constant (5.672×10^{-8} W/m^{2}K^4).

Several radiation models are currently available in the commercial CFD software FLUENT [64] used in this work. The Discrete Ordinates (DO) radiation model [66,67,68] and Discrete Transfer Radiation Model (DTRM) [69] are applicable for a wide range of optical thickness, the absorption coefficient times characteristic length of CFD simulation domain, while other radiation models such as P-1 model and Rosseland radiation model [65] are only suitable for thick optical thickness cases (>> 1). And, because the DTRM is not currently available for the parallel computation environment, the DO radiation model is a proper choice for the thin optical thickness and parallel computation. Also, the weighted-sum-of-gray-gases model (WSGGM) along with proper coefficients [65,70,71] is used to evaluate the absorption coefficient for the gas medium.

Favre-averaged mixture faction and mixture fraction variance

The mixing field of the nonpremixed combustion simulation is normally described by the mixture fraction and its variance:

$$\frac{\partial}{\partial x_k}\left(\bar{\rho}\tilde{u}_k\tilde{\xi}\right)=\frac{\partial}{\partial x_k}\left(\frac{\mu_t}{\sigma_f}\frac{\partial\tilde{\xi}}{\partial x_k}\right) \tag{2.42}$$

$$\frac{\partial}{\partial x_k}\left(\bar{\rho}\tilde{u}_k\widetilde{\xi''^2}\right)=\frac{\partial}{\partial x_k}\left(\frac{\mu_t}{\sigma_g}\frac{\partial\widetilde{\xi''^2}}{\partial x_k}\right)+C_{g1}\mu_t\left(\frac{\partial\tilde{\xi}}{\partial x_k}\right)^2-C_{g2}\bar{\rho}\frac{\tilde{\varepsilon}}{\tilde{k}}\widetilde{\xi''^2} \tag{2.43}$$

where $\tilde{\xi}$ is the Favre-averaged mixture fraction, $\widetilde{\xi''^2}$ is the Favre-averaged mixture fraction variance [72], $\sigma_f=1.0$, $\sigma_g=1.0$, $C_{g1}=2.86$ and $C_{g2}=2.0$. In two-stream nonpremixed system, the Favre-averaged mixture fraction is defined as

$$\tilde{\xi}=\frac{\tilde{Z}_i-\tilde{Z}_{i2}}{\tilde{Z}_{i1}-\tilde{Z}_{i2}}\left(=\frac{\tilde{h}-\tilde{h}_2}{\tilde{h}_1-\tilde{h}_2}\ \text{for adiabatic condition}\right) \tag{2.44}$$

where $\tilde{Z}_i$ is Favre-averaged mass fraction of i element, $\tilde{Z}_{i1}$ and $\tilde{Z}_{i2}$ are Favre-averaged mass fraction of i element in the stream of 1 and 2, respectively.

The mixing field described by the mixture fraction and mixture fraction variance depicts the mixing phenomenon in the multi-component system. The mixture fraction transport equation is derived under the assumption that the diffusivities of all species of the mixture are the same. Otherwise, all the species mass transport equations must be solved for the mixing field. Also, the mixture fraction and mixture fraction variance are widely used to determine the shape of a presumed PDF that will play an important role in estimating averaged scalar values.

Mass transport equation

The mass transport equation can be expressed in the form:

$$\frac{\partial}{\partial x_k}\left(\bar{\rho}\tilde{u}_k\tilde{Y}_j\right)=\frac{\partial}{\partial x_k}\left(\bar{\rho}D_l\frac{\partial\tilde{Y}_j}{\partial x_k}+\frac{\mu_t}{Sc_t}\frac{\partial\tilde{Y}_j}{\partial x_k}\right)+\bar{\dot{w}}_jW_j,\ j=1,...,l \tag{2.45}$$

where l is the number of mass transport equations, D_l is the representative diffusivity in laminar flow and Sc_t is turbulent Schmidt number (= 0.7). The number of the mass transport equations is basically the total number of species minus one ($l=n-1$). Note that one species mass fraction can be obtained by subtracting the summation of other species from unity. For the CFD simulation with a detailed chemical reaction mechanism, n is too large to be handled with present computational resources. In addition we are faced with the problem of estimating the mean production/destruction rate. Therefore, various assumptions have been used to decrease the number of the mass transport equations, as well as to deal with the estimation problem of the

mean production/destruction rate, so that l is zero or a small number (e.g. l =2 for 2-D manifolds).

2.4.2 Fast-chemistry approaches

The simplest technique to reduce the number of mass transport equations and avoid the estimation problem for the mean production/destruction rate is the fast-chemistry approach [40,60,61,73] in which the mixture state is assumed to be in the equilibrium state. The mixture state normally is described as the mixture fraction and mixture fraction variance. As a result, the mass transport equation, Eq.(2.45), becomes unnecessary for combustion CFD simulation.

Due to the statistical characteristics (randomness) of the turbulence, the probability approach is suggested to estimate averaged scalar values:

$$\tilde{\phi} = \int_0^1 \cdots \int_0^1 \cdots \int_{-\infty}^{\infty} \int_0^{\infty} \int_0^{\infty} \phi(\rho, T, u_x, ..., Y_1, ..., Y_n) \tilde{P}(\rho, T, u_x, ..., Y_1, ..., Y_n) d\rho dT du_x \cdots dY_1 \cdots dY_n \quad (2.46)$$

where $\tilde{\phi}$ is the Favre-averaged scalar value, ϕ is a function of the involved scalars and $\tilde{P}$ is the Favre-averaged joint PDF of the involved scalars. However, since it is impossible to integrate Eq.(2.46) with respect to this many variables as well as to form the multi-dimensional joint PDF and the multi-dimensional scalar value function, a simple one-dimensional PDF is often used in practice.

For a closed system the equilibrium state is uniquely determined by only three variables: pressure, enthalpy and mixture fraction. Among these, pressure is not seen as an important independent

variable because mild pressure change usually gives negligible effect on the equilibrium state. Thus, only enthalpy and mixture fraction are considered as key independent variables.

For adiabatic conditions, because enthalpy is determined by mixture fraction, see Eq.(2.44), the estimation of averaged scalar values can be simplified as

$$\tilde{\phi} = \int_0^1 \phi(\eta)\tilde{P}(\eta)d\eta \tag{2.47}$$

$$\overline{\phi} = \overline{\rho}\int_0^1 \frac{\phi(\eta)}{\rho(\eta)}\tilde{P}(\eta)d\eta \tag{2.48}$$

where $\tilde{\phi}$ and $\overline{\phi}$ are, respectively, the Favre-averaged and time-averaged scalar value, η is mixture fraction, $\rho(\eta)$ is density function of the mixture fraction and $\tilde{P}(\eta)$ is an one-dimensional Favre-averaged PDF of the mixture fraction. Note that the symbol η is used to express the mixture fraction as an independent variable and the symbol ξ, in the previous section, Eq.(2.42)~Eq.(2.44), as a dependent variable.

For non-adiabatic conditions where enthalpy cannot be determined by the mixture fraction, the averaged scalar values should be integrated,

$$\tilde{\phi} = \int_{-\infty}^{\infty}\int_0^1 \phi(\eta,h)\tilde{P}(\eta,h)d\eta dh \tag{2.49}$$

This equation is difficult to integrate because of the unknown two-dimensional joint PDF. Thus, it is generally assumed that the two-dimensional joint PDF is represented by two independent PDFs, $\tilde{P}_\eta(\eta)\tilde{P}_h(h)$, and further the independent PDF for enthalpy, $\tilde{P}_h(h)$, is the Dirac delta function. Then, Eq.(2.49) can be simplified to

$$\tilde{\phi} = \int_0^1 \phi(\eta, \tilde{h}) \tilde{P}(\eta) d\eta \tag{2.50}$$

where the Favre-averaged enthalpy ($\tilde{h}$) can be obtained from the energy equation, Eq.(2.38-b).

According to the fast-chemistry assumption, the scalar values ($\phi(\eta)$ and $\phi(\eta, \tilde{h})$) are replaced by the values at the equilibrium state ($\phi^e(\eta)$ and $\phi^e(\eta, \tilde{h})$). In order to save computation time, because of the estimation of the equilibrium state with enthalpy ($\phi^e(\eta, \tilde{h})$), a further assumption is often made that the non-adiabatic, Favre-averaged species composition is not far from that for adiabatic conditions. Based on this averaged species composition, the averaged temperature and density are calculated by the relation between enthalpy and temperature, and ideal gas law, respectively:

$$\begin{aligned} &\tilde{Y}_j = \int_0^1 Y_j^e(\eta) \tilde{P}(\eta) d\eta, \; j = 1, \ldots, n, \text{ and then,} \\ &\tilde{T} = f_h(\overline{p}, \tilde{h}, \tilde{Y}_1, \tilde{Y}_2, \ldots, \tilde{Y}_n), \; \overline{\rho} = f_T(\overline{p}, \tilde{T}, \tilde{Y}_1, \tilde{Y}_2, \ldots, \tilde{Y}_n) \end{aligned} \tag{2.51}$$

The steady laminar flamelet model, a well known fast chemistry approach, is widely used to treat the effect of detailed chemical reaction mechanisms on CFD simulation. Basically the steady laminar flamelet model can be considered as an extension of the above method. Scalar dissipation is added as a key independent variable affecting the equilibrium state. The resulting averaged scalar values are described by

$$\tilde{\phi} = \int_0^\infty \int_{-\infty}^\infty \int_0^1 \phi(\eta, h, \chi) \tilde{P}(\eta, h, \chi) d\eta dh d\chi \tag{2.52}$$

where χ is scalar dissipation,

$$\chi = 2D\left(\left(\frac{\partial \xi}{\partial x_1}\right)^2 + \left(\frac{\partial \xi}{\partial x_2}\right)^2 + \left(\frac{\partial \xi}{\partial x_3}\right)^2\right) \tag{2.53}$$

and D is a representative diffusion coefficient. Similar to previous procedure, this three-dimensional joint PDF, $\tilde{P}(\eta, h, \chi)$, is treated as the product of three independent PDFs, $\tilde{P}_\eta(\eta)\tilde{P}_h(h)\tilde{P}_\chi(\chi)$, and the two PDFs for enthalpy and scalar dissipation, $\tilde{P}_h(h)$ and $\tilde{P}_\chi(\chi)$, are modeled as the Dirac delta function. Then, Eq.(2.52) is simplified to

$$\tilde{\phi} = \int_0^1 \phi(\eta, \tilde{h}, \tilde{\chi})\tilde{P}(\eta)d\eta \tag{2.54}$$

where $\tilde{\chi}$ is Favre-averaged scalar dissipation that can be obtained from a modeled transport equation or from a modeled algebraic equation. The algebraic relationship commonly used is

$$\tilde{\chi} = C_\chi \frac{\tilde{\varepsilon}\widetilde{\xi''^2}}{\tilde{k}} \tag{2.55}$$

where $C_\chi = 2.0$. According to the fast-chemistry assumption, the scalar values in the function $\phi(\eta, \tilde{h}, \tilde{\chi})$ are replaced by the equilibrium state values, $\phi^e(\eta, \tilde{h}, \tilde{\chi})$. The equilibrium state is usually calculated from the adiabatic laminar flame model, 1-D transient PDE derived from the opposed diffusion flame. Once again, for simplification, the adiabatic average species compositions are used and averaged temperature and density are calculated based on this species composition:

$$\begin{aligned} &\tilde{Y}_j = \int_0^1 Y_j^e(\eta, \tilde{\chi})\tilde{P}(\eta)d\eta,\ j = 1,\ldots,n, \text{ and then,} \\ &\tilde{T} = f_h(\overline{p}, \tilde{h}, \tilde{Y}_1, \tilde{Y}_2, \ldots, \tilde{Y}_n),\ \overline{\rho} = f_T(\overline{p}, \tilde{T}, \tilde{Y}_1, \tilde{Y}_2, \ldots, \tilde{Y}_n) \end{aligned} \tag{2.56}$$

In combustion simulation the one-dimensional PDF is commonly modeled as the β-PDF [40,60, 61,74,75 ,76], i.e.,

$$\tilde{P}(\eta) = \frac{f_p(\eta;\alpha,\beta)}{beta(\alpha,\beta)} \tag{2.57}$$

$$f_p(\eta;\alpha,\beta) = \eta^{\alpha-1}(1-\eta)^{\beta-1} \tag{2.58}$$

$$beta(\alpha,\beta) = \int_0^1 \eta^{\alpha-1}(1-\eta)^{\beta-1} d\eta \tag{2.59}$$

where α and β are non-negative parameters of the β-PDF, which are calculated from the mixture fraction and the mixture fraction variance in Eq.(2.42) and (2.43) [76],

$$\alpha = \tilde{\xi}\left(\frac{(1-\tilde{\xi})\tilde{\xi}}{\widetilde{\xi''^2}} - 1 \right) \tag{2.60-a}$$

$$\beta = (1-\tilde{\xi})\left(\frac{(1-\tilde{\xi})\tilde{\xi}}{\widetilde{\xi''^2}} - 1 \right) \tag{2.60-b}$$

Theoretically the fast-chemistry approaches are valid when the physical mixing time scale is an order of magnitude larger than the chemical time scale. Unfortunately, in typical flameless combustion conditions, some chemical time scales are believed to be similar to or larger than the mixing time scale. This time scale problem is being addressed in studies on unsteady flamelet modeling, a topic of interest among a number of researchers [22,77,78,79].

2.4.3 Conditional Moment Closure

Conditional Moment Closure (CMC) methods [80,81,82], proposed independently by Klimenko and Bilger, suggest alternative forms of the transport equations for reactive scalars (mass fractions and enthalpy) to accurately estimate the mean (time-averaged) production/destruction

rate term. It is based on experimental observations [83] that the reactive scalars are strongly dependent on the mixture fraction in nonpremixed combustion.

According to the CMC method, the mass transport equation can be replaced by the first-order unclosed equation for the mass fraction of i species,

$$\frac{\partial\langle Y_i|\eta\rangle}{\partial t}+\langle\vec{v}|\eta\rangle\cdot\nabla\langle Y_i|\eta\rangle+\frac{\nabla\cdot\left(\langle\rho|\eta\rangle\langle\vec{v}''Y_i''|\eta\rangle P(\eta)\right)}{P(\eta)\langle\rho|\eta\rangle}-\langle N|\eta\rangle\frac{\partial^2\langle Y_i|\eta\rangle}{\partial\eta^2}=\langle\dot{\varpi}_i|\eta\rangle \qquad (2.61)$$

where $\langle\phi|\eta\rangle$ is conditional averaged value of the scalar ϕ, i.e. $\vec{v}''=\vec{v}-\langle\vec{v}|\eta\rangle$, $Y_i''=Y_i-\langle Y_i|\eta\rangle$ and $\dot{\varpi}_i=\frac{\dot{w}_i W_i}{\rho}$. $N\equiv D|\nabla\xi|^2$ is the conserved scalar dissipation rate (that is, the mixture fraction dissipation rate in nonpremixed combustion) and $P(\eta)$ is a presumed PDF. As seen in this CMC equation, the conditional mean production/destruction rate, $\langle\dot{\varpi}_i|\eta\rangle$, is substituted for the (unconditional) mean production/destruction rate, $\dot{\varpi}_i$. And, based on experimental observation [83] that the conditional variance, ϕ''^2, the square of the fluctuation about conditional averaged value, is negligible when compared with the square of the conditional averaged value, $\langle\phi|\eta\rangle^2$, the conditional mean production/destruction rate can be written in the form,

$$\begin{aligned}\langle\dot{\varpi}(h,\vec{Y})|\eta\rangle&=\langle\dot{\varpi}(\langle h|\eta\rangle+h'',\langle\vec{Y}|\eta\rangle+\vec{Y}'')|\eta\rangle\\&\approx\langle\dot{\varpi}(\langle h|\eta\rangle,\langle\vec{Y}|\eta\rangle)|\eta\rangle\\&=\dot{\varpi}(\langle h|\eta\rangle,\langle\vec{Y}|\eta\rangle,\eta)\end{aligned} \qquad (2.62)$$

where $\vec{Y}$ is species vector, $\vec{Y}=(Y_1,Y_2,\ldots,Y_n)$. Note that the effect of pressure on the reaction rate is ignored. Hence, the conditional mean production/destruction rate term needs to be described only by the mixture fraction and corresponding conditional mean value of enthalpy and mass fractions.

From the CMC method and the statistical approach we can derive an important relation between the conditional mean production/destruction rate and the (unconditional) mean production/destruction rate:

$$\overline{\dot{w}_i} = \bar{\rho} \int_0^1 \frac{\dot{w}_i(\eta)}{\rho(\eta)} \tilde{P}(\eta) d\eta \tag{2.63}$$

where $\tilde{\phi} = \widetilde{\langle \phi \rangle}$, $\bar{\phi} = \overline{\langle \phi \rangle}$ and $\phi(\eta) = \langle \phi | \eta \rangle$. Note that $\dot{w}_i$ and $\dot{\varpi}_i$ have a linear relation.

Although the CMC method handles the mean production/destruction rate estimation problem very well, it may not be practical for 3-D combustion CFD simulation with detailed chemical reactions because of the additional independent variable, i.e. the mixture fraction, which demands considerable additional computational resources. For simplification, we often adopt some reasonable assumptions, for example, the conditional scalars for the mixture fraction, $\langle \phi | \eta \rangle$, are same in the radial direction for jet flow combustion (based on experimental observation [82,84]). Accordingly, Eq.(2.61) (basically 3-D spatial, transient PDEs) can be reduced to 1-D spatial, transient PDEs.

2.4.4 Conditional Source-Term Estimation

The Conditional Source-term Estimate (CSE) method was proposed by Bushe and Steiner [26] to estimate the mean production/destruction rate term in a practical way by using the conditional mean scalar concept in the CMC method. In the CSE method, we can obtain the conditional mean scalars, $\langle \phi | \eta \rangle = \phi(\eta)$, by solving a set of algebraic equations instead of solving the PDEs, Eq.(2.61), directly. The set of algebraic equations is derived from a key assumption that the

conditional mean scalar values in the radial direction for a jet flow are the same [26,82,85,86]. The (unconditional) mean production/destruction rate term is then estimated by using the resulting conditional mean scalars and a proper chemical reaction expression.

The (unconditional) mean scalars ($\tilde{\phi}$ or $\overline{\phi}$) can be described by using Eq.(2.47) or (2.48). Note that basically this integration equation could be Eq.(2.50) or (2.54). According to the key assumption in the CSE method, we can split the simulation domain into many groups sharing the same conditional mean scalar values (sometimes the group is just called an ensemble) in the radial direction of a jet flow. Thus, the conditional mean scalar can be expressed as

$$\phi(\eta) = \phi(\eta)_G \tag{2.64}$$

where $\phi(\eta)_G$ is the conditional mean scalar in the split group, and Eq.(2.47) is then expressed as

$$\tilde{\phi} = \int_0^1 \phi(\eta)_G \tilde{P}(\eta) d\eta \tag{2.65}$$

By inverting this integral equation with the given unconditional mean scalar values and a presumed PDF, we can derive a set of algebraic equations to obtain the conditional mean scalar values in each group, $\phi(\eta)_G$. In CFD simulation, the unconditional mean (Favre-averaged) scalar (mass fraction) value and the presumed PDF (β-PDF) are obtained from the mass transport equation, Eq.(2.45), and the mixing field, Eq.(2.42) and (2.43), respectively. Hence the unconditional mean production/destruction rate term in Eq.(2.45) can be estimated by

$$\overline{\dot{w}_i} = \overline{\rho} \int_0^1 \frac{\dot{w}_i(\eta)_G}{\rho(\eta)_G} \tilde{P}(\eta) d\eta \tag{2.66}$$

2.4.5 A few numerical techniques

When the numerical integration related to the β-PDF (i.e. for Eq.(2.47) or (2.48)) is carried out, numerical difficulties often occur due to the singularity of the β-PDF at $\eta = 0$ or $\eta = 1$ and numerical overflow at large β-PDF parameters. Liu *et al.* [74] suggested an improved technique to handle these numerical difficulties:

$$\tilde{\phi} \approx \frac{1}{beta(\alpha,\beta)}\left(\frac{\varepsilon^{\alpha}}{\alpha}\phi(0) + \int_{\varepsilon}^{1-\varepsilon} \phi(\eta) f_p(\eta,\alpha,\beta) d\eta + \frac{\varepsilon^{\beta}}{\beta}\phi(1) \right) \tag{2.67}$$

$$beta(\alpha,\beta) \approx \frac{\varepsilon^{\alpha}}{\alpha} + \int_{\varepsilon}^{1-\varepsilon} f_p(\eta,\alpha,\beta) d\eta + \frac{\varepsilon^{\beta}}{\beta} \tag{2.68}$$

$$f_p(\eta;\alpha,\beta) = \eta^{\alpha-1}(1-\eta)^{\beta-1} \tag{2.69}$$

where $\varepsilon = 1.0 \times 10^{-6}$. The integration is divided into three parts: $[0, \varepsilon]$, $[\varepsilon, 1-\varepsilon]$ and $[1-\varepsilon, 1]$, and the integration values in the first and last parts (around at $\eta = 0$ or $\eta = 1$) are estimated as a simple power function. Hence, the remaining integral term can be estimated with no singularity at $\eta = 0$ and $\eta = 1$. In addition, the numerical overflow problem is avoided by limiting the parameters to a certain maximum value (a value of 500 was used in the present work) while the shape of the β-PDF is preserved qualitatively. Note that for proper spacing of the mixture fraction in the numerical quadrature, the shape of the other integrand function like $\phi(\eta)$ in Eq.(2.47) should be also considered as well as that of the β-PDF.

Eq.(2.65) is called the inhomogeneous Fredholm equation of the first kind and needs to be solved to obtain the conditional mean scalar values for each group, $\phi(\eta)_G$, in the CSE method, which is called the inverse problem [87]. This inverse problem is known to be extremely ill-posed, and the regularization method [87,88] which uses certain *a priori* information as a stabilizing functional,

(regularizing operator) is usually adopted in the solution procedure. The symbolized regularization method can be expressed as a minimization problem:

$$\min\{\mathcal{A} + \lambda\mathcal{B}\} \tag{2.70}$$

where $\mathcal{A}$ is a functional formulated from the original integration equation, $\mathcal{B}$ is a functional obtained from *a priori* information (called stabilizing functional), and λ is Lagrange multiplier (weighting coefficient). Depending on the specific inverse problem, the *a priori* information can be specified such as constant, linear or quadratic, etc. Huang and Bushe [89] specified the *a priori* information from the linear combination of the previous time solution and the effect of convection in their CSE application. While the Lagrange multiplier can assume any value in the range of $0 \sim \infty$, in practice, the ratio of the trace of the matrices representing $\mathcal{A}$ and $\mathcal{B}$ has been suggested [87,90] for this parameter.

Chapter 3
3-D physical model for the Strong-Jet/Weak-Jet problem

3.1 Introduction

A 3-D SJ/WJ physical model was developed to understand key characteristics of the jet mixing process for flameless combustion in the SJ/WJ burner. The governing equations of the physical model were formulated under isothermal, free jet conditions by using a Lagrangian perspective. The 3-D SJ/WJ physical model was validated by cold model experiment and compared with CFD simulation. Important design/operation controlling factors of the SJ/WJ configuration were identified from the 3-D SJ/WJ physical model and the effect of the controlling factors on the SJ/WJ system was investigated.

3.2 The 3-D SJ/WJ physical model

3.2.1 General equations for the isothermal, free multi-jet flow system

Since the SJ/WJ configuration is a special case of a multi-jet flow system, general equations are first derived and then by putting constraints of the SJ/WJ configuration on these general equations a 3-D SJ/WJ physical model is developed. The general equations for an isothermal, free multi-jet flow system were derived based on the Lagrangian reference frame, following a fluid element issued from i-th nozzle during a short time interval, δt. These equations are valid before the jets are merged, as shown in Figure 1.2.

A momentum balance equation on the fluid element issued from *i*-th nozzle during δt can be expressed as

$$\frac{D}{Dt}\left(\iiint_{V_i} \rho_i \vec{v}_i dV \right) = \sum_{l \neq i} \vec{F}_{i,l} \tag{3.1}$$

where subscript *i* represents the fluid element issued from *i*-th nozzle during the time, δt, *D/Dt* is substantial (material) derivative, *V* is the volume of the fluid element, $\vec{v}$ is velocity vector, ρ is density and $\vec{F}_{i,l}$ is the external force vector acting on the fluid element due to the entrainment effect of *l*-th jet flow. Since viscosity, gravity and pressure gradient terms can be ignored under the assumption of an isothermal, free jet and since the pressure field is nearly uniform, the external force arises only from the entrainment effects of other jets.

By employing the Favre space-averaging concept, we can define a representative velocity vector ($\tilde{\vec{v}}$) for a fluid element as follows:

$$\tilde{\vec{v}}_i = \frac{\iiint_{V_i} \rho_i \vec{v}_i dV}{\iiint_{V_i} \rho_i dV} \tag{3.2}$$

where $\iiint_{V_i} \rho_i dV = m_i$ is the mass of the fluid element issued from *i*-th nozzle during δt. It can be expressed as $m_i = \dot{m}_{i,o}\delta t + \dot{m}_{i,e}\delta t = \dot{m}_i \delta t$ by definition. Note that the time derivative of m_i is also expressed as $\frac{dm_i}{dt} = \frac{d}{dt}(\dot{m}_{i,e}\delta t) = \frac{d}{dt}(\dot{m}_i \delta t)$. Therefore, Eq.(3.1) can be expressed as

$$\frac{d}{dt}\left(\dot{m}_i \delta t \, \tilde{\vec{v}}_i \right) = \sum_{l \neq i} \vec{F}_{i,l} \tag{3.3}$$

Explicit expressions for the external force vector elements must next be specified for the SJ/WJ problem.

Position and velocity of the tracked element are defined by position vector ($\vec{q}$) and its time derivative

$$\frac{d\vec{q}_i}{dt} = \vec{\tilde{v}}_i \tag{3.4}$$

where $\vec{q}_i = r_i\vec{e}_r + z_i\vec{e}_z$, $\vec{e}_k$ being the unit vector in the *k*-direction. The time derivative of the arc length, s_i, of a fluid element trajectory issued from *i*-th nozzle (i.e. its velocity magnitude) is

$$\frac{ds_i}{dt} = \left(\frac{d\vec{q}_i}{dt} \cdot \frac{d\vec{q}_i}{dt} \right)^{1/2} \tag{3.5}$$

When there is no reaction and diffusion term, that is an inactive convection-dominated flow, the mass balance equation of the *j*-th species along with *i*-th jet flow can be expressed as

$$\frac{D}{Dt}\left(\iiint_{V_i} \rho_i \omega_i^j dV \right) = J_{e,i}^j \tag{3.6}$$

where ω_i^j is the mass fraction of the *j* species in the fluid element issued from *i*-th nozzle during δt and $J_{e,i}^j$ is the mass flow of the *j* species into the fluid element issued from the *i*-th nozzle during δt due to the entrainment effect. It can be expressed as $J_{e,i}^j = \frac{d}{dt}(\omega_\infty^j \dot{m}_{i,e} \delta t)$ by definition. Here, ω_∞^j is the mass fraction of the *j* species in the surrounding fluid. Similar to Eq.(3.2), a representative mass fraction of the *j* species for the fluid element issued from *i*-th nozzle during δt can be expressed as

$$\tilde{\omega}_i^j = \frac{\iiint_{V_i} \rho_i \omega_i^j dV}{\iiint_{V_i} \rho_i dV} \tag{3.7}$$

Hence, Eq.(3.6) can be expressed as

$$\frac{d}{dt}\left(\tilde{\omega}_i^j \dot{m}_i \delta t\right) = \frac{d}{dt}(\omega_\infty^j \dot{m}_{i,e} \delta t) \tag{3.8}$$

Also, the mass balance equation for the entire fluid element issued from the *i*-th nozzle during δt can be expressed as

$$\frac{D}{Dt}\left(\iiint_{V_i} \rho_i dV\right) = J_{e,i} \tag{3.9}$$

where $J_{e,i}$ is the mass flow into the fluid element issued from the *i*-th nozzle during δt due to the entrainment effect and by definition can be expressed as $J_{e,i} = \frac{d}{dt}(\dot{m}_{i,e} \delta t)$. Similarly, a representative density for the fluid element issued from the *i*-th nozzle during δt is

$$\overline{\rho}_i = \frac{\iiint_{V_i} \rho_i dV}{\iiint_{V_i} dV} \tag{3.10}$$

Therefore, Eq.(3.9) can be expressed as

$$\frac{d}{dt}\left(\overline{\rho}_i V_i\right) = \frac{d}{dt}(\dot{m}_{i,e} \delta t) \tag{3.11}$$

A supplementary equation is required for V_i to complete Eq.(3.11). It can be obtained from the ideal gas law and the assumption of constant pressure and temperature fields.

$$V_i = \frac{RT_i}{p_i}(\dot{m}_i \delta t)\sum_j \frac{\tilde{\omega}_i^j}{W_j} = \frac{RT_\infty}{p_\infty}(\dot{m}_i \delta t)\sum_j \frac{\tilde{\omega}_i^j}{W_j} \tag{3.12}$$

where R is the gas constant, W_j is the molecular weight of the j species, T_∞ and p_∞ are temperature and pressure of the free multi-jet flow system, respectively.

3.2.2 Governing equations of the 3-D SJ/WJ physical model

The governing equations of the 3-D SJ/WJ physical model can be derived by applying constraints of the SJ/WJ problem to the general equations for the isothermal, free, multi-jet flow system, using a cylindrical coordinate system. A sketch of the 3-D SJ/WJ problem is shown in Figure 3.1. Since the SJ has considerably larger momentum than the WJ, the SJ trajectory (s_2) can be assumed to be a straight line along the z -coordinate. On the other hand, the WJ trajectory (s_1) is curved toward the SJ because of the entrainment flow effect of the SJ. The origin of the coordinate system is located at the SJ nozzle and the open circle symbol in Figure 3.1 represents the fluid element issued from the WJ nozzle during the time δt . The WJ fluid element is directed at an angle ϕ relative to the *r*-direction vector in the $r\theta$ plane and at an inclination angle φ from that plane.

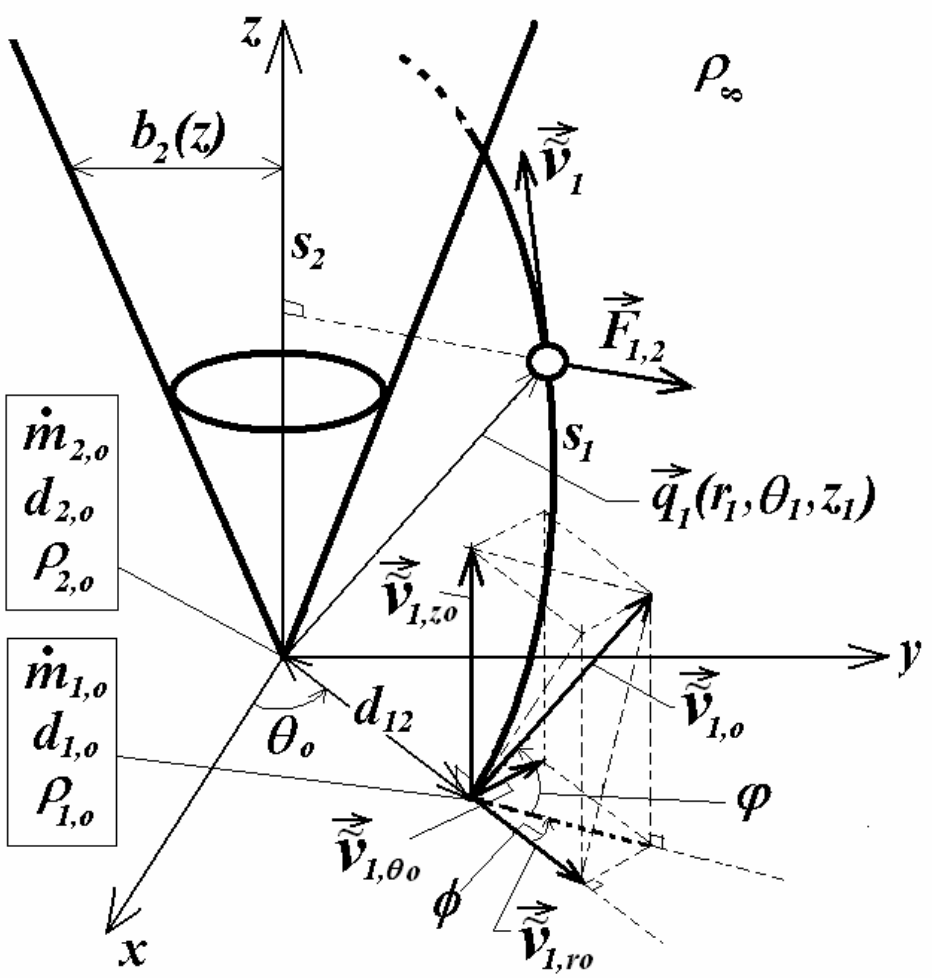

Figure 3.1. A 3-D schematic diagram of the SJ/WJ problem.

The external forces in Eq.(3.1) must first be specified. According to the definition of the SJ/WJ problem, the external force vectors of SJ and WJ are, respectively,

$$\vec{F}_{1,2} = \left|\vec{F}_{1,2}\right|(-\vec{e}_r) \quad \text{and} \quad \vec{F}_{2,1} = 0 \tag{3.13}$$

The norm of the external force vector can be derived by using the expression for the radial velocity ($u_{2,r}$) as the entrainment flow occurring due to the effect of the SJ flow, see Eq.(2.6) in Chapter 2.

$$\left|\vec{F}_{1,2}\right| = \left|\frac{d}{dt}(m_1 u_{2,r})\right| = \left|\frac{d}{dt}(\dot{m}_1 \delta t\, u_{2,r})\right| =$$

$$= \begin{cases} \dot{m}_1 \delta t \dfrac{{C_{1,2}}^2}{r_1^3} + \dfrac{C_{1,2}}{r_1}\dfrac{d}{dt}(\dot{m}_1 \delta t) & \text{for } z_1 > z_{2,o},\ r_1 \geq b_2(z_1) \\ 0 & \text{for } 0 \leq z_1 \leq z_{2,o},\ r_1 \geq b_2(z_1) \end{cases} \tag{3.14}$$

where $C_{1,2} = \dfrac{C_{e,2}}{2\pi}\dfrac{\dot{m}_{2,o}}{d_{2,o}}\dfrac{1}{\rho_\infty}\left(\dfrac{\rho_\infty}{\rho_{2,o}}\right)^{\frac{1}{2}}$ assuming the jet density equal to the ambient fluid density and $z_{2.o}$ is the virtual origin of the SJ. The jet width boundary, b, is approximated at the position of 50% intermittency, Becker *et al.* [91] suggested $b(z) = 0.194z$, based on experimental data. In the following equations the interface continuity rule is applied for the discontinuity caused by the virtual origin.

With this background, we can now obtain an ordinary differential equation (ODE) for the SJ and three ODEs for the WJ from Eq.(3.4). The condition that $r_1 \geq b_2(z_1)$ will be assumed implicitly in subsequent analysis.

$$\frac{dz_i}{dt} = \tilde{v}_{i,z}, \quad i = 1,2 \tag{3.15}$$

$$\frac{d\theta_1}{dt} = \frac{\tilde{v}_{1,\theta}}{r_1} \tag{3.16}$$

$$\frac{dr_1}{dt} = \tilde{v}_{1,r} \tag{3.17}$$

where $\tilde{v}_{i,k}$ is velocity component in the *k*-th direction of the fluid element issued from the *i*-th nozzle during δt.

By substituting Eq.(3.13) and (3.14) into Eq.(3.3), we can derive one ODE for the SJ and three ODEs for the WJ. Note that δt cancels out in these equations.

z direction:

$$\frac{d\tilde{v}_{i,z}}{dt} = -\frac{\tilde{v}_{i,z}{}^2}{C_{2,i}}\frac{d\dot{m}_i}{dt}, \qquad i = 1,2 \tag{3.18}$$

where $C_{2,i} = \dot{m}_{i,o}\tilde{v}_{i,zo}$ and $\tilde{v}_{i,ko}$ is the velocity component in the k-th direction of the fluid element at the i-th nozzle exit.

r direction:

$$\frac{d\tilde{v}_{1,r}}{dt} = \begin{cases} \dfrac{\tilde{v}_{1,\theta}{}^2}{r_1} - \dfrac{C_{1,2}{}^2}{r_1^3} - \dfrac{\tilde{v}_{1,z}}{C_{2,1}}\left\{\tilde{v}_{1,r} + \dfrac{C_{1,2}}{r_1}\right\}\dfrac{d\dot{m}_1}{dt} & \text{for } z_1 > z_{2,o} \\ \dfrac{\tilde{v}_{1,\theta}{}^2}{r_1} - \dfrac{\tilde{v}_{1,z}\tilde{v}_{1,r}}{C_{2,1}}\dfrac{d\dot{m}_1}{dt} & \text{for } 0 \le z_1 \le z_{2,o} \end{cases} \tag{3.19}$$

θ direction:

$$\frac{d\tilde{v}_{1,\theta}}{dt} = -\frac{\tilde{v}_{1,r}\tilde{v}_{1,\theta}}{r_1} - \frac{\tilde{v}_{1,\theta}\tilde{v}_{1,z}}{C_{2,1}}\frac{d\dot{m}_1}{dt} \tag{3.20}$$

The time derivative of the mass flow rate of both jets is derived from Eq.(2.2) in Chapter 2:

$$\frac{d\dot{m}_i}{dt} = \frac{d\dot{m}_{i,e}}{dt} = \begin{cases} \dfrac{\dot{m}_{i,o}C_{e,i}}{d_{i,o}}\left(\dfrac{\rho_\infty}{\rho_{i,o}}\right)^{\frac{1}{2}}\dfrac{ds_i}{dt} & \text{for } s_i > s_{i,o} \\ 0 & \text{for } 0 \le s_i \le s_{i,o} \end{cases} \tag{3.21}$$

The time derivative of arc length is obtained from Eq.(3.5):

$$\frac{ds_1}{dt} = \left(\tilde{v}_{1,r}{}^2 + \tilde{v}_{1,\theta}{}^2 + \tilde{v}_{1,z}{}^2\right)^{1/2} \tag{3.22}$$

and

$$\frac{ds_2}{dt} = \tilde{v}_{2,z}. \tag{3.23}$$

Since $s_2 = z_2$, Eq.(3.23) is identical to Eq.(3.15).

In addition to the main set of governing equations, we can develop the other equations describing mass fraction and density evolution along the SJ and WJ trajectory. Assuming that the ambient mass fraction is constant, ω_∞^j =const., from Eq.(3.8), (3.11) and (3.12) the mass fraction evolution can be expressed as

$$\frac{d\tilde{\omega}_i^j}{dt} = \begin{cases} (\omega_\infty^j - \tilde{\omega}_i^j)\dfrac{1}{(s_i - s_{i,o} + 1/C_{3,i})}\dfrac{ds_i}{dt} & \text{for } s_i > s_{i,o} \\ 0 & \text{for } 0 \le s_i \le s_{i,o} \end{cases} \tag{3.24}$$

where $C_{3,i} = \dfrac{C_{e,i}}{d_{i,o}}\left(\dfrac{\rho_\infty}{\rho_{i,o}}\right)^{1/2}$.

Similarly, the density evolution can be expressed as

$$\frac{d\bar{\rho}_i}{dt} = \begin{cases} \dfrac{p_\infty}{RT_\infty}\dfrac{1}{\dot{m}_i\sum_j \dfrac{\tilde{\omega}_i^j}{W_j}}\dfrac{d\dot{m}_i}{dt} - \bar{\rho}_i\dfrac{\sum_j \dfrac{1}{W_j}\dfrac{d\tilde{\omega}_i^j}{dt}}{\sum_j \dfrac{\tilde{\omega}_i^j}{W_j}} - \bar{\rho}_i\dfrac{1}{\dot{m}_i}\dfrac{d\dot{m}_i}{dt} & \text{for } s_i > s_{i,o} \\ 0 & \text{for } 0 \le s_i \le s_{i,o} \end{cases} \tag{3.25}$$

For all the relations above, the initial conditions (at the nozzle exit) can be set up in the following way (cf. Figure 3.1):

$$z_i\big|_{t=0} = 0; \qquad \theta_1\big|_{t=0} = \theta_o; \qquad r_1\big|_{t=0} = d_{12}; \qquad s_1\big|_{t=0} = 0$$

$$\tilde{v}_{1,z}\big|_{t=0} = \left|\vec{\tilde{v}}_{1,o}\right| \sin\varphi = \tilde{v}_{1,zo}\,; \qquad \tilde{v}_{2,z}\big|_{t=0} = \left|\vec{\tilde{v}}_{2,o}\right| = \tilde{v}_{2,zo}\,; \quad \tilde{v}_{1,r}\big|_{t=0} = \left|\vec{\tilde{v}}_{1,o}\right| \cos\varphi\cos\phi = \tilde{v}_{1,ro}\,;$$

$$\tilde{v}_{1,\theta}\big|_{t=0} = \left|\vec{\tilde{v}}_{1,o}\right| \cos\varphi\sin\phi = \tilde{v}_{1,\theta o}\,; \qquad \tilde{\omega}_i^j\big|_{t=0} = \tilde{\omega}_{i,o}^j\,; \quad \overline{\rho}_i\big|_{t=0} = \rho_{i,o}$$

3.2.3 Dimensionless governing equations for the 3-D SJ/WJ physical model

Dimensionless governing equations of the SJ/WJ problem can be formed by introducing the following dimensionless variables,

$$z_i^* = \frac{z_i}{d_{12}}, \qquad r_1^* = \frac{r_1}{d_{12}}, \qquad \theta_1^* = \theta_1, \qquad \tilde{v}_{i,z}^* = \frac{\tilde{v}_{i,z}}{\left|\vec{\tilde{v}}_{i,o}\right|}, \qquad \tilde{v}_{1,r}^* = \frac{\tilde{v}_{1,r}}{\left|\vec{\tilde{v}}_{1,o}\right|}, \qquad \tilde{v}_{1,\theta}^* = \frac{\tilde{v}_{1,\theta}}{\left|\vec{\tilde{v}}_{1,o}\right|},$$

$$t_i^* = \frac{\left|\vec{\tilde{v}}_{i,o}\right|}{d_{12}} t, \qquad s_1^* = \frac{s_1}{d_{12}}, \qquad \tilde{\omega}_i^{j*} = \tilde{\omega}_i^j \qquad \text{and} \qquad \overline{\rho}_i^* = \frac{\overline{\rho}_i}{\rho_{i,o}}.$$

We can also define the momentum flow ratio of the WJ to the SJ as a useful design/operation dimensionless parameter, as suggested by Grandmaison *et al.* [13]. If the velocity profile at the exit of the jet nozzle is uniform, we can define the momentum flow ratio as:

$$\psi_{12} = \left(\frac{\rho_{1,o}}{\rho_{2,o}}\right)\left(\frac{d_{1,o}\left|\vec{\tilde{v}}_{1,o}\right|}{d_{2,o}\left|\vec{\tilde{v}}_{2,o}\right|}\right)^2 \tag{3.26}$$

Then

$$\frac{dz_i^*}{dt_i^*} = \tilde{v}_{i,z}^* \tag{3.27}$$

$$\frac{dr_1^*}{dt_1^*} = \tilde{v}_{1,r}^* \tag{3.28}$$

$$\frac{d\theta_1^*}{dt_1^*} = \frac{\tilde{v}_{1,\theta}^*}{r_1^*} \tag{3.29}$$

$$\frac{d\tilde{v}_{i,z}^*}{dt_i^*} = -C_{2,i}^* \tilde{v}_{i,z}^{*\,2} \frac{ds_i^*}{dt_i^*} \tag{3.30}$$

where $C_{2,i}^* = C_{e,i} \frac{d_{12}}{d_{i,o}} \frac{\left|\vec{\tilde{v}}_{i,o}\right|}{\tilde{v}_{i,zo}} \left(\frac{\rho_\infty}{\rho_{i,o}}\right)^{1/2}$, $\frac{\left|\vec{\tilde{v}}_{2,o}\right|}{\tilde{v}_{2,zo}} = 1$ and $\frac{\left|\vec{\tilde{v}}_{1,o}\right|}{\tilde{v}_{1,zo}} = \frac{1}{\sin\varphi}$.

$$\frac{d\tilde{v}_{1,r}^*}{dt_1^*} = \begin{cases} \dfrac{\tilde{v}_{1,\theta}^{*\,2}}{r_1^*} - \dfrac{C_{1,2}^{*\,2}}{r_1^{*3}} - C_{2,1}^* \left(\tilde{v}_{1,r}^* + \dfrac{C_{1,2}^*}{r_1^*}\right) \tilde{v}_{1,z}^* \dfrac{ds_1^*}{dt_1^*} & \text{for } z_1^* > z_{2,o}^* \\ \dfrac{\tilde{v}_{1,\theta}^{*\,2}}{r_1^*} - C_{2,1}^* \tilde{v}_{1,r}^* \tilde{v}_{1,z}^* \dfrac{ds_1^*}{dt_1^*} & \text{for } 0 \le z_1^* \le z_{2,o}^* \end{cases} \tag{3.31}$$

where $C_{1,2}^* = \frac{C_{e,2}}{2\pi} \frac{1}{\rho_\infty} \left(\frac{\rho_\infty}{\rho_{2,o}}\right)^{1/2} \frac{\dot{m}_{2,o}}{d_{2,o}} \frac{1}{\left|\vec{\tilde{v}}_{1,o}\right| d_{12}}$. Using Eq.(3.26), this dimensionless parameter can be transformed to $C_{1,2}^* = \frac{C_{e,2}}{8} \left(\frac{\rho_{1,o}}{\rho_\infty}\right)^{1/2} \frac{d_{1,o}}{d_{12}} \left(\frac{1}{\psi_{12}}\right)^{1/2}$.

$$\frac{d\tilde{v}_{1,\theta}^*}{dt_1^*} = -\frac{\tilde{v}_{1,r}^* \tilde{v}_{1,\theta}^*}{r_1^*} - C_{2,1}^* \tilde{v}_{1,\theta}^* \tilde{v}_{1,z}^* \frac{ds_1^*}{dt_1^*} \tag{3.32}$$

$$\frac{ds_1^*}{dt_1^*} = \left(\tilde{v}_{1,r}^{*\,2} + \tilde{v}_{1,\theta}^{*\,2} + \tilde{v}_{1,z}^{*\,2}\right)^{1/2} \tag{3.33}$$

and

$$\frac{ds_2^*}{dt_2^*} = \tilde{v}_{2,z}^* \tag{3.34}$$

Note that Eq.(3.34) is identical to Eq.(3.27) for $i = 2$.

The set of governing equations for the WJ can be divided into 4 different regions, shown in Figure 3.2, in order to account for the positions of the virtual origins of the SJ and WJ.

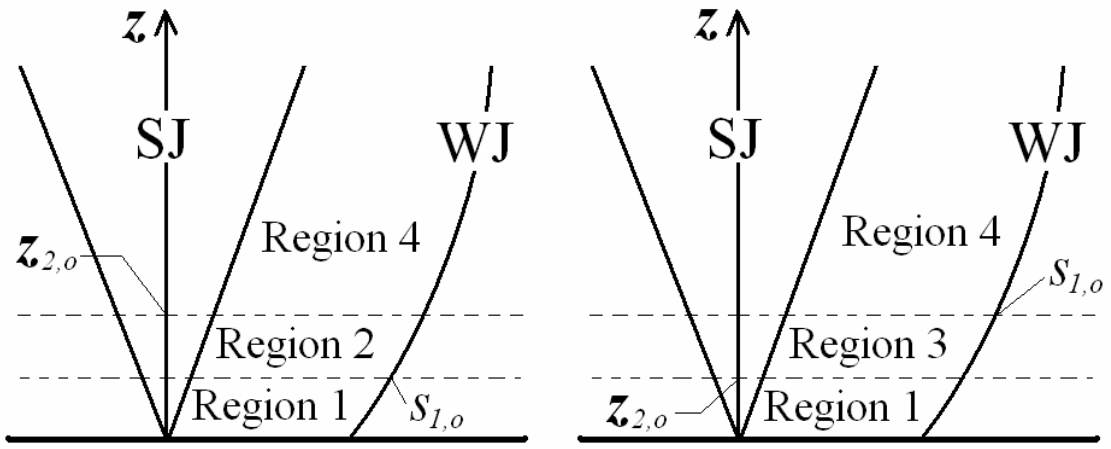

Figure 3.2. A schematic diagram for the different regions due to virtual origin positions in the SJ and WJ: Region 1: ($z_{2,o} > s_{1,o}$ and $0 \le z_1 \le s_{1,o}$) or ($z_{2,o} \le s_{1,o}$ and $0 \le z_1 \le z_{2,o}$); Region 2: $z_{2,o} > s_{1,o}$ and $s_{1,o} < z_1 \le z_{2,o}$; Region 3: $z_{2,o} \le s_{1,o}$ and $z_{2,o} < z_1 \le s_{1,o}$; Region 4: ($z_{2,o} > s_{1,o}$ and $z_1 > z_{2,o}$) or ($z_{2,o} \le s_{1,o}$ and $z_1 > s_{1,o}$).

Depending on the region, the constants in Eq.(3.30), (3.31) and (3.32) are set as follows:

Region 1: $C_{1,2}^* = 0$ and $C_{2,1}^* = 0$

Region 2: $C_{1,2}^* = 0$ and $C_{2,1}^* \neq 0$

Region 3: $C_{1,2}^* \neq 0$ and $C_{2,1}^* = 0$

Region 4: $C_{1,2}^* \neq 0$ and $C_{2,1}^* \neq 0$

The other equations are transformed into dimensionless forms as follows:

$$\frac{d\tilde{\omega}_i^{j*}}{dt_i^*} = \begin{cases} (\omega_\infty^{j*} - \tilde{\omega}_i^{j*}) \dfrac{1}{(s_i^* - s_{i,o}^* + 1/C_{3,i}^*)} \dfrac{ds_i^*}{dt_i^*} & \text{for } s_i^* > s_{i,o}^* \\ 0 & \text{for } 0 \le s_i^* \le s_{i,o}^* \end{cases} \tag{3.35}$$

where $C_{3,i}^* = C_{e,i} \dfrac{d_{12}}{d_{i,o}} \left(\dfrac{\rho_\infty}{\rho_{i,o}} \right)^{1/2}$ and $C_{3,2}^* = C_{2,2}^*$ since $\dfrac{\left|\vec{\tilde{v}}_{2,o}\right|}{\tilde{v}_{2,zo}} = 1$.

$$\frac{d\overline{\rho}_i^*}{dt_i^*} = \begin{cases} C_{4,i}^* \left\{ \left(s_i^* - s_{i,o}^* + \dfrac{1}{C_{3,i}^*} \right) \sum_j \dfrac{\tilde{\omega}_i^{j*}}{W_j} \right\}^{-1} \dfrac{ds_i^*}{dt_i^*} \\ \quad - \overline{\rho}_i^* \left\{ \left(\sum_j \dfrac{\tilde{\omega}_i^{j*}}{W_j} \right)^{-1} \sum_j \dfrac{1}{W_j} \dfrac{d\tilde{\omega}_i^{j*}}{dt_i^*} + \left(s_i^* - s_{i,o}^* + \dfrac{1}{C_{3,i}^*} \right)^{-1} \dfrac{ds_i^*}{dt_i^*} \right\} & \text{for } s_i^* > s_{i,o}^* \\ 0 & \text{for } 0 \le s_i^* \le s_{i,o}^* \end{cases} \tag{3.36}$$

where $C_{4,i}^* = \dfrac{p_\infty}{\rho_{i,o} R T_\infty}$.

The dimensionless initial conditions (at the nozzle exit) are transformed as follows:

$$z_i^*\Big|_{t_i^*=0} = 0; \qquad \theta_1^*\Big|_{t_1^*=0} = \theta_o^*; \qquad r_1^*\Big|_{t_1^*=0} = 1; \qquad s_1^*\Big|_{t_1^*=0} = 0;$$

$$\tilde{v}_{1,z}^*\Big|_{t_1^*=0} = \sin\varphi; \qquad \tilde{v}_{2,z}^*\Big|_{t_2^*=0} = 1; \qquad \tilde{v}_{1,r}^*\Big|_{t_1^*=0} = \cos\varphi\cos\phi;$$

$$\tilde{v}_{1,\theta}^*\Big|_{t_1^*=0} = \cos\varphi\sin\phi; \quad \tilde{\omega}_i^{j*}\Big|_{t_i^*=0} = \tilde{\omega}_{i,o}^{j\,*}; \qquad \overline{\rho}_i^*\Big|_{t_i^*=0} = 1.$$

From this main set of the dimensionless governing equations, Eq.(3.27) with $i=1$, (3.28), (3.29), (3.30) with $i=1$, (3.31), (3.32) and (3.33), we can obtain the important design/operation controlling factors for the SJ/WJ problem. Note that the SJ trajectory is already defined.

We can first analyze the two parameters, $C_{1,2}^{*}$ and $C_{2,1}^{*}$ in the governing equations. They depend on the momentum ratio, ψ_{12}, the distance between the SJ and WJ nozzles, d_{12}, the WJ injection angle, φ, the WJ nozzle diameter, $d_{1,o}$, the WJ and SJ entrainment coefficients, $C_{e,1}$ and $C_{e,2}$, and the density of the WJ and the surrounding fluid. The WJ nozzle diameter, $d_{1,o}$ (along with the SJ nozzle diameter, $d_{2,o}$) is usually determined by the desired firing rate or energy output level for the furnace, fuel equivalence ratio and the momentum flow ratio, ψ_{12}. The corresponding entrainment coefficients and related densities are pre-determined. Therefore, we are essentially setting the value of the two controlling parameters by selecting the values of the momentum flow ratio, ψ_{12}, the distance between nozzles, d_{12}, and the WJ injection angle, φ. We can next note that from the initial conditions, the WJ injection angles (φ, ϕ) are easily recognized as controlling factors. Finally, the two virtual origins, $s_{1,o}^{*}$ and $s_{2,o}^{*}$, are also controlling factors because they determine the calculation regions. They cannot be chosen in advance, but should be determined experimentally for each particular burner design. In summary, the two model parameters, $C_{1,2}^{*}$ and $C_{2,1}^{*}$, do not bear physical meaning *per se*, but are rather governed by four physical parameters: the momentum flow ratio, the WJ injection angle, the nozzle distance and the positions of the SJ and WJ virtual origins. The first three of these can be selected prior to design/operation while the fourth has to be obtained experimentally.

To estimate species mass fractions such as oxygen and hydrocarbon at the merging point where the center of the WJ touches the boundary of the SJ, we define a dilution index,

$$\tilde{\omega}^{j^*}\Big|_{merging} = \frac{\tilde{\omega}_1^{j^*}\dot{m}_1\Big|_{merging} + \tilde{\omega}_2^{j^*}\dot{m}_2\Big|_{merging}}{\dot{m}_1\Big|_{merging} + \dot{m}_2\Big|_{merging}} \tag{3.37}$$

3.2.4 Solution of the dimensionless governing equations

An analytical solution can be obtained for all ODEs of the SJ flow (when $i = 2$) and some ODEs for the WJ flow – the mass fraction, Eq.(3.35), and density, Eq.(3.36), because they can be decoupled when the time independent variable is replaced by the arc length independent variable, Eq.(3.30) for $i = 2$ (note that $s_2^* = z_2^*$):

$$\frac{d\tilde{v}_{2,z}^*}{dz_2^*} = \begin{cases} -C_{2,2}^*\tilde{v}_{2,z}^{*\,2} & \text{for } z_2^* > z_{2,o}^* \\ 0 & \text{for } 0 \le z_2^* \le z_{2,o}^* \end{cases} \tag{3.38}$$

Using the chain rule, Eq.(3.35) and (3.36) can be transformed into

$$\frac{d\tilde{\omega}_i^{j^*}}{ds_i^*} = \begin{cases} (\tilde{\omega}_\infty^{j^*} - \tilde{\omega}_i^{j^*})\dfrac{1}{(s_i^* - s_{i,o}^* + 1/C_{3,i}^*)} & \text{for } s_i^* > s_{i,o}^* \\ 0 & \text{for } 0 \le s_i^* \le s_{i,o}^* \end{cases} \tag{3.39}$$

$$\frac{d\bar{\rho}_i^*}{ds_i^*} = \begin{cases} C_{4,i}^*\left\{(s_i^* - s_{i,o}^* + \dfrac{1}{C_{3,i}^*})\sum_j \dfrac{\tilde{\omega}_i^{j^*}}{W_j}\right\}^{-1} \\ \quad -\bar{\rho}_i^*\left\{\left(\sum_j \dfrac{\tilde{\omega}_i^{j^*}}{W_j}\right)^{-1}\sum_j \dfrac{1}{W_j}\dfrac{d\tilde{\omega}_i^{j^*}}{ds_i^*} + (s_i^* - s_{i,o}^* + \dfrac{1}{C_{3,i}^*})^{-1}\right\} & \text{for } s_i^* > s_{i,o}^* \\ 0 & \text{for } 0 \le s_i^* \le s_{i,o}^* \end{cases} \tag{3.40}$$

leading to the following analytical solution.

$$\tilde{v}_{2,z}^{*}(z_2^{*}) = \begin{cases} \left\{ C_{2,2}^{*}(z_2^{*} - z_{2,o}^{*}) + 1 \right\}^{-1} & \text{for } z_2^{*} > z_{2,o}^{*} \\ 1 & \text{for } 0 \le z_2^{*} \le z_{2,o}^{*} \end{cases} \tag{3.41}$$

$$\tilde{\omega}_i^{j*}(s_i^{*}) = \begin{cases} \omega_{\infty}^{j*} - \dfrac{\omega_{\infty}^{j*} - \tilde{\omega}_i^{j*}\big|_{s_i^{*}=0}}{C_{3,i}^{*}(s_i^{*} - s_{i,o}^{*}) + 1} & \text{for } s_i^{*} > s_{i,o}^{*} \\ \tilde{\omega}_i^{j*}\big|_{s_i^{*}=0} & \text{for } 0 \le s_i^{*} \le s_{i,o}^{*} \end{cases} \tag{3.42}$$

and

$$\overline{\rho}_i^{*}(s_i^{*}) = \begin{cases} \dfrac{\dfrac{C_{4,i}^{*}}{B} C_{3,i}^{*}(s_i^{*} - s_{i,o}^{*}) + (1 - \dfrac{A_i}{B})}{C_{3,i}^{*}(s_i^{*} - s_{i,o}^{*}) + (1 - \dfrac{A_i}{B})} & \text{for } s_i^{*} > s_{i,o}^{*} \\ 1 & \text{for } 0 \le s_i^{*} \le s_{i,o}^{*} \end{cases} \tag{3.43}$$

where $A_i = \sum_j \dfrac{\omega_{\infty}^{j*} - \tilde{\omega}_i^{j*}\big|_{s_i^{*}=0}}{W_j}$ and $B = \sum_j \dfrac{\omega_{\infty}^{j*}}{W_j}$.

By substituting Eq.(3.41) into Eq.(3.27) for $i = 2$, we can obtain a dimensionless transit time, t_2^{*}, for the fluid element of the SJ at the location z_2^{*}:

$$t_2^{*}(z_2^{*}) = \begin{cases} \left(z_2^{*} - z_{2,o}^{*}\right)\left\{ \dfrac{C_{2,2}^{*}}{2}(z_2^{*} - z_{2,o}^{*}) + 1 \right\} + z_{2,o}^{*} & \text{for } z_2^{*} > z_{2,o}^{*} \\ z_2^{*} & \text{for } 0 \le z_2^{*} \le z_{2,o}^{*} \end{cases} \tag{3.44}$$

The other seven ODEs, Eq.(3.27) for $i = 1$, (3.28), (3.29), (3.30) for $i = 1$, (3.31), (3.32) and (3.33), can be solved numerically.

3.3 Cold model experiment

Cold model experiments were performed to obtain data for the validation of the 3-D SJ/WJ physical model and later CFD simulation in this work. A dual jet arrangement, Figure 3.3, simulating the SJ/WJ model was used for this purpose. The jet nozzles were manufactured from 25.4 mm diameter aluminum bar stock with exit port diameters of 11.9 mm and 6.35 mm for SJ and WJ respectively. Each nozzle was bored with a 7° taper from an internal diameter of 20.5 mm at one end of a 70 mm bar to the final exit diameter as shown in Figure 3.4. These nozzles were mounted in support blocks at the different separation distances, d_{12}, and angles, φ and ϕ, noted in Table 3.1.

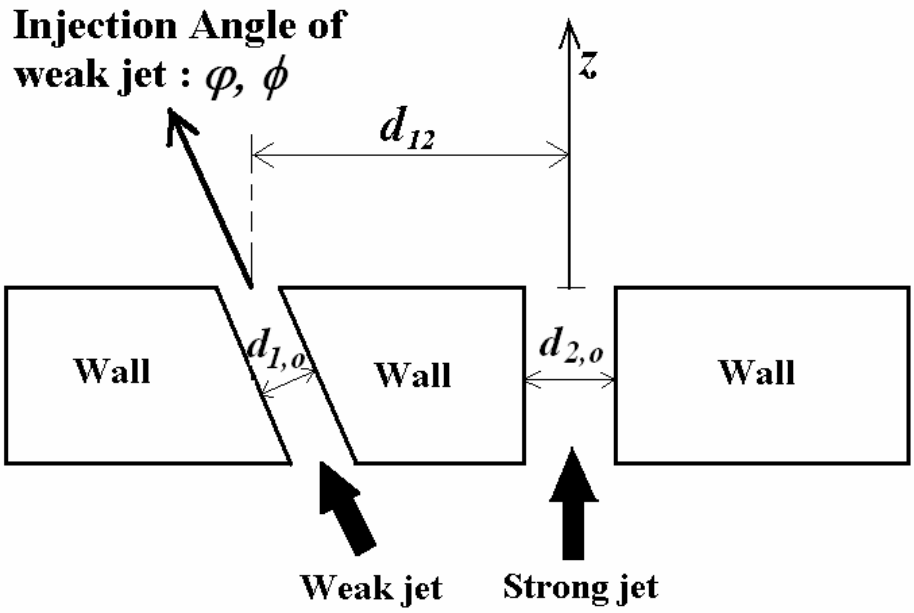

Figure 3.3. A schematic diagram of the cold model experiment system.

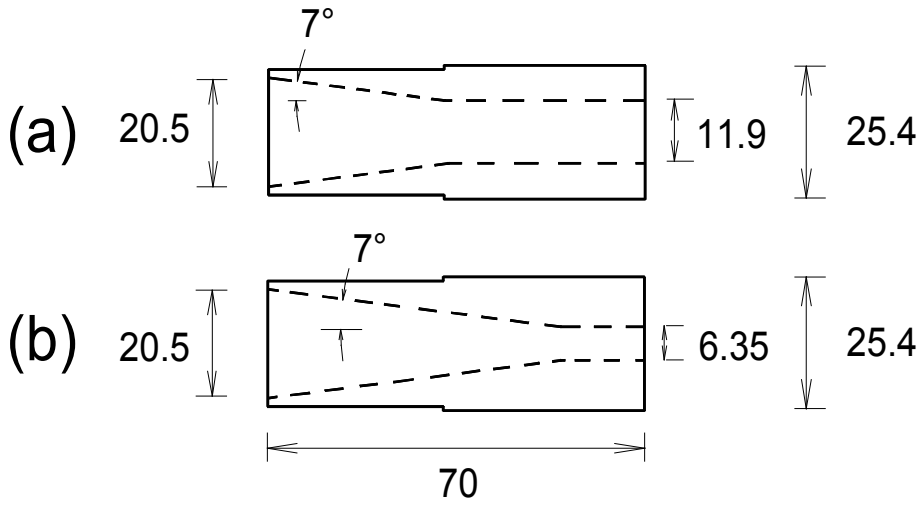

Figure 3.4. Nozzle geometries for (a) the strong jet and (b) the weak jet (Unit: mm).

Table 3.1. Cold model experiment conditions.

Injection angle of WJ, (φ,ϕ)	Momentum flow ratio	Distance between nozzles, m
(80°,0°)		
(70°,0°)	0.02	0.127
(75.89°,44.56°)	0.01	0.0635
(62.01°,43.22°)	0.005	
(67.73°,62.73°)		

The air supply for the jets was provided by independent sources, a high-pressure blower for the SJ and a compressor system for the WJ. The SJ flow rate was controlled by a gate valve and monitored by an orifice meter. The WJ flow rate was controlled by a pressure regulator, using a previously obtained calibration curve. The SJ air temperature was about 45°C, the WJ temperature was about 29°C and the ambient temperature was about 27°C. This experiment system was operated in a large room with precautions and tests taken to verify that the impact of external drafts on the jet flow field was negligible.

Velocity measurements were obtained with a 1.59 mm diameter Kiel probe and an impact probe constructed from stainless steel hypodermic tubing (0.90 mm O.D. and 0.50 mm I.D.). These probes were calibrated against a standard Pitot probe in a wind tunnel over the velocity range of 3 ~ 30 m/s. The coefficients for both probes were 0.99 ~ 1.00 over this velocity range. The Kiel probe provides accurate estimates of the velocity field over a wide range of pitch and yaw angles (typically ± 40°). The impact probe was used to provide estimates of the mean velocity field at the exit of the two nozzles as well as the primary data for the centerline velocity measurements. The Kiel probe was used to estimate the magnitude of the velocity vector and trajectory for the WJ. Pressure readings were obtained with Datametric Inc. Barocell pressure transducers with ranges of 0 ~ 2.5 and 0 ~ 10 kPa. The transducer output was processed with a Hewlett Packard 5328A Universal Counter adapted to provide time averaged voltage readings over 10s and 100s time periods.

Velocity profiles at the exits of SJ and WJ nozzles were obtained and found to exhibit flat profiles within ±1.5% of the source velocity over 85% of the inner area of each port. A typical velocity profile is shown in Figure 3.5. The larger spread in the data near the wall was due to positioning error of the probe. The centerline mean velocity decay for the SJ and the WJ was also measured, Figure 3.6. The virtual origin and the centerline velocity decay constant were determined from these results.

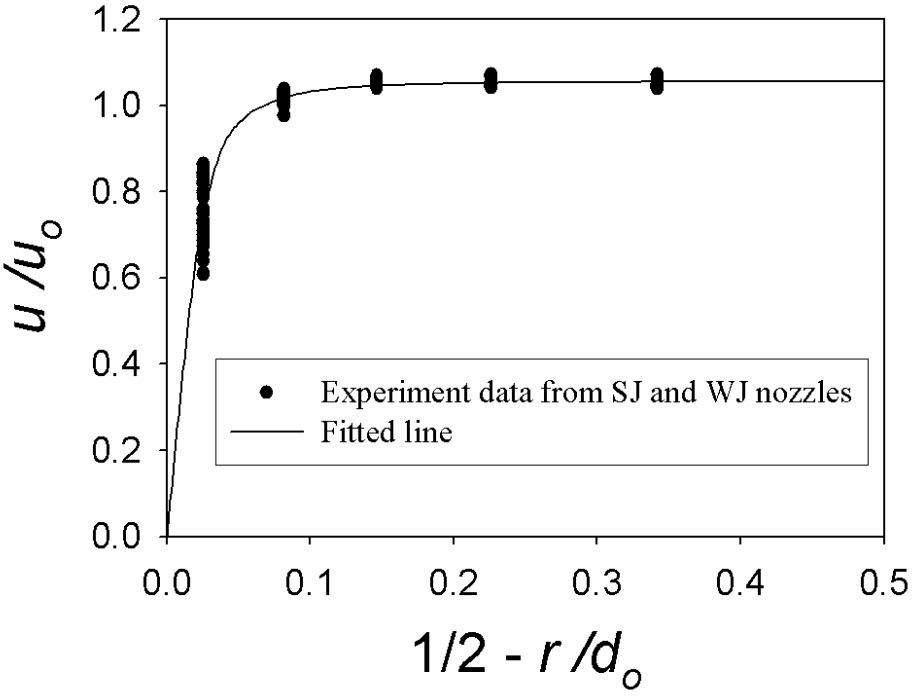

Figure 3.5. Velocity profile at the exit of the SJ and the WJ nozzles.

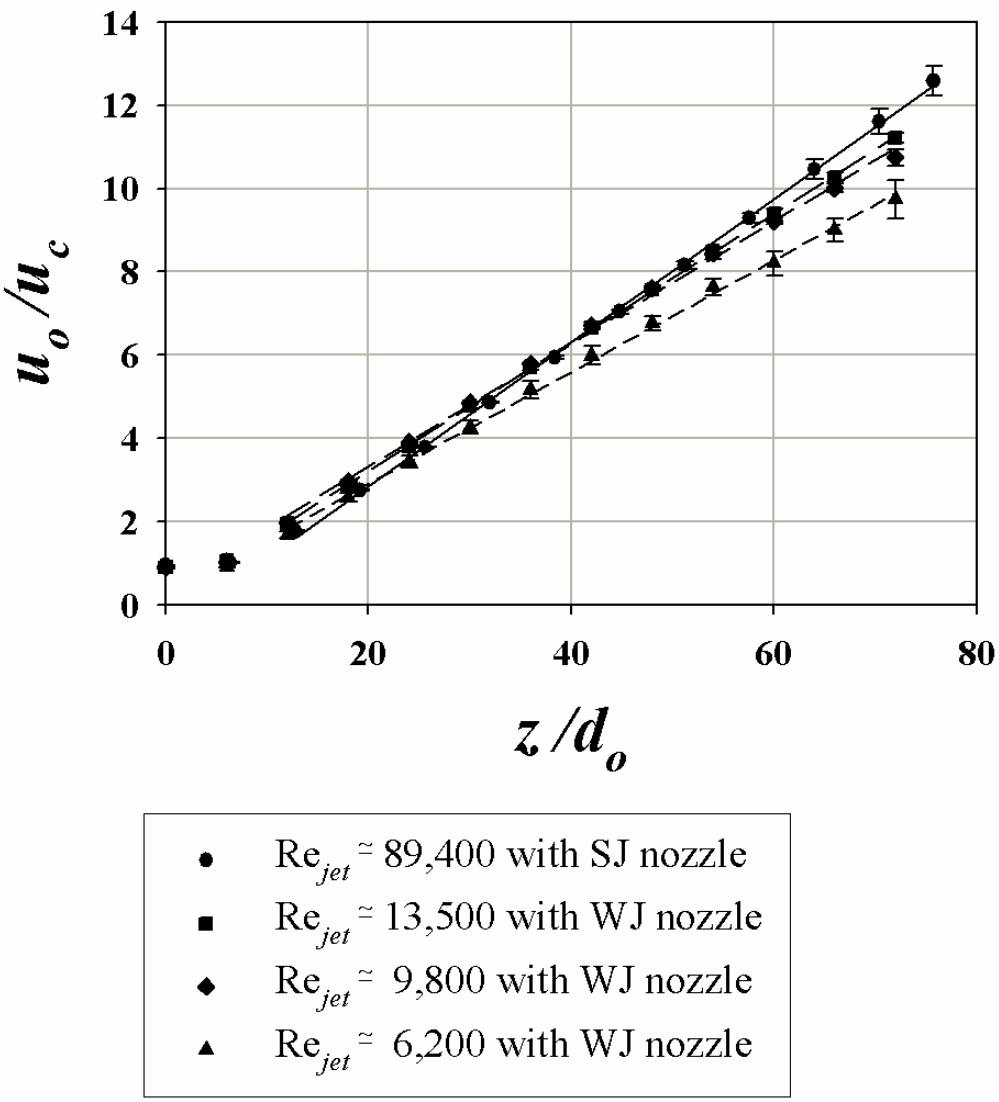

Figure 3.6. Centerline mean velocity with measurement variance indicated by error bars.

The experimental conditions and jet flow properties during the trajectory testing runs are shown in Table 3.2. The SJ was kept at a constant flow rate of around 0.0178 kg/s (source velocity of 137 m/s), corresponding to a Reynolds number of 93,800 while the WJ was varied with flow rates of 0.669 ~ 1.33×10^{-3} kg/s (source velocity of 18.2 ~ 36.4 m/s), corresponding to Reynolds numbers of about 7,400 ~ 14,500.

Table 3.2. Initial jet flow properties used to estimate the WJ trajectory (cold model experiments).

	Diameter, mm	Density, kg/m^3	Source velocity, m/s	Mass flow rate, kg/s	Jet Reynolds number
SJ (45 °C)	11.91	1.1150	137.2	0.01783	93885
WJ (29 °C)	6.35	1.1746	36.2	0.001325	14532
			25.5	0.000949	10421
			18.5	0.000669	7378

Ambient temperature is 27 °C

The WJ trajectory was initially tracked by a simple flow visualization method, a fine thread mounted on a wire holder just above the nozzle exit, Figure 3.7. These observations helped to select feasible locations for more detailed mean velocity measurements with the Kiel probe. In most cases a total of 5 downstream measurement locations were chosen for trajectory mapping. At each of these downstream locations detailed traverses were made in the *xy* plane. Two profiles around the expected velocity maximum were obtained, one along the x- and the other along the y-axis, 9 points each. A Gaussian curve fit was passed through these data. An example of the two velocity profiles of WJ at a certain plane and the fitted Gaussian curve are shown in Figure 3.8. The location of the maximum velocity was identified as the trajectory of the WJ and the distance between the points where the local velocity was 50% of the maximum was used as a measure of the jet width.

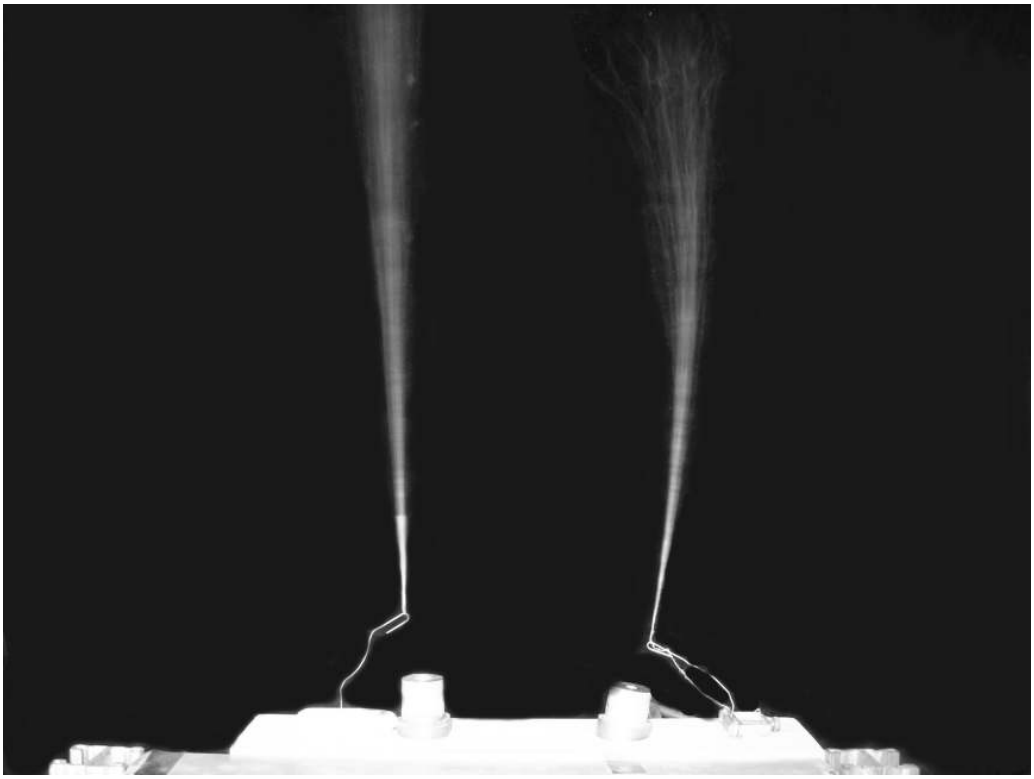

Figure 3.7. Visual indication of the SJ and the WJ trajectories traced by light threads suspended above the nozzles.

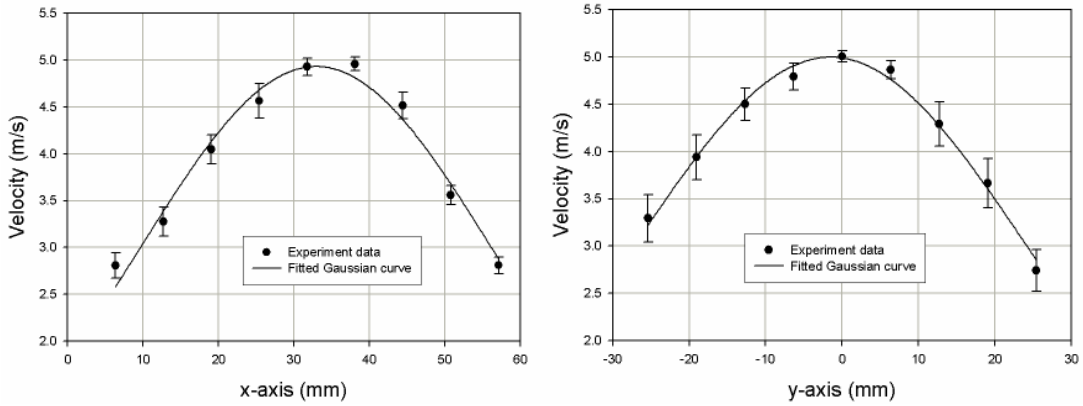

Figure 3.8. Velocity profiles of WJ along x- and y-axis at a certain selected plane and fitted Gaussian curve. Error bars represent the standard deviation of the measurement at each point.

3.4 Reynolds-Averaged Navier-Stokes simulation

The SJ/WJ problem was simulated with the standard k-ε turbulence model as an isothermal flow, using the FLUENT 6.0 CFD package. The geometry of the simulation domain is described in Table 3.3 and Figure 3.9.

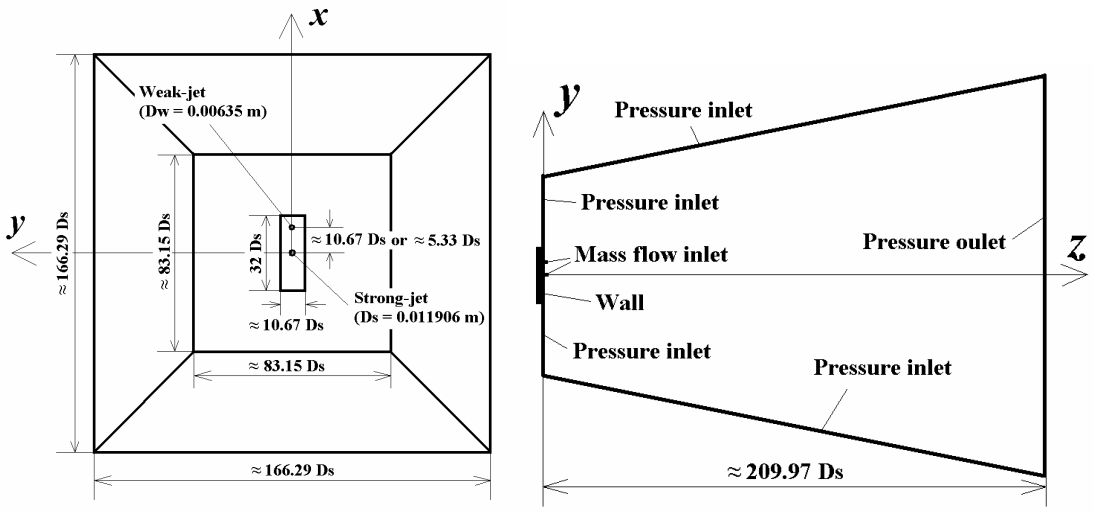

Figure 3.9. Schematic diagrams of the simulation domain.

Table 3.3. Geometric size of the simulation domain.

Chamber	Diagonal of the upper face: 2.8 m Diagonal of the lower face: 1.4 m Height: 2.5 m
Strong jet nozzle	Radius: 0.005953 m
Weak jet nozzle	Radius: 0.003175 m
Bottom supporting block	0.127 m × 0.381 m
Distance between nozzles	0.127 m or 0.0635 m

The domain is defined as a four-sided truncated pyramid, with the face magnification ratio of 2:1. The domain is meshed by a Cooper mesh scheme, with the source faces paved by triangular mesh with appropriate node concentration around the jet nozzles, Figure 3.10. The preliminary grid dependency test was performed for three mesh sizes: 583,320, 270,960 and 187,080 cells and for first-order and second-order upwind discretization. As indicated by the *z*-velocity profile along the SJ axis in Figure 3.11, there is only a marginal difference between the profiles for these mesh sizes and discretization schemes. Although the coarsest mesh and a first-order upwind scheme would suffice, all simulations were conducted by using the finest mesh (583,320 cells) and the second-order upwind scheme.

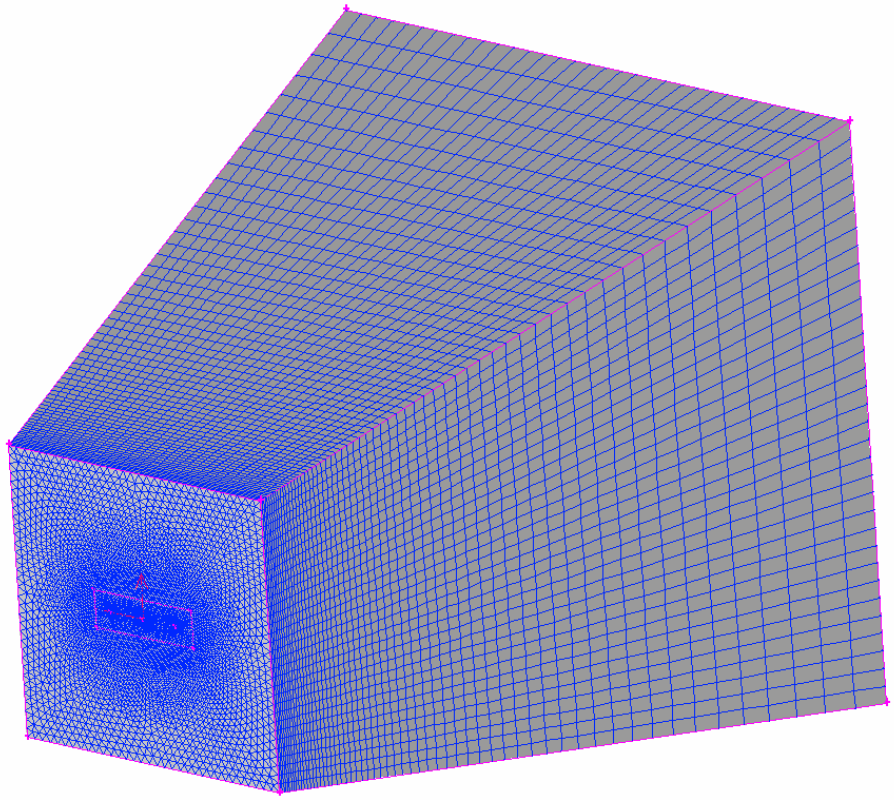

Figure 3.10. Mesh scheme for the simulation domain.

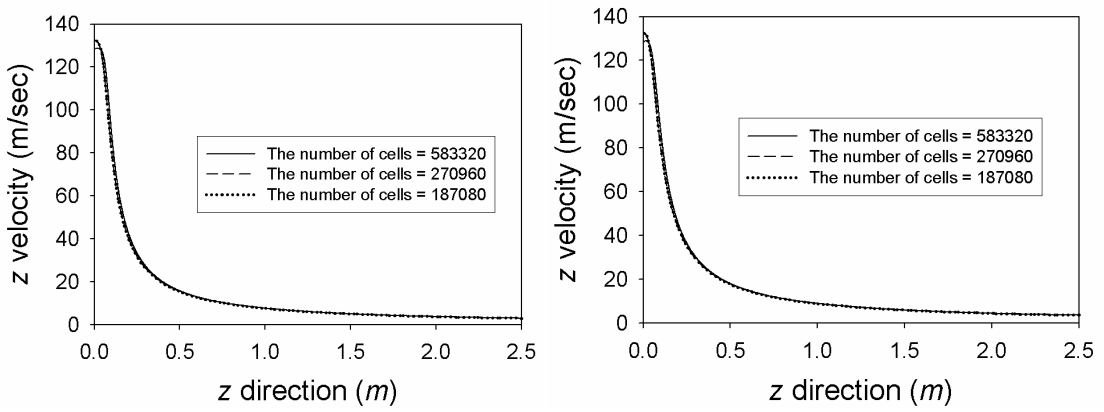

(a) First-order upwind differencing (b) Second-order upwind differencing

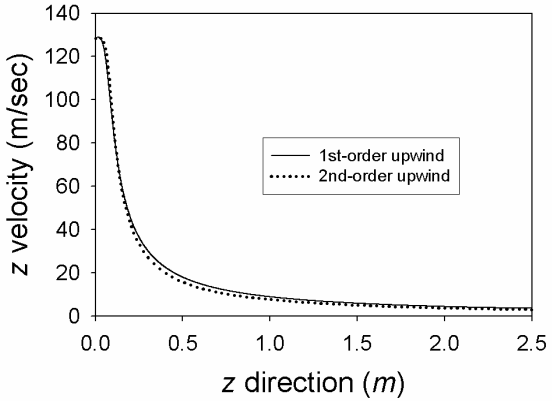

(c) At the finest grid; 583,320 cells

Figure 3.11. Comparisons of z-velocity decay along the SJ axis for different grid sizes and differencing schemes: (a) First-order upwind differencing; (b) Second-order upwind differencing; (c) results at the finest grid (583,320 cells). Other parameters: injection angles (φ, ϕ) = (80°, 0°), the momentum ratio, ψ_{12} = 0.02 and the nozzle distance, d_{12} = 0.127 m.

Boundary conditions were used to mimic the experimental conditions as close as possible. There is a rectangular "wall" block surrounding the two jet nozzles, matching the solid block surface in the experimental setup. The entrainment conditions at the open boundaries were set with 1% turbulence intensity and 1 m hydraulic diameter in order to simulate entrained stagnant fluid. Inlets turbulent conditions for the SJ and the WJ were set at 5% turbulence intensity and

hydraulic diameters of 0.012 and 0.006 m, respectively. Mass flow rates of each jet, density and viscosity were obtained from the corresponding experimental data.

The validity of the RANS simulation setup was tested by comparing the entrainment flow of the SJ with that calculated from Eq.(2.2) in Chapter 2. The average difference was 1.22%, the maximum was 1.77%, through all RANS simulations. Figure 3.12 shows a typical WJ trajectory identified by a velocity magnitude contour plot on the symmetry plane (for the case of 2-D SJ/WJ system). The trajectory of the WJ was traced from the velocity magnitude contour plot on many selected *xy* planes along the z-axis.

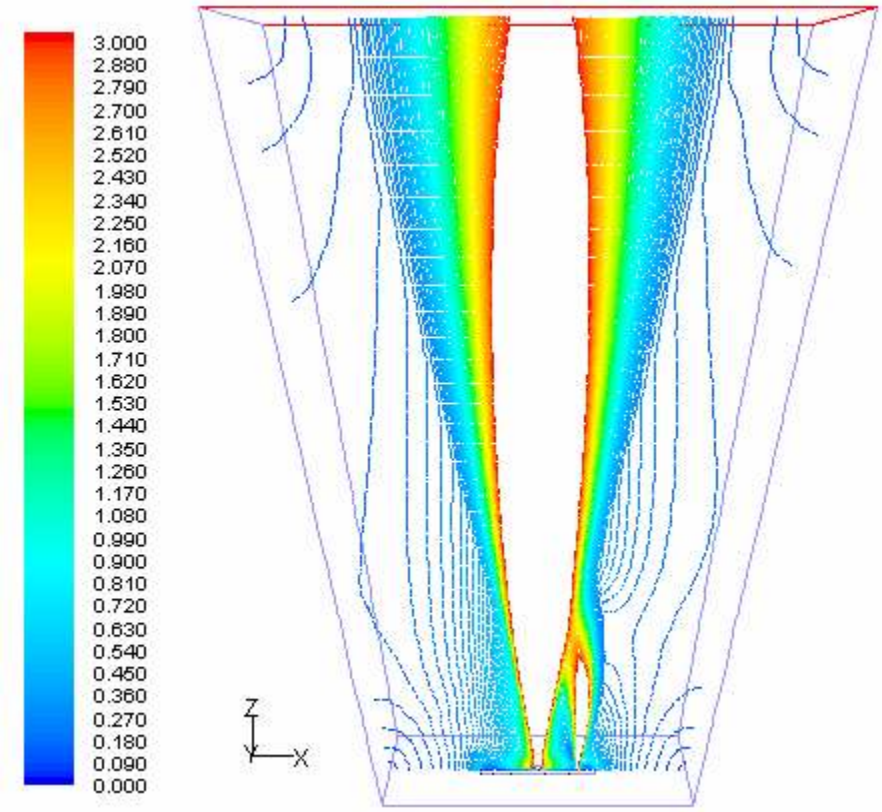

Figure 3.12. A typical velocity magnitude contour (m/s) on the symmetry plane (2-D SJ/WJ case).

3.5 Results and discussion

3.5.1 Virtual origin and entrainment coefficient for the low jet Reynolds number flow

The virtual origin and the centerline velocity decay constant in Eq.(2.1) in Chapter 2 were measured for the SJ and the WJ in a preliminary experiment. The results for different jet Reynolds numbers are shown in Table 3.4.

Table 3.4. The virtual origin and the centerline velocity decay constant for the SJ and the WJ.

	Re_{jet}	C_c	z_o/d_o	R^2
SJ	89376.5	0.1725	3.46	0.9995
WJ	13542.6	0.1543	-0.87	0.9999
	9821.0	0.1470	-2.67	0.9980
	6244.3	0.1342	-1.68	0.9983

By fitting the above values into Eq.(2.3), we can estimate the entrainment coefficient for the WJ:

$$C_{e,1} \approx \frac{0.32}{0.1725}\left(2.749\times10^{-6}\cdot \mathrm{Re}_{jet}+0.118\right) \text{ with } R^2 \approx 0.972 \tag{3.45}$$

The virtual origin of the WJ was negative in all cases, thus it has no effect on the 3-D SJ/WJ physical model. From the RANS simulations, the centerline mean velocity decay constant and the virtual origin for the SJ were 0.170 and 0.290, respectively.

3.5.2 The comparison of the 3-D SJ/WJ physical model, cold model experiment and RANS simulation

The system of the seven coupled ODEs, Eq.(3.27) for $i = 1$, (3.28), (3.29), (3.30) for $i = 1$, (3.31), (3.32) and (3.33), comprising the main set of the 3-D SJ/WJ physical model, was solved by the Rosenbrock method [92] and compared with the experimental data and RANS simulation results.

The WJ trajectories for the momentum ratios of ψ_{12} = 0.005, 0.01 and 0.02 are shown in Figure 3.13 for d_{12} = 0.127 m, (φ, ϕ) = (80°,0°), Figure 3.14 for d_{12} = 0.0635 m, (φ, ϕ) = (80°,0°), Figure 3.15 for d_{12} = 0.127 m, (φ, ϕ) = (70°,0°), Figure 3.16 for d_{12} = 0.127 m, (φ, ϕ) = (75.89°,44.56°), Figure 3.17 for d_{12} = 0.127 m, (φ, ϕ) = (62.01°,43.22°), and Figure 3.18 for d_{12} = 0.127 m, (φ, ϕ) = (67.73°,62.73°). These cases fall into two categories: the 2-D SJ/WJ system with (φ, ϕ) = (80°,0°), (70°,0°) and the 3-D SJ/WJ system with (φ, ϕ) = (75.89°,44.56°), (62.01°,43.22°) and (67.73°,62.73°). The error bars in Figure 3.13 ~ Figure 3.15 indicate the WJ width defined as the half maximum velocity location, obtained from the Gaussian curve fit. The experimental data in Figure 3.16 ~ Figure 3.18 (3-D plots) have similar WJ width scales although not shown in the 3-D graphs.

As seen in Figure 3.13 ~ Figure 3.15 (2-D SJ/WJ system), this 3-D SJ/WJ physical model predicts the WJ trajectory quite well even though trajectories from this model are slightly shorter than those obtained experimentally. On the other hand, the WJ trajectories predicted from the RANS simulation are more curved, leading to lower estimates for the position of confluence for the jets. Similar observations are also found in Figure 3.16 ~ Figure 3.18 (3-D SJ/WJ system).

This under-prediction of RANS simulation may be attributed to the small differences of the entrainment flow mentioned in section 3.4 and limitations of standard k-ε model that is a semi-empirical model with adjustable parameters for fully-developed, isotropic turbulence. Jet flow is an anisotropic flow. Also, note that the original parameters of the standard k-ε model (see section 2.4.1) were used in this RANS simulation.

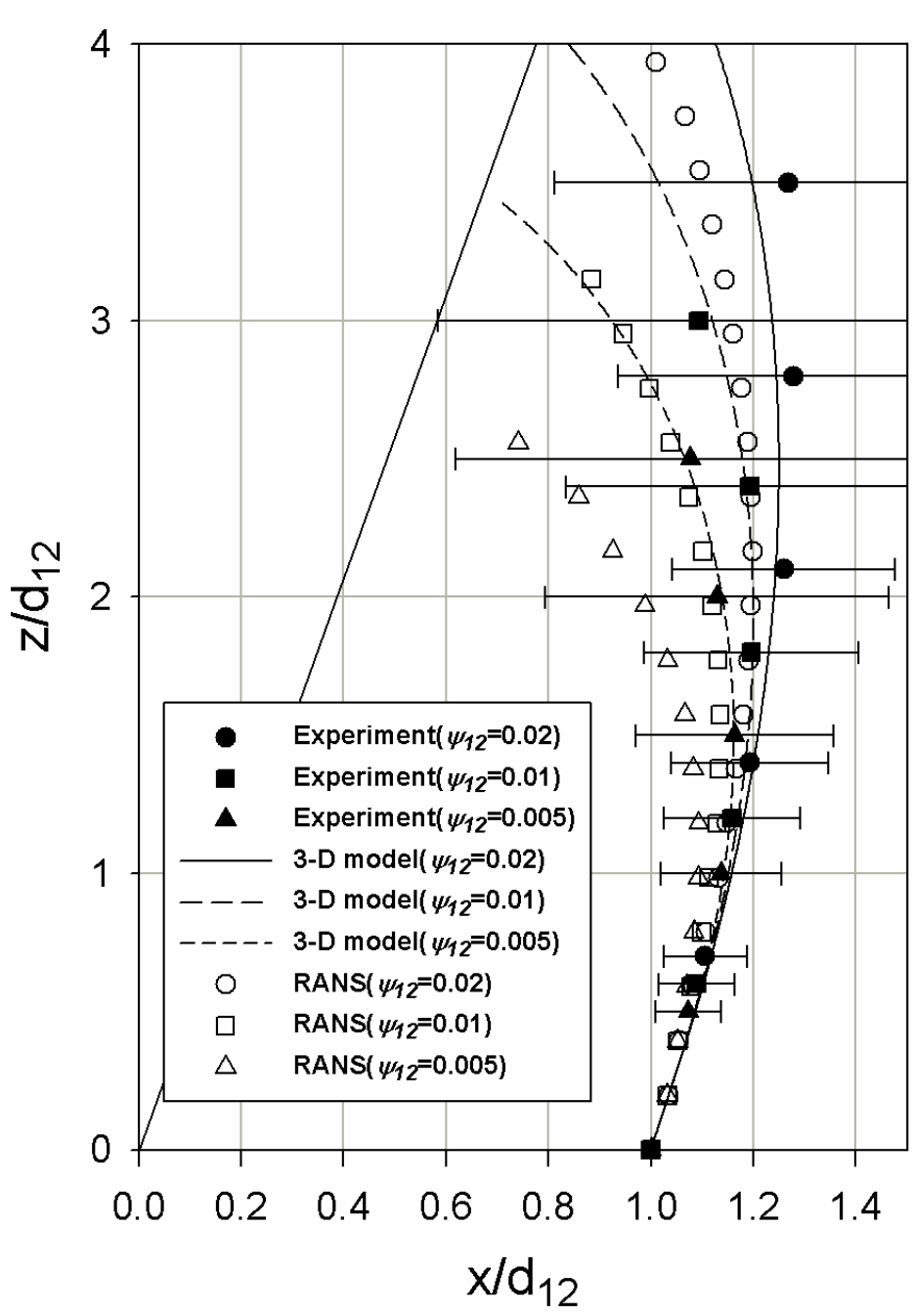

Figure 3.13. WJ trajectories from the 3-D SJ/WJ physical model, cold model experimental data and RANS simulations with various momentum ratios at the injection angle of (φ, ϕ) = (80°,0°) and the nozzle distance of d_{12} = 0.127 m (error bars represent the WJ width at the half centerline velocity).

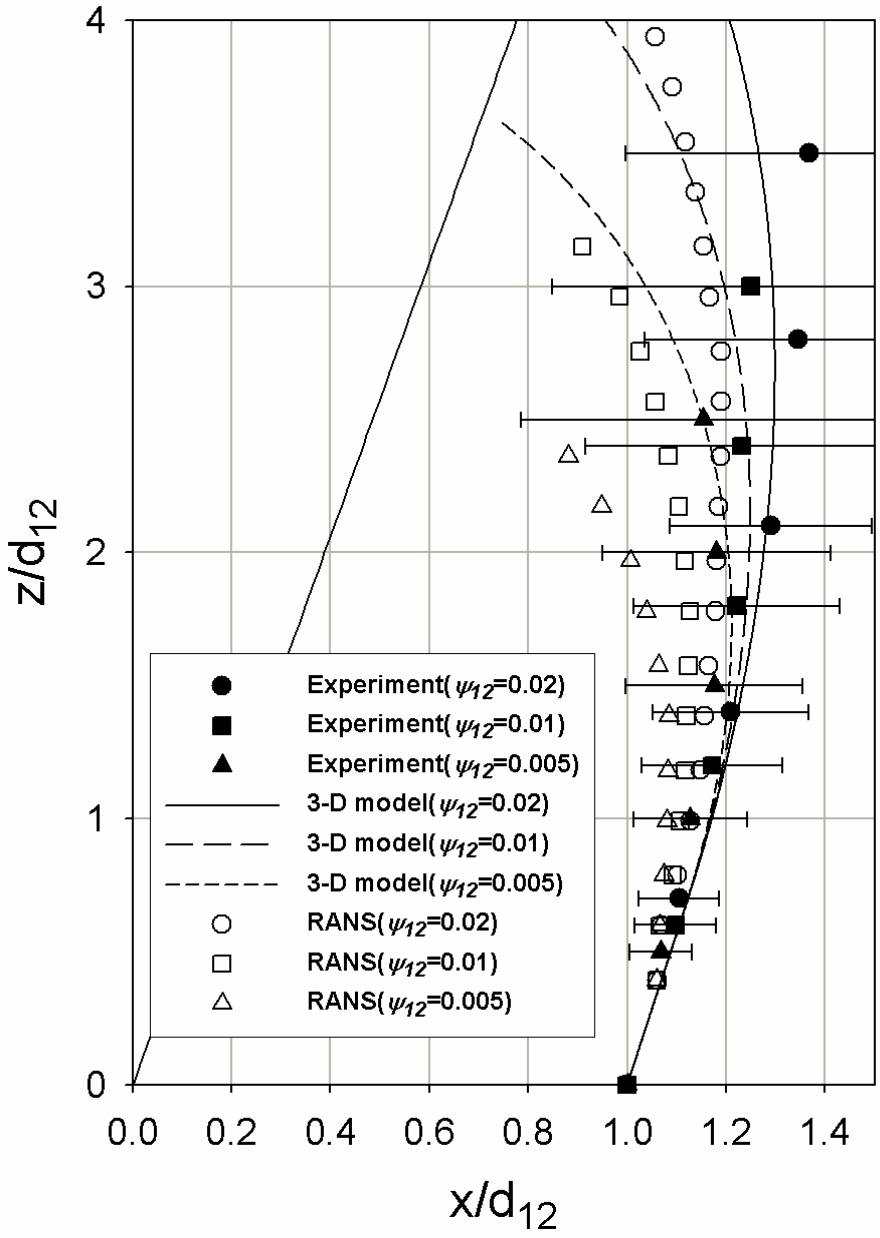

Figure 3.14. WJ trajectories from the 3-D SJ/WJ physical model, cold model experimental data and RANS simulations with various momentum ratios at the injection angle of (φ, ϕ) = (80°,0°) and the nozzle distance of d_{12} = 0.0635 m (error bars represent the WJ width at the half centerline velocity).

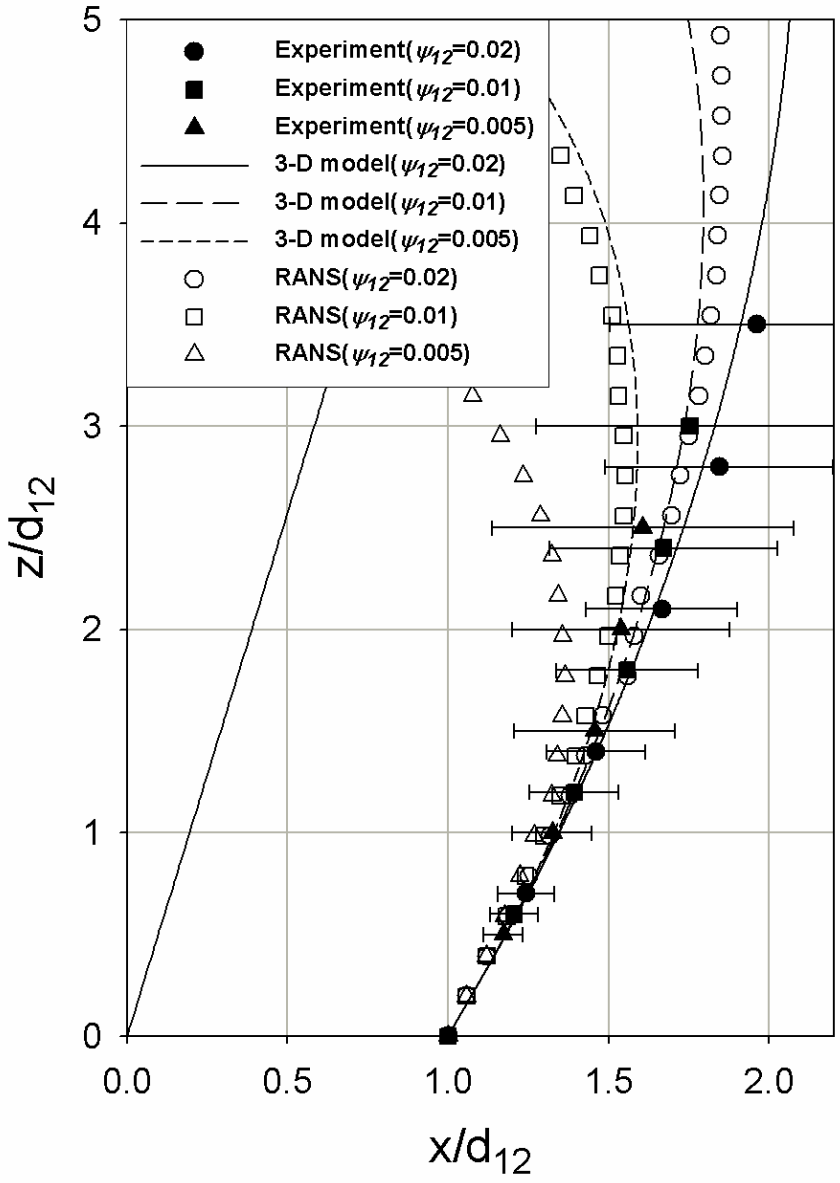

Figure 3.15. WJ trajectories from the 3-D SJ/WJ physical model, cold model experimental data and RANS simulations with various momentum ratios at the injection angle of (φ, ϕ) = (70°,0°) and the nozzle distance of d_{12} = 0.127 m (error bars represent the WJ width at the half centerline velocity).

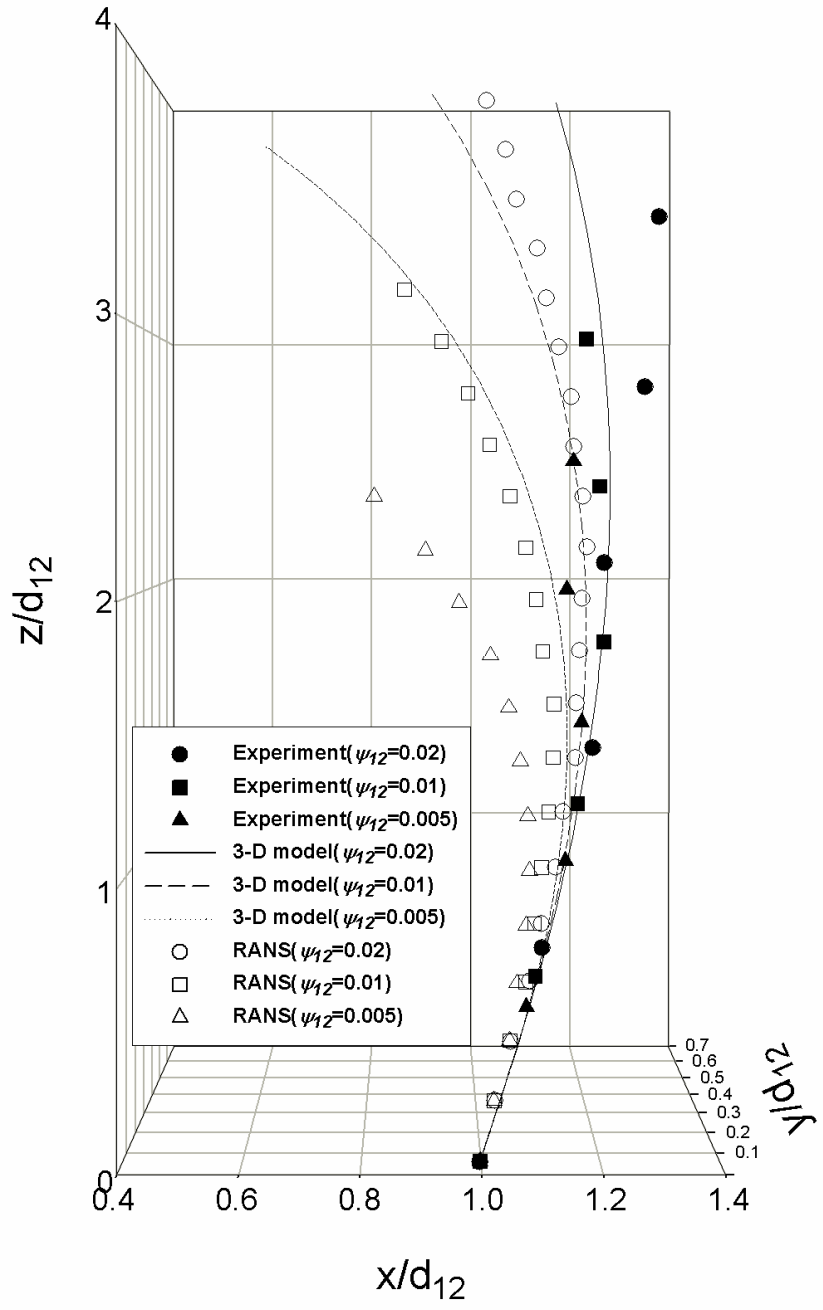

Figure 3.16. WJ trajectories from the 3-D SJ/WJ physical model, cold model experimental data and RANS simulations with various momentum ratios at the injection angle of (φ, ϕ) = (75.89°, 44.56°) and the nozzle distance of d_{12} = 0.127 m.

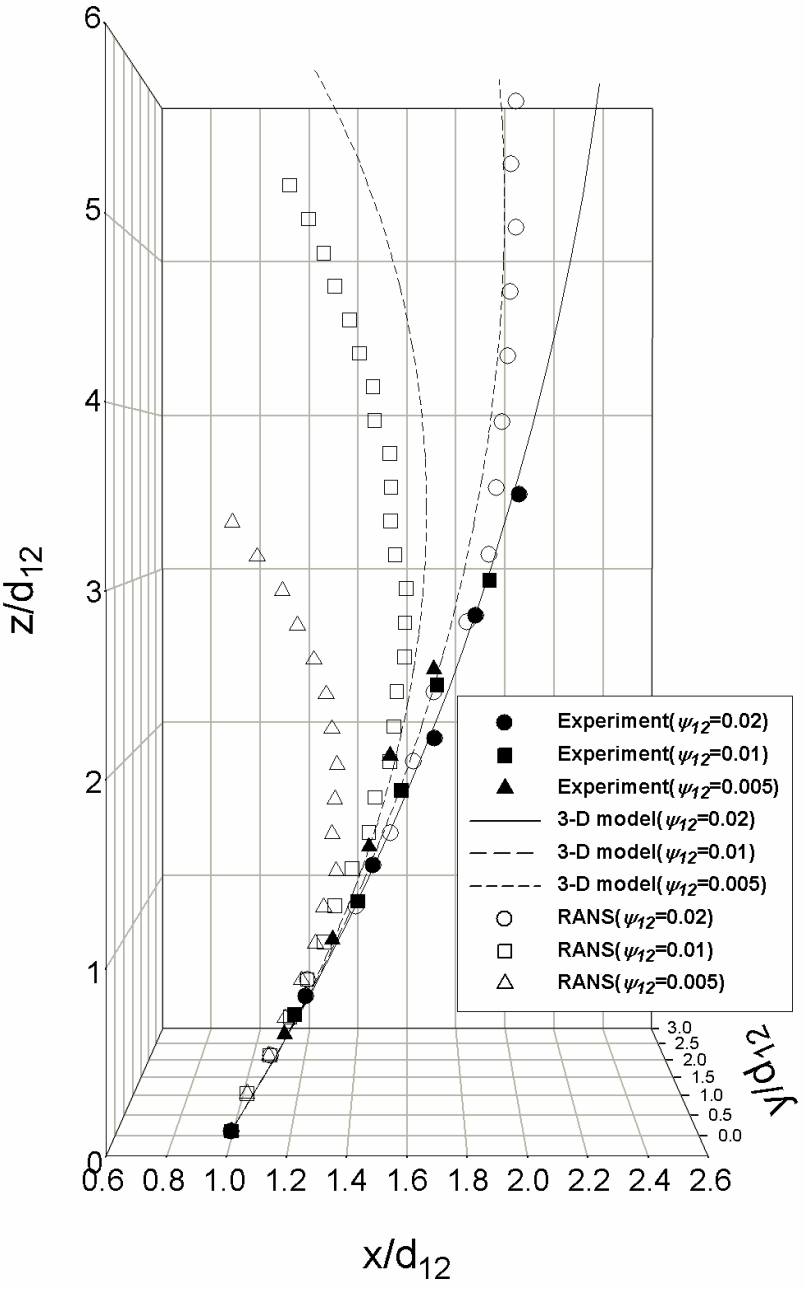

Figure 3.17. WJ trajectories from the 3-D SJ/WJ physical model, cold model experimental data and RANS simulations with various momentum ratios at the injection angle of (φ, ϕ) = (62.01°, 43.22°) and the nozzle distance of d_{12} = 0.127 m.

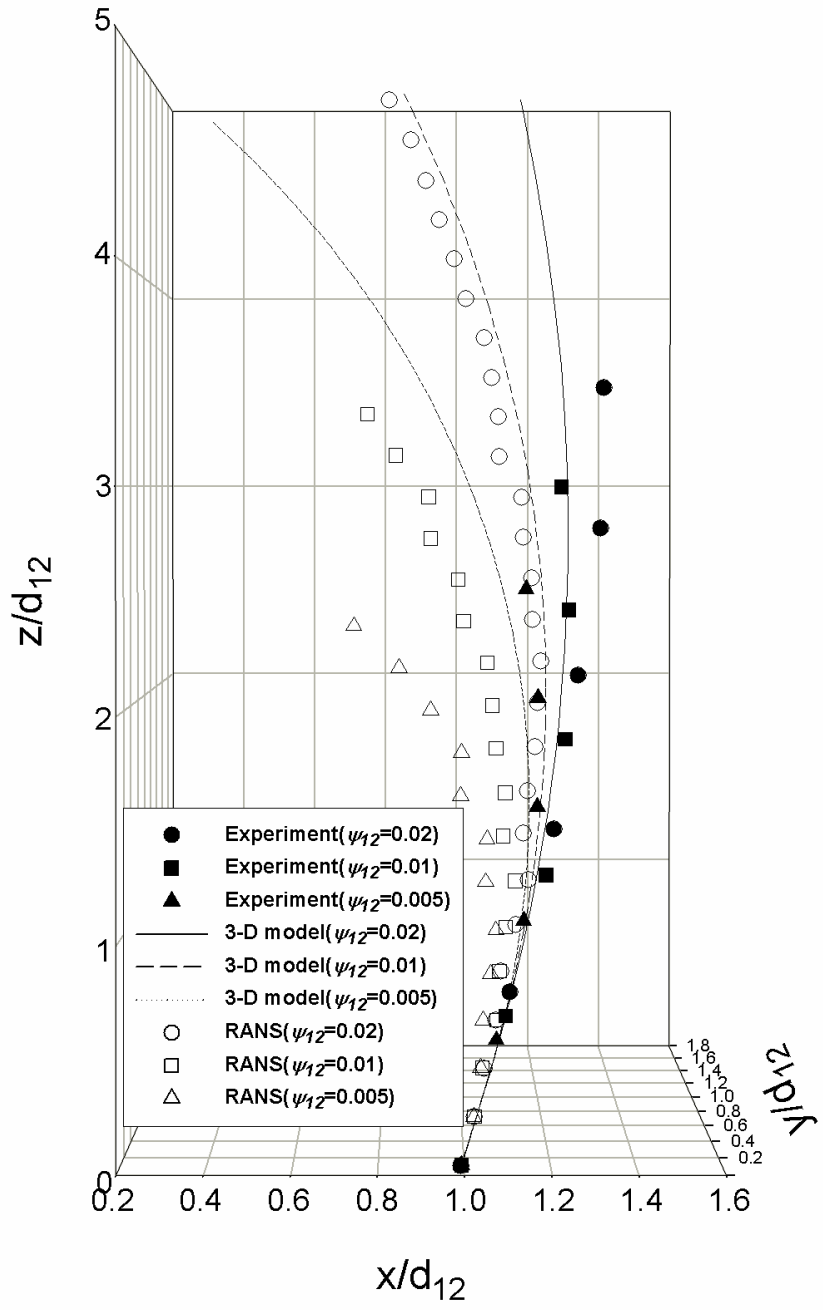

Figure 3.18. WJ trajectories from the 3-D SJ/WJ physical model, cold model experimental data and RANS simulations with various momentum ratios at the injection angle of (φ, ϕ) = (67.73°, 62.73°) and the nozzle distance of d_{12} = 0.127 m.

3.5.3 The effects of the design/operation controlling factors on the SJ/WJ system

As noted above, four design/operation controlling factors were identified for the SJ/WJ system: the momentum flow ratio, ψ_{12}; the injection angle of WJ, (φ, ϕ); the distance between SJ and WJ nozzle, d_{12}, and the virtual origins of SJ and WJ, $z_{2,o}$ and $s_{1,o}$. The effect of the momentum ratio and the injection angle of WJ on the SJ/WJ system was noted in the previous subsection, i.e. the WJ trajectory is longer at larger momentum ratios and when the WJ injection angle is more divergent (as expected).

In addition, the 3-D SJ/WJ physical model helps us understand the effect of the virtual origin and the nozzle separation distance. The WJ trajectory in Figure 3.19 and Figure 3.20 was calculated for the 'Virtual origin' case ($z_{2,o}/d_{2,o}$ = 3.46 and $s_{1,o}/d_{1,o}$ = 0) and 'No virtual origin' case ($z_{2,o}/d_{2,o}$ = 0 and $s_{1,o}/d_{1,o}$ = 0) at various momentum ratios, the WJ injection angle of (φ, ϕ) = (80°,0°) and the nozzle distance of d_{12} = 0.127 and 0.0635 m, respectively. Clearly, the positive virtual origin value of the SJ makes the WJ trajectory longer because the WJ fluid element in the region below SJ virtual origin is not affected by the entrainment flow of the SJ (the region 1 and region 2 in Figure 3.2). For the lack of a better term, we call this region the 'offset region'. Comparing the WJ trajectories in Figure 3.19 to those in Figure 3.20, the effect of a positive virtual origin of SJ flow is inversely proportional to the nozzle distance, when the SJ virtual origin position in physical units is kept constant ($z_{2,o}$ = 0.0412 m). This is because the nozzle distance, d_{12}, is used as a characteristic length of the dimensionless governing equation in the SJ/WJ system.

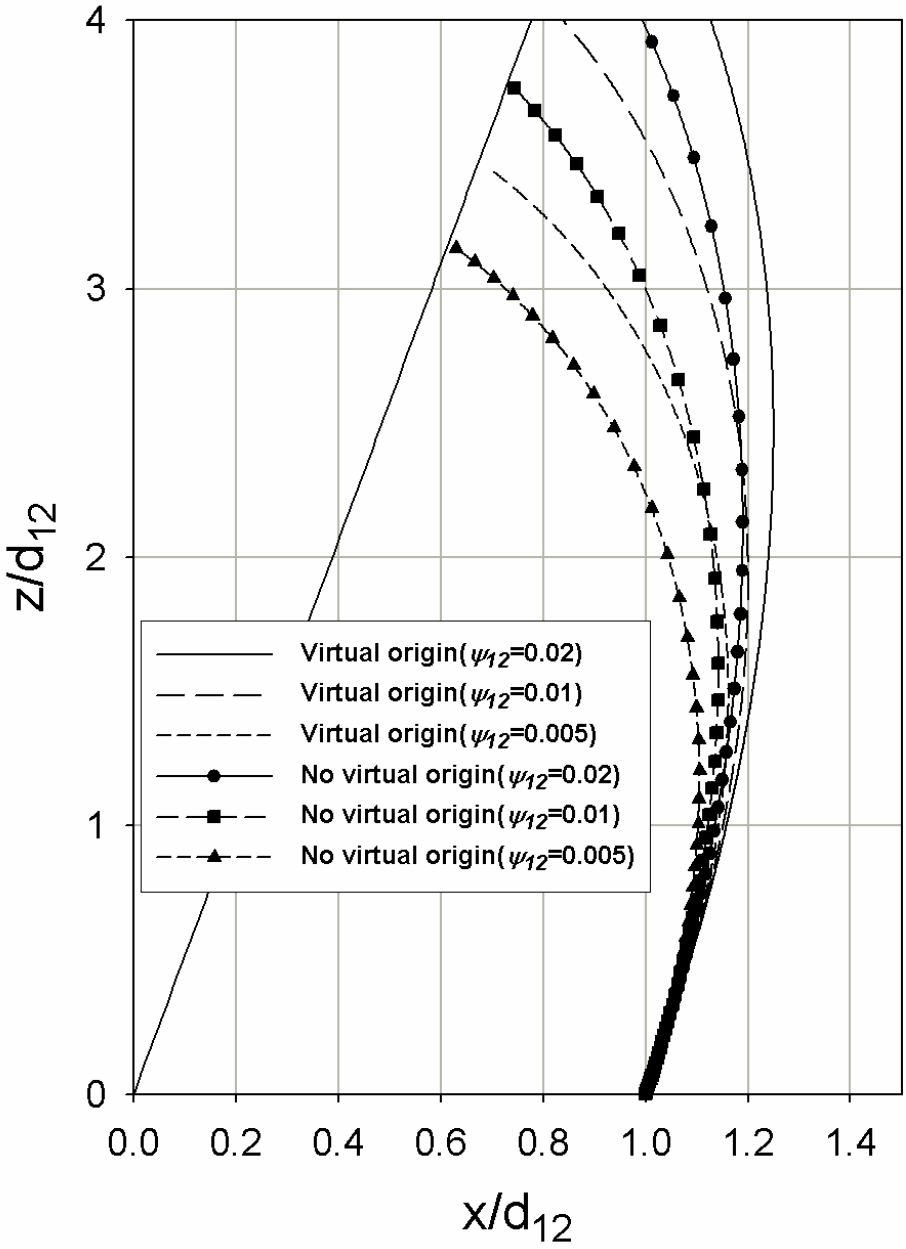

Figure 3.19. The effect of virtual origin on the SJ/WJ system at various momentum ratios when the WJ injection angle of (φ, ϕ) = (80°,0°) and the nozzle distance of d_{12} = 0.127 m; 'Virtual origin' indicates that $z_{2,o}/d_{2,o}$ = 3.46 and $s_{1,o}/d_{1,o}$ = 0 and 'No virtual origin' indicates that $z_{2,o}/d_{2,o}$ = 0 and $s_{1,o}/d_{1,o}$ = 0.

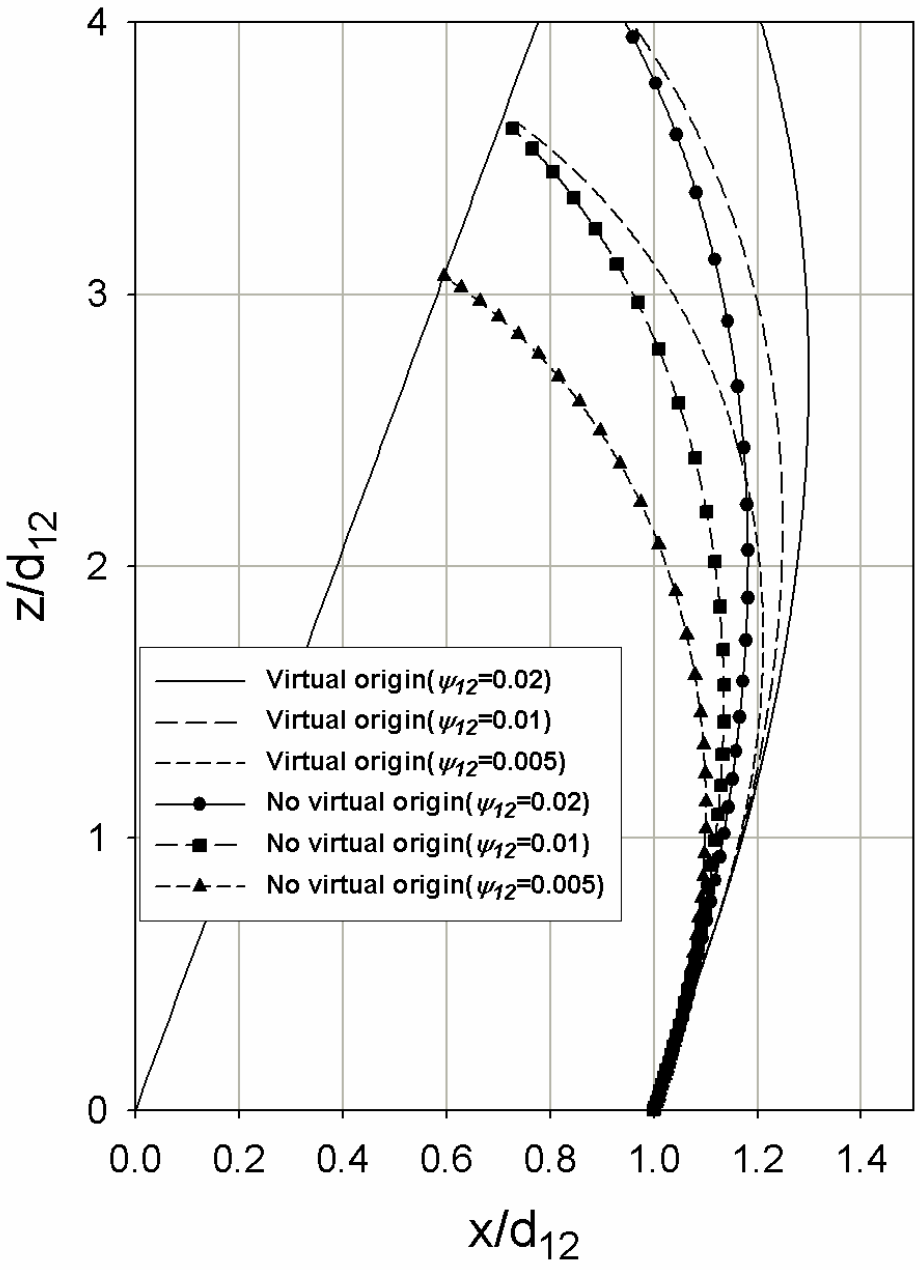

Figure 3.20. The effect of virtual origin on the SJ/WJ system at various momentum ratios when the WJ injection angle of (φ, ϕ) = (80°,0°) and the nozzle distance of d_{12} = 0.0635 m; 'Virtual origin' indicates that $z_{2,o}/d_{2,o}$ = 3.46 and $s_{1,o}/d_{1,o}$ = 0 and 'No virtual origin' indicates that $z_{2,o}/d_{2,o}$ = 0 and $s_{1,o}/d_{1,o}$ = 0.

To see the effect of the nozzle distance, the WJ trajectory calculated from the 3-D SJ/WJ physical model was plotted for the case of the 'No virtual origin' ($z_{2,o}/d_{2,o}$ = 0 and $s_{1,o}/d_{1,o}$ = 0) in Figure 3.21 and 'Virtual origin' ($z_{2,o}/d_{2,o}$ = 3.46 and $s_{1,o}/d_{1,o}$ = 0) in Figure 3.22 at various momentum ratios and various nozzle distances with the WJ injection angle of (φ , ϕ) = (80°,0°). The effect of the nozzle distance on the SJ/WJ system is minimal in the 'No virtual origin' case (Figure 3.21), however, when the SJ virtual origin is included (Figure 3.22), the nozzle distance has considerable impact on the WJ trajectory. This effect can be explained by the change of the offset region length, relative to the nozzle distance. The length of the WJ trajectory, above the offset region, is proportional to the nozzle distance, as sketched in Figure 3.23. Since, in many jet flow cases, the virtual origin is positive finite, the nozzle distance should be considered as important design/operation controlling factor in the SJ/WJ system.

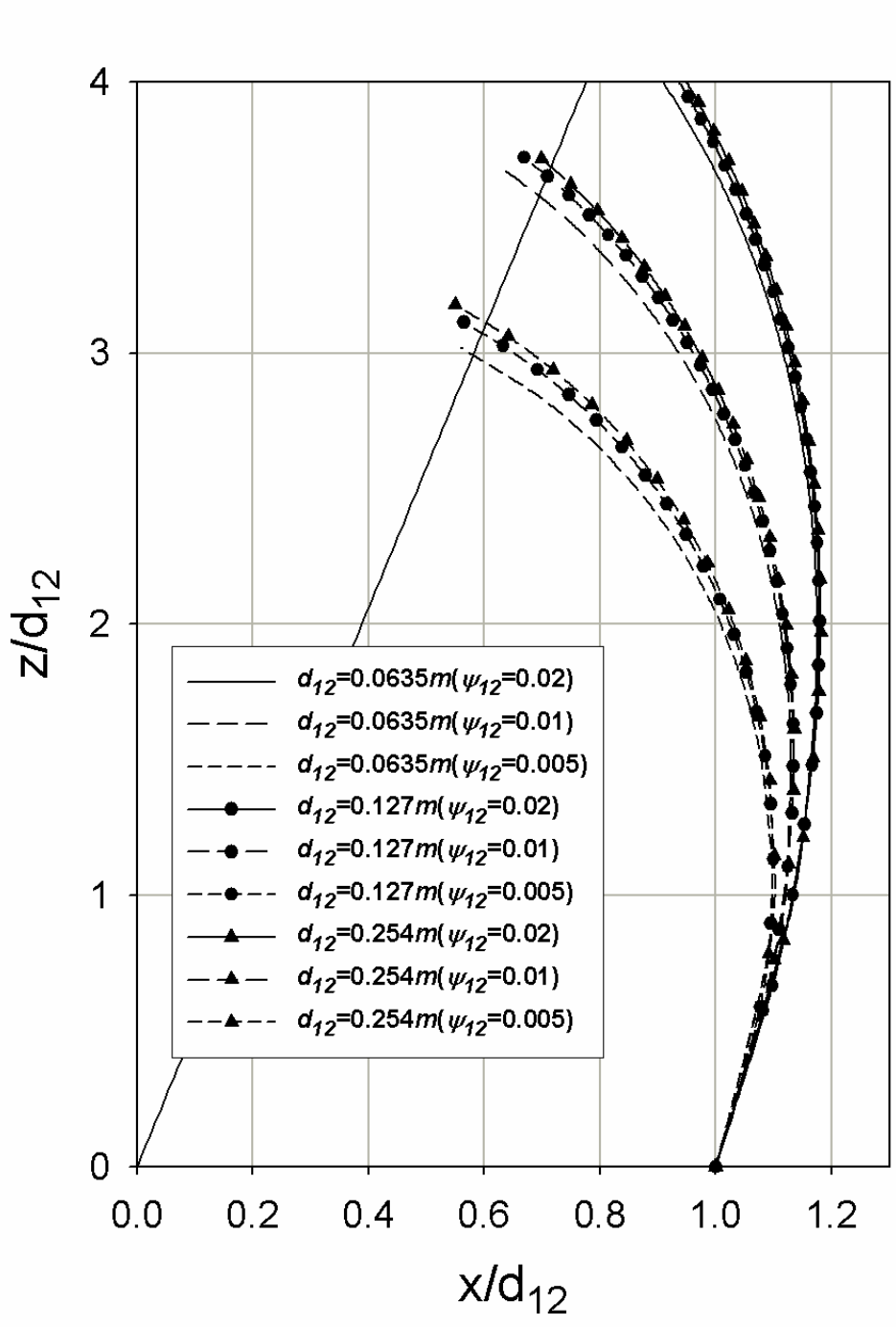

Figure 3.21. The effect of the nozzle distance on the SJ/WJ system at various momentum ratios for the WJ injection angle of (φ, ϕ) = (80°,0°) and the 'No virtual origin' case ($z_{2,o}/d_{2,o}$ = 0 and $s_{1,o}/d_{1,o}$ = 0).

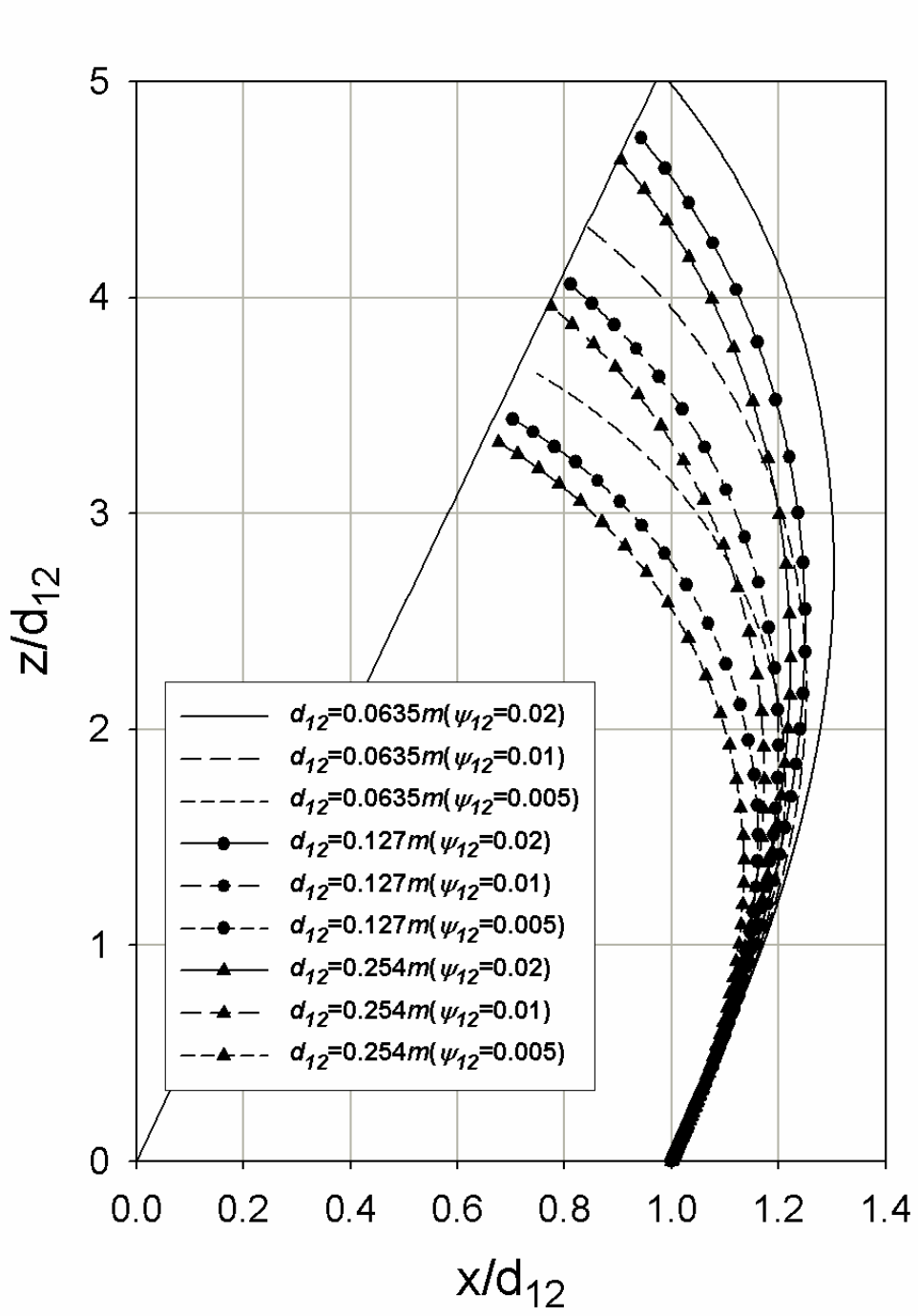

Figure 3.22. The effect of the nozzle distance on the SJ/WJ system at various momentum ratios for the WJ injection angle of (φ, ϕ) = (80°,0°) and the 'Virtual origin' case ($z_{2,o}/d_{2,o}$ = 3.46 and $s_{1,o}/d_{1,o}$ = 0).

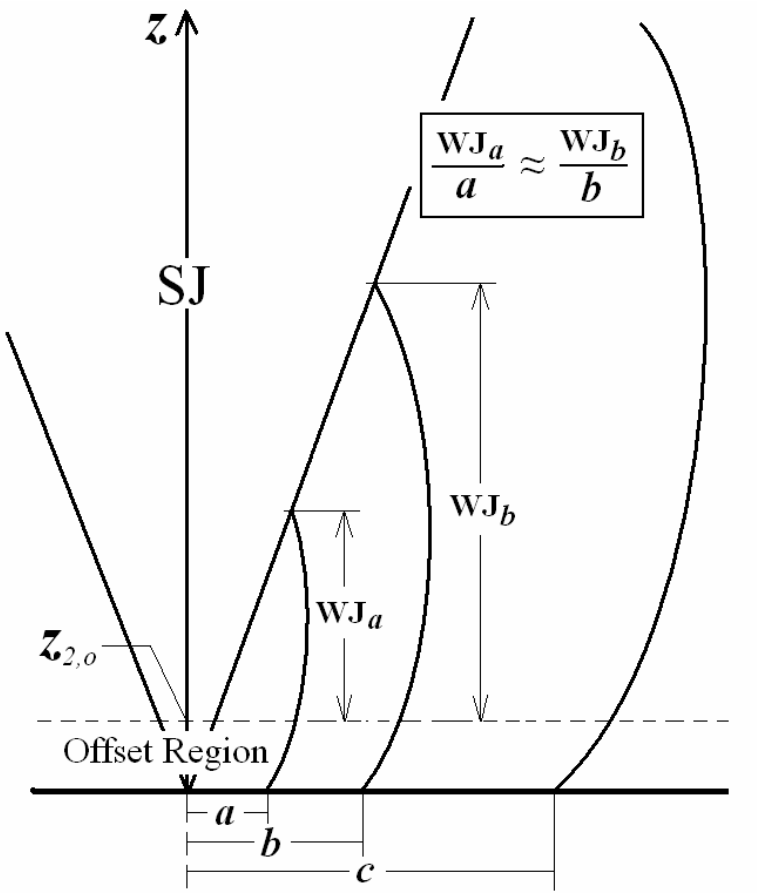

Figure 3.23. A schematic diagram of the WJ trajectories for different nozzle distances.

3.5.4 Characteristics of the confluence in the SJ/WJ system

Averaged mass fraction and density of a WJ fluid element was calculated along with the arc length. To eliminate the nozzle distance factor in $C^*_{3,i}$ of Eq.(3.42) and (3.43), we can rewrite them with another dimensionless definition; $s_i^+ = s_i / d_{i,o}$, $\widetilde{\omega}_i^{j+} = \widetilde{\omega}_i^j$ and $\overline{\rho}_i^+ = \overline{\rho}_i / \rho_{i,o}$:

$$\tilde{\omega}_i^{j+}(s_i^+)=\begin{cases}\omega_\infty^{j+}-\dfrac{\omega_\infty^{j+}-\tilde{\omega}_i^{j+}\Big|_{s_i^+=0}}{C_{3,i}^+(s_i^+-s_{i,o}^+)+1} & \text{for } s_i^+ > s_{i,o}^+ \\ \tilde{\omega}_i^{j+}\Big|_{s_i^+=0} & \text{for } 0\le s_i^+ \le s_{i,o}^+\end{cases} \tag{3.46}$$

where $C_{3,i}^+=C_{e,i}\left(\dfrac{\rho_\infty}{\rho_{i,o}}\right)^{1/2}$, and

$$\overline{\rho}_i^+(s_i^+)=\begin{cases}\dfrac{\dfrac{C_{4,i}^+}{B^+}C_{3,i}^+(s_i^+-s_{i,o}^+)+(1-\dfrac{A_i^+}{B^+})}{C_{3,i}^+(s_i^+-s_{i,o}^+)+(1-\dfrac{A_i^+}{B^+})} & \text{for } s_i^+ > s_{i,o}^+ \\ 1 & \text{for } 0\le s_i^+ \le s_{i,o}^+\end{cases} \tag{3.47}$$

where $C_{4,i}^+=\dfrac{P_\infty}{\rho_{i,o}RT_\infty}$, $A_i^+=\sum_j\dfrac{\omega_\infty^{j+}-\tilde{\omega}_i^{j+}\Big|_{s_i^+=0}}{W_j}$ and $B^+=\sum_j\dfrac{\omega_\infty^{j+}}{W_j}$.

Using Eq.(3.46) and (3.47) instead of Eq.(3.42) and (3.43), we can plot the average mass fraction and average density of the WJ fluid element along the arc length at several levels of $C_{3,1}^+$ as shown in Figure 3.24 and Figure 3.25, respectively. In this analysis a realistic range of $0.24\le C_{3,1}^+\le 0.32$ was used. Other conditions are listed in the figure captions. The plots demonstrate that the jet flow is quickly dominated by the surrounding fluid, i.e. the mass fraction and density of the issued fluid element very quickly approaches values of the surrounding fluid after the virtual origin. As the parameter, $C_{3,1}^+$ increases, so does the entrainment coefficient, resulting in faster decay of the concentration and density, although this change is small compared to the overall pattern.

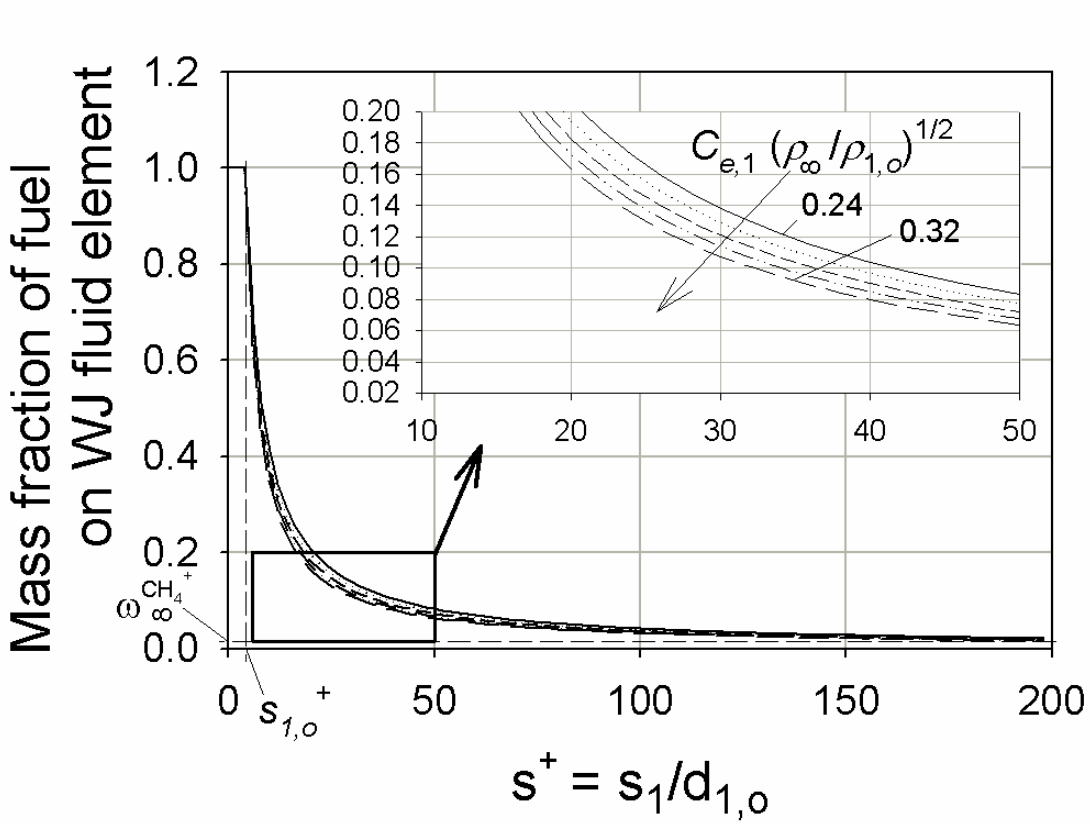

Figure 3.24. Average mass fraction of CH_4 of WJ fluid element along the arc length for $0.24 \le C_{e,1}(\rho_\infty/\rho_{1,o})^{1/2} \le 0.32$, $s_{1,o}{}^{+} = 4$, $\widetilde{\omega}_1^{CH_4{}^+}\Big|_{s_1^+=0} = 1$ and $\omega_\infty^{CH_4{}^+} = 0.0001$ in Eq.(3.46).

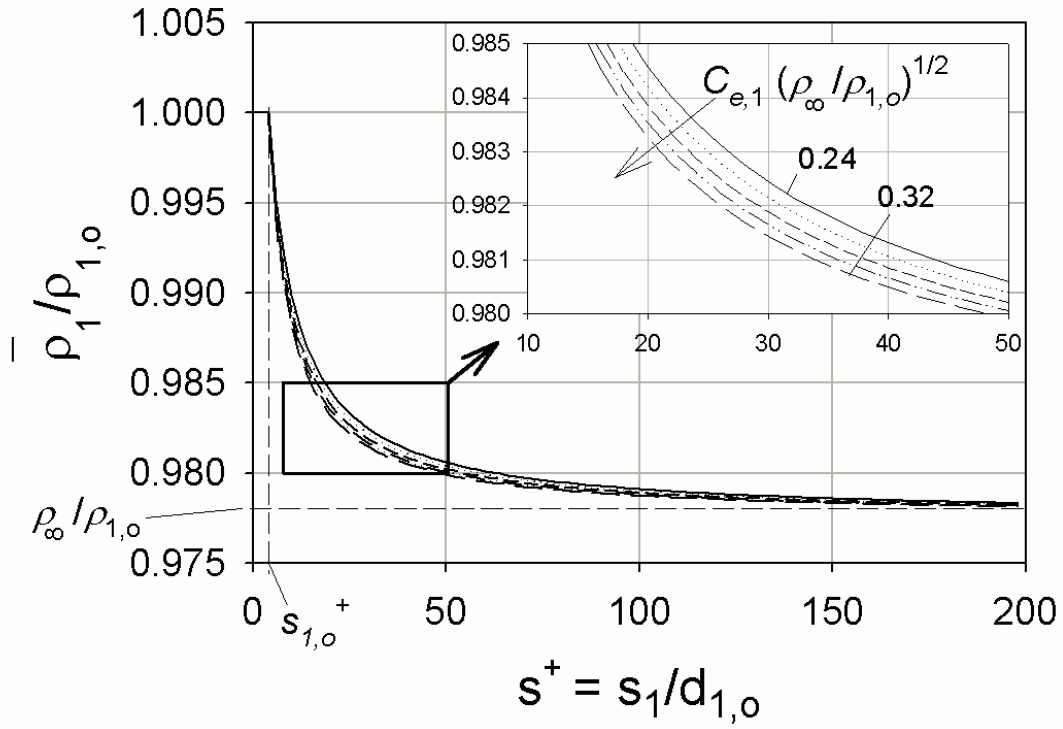

Figure 3.25. Average density of WJ fluid element along the arc length for $0.24 \le C_{e,1}(\rho_\infty/\rho_{1,o})^{1/2} \le 0.32$, $s_{1,o}{}^+ = 4$, $\tilde{\omega}_1^{CH_4{}^+}\Big|_{s_1^+=0} = 1$, $\omega_\infty^{CH_4{}^+} = 0.0001$, $\omega_\infty^{O_2{}^+} = 0.02$, $\omega_\infty^{N_2{}^+} = 0.9799$, $\rho_{1,o} = 1.1750\text{kg/m}^3$, $p_\infty = 1\text{atm}$, $T_\infty = 298\ K$ **in Eq.(3.47).**

Mass fractions in the confluence region of the SJ/WJ system, defined by Eq.(3.37), were calculated with respect to the WJ injection angle, φ (at $\phi = 0$), the momentum ratio, ψ_{12}, and the nozzle distance, d_{12}. The contours of the merging location, mass fraction of fuel and oxygen at the merging location (confluence location) are respectively plotted in Figure 3.26 in terms of the WJ injection angle, φ (at $\phi = 0$), and the momentum ratio, ψ_{12}, at d_{12} = 0.127 m and in Figure 3.27 in terms of the WJ injection angle, φ (at $\phi = 0$), and the nozzle distance, d_{12}, at

ψ_{12} = 0.01190. Through this kind of mapping, we may determine feasible ranges of the design/operation controlling factors corresponding to certain target mass fractions in the confluence zone. For example, if the mass fractions of $O_2 \approx 0.03$ and $CH_4 \approx 0.003$ are desired in the confluence, we can highlight the target area from Figure 3.26 and Figure 3.27, and identify corresponding values of the controlling factors. Note that the confluence zone could be considered as the main combustion reaction zone.

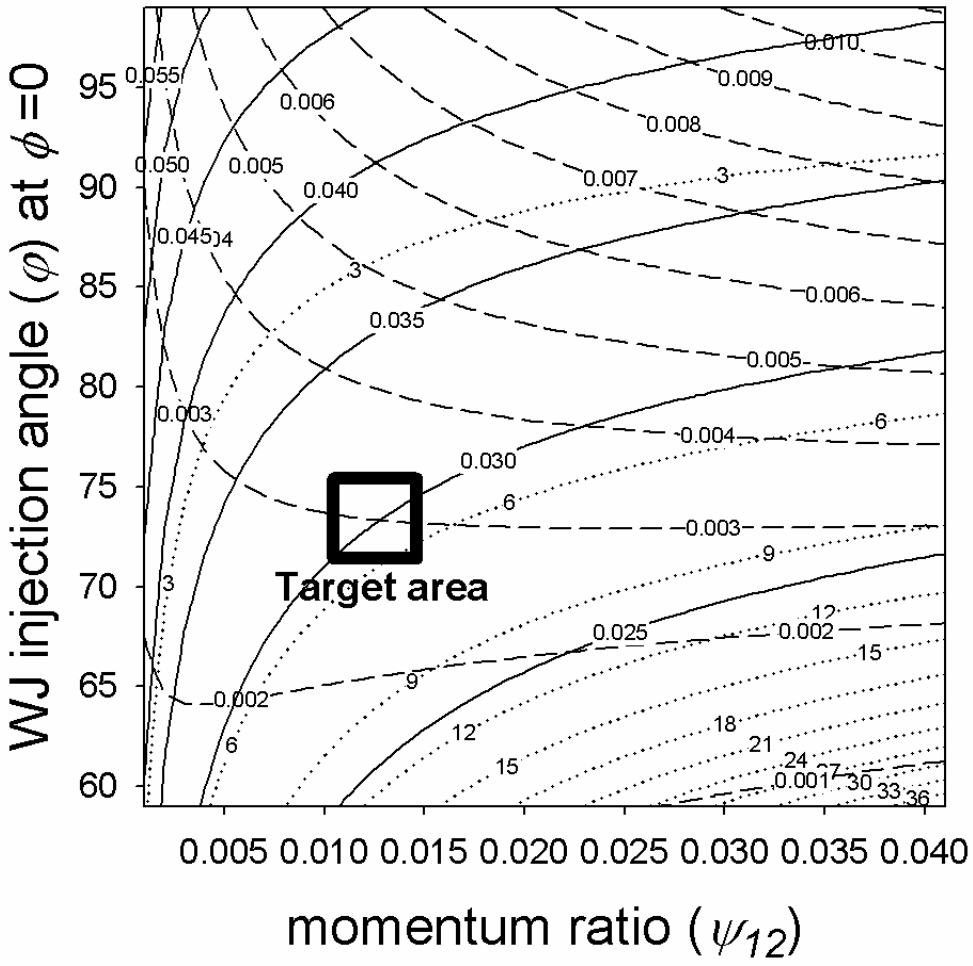

Figure 3.26. Contours of the merging location (…), mass fraction of fuel (– – –) and mass fraction of oxygen (——) at the merging location with respect to the WJ injection angle, φ (at ϕ=0), and the momentum ratio, ψ_{12}. Other conditions: d_{12} = 0.127 m, zero virtual origin, P_∞ = 1 atm, T_∞ = 298 °K, mass fractions of CH_4=0.0001, O_2=0.02, N_2=0.9799 for surrounding fluid, mass fractions of O_2 = 0.233, N_2 = 0.767 at the SJ nozzle exit, mass fraction of CH_4 = 1.0 and Re_{jet}=13,819 at the WJ nozzle exit.

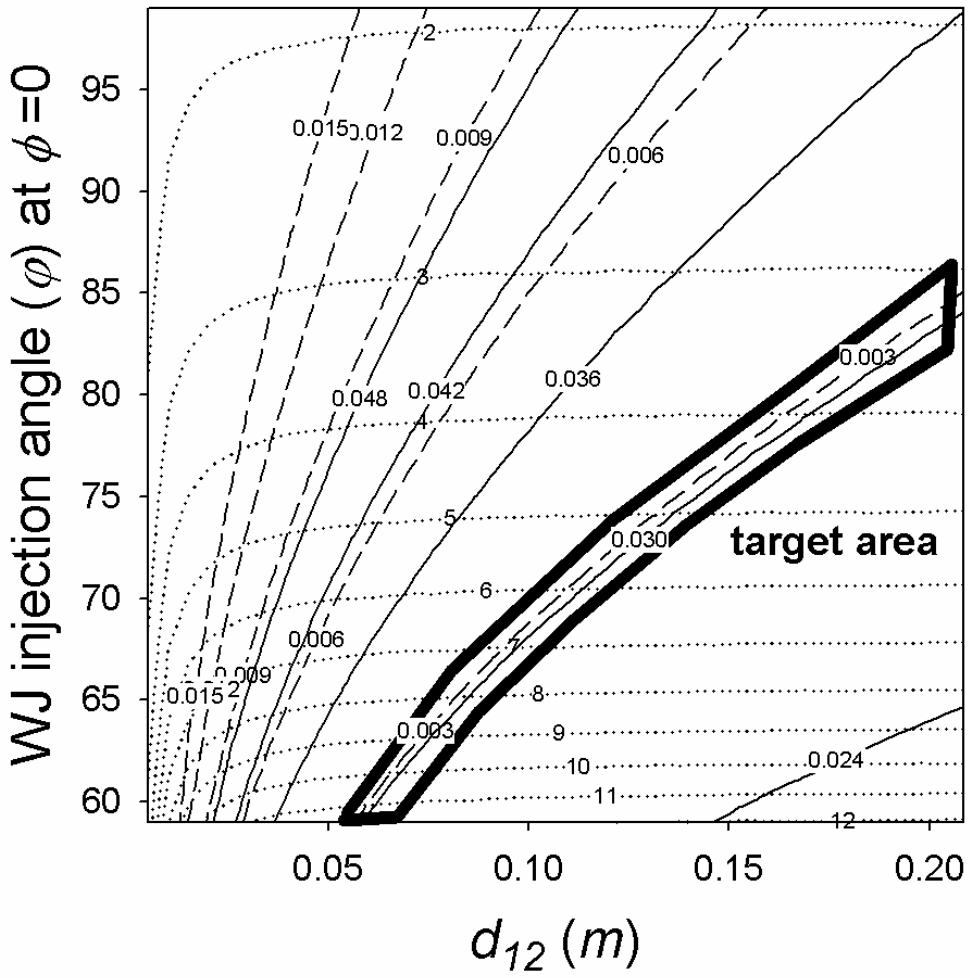

Figure 3.27. Contours of the merging location (…), mass fraction of fuel (– – –) and mass fraction of oxygen (——) at the merging location with respect to the WJ injection angle, φ (at ϕ =0), and the nozzle distance, d_{12}. Other conditions: ψ_{12} =0.01190, zero virtual origin, P_∞ = 1 atm, T_∞ = 298 °K, mass fractions of CH_4=0.0001, O_2=0.02, N_2=0.9799 for surrounding fluid, mass fractions of O_2 = 0.233, N_2 = 0.767 at the SJ nozzle exit, mass fraction of CH_4 = 1.0 and Re_{jet}=13,819 at the WJ nozzle exit.

3.6 Conclusion

A set of the general governing equations for the isothermal, free multi-jet flow system was developed, based on the momentum and mass balance in a Lagrangian reference frame. From this analysis, the 3-D SJ/WJ physical model was derived for the SJ/WJ system. It showed good agreement with the cold model experiment results while RANS simulations considerably under-predicted the WJ trajectory length.

The four important design/operation controlling factors of the SJ/WJ system were extracted from the main set of the governing equations: the momentum flow ratio of the WJ to the SJ at the nozzle exits, the injection angle of the WJ, the nozzle separation distance and the virtual origins of the SJ and the WJ. By the analysis of the 3-D SJ/WJ physical model solution, using the dilution index defined in this study, we can propose feasible ranges for the controlling factors for certain desired concentrations of fuel and oxidant in the confluence region of the jets.

In this work the entrainment coefficient for a jet with low Reynolds number was estimated by using the centerline decay constant obtained from the experiment results.

This 3-D SJ/WJ physical model can be used to help design and operate the flameless combustion burner adopting this SJ/WJ configuration. This model may also serve as a validation tool for RANS simulation (turbulence model) of this type of multi-jet system.

Chapter 4
Simplification of detailed chemical reaction mechanism

4.1 Introduction

In this chapter, a detailed chemical reaction mechanism of natural gas combustion was simplified into 2-D manifolds system for flameless combustion. This was done in two steps. The detailed chemical reaction mechanism was first reduced to a skeletal mechanism by removing irrelevant sub-mechanisms and less important reactions. Principal Component Analysis (PCA) combined with sensitivity analysis and reaction flow analysis was used to identify the less important reactions in the detailed chemical reaction mechanism. In the second step, the skeletal mechanism was further simplified into a set of 2-D manifolds system (each 2-D manifolds system is represented by one mixture fraction defined for a two-stream system: natural gas and air) by using the TGLDM method. For validation, the set of 2-D manifolds system was compared with the skeletal chemical reaction mechanism through the Batch Reactor (BR) model and the Perfect Stirred Reactor (PSR) model.

GRI-Mech 3.0 was used as the detailed chemical reaction mechanism and mole composition of the natural gas was simulated as 95% of CH_4, 2.8% of C_2H_6, 0.6% of CO_2, and 1.6% of N_2, based on product specification provided by local natural gas supplier, Utilities Kingston. CHEMKIN [93] was used to estimate thermodynamic properties such as the chemical reaction rates. QSHEP2D [94] or TRIPACK/SRFPACK [95,96] was used to interpolate the 2-D manifolds: these two algorithms show nearly equivalent performance, but TRIPACK/SRFPACK needs around 2.4 times more storage space than QSHEP2D. DVODE [97] and the Newton-Raphson method [87] were used to solve a set of stiff ODEs and algebraic equations, respectively.

4.2 Reduced chemical reaction mechanism

Reduced chemical reaction mechanisms for natural gas combustion were derived from GRI-Mech 3.0 to simulate flameless combustion conditions. The initial gas composition was selected based on mixing the natural gas/air mixture (fuel equivalence ratio of 0.77 ~ 1.1) with the product gas (the equilibrium composition corresponding to the fuel equivalence ratio of the natural gas/air mixture) so that the initial mole fraction of O_2 was controlled at a target value (mole fraction = 0.04 ~ 0.06), a temperature range of 1120 ~ 1373 K, and a pressure of 1 atm. Under these conditions, the total sensitivity coefficient and total reaction rate matrices were obtained. These matrices were then processed through PCA using four different orders of criteria, Eq.(2.13), to obtain four different reduced chemical reaction mechanisms. From these four mechanisms, one was selected (the skeletal mechanism) which had the least number of species and reactions while still exhibiting the least discrepancy from the GRI-Mech 3.0 calculations.

4.2.1 Candidates for the reduced chemical reaction mechanism

The chemical reaction flow structure of a chemical reaction mechanism can be described by important pathways that are identified through reaction flow analysis. In this work, total pathways for typical conventional and flameless combustion conditions were identified, shown in Figure 4.1 and Figure 4.2 respectively. In these diagrams, the relative contributions associated with each reaction are shown by the numerical values depicted in the individual reactions. For example, the $CH_3 \rightarrow C_2H_6$ pathway is strengthened in flameless combustion (Figure 4.2) compared to the conventional combustion case (Figure 4.1). In contrast, some minor pathways such as $CH_3O \rightarrow CH_3OH$ were weakened. However, the overall differences between these two

mechanisms may not be too large and existing reduced chemical reaction mechanisms for natural gas combustion (methane oxidation) in the literature, developed under conventional combustion conditions by various reduction methods, may be justified for the flameless combustion case. These pathways also suggest that the C_2 hydrocarbon oxidation mechanism plays a more important role in flameless combustion compared to conventional combustion. In this study, a new reduced chemical reaction mechanism for flameless combustion was developed by using PCA sensitivity analysis and reaction flow analysis.

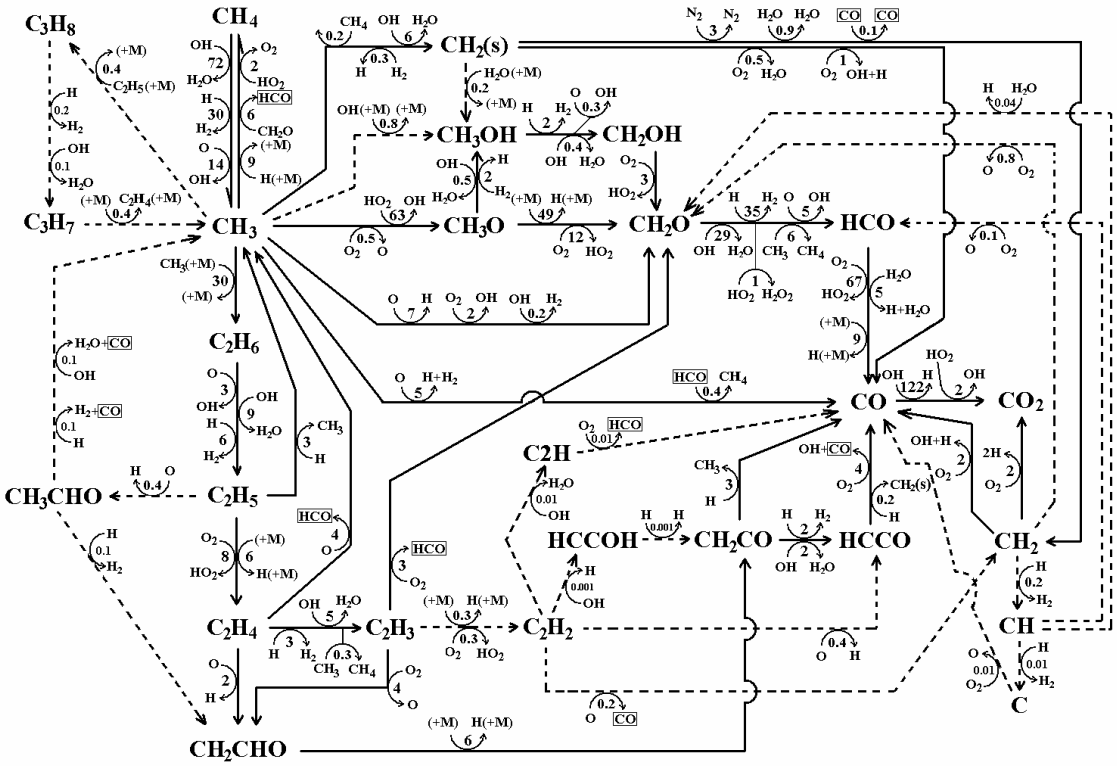

Figure 4.1. Total chemical reaction flow structure for typical conventional combustion: stoichiometric natural gas/air mixture at a constant pressure of 1 atm and a constant temperature of 1300 K.

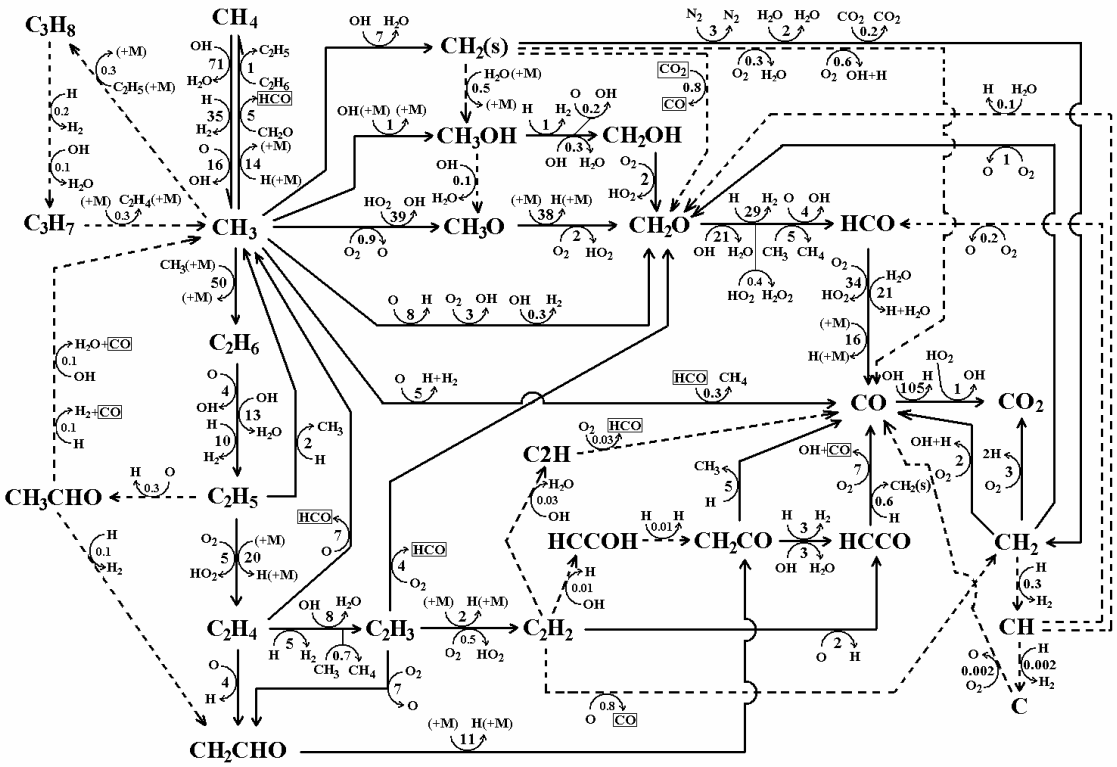

Figure 4.2. Total chemical reaction flow structure for typical flameless combustion: mixture of stoichiometric natural gas/air and the product gas to be O_2 mole fraction of 0.05 at a constant pressure of 1 atm and a constant temperature of 1300 K.

For an example of this procedure, several results of the PCA with sensitivity analysis and reaction flow analysis under a typical condition for flameless combustion – a constant pressure of 1atm, a constant temperature of 1300 K, an initial mixture of stoichiometric natural gas/air and the equilibrium composition for initial O_2 mole fraction of 0.05 – are plotted in Figure 4.3. Figure 4.3(a) shows the magnitude of eigenvalues for each PC from the total sensitivity coefficient matrix. In this case, only the first PC seems meaningful because other eigenvalues are very small compared with the first eigenvalue. However, all the PCs are involved in obtaining the overall vector, Eq.(2.12), by using all eigenvalues as the corresponding weighing factor. The overall sensitivity vector, which indicates the relative importance of reactions, is described in Figure

4.3(b) – the results are shown with an arbitrary user-defined criteria value depicted by the dashed vertical line in this graph (elements above or below this level are deemed important or not). Similarly, this procedure was carried out for the total reaction rate matrix. In Figure 4.3(c), the magnitudes of the eigenvalues are plotted for each PC. In contrast to the results in Figure 4.3(a), there are no highly dominant eigenvalues and use of only a few PCs would lead to a loss of information of the matrix. Hence use of all the eigenvalues as weighting factors is highly recommended in evaluating the overall vector. Comparing Figure 4.3(d) with Figure 4.3(b), we can see that the important reactions, respectively identified from the total sensitivity coefficient matrix and the total reaction rate matrix, are considerably different from each other. This means that using only one of them will easily lead to an inadequate reduced chemical reaction mechanism. Accordingly, we develop the reduced chemical reaction mechanism by summing the important reactions identified from both.

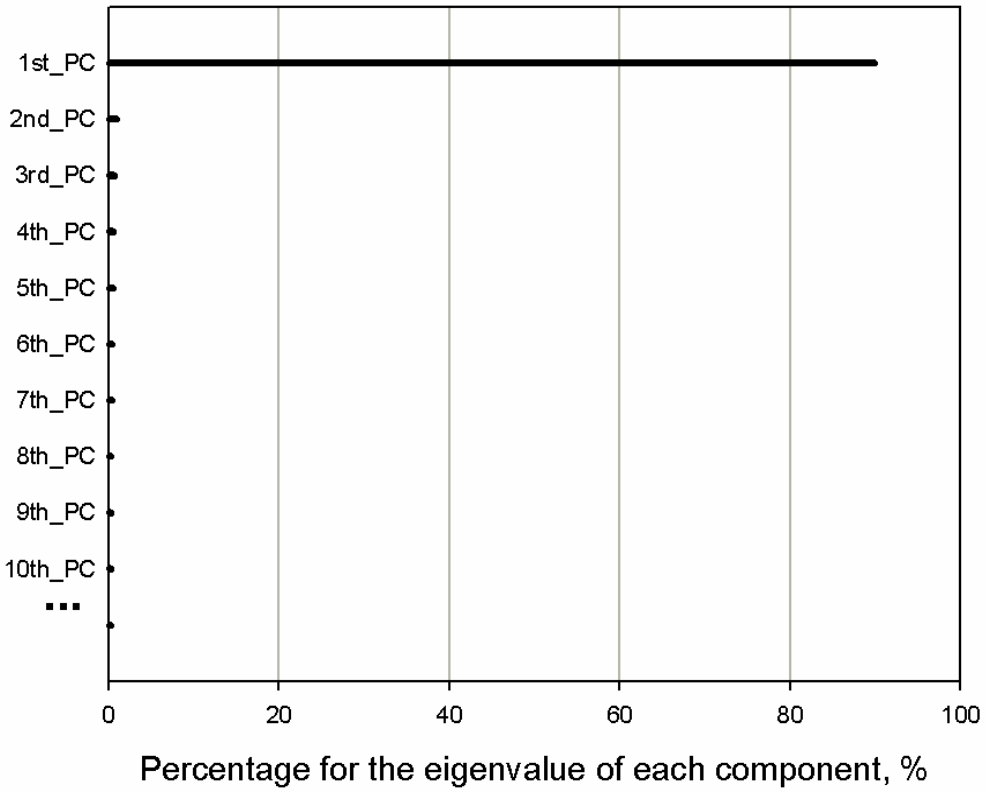

(a) Magnitude of eigenvalue of PC from the total sensitivity coefficient matrix

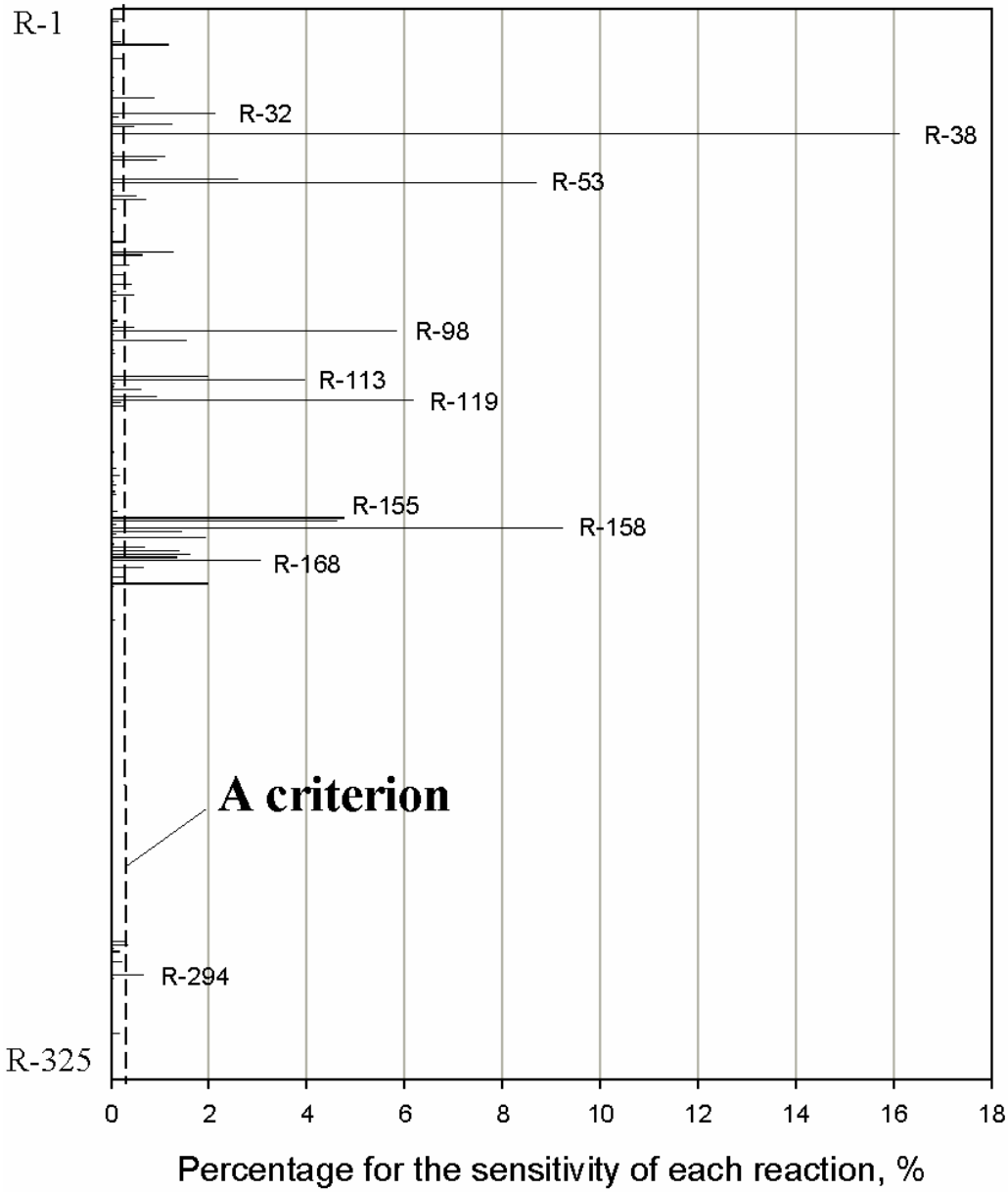

(b) Overall sensitivity for each reaction from the total sensitivity coefficient matrix

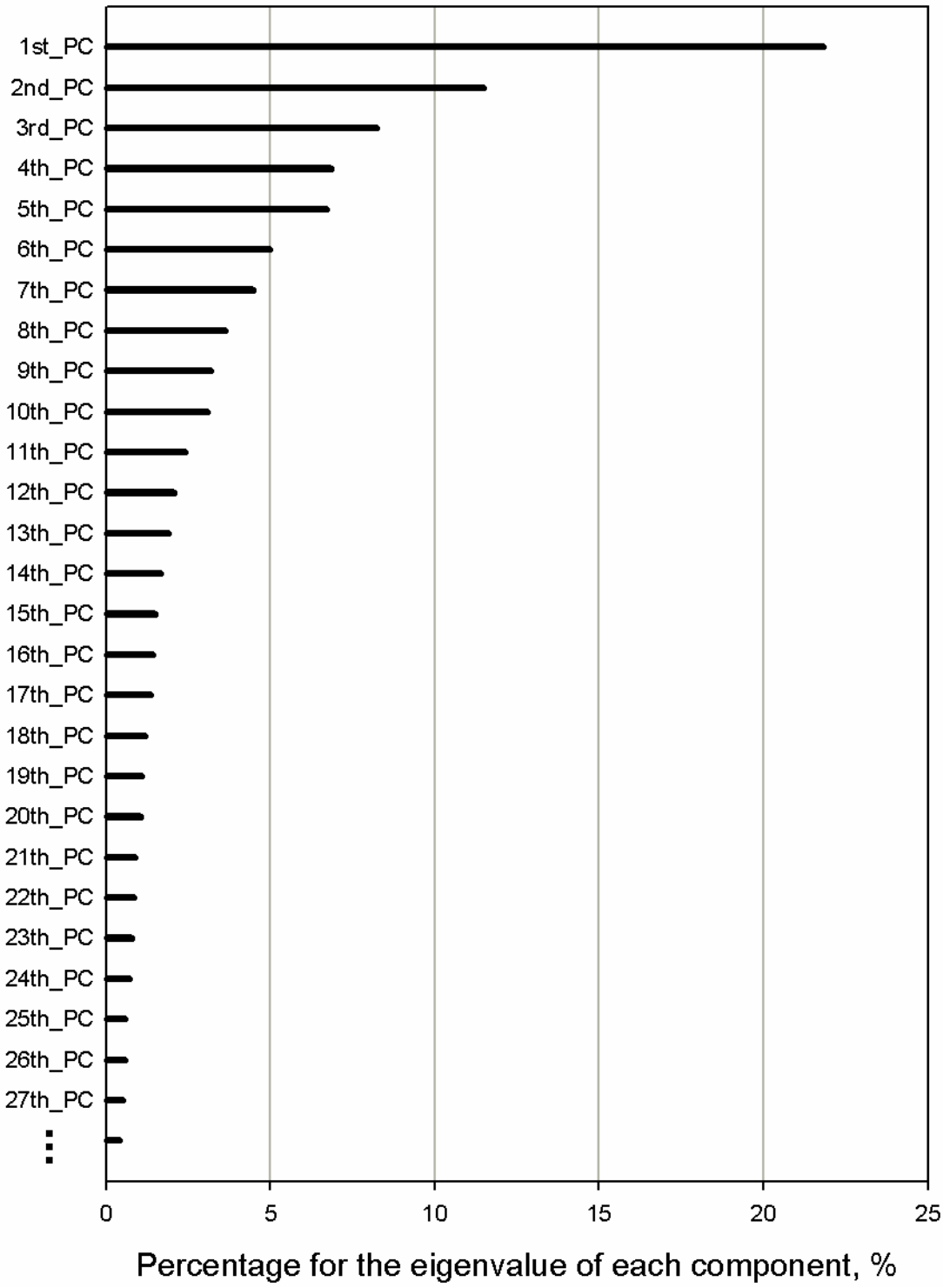

(c) Magnitude of eigenvalue of PC from the total reaction rate matrix

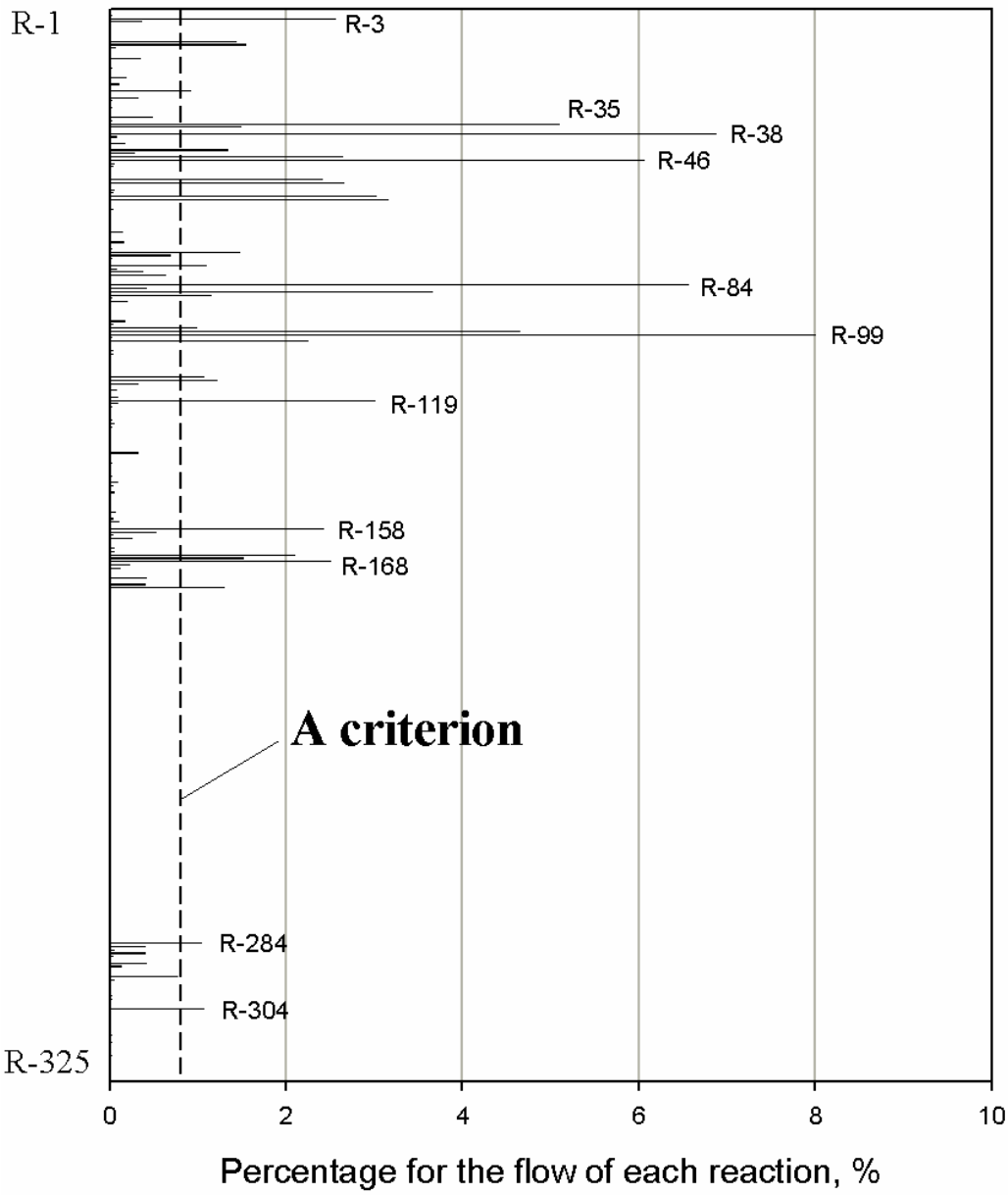

(d) Overall reaction rate for each reaction from the total reaction rate matrix

Figure 4.3. PCA results calculated under the conditions of a constant pressure of 1atm, a constant temperature of 1300K, initial mixture of stoichiometric natural gas/air and the equilibrium composition for initial O_2 mole fraction of 0.05.

Four candidates for the reduced chemical reaction mechanism were proposed based on different criteria in the above PCA reduction procedure conducted under various specific flameless combustion conditions. In addition, the total chemical reaction flow structure produced by the reaction flow analysis was used to double-check the validity of the proposed reduced chemical reaction mechanisms.

The reduction was made, first, by subtracting the subset reaction mechanism related to NOx and Ar reactions from GRI-Mech 3.0. In subsequent discussion, this subtracted chemical reaction mechanism will be called the "GRI-without-NOx" mechanism – it contains 35 species and 217 reversible reactions. Unimportant reactions determined by the PCA procedure were removed from the "GRI-without-NOx" mechanism. Several reactions, although found to be unimportant, were not removed because they were necessary to maintain the consistency in the chemical reaction flow structure. The number of species and reversible reactions involved in the proposed reduced chemical reaction mechanisms, which were named Reduced mech-1 ~ Reduced mech-4, are described in Table 4.1, and the corresponding chemical reaction flow structures are shown in Figure 4.4 ~ Figure 4.8.

A limitation for this sensitivity and flow reaction analysis can be observed – for the imposed criteria, the number of reactions is significantly decreased but the reduction in the number of species is not as large. This is because this analysis basically identifies unimportant reactions, not species. We can also note that while the Reduced mech-4 model, Figure 4.8, seems remarkably simple, the number of species and reactions are not significantly reduced compared to the other reduced models.

Table 4.1. Four reduced chemical reaction mechanisms for the flameless combustion.

Reduced mech-1	Reduced mech-2	Reduced mech-3	Reduced mech-4
29 species, 94 reversible reactions	26 species, 84 reversible reactions	25 species, 61 reversible reactions	21 species, 43 reversible reactions
1. H_2	1. H_2	1. H_2	1. H_2
2. H	2. H	2. H	2. H
3. O	3. O	3. O	3. O
4. O_2	4. O_2	4. O_2	4. O_2
5. OH	5. OH	5. OH	5. OH
6. H_2O	6. H_2O	6. H_2O	6. H_2O
7. HO_2	7. HO_2	7. HO_2	7. HO_2
8. H_2O_2	8. H_2O_2	8. H_2O_2	8. H_2O_2
9. CH	9. CH_2	9. CH_2	9. CH_2
10. CH_2	10. $CH_2(S)^*$	10. $CH_2(S)^*$	10. CH_3
11. $CH_2(S)^*$	11. CH_3	11. CH_3	11. CH_4
12. CH_3	12. CH_4	12. CH_4	12. CO
13. CH_4	13. CO	13. CO	13. CO_2
14. CO	14. CO_2	14. CO_2	14. HCO
15. CO_2	15. HCO	15. HCO	15. CH_2O
16. HCO	16. CH_2O	16. CH_2O	16. CH_3O
17. CH_2O	17. CH_3O	17. CH_3O	17. C_2H_3
18. CH_2OH	18. C_2H_2	18. C_2H_3	18. C_2H_4
19. CH_3O	19. C_2H_3	19. C_2H_4	19. C_2H_5
20. CH_3OH	20. C_2H_4	20. C_2H_5	20. C_2H_6
21. C_2H_2	21. C_2H_5	21. C_2H_6	21. N_2
22. C_2H_3	22. C_2H_6	22. HCCO	
23. C_2H_4	23. HCCO	23. CH_2CO	
24. C_2H_5	24. CH_2CO	24. N_2	
25. C_2H_6	25. N_2	25. CH_2CHO	
26. HCCO	26. CH_2CHO		
27. CH_2CO			
28. N_2			
29. CH_2CHO			

* (S) is solid

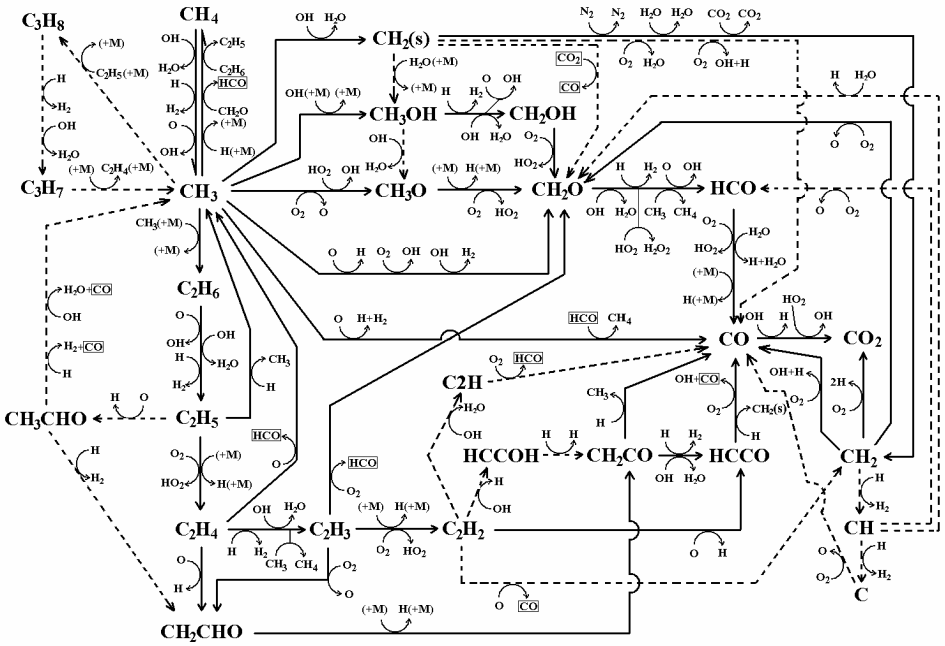

Figure 4.4. Chemical reaction flow structure from the "GRI-without-NOx".

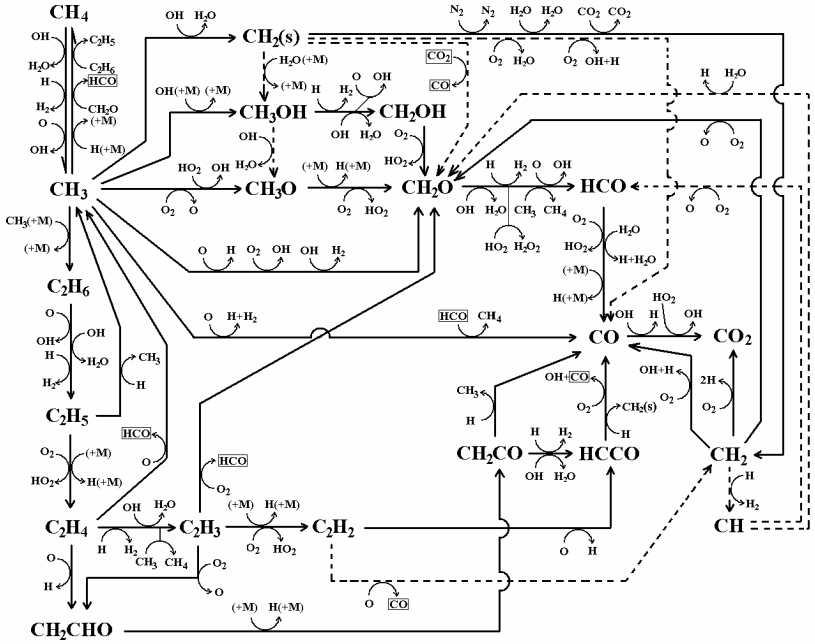

Figure 4.5. Chemical reaction flow structure from the Reduced mech-1.

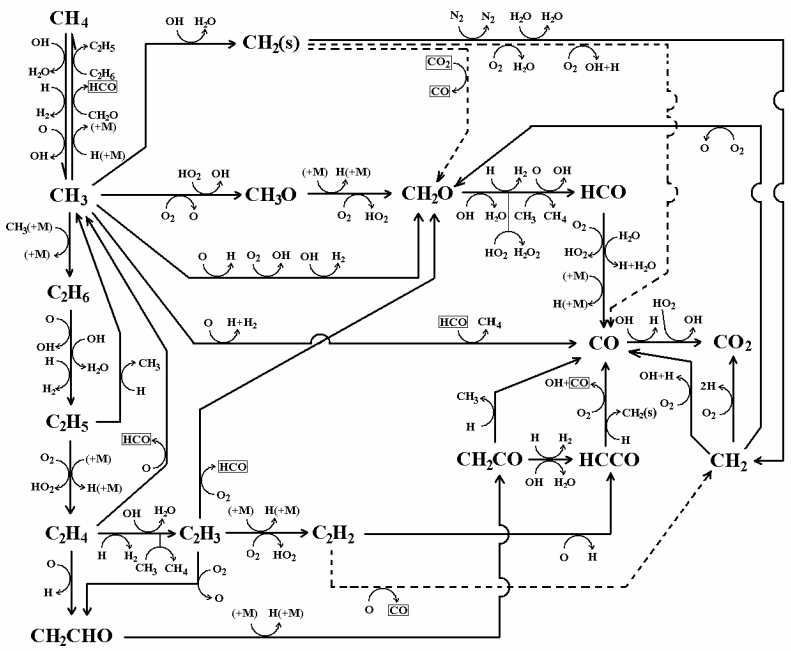

Figure 4.6. Chemical reaction flow structure from the Reduced mech-2.

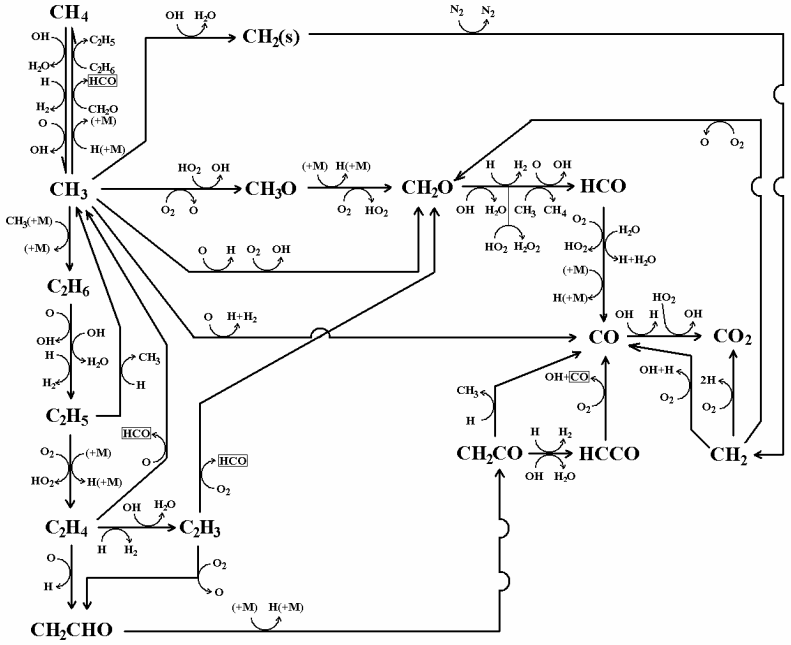

Figure 4.7. Chemical reaction flow structure from the Reduced mech-3.

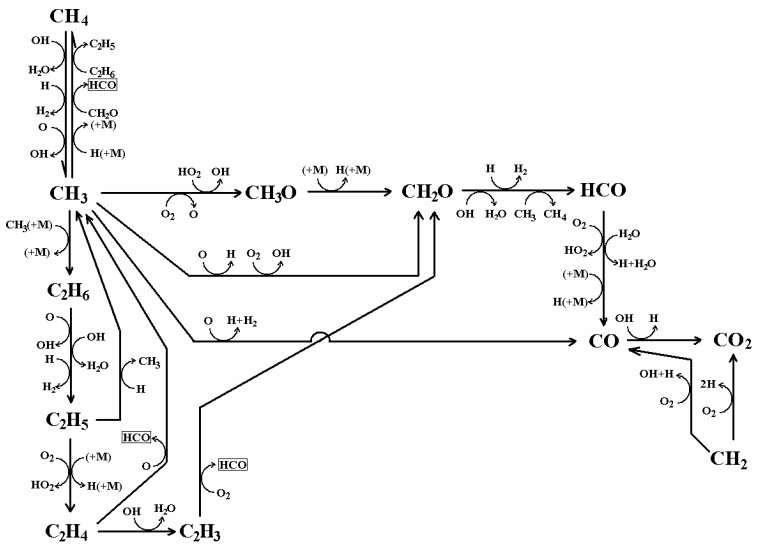

Figure 4.8. Chemical reaction flow structure from the Reduced mech-4.

4.2.2 Comparison of the reduced mechanisms

One of the four proposed reduced chemical reaction mechanisms was selected for the flameless combustion by comparison with the "GRI-without-NOx" mechanism in the BR model simulation. Typical comparison results are plotted with respect to the mole fraction of CH_4, CO_2, H_2O, CO, H_2, OH, H and O in Figure 4.9 ~ Figure 4.11. All the reduced chemical reaction mechanisms except for the Reduced mech-4 show very good agreement with the "GRI-without-NOx" mechanism with some discrepancies evident for the minor species.

For the ignition time, indicated by the peak concentration of OH, the Reduced mech-4 shows unacceptable delay while others are similar. In conclusion, the Reduced mech-3 was selected as

the best reduced chemical reaction mechanism for the flameless combustion because it maintains the principle characteristics of the "GRI-without-NOx" mechanism, while requiring the least number of species and reactions among the other possible proposed candidates. The reactions of the Reduced mech-3 are listed in Appendix A. In subsequent sections, the Reduced mech-3 will be called the skeletal chemical reaction mechanism and it will be used for further simplification in next section.

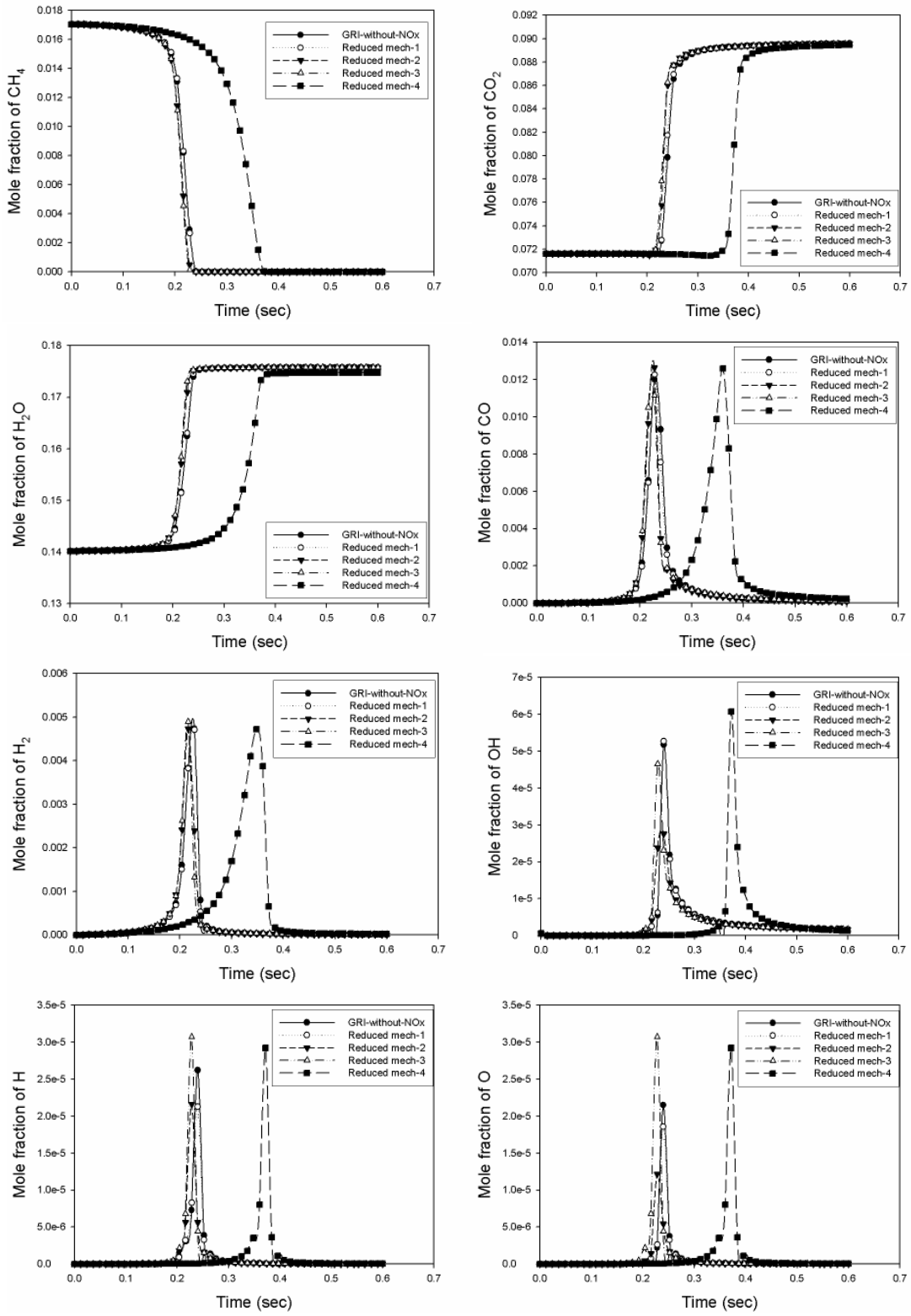

Figure 4.9. Comparison of the reduced chemical mechanisms: a constant pressure of 1atm, a constant temperature of 1123K, excess air of 0% and O_2 mole fraction of 0.05.

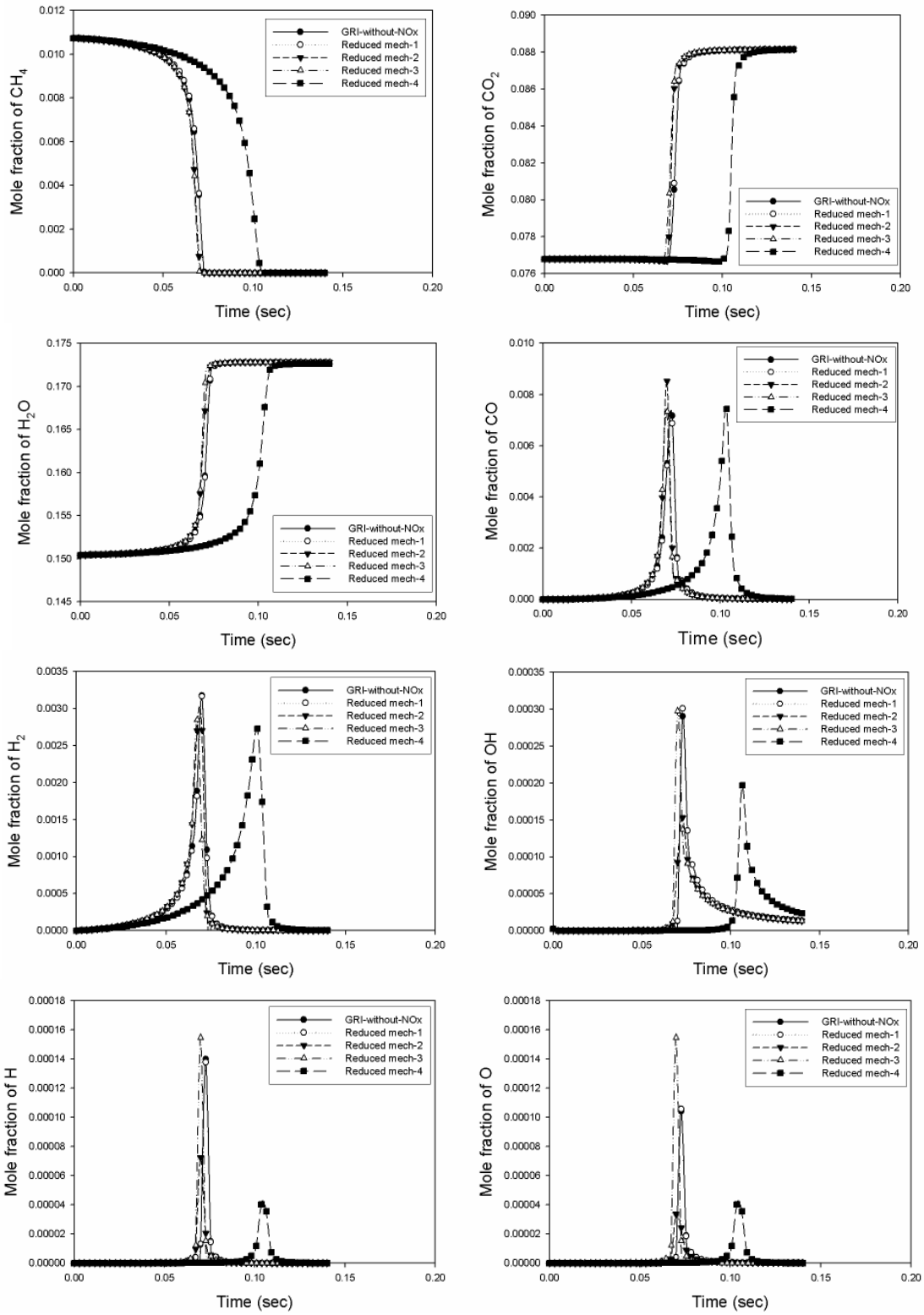

Figure 4.10. Comparison of the reduced chemical mechanisms: a constant pressure of 1atm, a constant temperature of 1223K, excess air of 10% and O_2 mole fraction of 0.04.

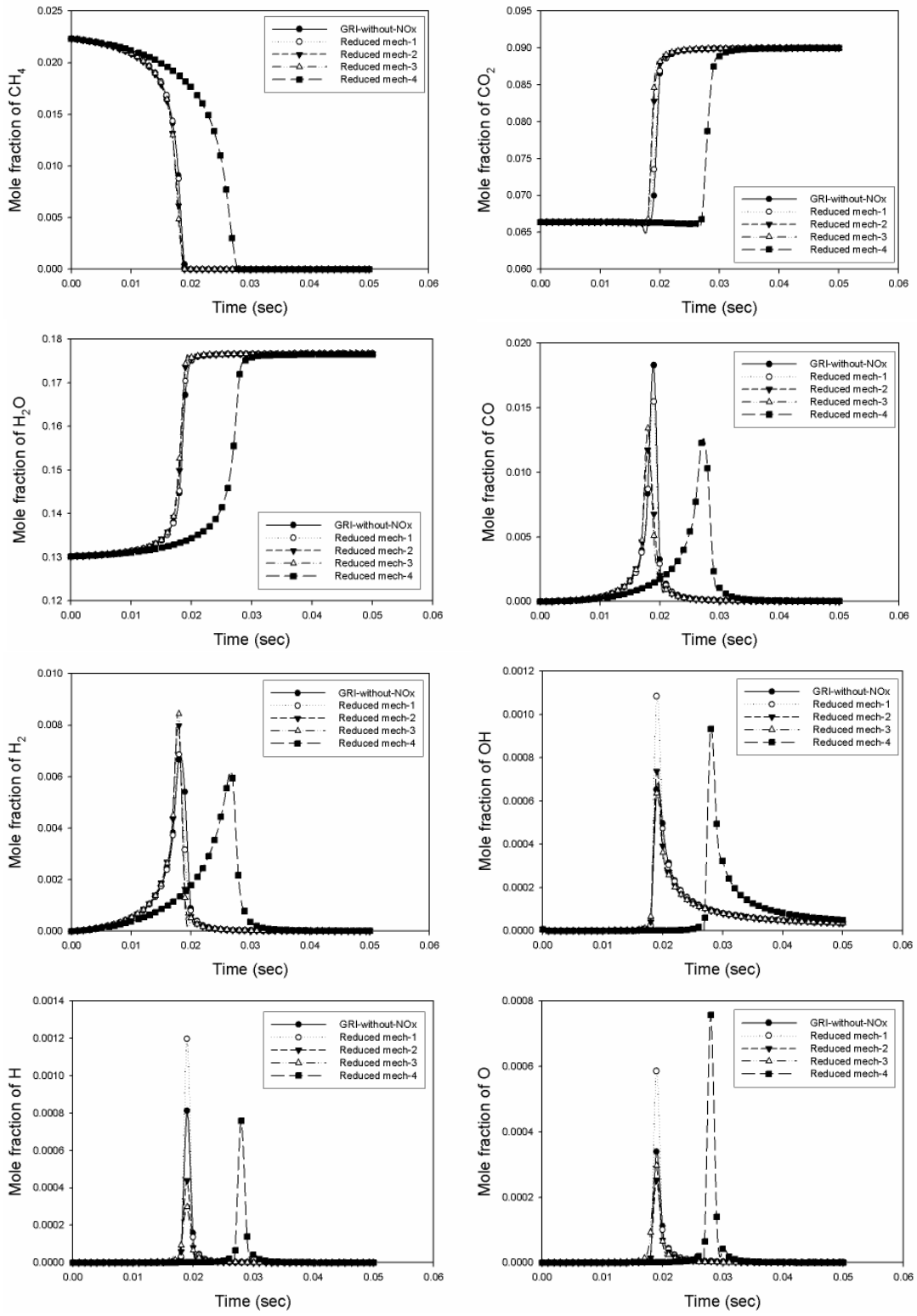

Figure 4.11. Comparison of the reduced chemical mechanisms: a constant pressure of 1atm, a constant temperature of 1323K, excess air of 0% and O_2 mole fraction of 0.06.

4.3 Two-dimensional manifolds by TGLDM method

By using the TGLDM method, two-dimensional manifolds were constructed from the skeletal chemical reaction mechanism at various mixture fractions. For validation, the set of the 2-D manifolds whose element 2-D manifolds was represented by one mixture fraction value was tested by the BR and PSR models.

4.3.1 Construction of 2-D manifolds

In natural gas combustion, the 2-D manifolds can be naturally parameterized by the mass fractions of CO_2 and H_2O because both have similar and relatively long time scales of evolution. In addition using a single species as a parameter is much easier than using a combination of species as a parameter.

The 2-D manifolds were independently constructed for 83 mixture fractions defined at the non-premixed two-stream system: CH_4 fuel stream and air stream at the exit condition of 1 atm and 300 K. For adiabatic conditions, specific enthalpy of the mixture can be calculated from the mixture fraction, see Eq.(2.44). The 83 mixture fractions were densely distributed around the stoichiometric mixture fraction, ξ_{st} =0.05516. Figure 4.12 shows the distribution of the 83 mixture fractions by plotting density, temperature and mass fractions of CO_2 and H_2O of the corresponding equilibrium state.

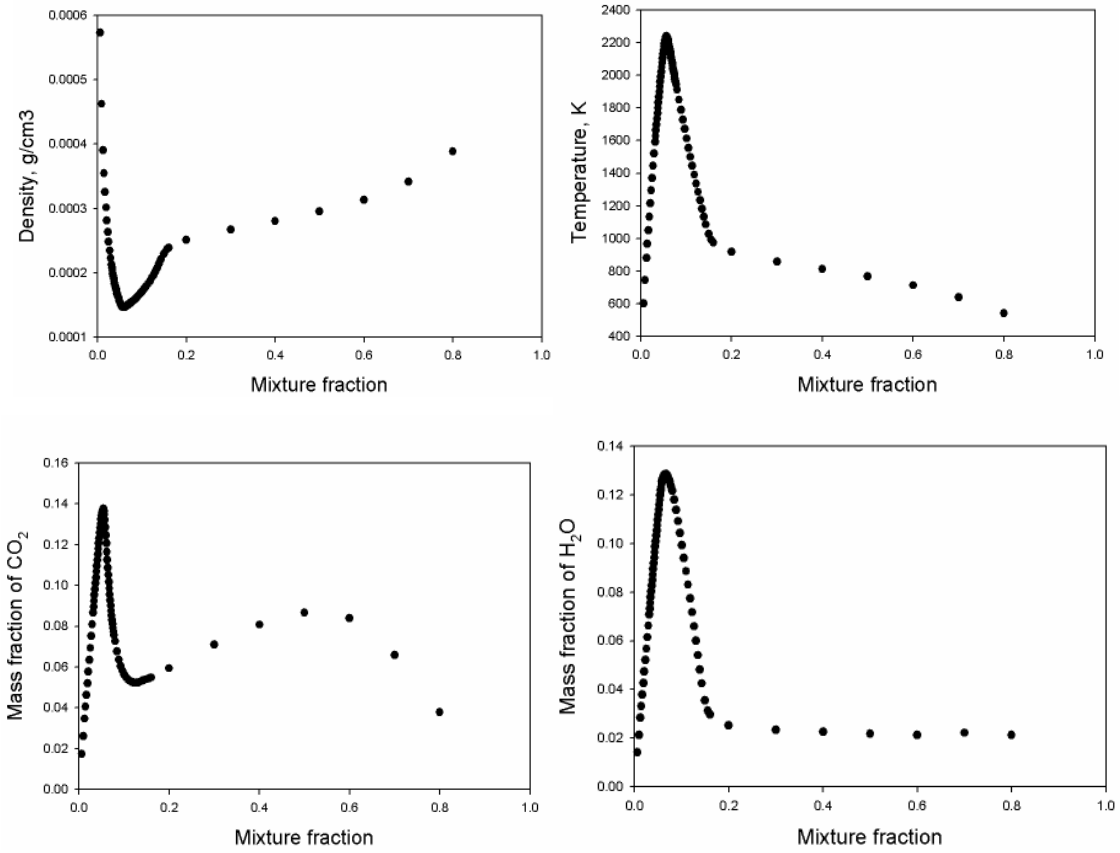

Figure 4.12. Profiles of density, temperature and mass fractions of CO_2 and H_2O with the mixture fraction at equilibrium state: CH_4 fuel stream and air stream at the exit condition of 1 atm and 300 K.

For each mixture fraction, Eq.(2.21), (2.22) and (2.23) were numerically solved with the initial conditions that were defined by the 'extreme values of major species' concept [27]. In addition, the initial conditions were, if necessary, determined by adding the corresponding equilibrium composition so that the initial temperature was high enough to ensure that the reaction occurred. The reaction trajectories obtained were used to construct 2-D manifolds.

In constructing the 2-D manifolds, an overlap region where trajectories crossed each other on the low-dimensional parameter space, that is, the Y_{CO2}-Y_{H2O} plane, can appear because the dimension of the original system (25-dimension) was much higher. The overlap region caused manifolds not to be uniquely mapped from the parameter space to the original composition space. To avoid this manifold mapping problem, selection of alternative parameters to represent such low-dimensional manifolds can be difficult. In this work the overlapped data were deleted to maintain the shape of lower manifolds, here a 1-D manifold.

Density, temperature, reaction rates of CO_2 and H_2O, and mass fractions of all species were tabulated with respect to the mass fractions of CO_2 and H_2O. In addition, the total formation enthalpy release rate ($\sum_{j}^{n} h_j^o \dot{w}_j W_j$) was also tabulated to be used in the form of the energy equation explicitly containing the heat of chemical reaction term such as Eq.(2.38-a). It was tested in the PSR model when this kind of energy equation was included. The projection matrix was not tabulated. Instead, when the orthogonal projection was applied in the PSR model test, it was conducted by the geometry of 2-D manifolds during run-time calculation.

In Figure 4.13, distributions of the reaction rates of CO_2 and H_2O and the total formation enthalpy release rate for the stoichiometric mixture fraction of 0.05516 are plotted on the Y_{CO2}-Y_{H2O} plane. Red dots and mesh plots represent the TGLDM data and the interpolated values, respectively. For each mixture fraction, the interpolated mesh seemed to follow the TGLDM data well.

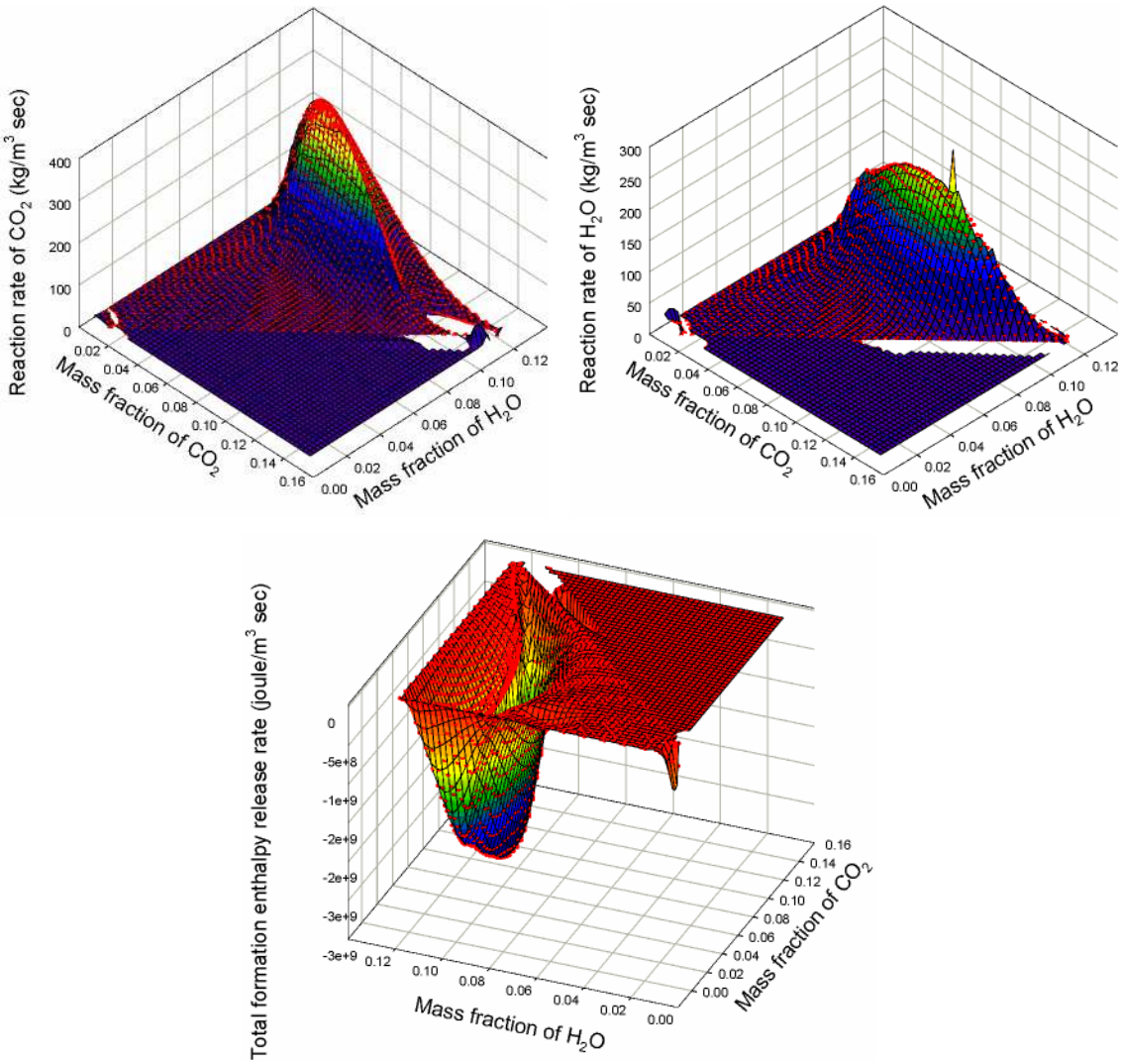

Figure 4.13. Distributions of reaction rates of CO_2 and H_2O and total formation enthalpy release rate on the Y_{CO2}-Y_{H2O} plane at the stoichiometric mixture fraction of 0.05516: red dot - TGLDM data, mesh plot - the interpolated value, and white area - negative values.

4.3.2 Test of the 2-D manifolds by batch reactor and perfect stirred reactor model

The BR and PSR model were used to test the constructed TGLDM for each mixture fraction. The BR model tests were used to test the validation of the chemical reaction rates and the mapping of parameters into the original space of the TGLDM while the PSR model was used to test the additional effect, i.e. the physical perturbation (convection effect). In both models, the energy equation explicitly containing the total formation enthalpy release rate term was examined. Also, in the PSR model, the orthogonal and perpendicular projections were tested.

The governing equations of PSR model for single phase system can be expressed as

$$\frac{dY_i}{dt} = \frac{q^{in}}{\rho}(Y_i^{in} - Y_i) + \frac{\dot{w}_i W_i}{\rho},\ i = 1,...,l \tag{4.1}$$

$$\frac{d(\Delta h)}{dt} = \frac{q^{in}}{\rho}(\Delta h^{in} - \Delta h) - \frac{1}{\rho}\sum_{j=1}^{n} h_j^o \dot{w}_j W_j + Q_{ext} \text{ with } \int_{T_{ref}}^{T}\left(\sum_{j=1}^{n} Y_j c_{p,j}\right)dT - \Delta h = 0 \tag{4.2}$$

where n is the number of the involved species, l is the dimension of the system, i.e. $l = n$ for the skeletal chemical reaction mechanism and l=2 for the 2-D manifolds, ρ is the density of the system, Y_i is the mass fraction of i species, W_i is the molecular weight of i species, $\dot{w}_i$ is the molar production rate of i species, q^{in} is inflow rate per unit reactor volume, Y_i^{in} is the mass fraction of i species at inflow, Δh is the sensible enthalpy($= h - h^o$), Δh^{in} is the sensible enthalpy at inflow, h_j^o is the standard specific enthalpy of formation of j species (at 1 atm, 298 K) and Q_{ext} is the external heat supply. In addition, when the energy equation is included, the ideal gas equation of state is used to calculate the density. Note that for adiabatic conditions, the

temperature and density can be obtained from the TGLDM without solving the energy equation and the ideal gas law.

The governing equations of the BR model can be easily derived from the PSR model by setting $q^{in} = 0.0$ in Eq.(4.1) and (4.2). Note that in this BR model, the outflow is not zero to keep the pressure and volume of the reactor constant.

BR model test

Using the 2-D manifolds, the BR model was solved under a constant pressure of 1 atm and adiabatic conditions, i.e. Q_{ext} = 0.0, for the 83 mixture fractions, and the results were compared with those from the skeletal chemical reaction mechanism. Temperature and density were obtained by directly interpolating the TGLDM (without the energy equation) or from solving the energy equation and the ideal gas law (with the energy equation). As an example, Figure 4.14, the calculated trajectories from the 2-D manifolds for the stoichiometric mixture fraction of 0.05516 were plotted on the Y_{CO2}-Y_{H2O} plane along with the corresponding TGLDM data, indicating trajectories from the skeletal chemical reaction mechanism (black points). The trajectories obtained from the TGLDM with or without the energy equation are very consistent with those from the skeletal chemical reaction mechanism. This indicates that the skeletal chemical reaction mechanism is well represented by the 2-D TGLDM. Additional detail in terms of the time evolution of several important scalars from an initial state to the equilibrium state is plotted in Figure 4.15.

On the other hand, from the tests for the BR model (all 83 mixture fractions) it was found that for the high fuel-rich range (mixture fraction above 0.0800), the results from the TGLDM did not agree well with the skeletal reaction mechanism. This discrepancy appears to arise because the reaction rates of CO_2 and H_2O in the high fuel-rich range are not distinctly large enough to ignore the influence of the error caused by the nature of interpolation. Hence, the TGLDMs in the range of the mixture fraction above 0.0800 were discarded and the remaining 57 TGLDMs in the mixture fraction range of 0 ~ 0.0800 were used in subsequent calculations such as the PSR model test and CFD simulation.

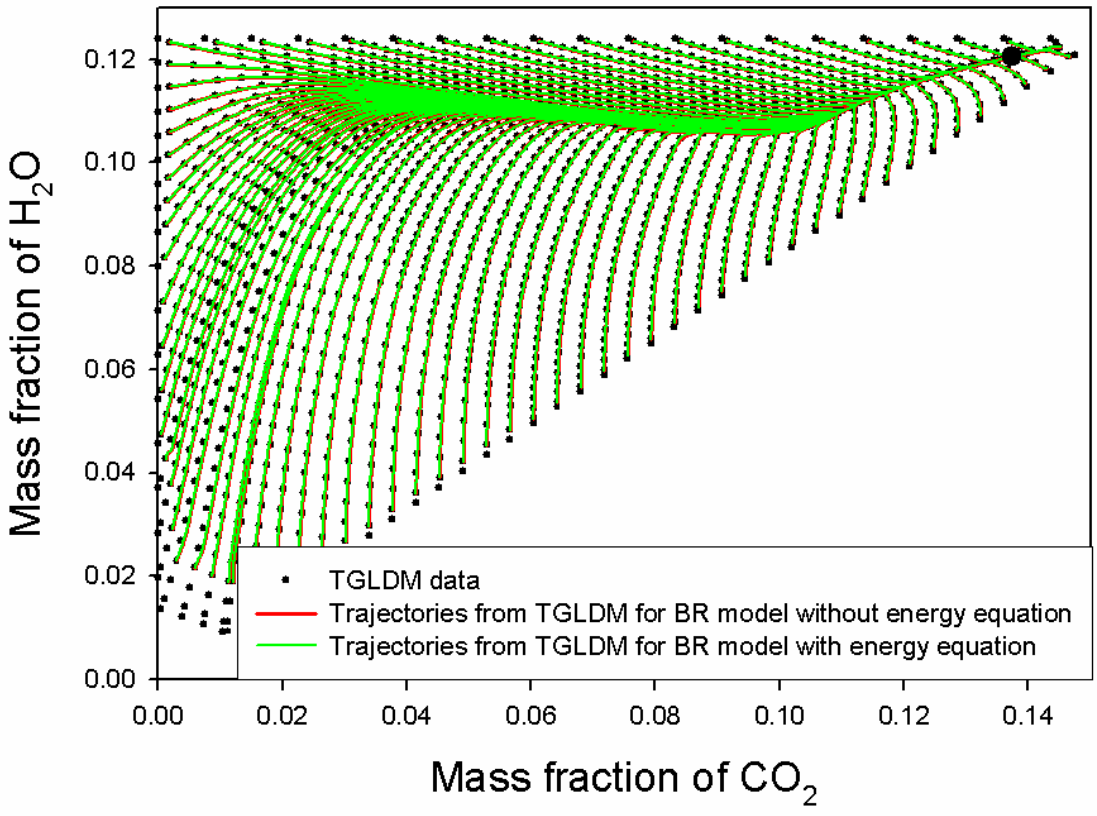

Figure 4.14. Trajectories from the TGLDM with and without the energy equation at the stoichiometric mixture fraction of 0.05516 and the constant pressure of 1 atm in BR model: large black circle is equilibrium point.

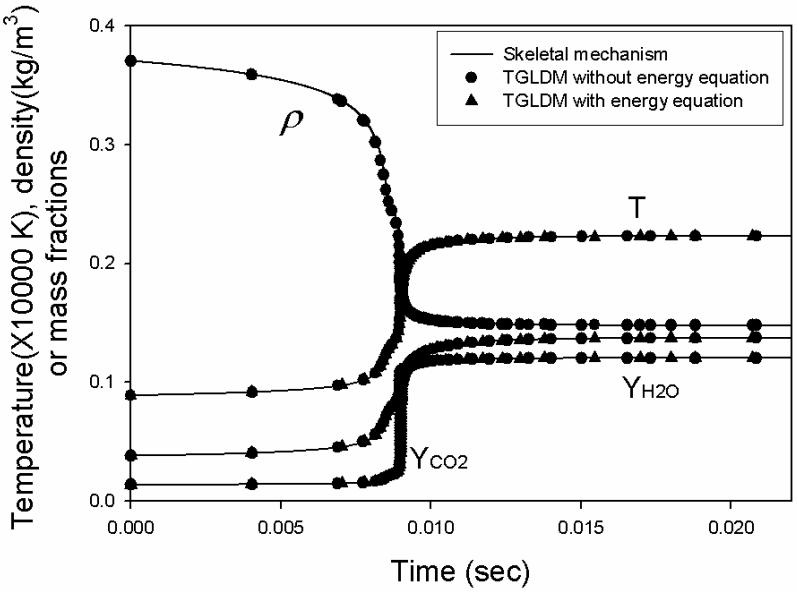

(a) Density, temperature and mass fractions of CO_2 and H_2O

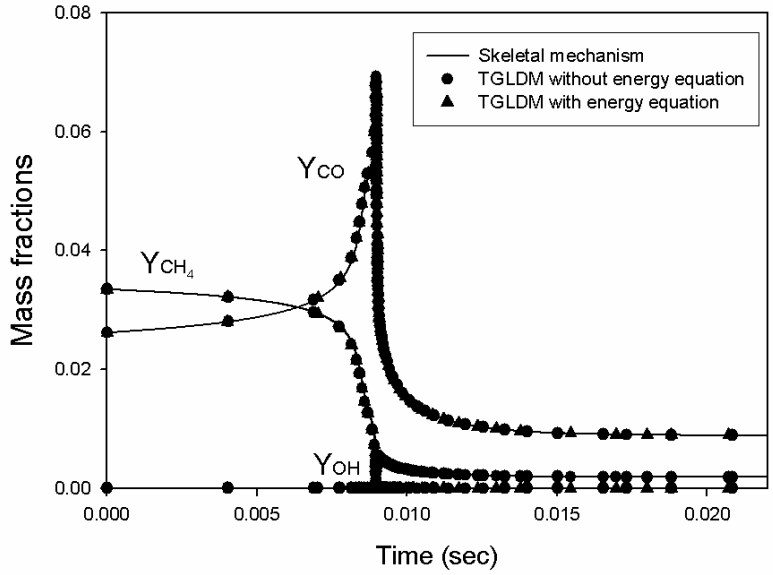

(b) Mass fractions of CH_4, CO and OH

Figure 4.15. Comparisons of the TGLDM with and without the energy equation and the skeletal mechanism with time evolution at the stoichiometric mixture fraction of 0.05516 and the constant pressure of 1 atm in BR model.

PSR model test

Unlike the BR model, the PSR model contains the physical perturbation term (the first term on the right side in Eq.(4.1)). The physical perturbation causes the state of the system to be off the manifolds. Thus, a projection matrix forcing the off-state onto the manifolds may be needed, as discussed in Chapter 2. Application of the projection matrix generally requires a significant additional amount of computational time and data storage space for the tabulation. In this PSR model test, the orthogonal and perpendicular projections were tested, and the orthogonal projection matrix was obtained during the run-time calculation by using TRIPACK/SRFPACK.

The PSR model was tested for the 57 mixture fractions. Two inflow rates of 600 and 1200 kg/m^3sec with a given inflow composition with density ~0.516 kg/m^3 and temperature ~643.0 K were set and the equilibrium state corresponding to the mixture fraction was set as the initial state of the PSR system. The PSR pressure was 1 atm. In this PSR system the blow-out inflow rate was about 2053.3 kg/m^3sec which is the maximum inflow rate to sustain reaction. Like the BR model test, temperature and density were calculated by directly interpolating the TGLDM (without the energy equation) or from solving the energy equation and ideal gas law (with the energy equation).

In Figure 4.16 the trajectories in the Y_{CO2}-Y_{H2O} plane from the skeletal chemical reaction mechanism for the stoichiometric mixture fraction of 0.05516 and the TGLDM adopting the orthogonal projection with or without the energy equation are plotted for the inflow rates of 600, 1200 kg/m^3sec. The corresponding time evolution of several important scalars is also plotted for each inflow rate in Figure 4.17 and Figure 4.18. Similarly, results when adopting the perpendicular projection are plotted in Figure 4.19 ~ Figure 4.21. Based on these results it is

difficult to say whether the orthogonal projection is more suitable for the treatment of the physical perturbation than the perpendicular projection (it needs more computational time). Some of the results from the perpendicular projection appeared to be better in some respects, e.g. the early stage of the trajectory progress in Figure 4.19 when compared to that in Figure 4.16. The trajectories calculated from the TGLDM with and without the energy equation were quite similar in the perspective of the Y_{CO2}-Y_{H2O} plane, Figure 4.16 and Figure 4.19. But the time evolution of the temperature and density data, with and without the energy equation, showed some differences over the complete time period displayed in Figure 4.17 and Figure 4.18, and Figure 4.20 and Figure 4.21. This difference appears to arise because the change of the total formation enthalpy release rate with respect to the mass fraction of CO_2 and H_2O is too steep to be properly projected on the 2-D manifolds. Therefore, in cases when an energy equation needs to be solved, other forms of the energy equation, i.e. one implicitly containing the chemical reaction heat term such as Eq.(2.38-b), may be preferable to evaluate the temperature. A similar tendency was observed for all mixture fractions.

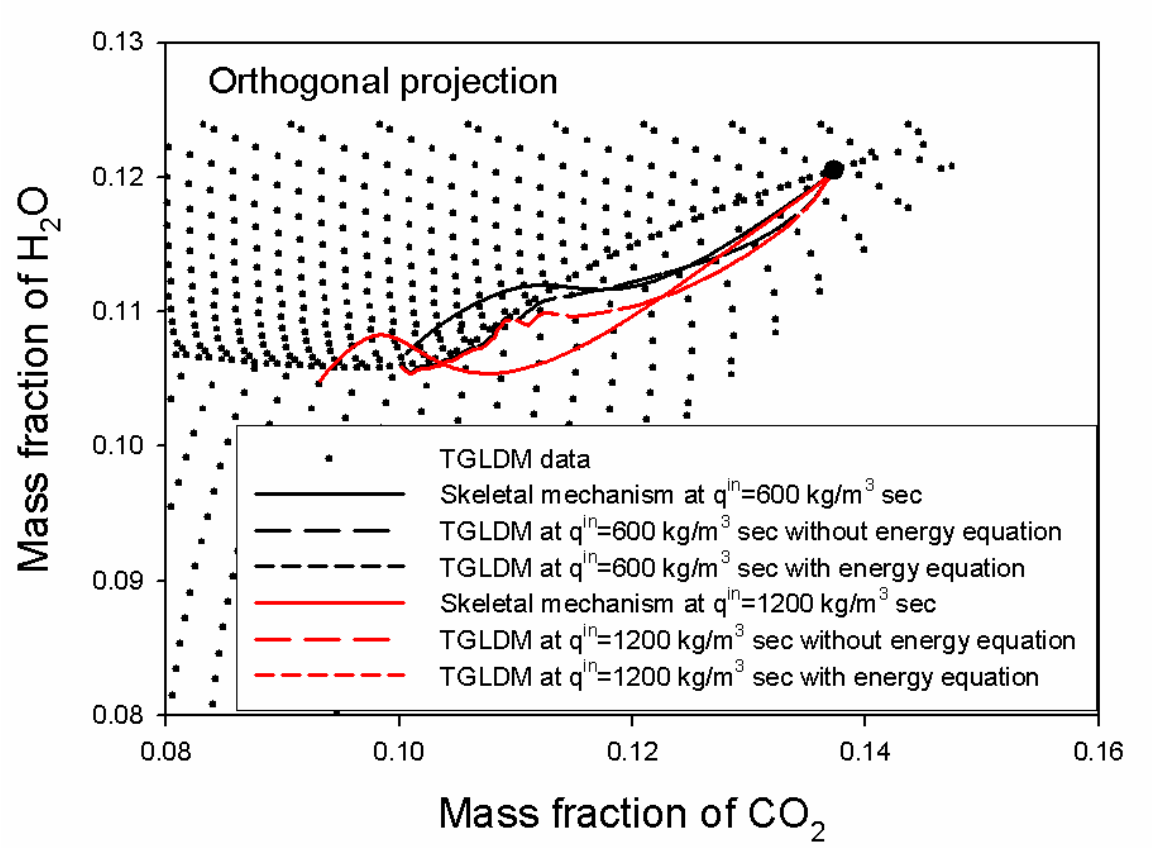

Figure 4.16. Trajectories from the TGLDM with and without the energy equation at q^{in} =600 and 1200 kg/m^3 sec, the stoichiometric mixture fraction of 0.05516 and the constant pressure of 1 atm by adopting orthogonal projection in PSR model: large black circle is equilibrium point.

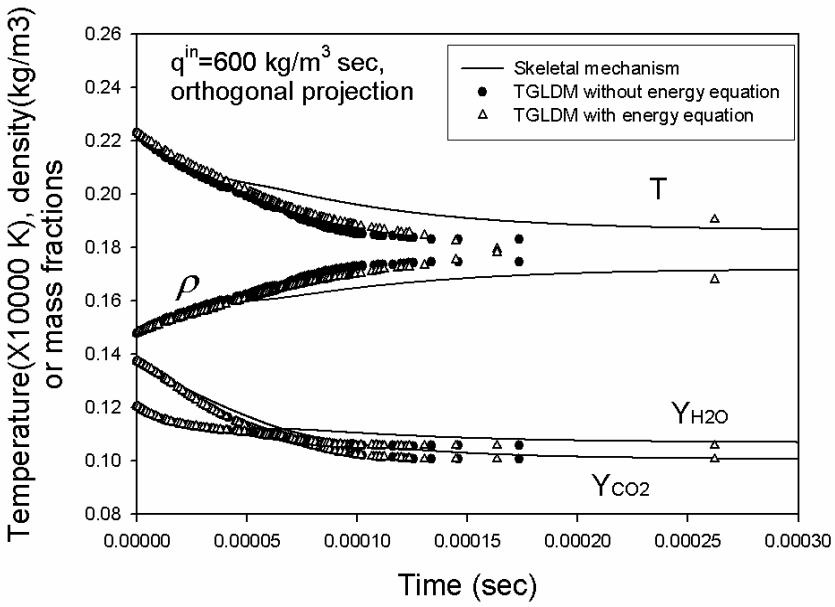

(a) Density, temperature and mass fractions of CO_2 and H_2O

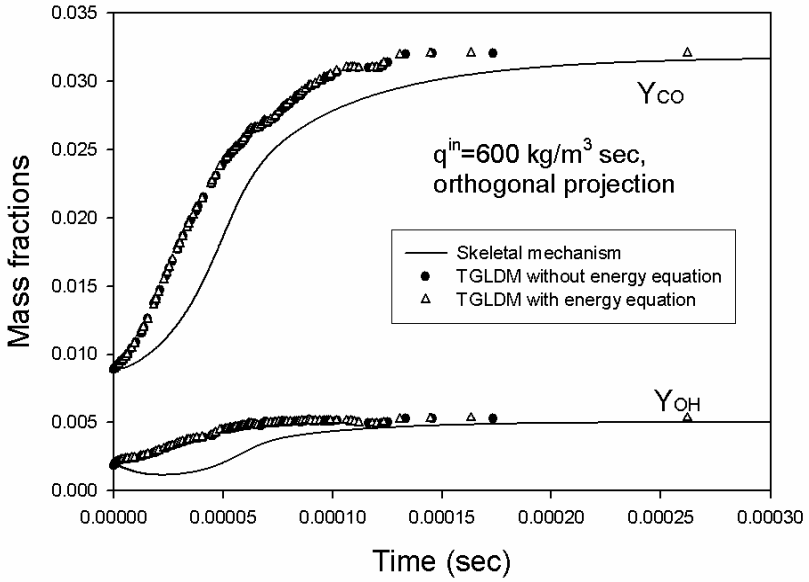

(b) Mass fractions of CH_4, CO and OH

Figure 4.17. Comparisons of the TGLDM with and without the energy equation and the skeletal mechanism with time evolution at q^{in} =600 kg/m^{3}sec, the stoichiometric mixture fraction of 0.05516 and the constant pressure of 1 atm by adopting orthogonal projection in PSR model.

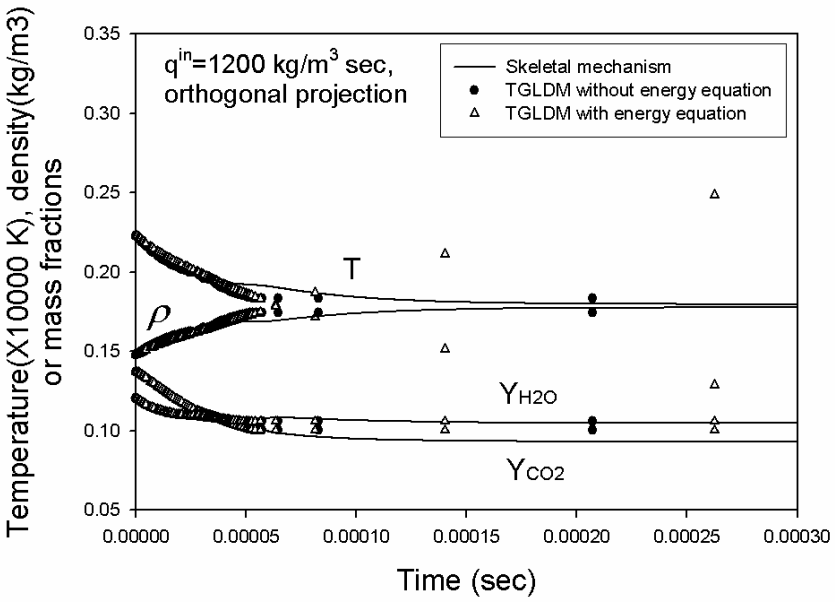

(a) Density, temperature and mass fractions of CO_2 and H_2O

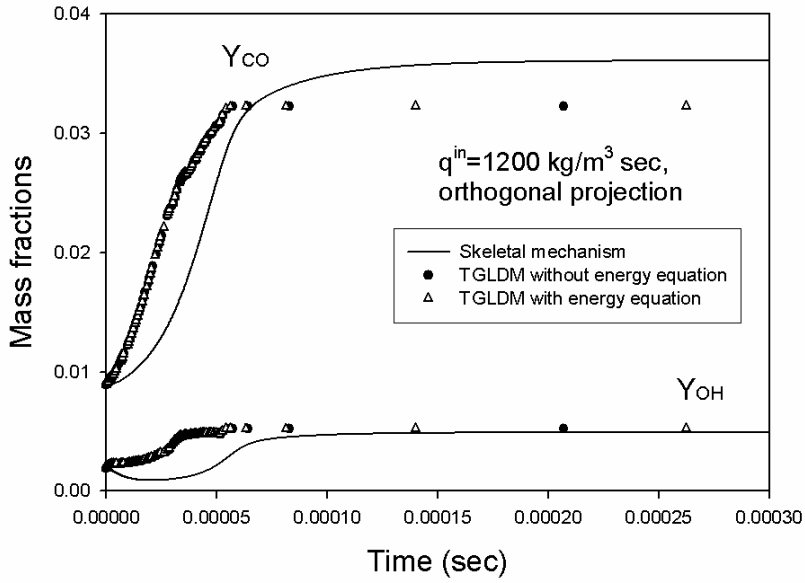

(b) Mass fractions of CH_4, CO and OH

Figure 4.18. Comparisons of the TGLDM with and without the energy equation and the skeletal mechanism with time evolution at q^{in} =1200 kg/m^{3}sec, the stoichiometric mixture fraction of 0.05516 and the constant pressure of 1 atm by adopting orthogonal projection in PSR model.

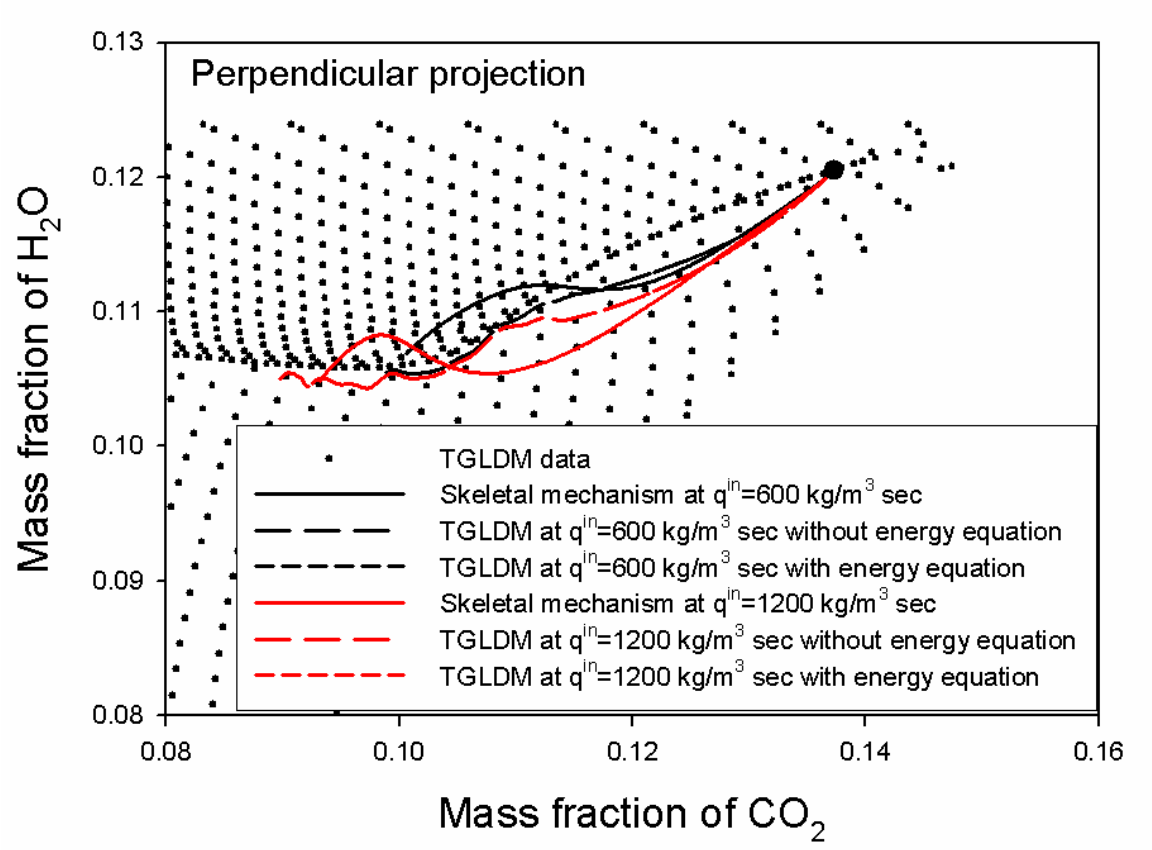

Figure 4.19. Trajectories from the TGLDM with and without the energy equation at q^{in} =600 and 1200 kg/m^3 sec, the stoichiometric mixture fraction of 0.05516 and the constant pressure of 1 atm by adopting perpendicular projection in PSR model: large black circle is equilibrium point.

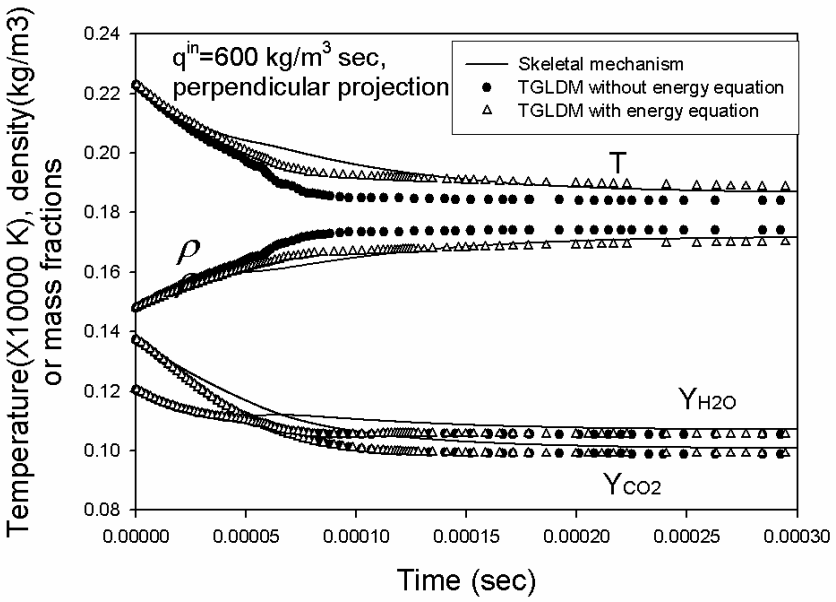

(a) Density, temperature and mass fractions of CO_2 and H_2O

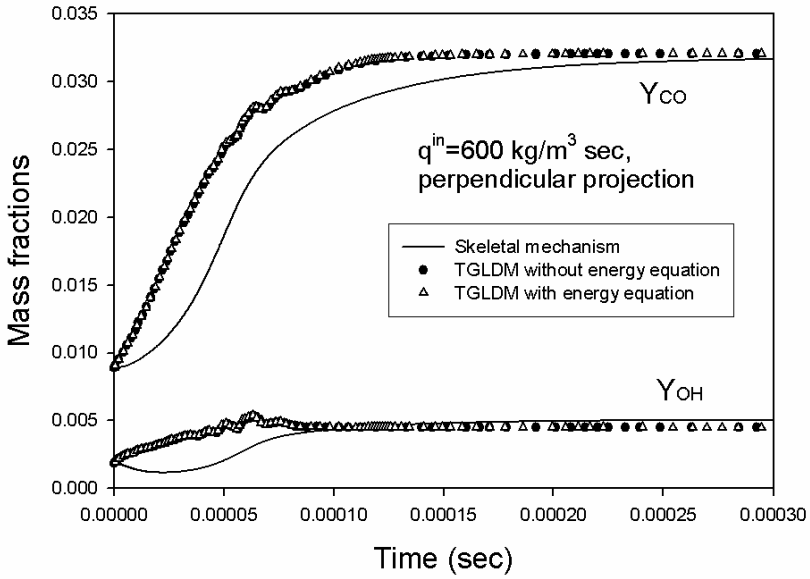

(b) Mass fractions of CH_4, CO and OH

Figure 4.20. Comparisons of the TGLDM with and without the energy equation and the skeletal mechanism with time evolution at q^{in} =600 kg/m^{3}sec, the stoichiometric mixture fraction of 0.05516 and the constant pressure of 1 atm by adopting perpendicular projection in PSR model.

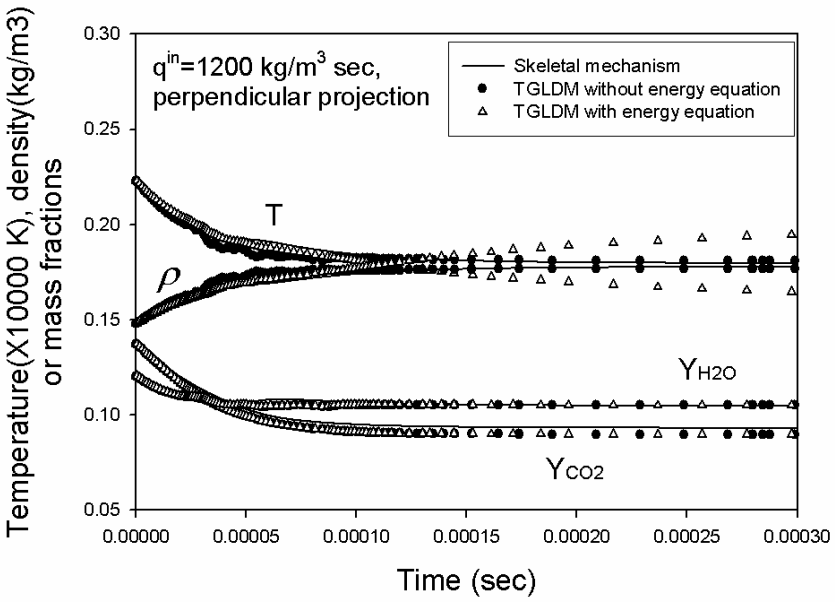

(a) Density, temperature and mass fractions of CO_2 and H_2O

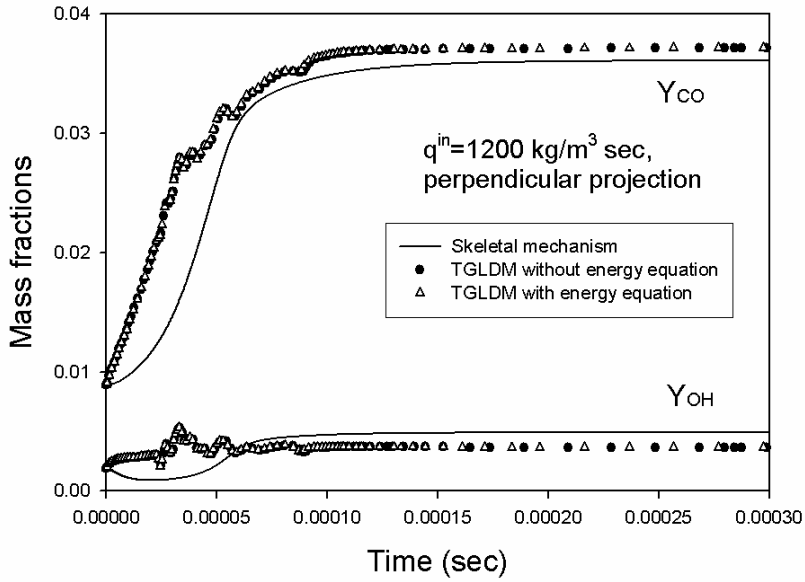

(b) Mass fractions of CH_4, CO and OH

Figure 4.21. Comparisons of the TGLDM with and without the energy equation and the skeletal mechanism with time evolution at q^{in} =1200 kg/m^{3}sec, the stoichiometric mixture fraction of 0.05516 and the constant pressure of 1 atm by adopting perpendicular projection in PSR model.

4.4 Conclusion

For the flameless combustion of natural gas the skeletal chemical reaction mechanism (25 species and 61 reversible reactions) was developed from GRI-Mech 3.0 by removing the NOx sub-mechanism and using PCA combined with sensitivity analysis and reaction flow analysis. The TGLDM method was applied to the skeletal reaction mechanism to provide a simplified set of 2-D manifolds corresponding to 57 mixture fractions.

The set of 2-D manifolds was tested in the BR and PSR model. The chemical perturbation related to the chemical reaction rates and total formation enthalpy release rate were satisfactorily handled by the 2-D manifolds.

For the treatment of the physical perturbation, the perpendicular projection assumption that can provide great benefits like the considerable saving of computational time and data storage space seemed acceptable compared with the orthogonal projection assumption.

The energy equation implicitly describing chemical reaction heat effects, such as Eq.(2.38-b), may be preferable to evaluate the temperature instead of the energy equation explicitly containing the total formation enthalpy release rate term.

Chapter 5
RANS simulation of flameless combustion

5.1 Introduction

He[15] performed numerical simulation of the flameless combustion process in the SJ/WJ furnace using the Eddy-Dissipation Model (EDM) [64,98] with a 2-step methane-air reaction model. The CFD simulation of turbulent reacting flows with a global few-step chemical reaction model is practical and successful in some respects and offers a relatively inexpensive computational resource and easy solution convergence. However, it is often criticized because of the oversimplification of the chemical kinetics and the limited application of the associated reaction parameters only to typical conventional combustion conditions. Hence, various attempts to link detailed chemical reaction mechanism to CFD simulation have been made.

In this chapter the set of the 2-D TGLDM representing detailed chemical reaction kinetics was combined with RANS simulation for flameless combustion in the SJ/WJ furnace. For the estimation of the unconditional mean production/destruction rate of reaction progress variables (the parameters of the 2-D TGLDM) in the transport equation, Eq.(2.45), the Conditional Source-term Estimation (CSE) method was used.

5.2 Experiment of flameless combustion in the SJ/WJ furnace

The experimental data reported by He [15] serves to provide a good database for validating some of the numerical work presented in the present study. The present author was involved with these tests which were carried out to investigate flameless combustion with the SJ/WJ furnace. This test facility is a 48 kW, nonpremixed furnace fired with natural gas and non-preheated air through a single pair of jets providing the mixing field that is characteristic of this low NOx burner technology. Figure 5.1 shows a schematic diagram of the SJ/WJ furnace. The pair of jets constituting the SJ/WJ burner was installed in the burner plate at the base of the furnace and combustion product gas is through the outer gap in the bottom plate. This internal gas flow pattern ensures that the jets entrain the product gas. Probes can be inserted through the furnace wall, into the jet mixing region to monitor local gas temperature and gas composition. The sampling location can be changed by moving the furnace burner plate and/or the location of the modular section furnace wall fitted with the sampling port.

For the measurement of temperature and gas concentrations, a water-cooled sampling probe consisting of a gas sampling tip (inner diameter = 0.63 mm, outer diameter = 1.27 mm) and a thin-wire type-K thermocouple (diameter = 0.254 mm) was mounted in a traversable support that could be moved in the *xy* plane, Figure 5.1. Sampled gas was delivered to a gas analyzer system at a constant flow rate of about 0.75 L/min: a chemiluminescence NOx analyzer for NO and NOx (Rosemount, Model 951C), three infrared analyzers for CH_4, CO and CO_2 (California Analytical, Model ZRH) and a flue gas analyzer for O_2 (Nova Analytical Systems, Model 7550P5B). The sampling line was heated to 80°C to prevent condensation of water vapor inside tube, and water

vapor was removed in a pre-conditioner upstream from the gas analyzer system. Measured gas concentrations reported in this work are expressed on a dry volume basis.

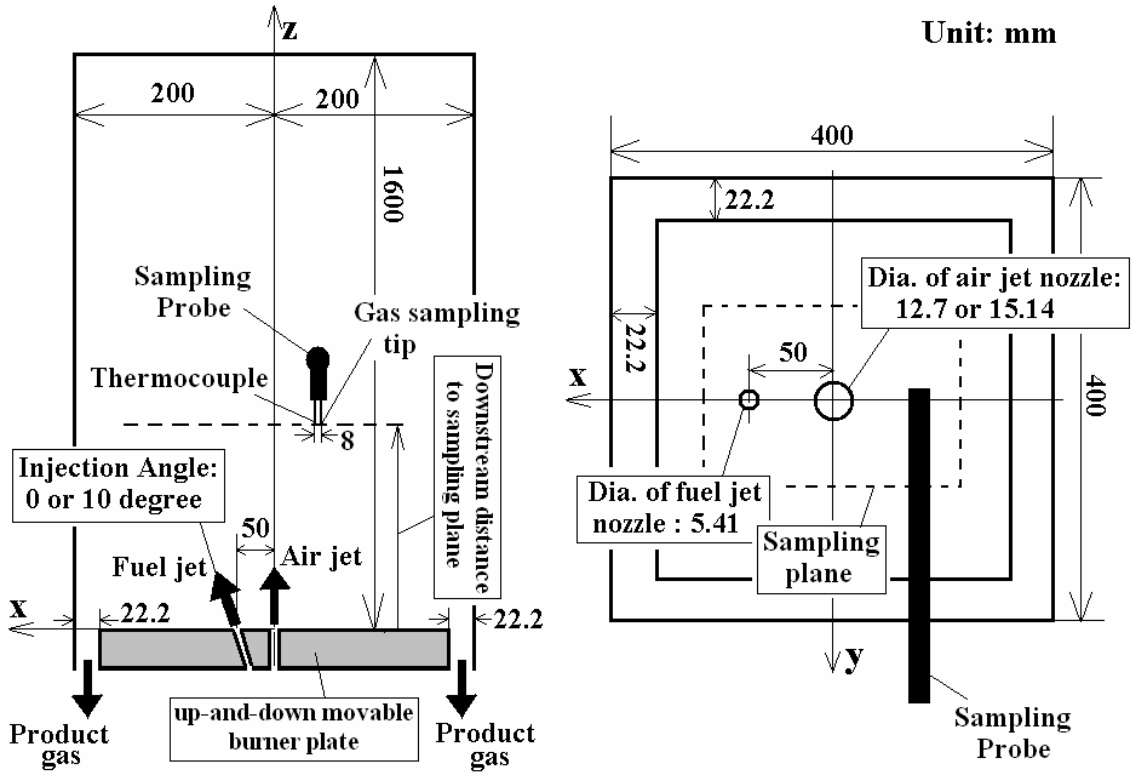

(a) Front view (b) Bottom view

Figure 5.1. A schematic diagram of the SJ/WJ furnace.

5.2.1 Experimental conditions

As shown in Figure 5.1 (a) and (b), the SJ/WJ nozzles supplying the fuel and air to the furnace were mounted with the air jet at the centre of the furnace axis and the fuel jet located 50 mm from the air jet. The fuel jet (the Weak Jet or WJ) was set at angles of 0° and 10° relative to the air jet (the Strong Jet or SJ) and axis of the furnace (*xz* plane). Natural gas (CH_4: 95%, C_2H_6: 2.8%,

CO_2: 0.6%, and N_2: 1.6% in mole basis) was injected through the fuel nozzle (5.41 mm diameter) at the mass flow rate of about 0.000871 kg/s, about 20°C. Air was injected through the air nozzle (two cases were used: 12.7 and 15.14 mm diameter) at a mass flow rate of about 0.0162 kg/s and ~50°C (excess air of about 15%). The fuel/air momentum flow ratio, Eq.(3.26), was about 0.0275 or 0.0390 for the SJ nozzle diameter of 12.7 or 15.14 mm, respectively. Four different experimental conditions used for these tests are described in Table 5.1.

Table 5.1. Experimental conditions for flameless combustion.

	Case A	Case B	Case C	Case D
WJ injection angle	0°	10°	0°	10°
Momentum flow ratio	0.0275	0.0275	0.0390	0.0390
Diameter of SJ nozzle	12.7 mm	12.7 mm	15.14 mm	15.14 mm
Diameter of WJ nozzle	5.41 mm	5.41 mm	5.41 mm	5.41 mm

Distance of SJ and WJ: 50 mm

Mass flow rate of combustion air and temperature at SJ nozzle: 0.0162 kg/s, 50°C

Mass flow rate of natural gas and temperature at WJ nozzle: 0.000871 kg/s, 20°C

In order to sustain flameless combustion, the temperature inside furnace must be kept above a threshold temperature to prevent reaction extinction. Although this threshold temperature depends strongly on fuel properties and various combustion conditions (scalar dissipation rate, etc.), it is usually known to be in the range of 740 ~ 850°C [2,15,99]. A premixed pilot flame burner was used to preheat the furnace and in this work, it was found that a preheat temperature of about 800°C was sufficient to maintain stable combustion before switching into the flameless combustion mode. After that, the pilot flame was turned off, and the furnace combustion was stabilized for about 2 hours to ensure steady-state conditions for experimental measurements.

Measurements of gas concentration and temperature inside the furnace were obtained in two planes, 104 mm and 182 mm downstream from the burner plate. At each sampling plane, temperature and gas concentrations were measured along three characteristic lines shown in Figure 5.2 and labeled 1, 2, and 3. The locations for lines 1 and 2 were fixed, intersecting the locations of the SJ and WJ nozzles. Line 3 was determined during the experimental runs so that the intersection of lines 1 and 3 was aligned with the locus of the fuel jet stream (having the maximum velocity) at the sampling point. Flue gas concentrations were also measured with gas samples withdrawn from the furnace exhaust line.

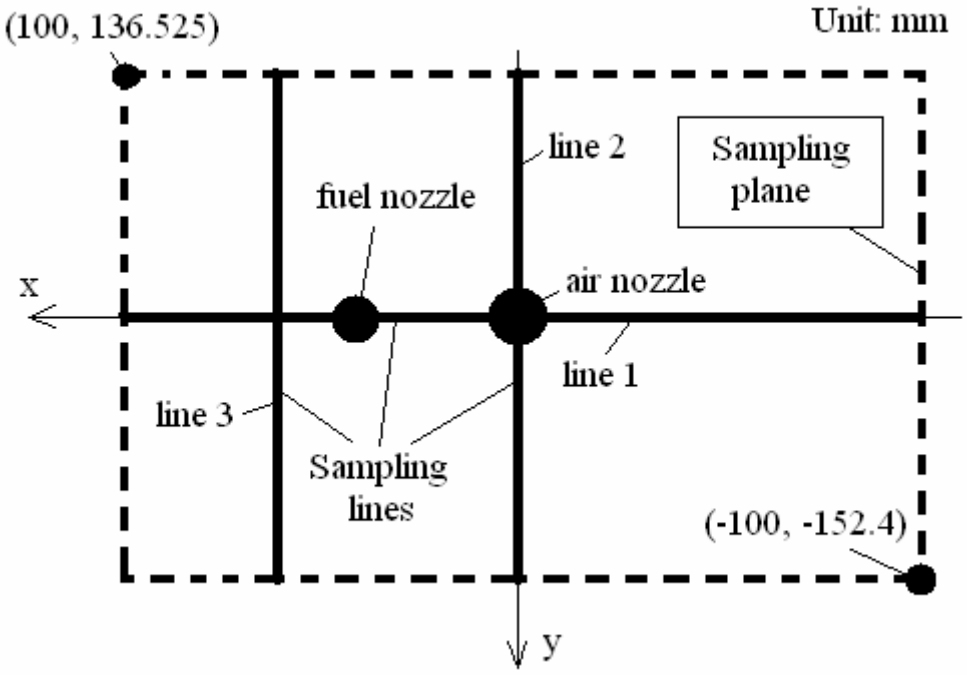

Figure 5.2. Three measuring lines in the sampling plane.

5.2.2 Results and discussion

A picture of the near field region of the SJ/WJ combustor in full operation, showing the features of flameless combustion, is depicted in Figure 5.3. This picture provides clear evidence that there isn't a discernible flame front typical of conventional combustion processes.

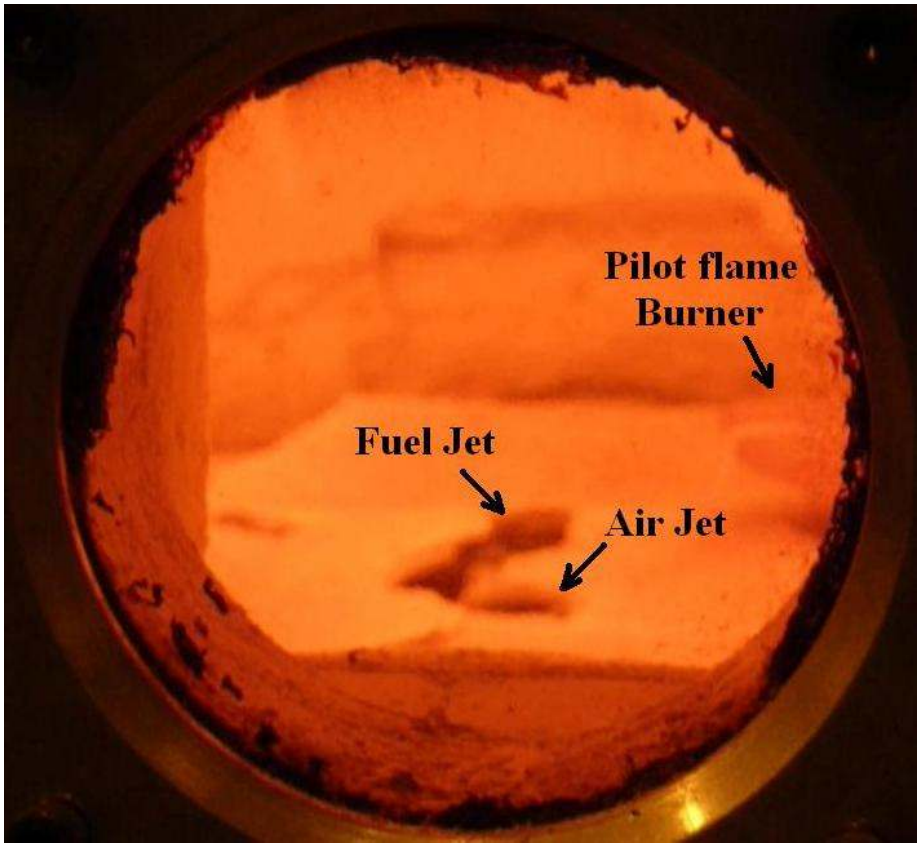

Figure 5.3. A typical appearance of the flameless combustion.

Flue gas concentrations for the four experimental cases examined in this work are shown in Table 5.2. The low concentrations of NOx, 7 ~ 13 ppm, corresponding to the low in-furnace temperature, 955 ~ 966 °C, are evident in all cases. The current emission limits for NOx (as

NO_2) for natural gas fired facilities in Canada are 49.6 ppm (3% O_2, dry basis, for a capacity of 10.5 ~ 105 GJ/hr); the regulations in Europe are even more stringent, e.g. about 28 ppm (3% O_2, dry basis) in the Netherlands [100]. The CO_2, CO, CH_4 and O_2 concentrations are consistent with typical flue gas concentrations in the air/natural gas combustion.

Table 5.2. Flue gas concentrations for four experiment cases.

	Case A	Case B	Case C	Case D
CO_2 (%)	10.4	9.8	10.4	10.4
CO (ppm)	74.5	101.2	110.1	147.3
CH_4 (%)	0.0*	0.0*	0.0*	0.0*
O_2 (%)	2.3	3.3	2.4	2.6
NO (ppm)	4.5	7.4	5.0	6.7
NOx (ppm)	6.7	13.0	7.7	10.9
In-furnace temperature** (°C)	~966	~955	~966	~962

Measurement is in dry basis

ppm: parts per million by volume

*: Not detectable

**: Averaged temperature from the in-furnace measurements excluding the jet stream temperatures

Data for the gas composition and temperature for Cases A ~ D, measured along the three sampling lines are shown in Figure 5.4 ~ Figure 5.7. It should be noted that CH_4 concentrations in the fuel-rich regions could not be obtained because these results were outside the composition range for our gas analyzer (0 ~ 20% CH_4). Mistakenly the NOx (as $NO+NO_2$) concentration was not measured in some samplings of Case B (line 1 at z =104 and 182 mm, line 2 at z =182 mm and line 3 at z =182 mm) while the NO concentration was measured for all samplings.

These figures show typical concentration and temperature profiles for the SJ/WJ configuration. At each jet core, the CO_2 concentration and temperature decreases. The CH_4 and O_2 concentrations showed their maximum value at each corresponding jet core, the fuel and air jets, respectively. The peak in the CO concentration, considered as an indicator of intense combustion reaction, along with the OH concentration (not measured in this work), tended to be formed around the edges of the jets. It should be noted that the CO data have significant uncertainty because the concentration readings exhibited very large fluctuations. As expected, the NOx concentration profiles followed a pattern similar to the temperature profile with higher NOx readings occurring at higher temperatures. More detail analyses for these experimental data can be found in a previous study [15].

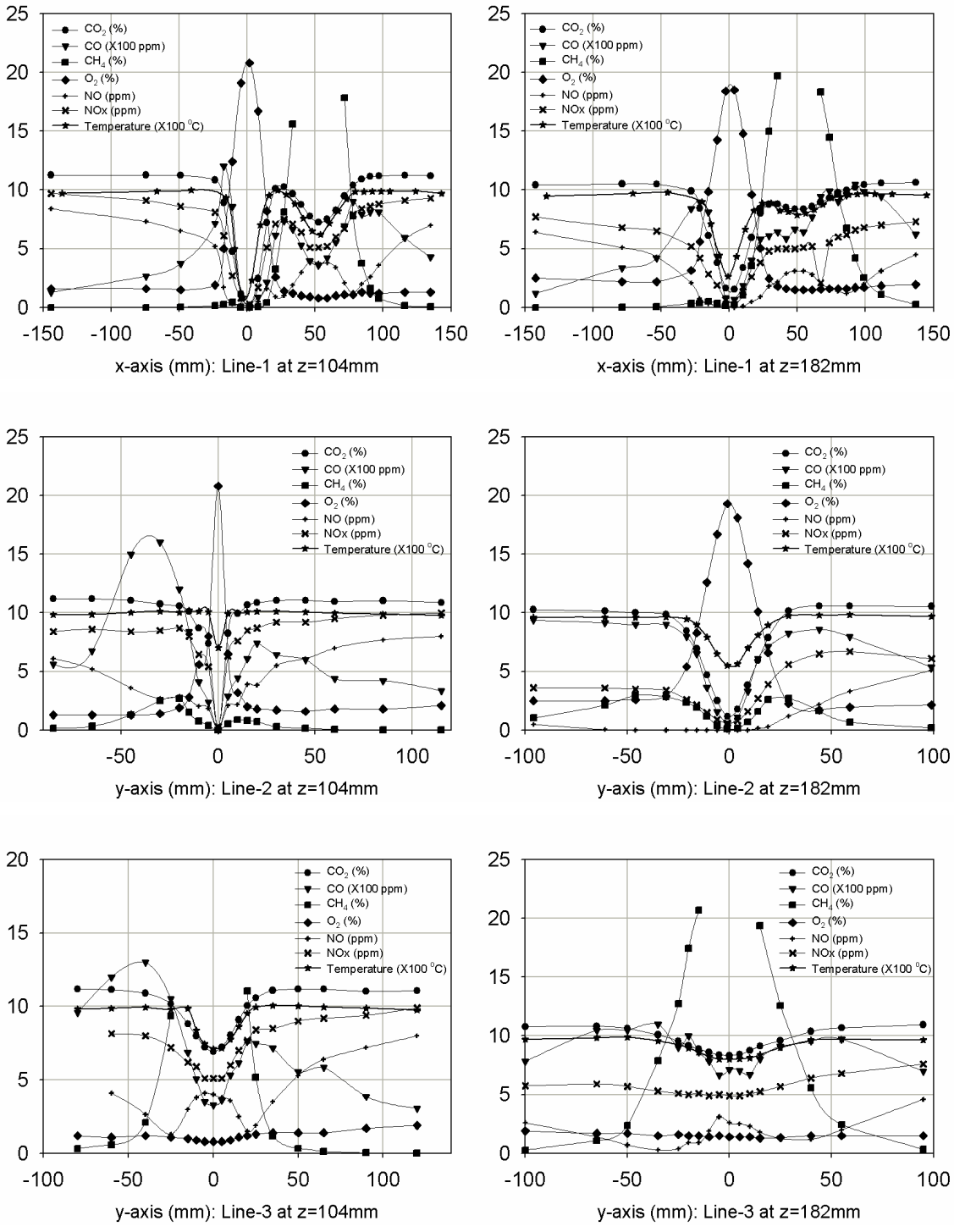

Figure 5.4. In-furnace measurements for the Case A.

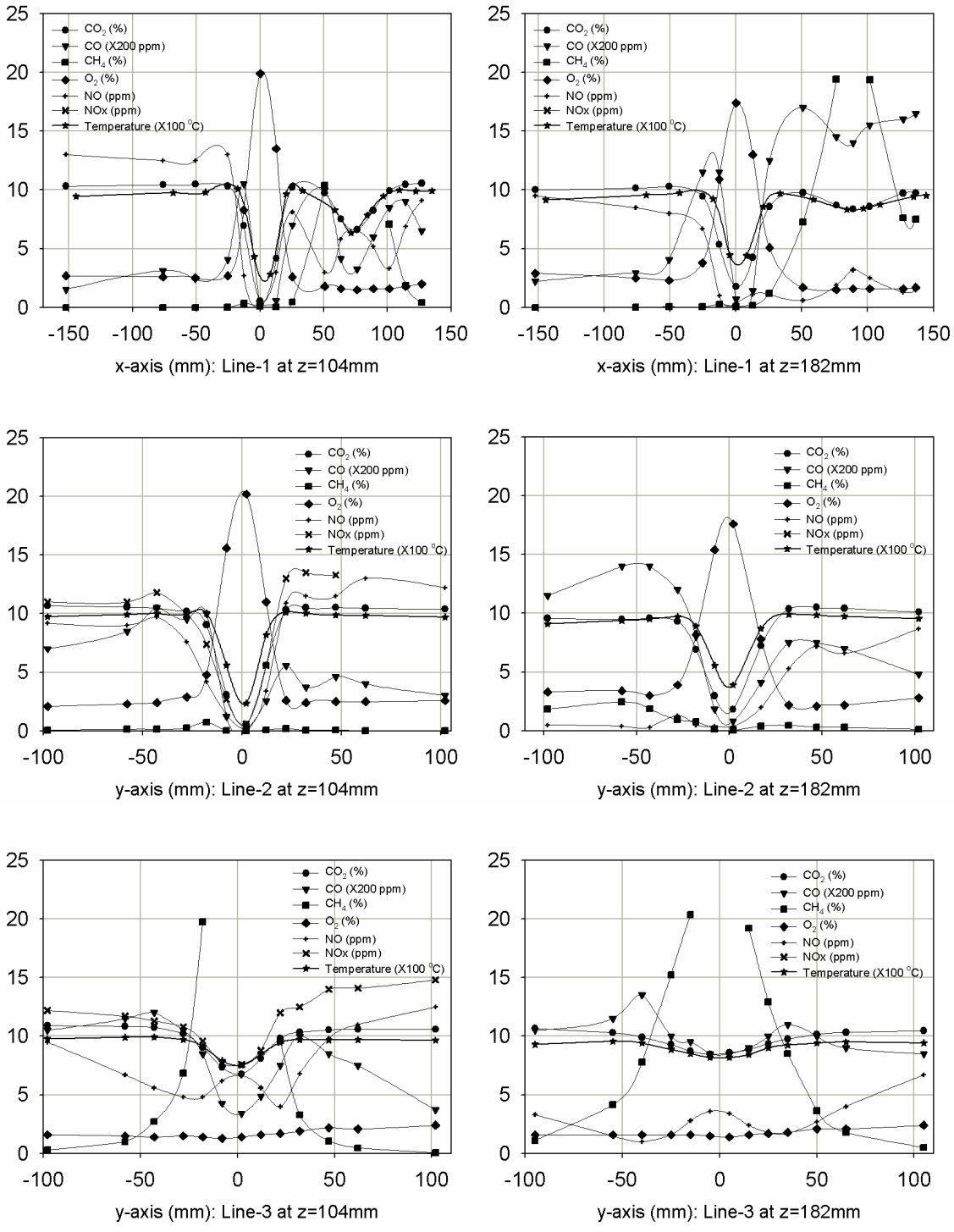

Figure 5.5. In-furnace measurements for the Case B.

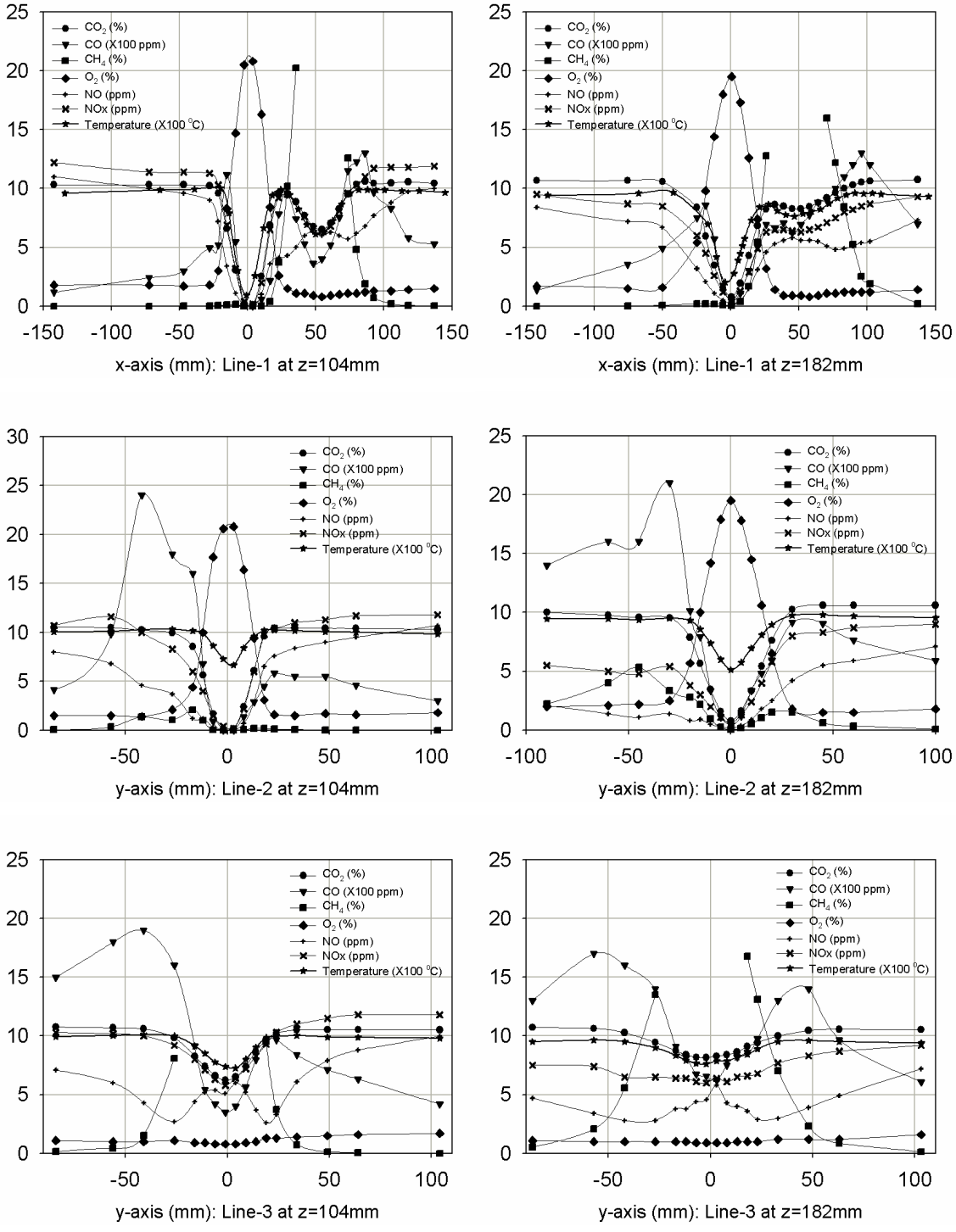

Figure 5.6. In-furnace measurements for the Case C.

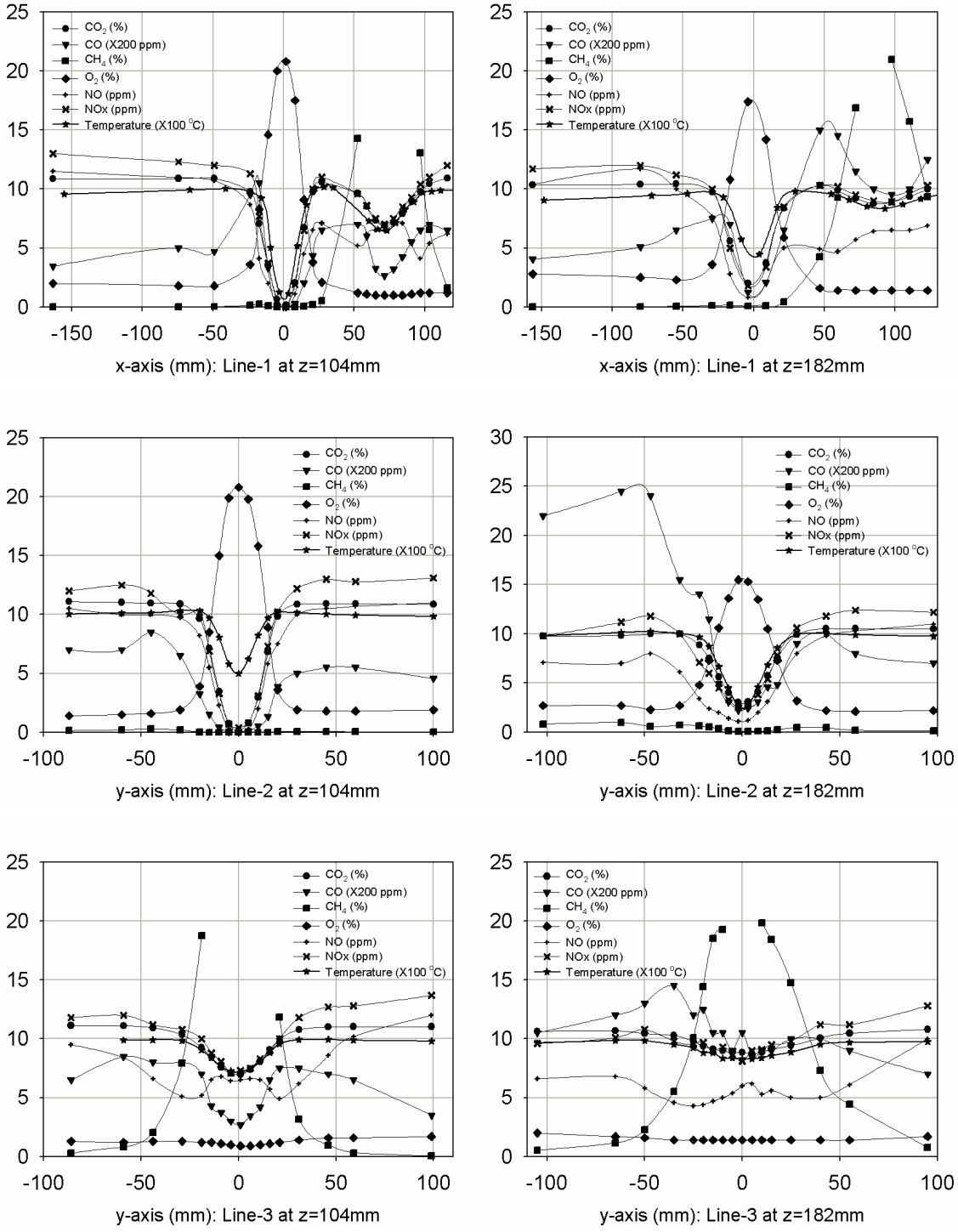

Figure 5.7. In-furnace measurements for the Case D.

5.3 RANS model for flameless combustion in the SJ/WJ furnace

Flameless combustion in the SJ/WJ furnace was simulated by the steady-state RANS turbulence model based on Favre-averaged governing equations as described in Chapter 2. The simulation was carried out for four combustion models that are in the category of PDF/Mixing approach: the adiabatic equilibrium chemistry model, the adiabatic CSE-TGLDM model, the non-adiabatic steady flamelet model, and the non-adiabatic CSE-TGLDM model.

For non-adiabatic simulations, the energy equation in terms of Favre-averaged specific enthalpy, Eq.(2.38-b), was always solved with radiation heat transfer. Accordingly, the Favre-averaged temperature was estimated from the Favre-averaged specific enthalpy and the Favre-averaged mass fractions that can be calculated by the steady flamelet (see Eq.(2.56)) or the CSE-TGLDM model, and the time-averaged density was then calculated by using the ideal gas law for compressible flow. The pressure was obtained from the continuity equation. Details of CSE-TGLDM model will be explained in the following subsections.

The Sunfire 25000 server with dual-core UltraSPARC-IV+ 1.5GHz or 1.8GHz processors, operated by the High Performance Computing Virtual Laboratory(HPCVL) at Queen's University [101], was used for the flameless combustion simulations. Ten CPUs were used simultaneously for each simulation. FLUENT 6.3.26 was used for the CFD code and our own in-house CSE-TGLDM code (including β-PDF) was written in the C programming language.

5.3.1 Interaction of CFD, CSE and TGLDM

Two transport equations, Eq.(2.45), were used for the combustion progress variables, $\tilde{Y}_{CO_2}$, $\tilde{Y}_{H_2O}$, in the CSE-TGLDM model. In Figure 5.8, the interaction of CFD, CSE, and the TGLDM lookup table is described. The unconditional mean scalar values of the mixing field ($\tilde{\xi}$, $\widetilde{\xi''^2}$) and the progress variables ($\tilde{Y}_{CO_2}$, $\tilde{Y}_{H_2O}$) were obtained from the CFD calculation (Eq.(2.42), (2.43) and (2.45)). And then, through the CSE code associated with the presumed PDF (β-PDF), the conditional mean scalar values of the progress variables ($\langle Y_{CO_2}|\eta\rangle$, $\langle Y_{H_2O}|\eta\rangle$) that are the parameters of the 2-D TGLDM lookup table were estimated. From the estimated conditional mean progress variables, the conditional mean mass fractions ($\langle Y_j|\eta\rangle$, j=1,…,n, $j\neq$CO$_2$, H$_2$O) were interpolated by the set of TGLDM lookup tables (corresponding to 57 mixture fractions).

The conditional mean production/destruction rates of the progress variables ($\langle \dot{w}_{CO_2}|\eta\rangle$, $\langle \dot{w}_{H_2O}|\eta\rangle$) were integrated during the calculation of the conditional mean progress variables in the next time step (for example, the smallest retention time among the CFD cells) by setting the estimated conditional mean progress variables as the initial condition. If necessary (for adiabatic conditions), the conditional mean density ($\langle \rho|\eta\rangle$) and the conditional mean temperature ($\langle T|\eta\rangle$) were also interpolated. By using the presumed PDF again these conditional mean values were converted into the unconditional mean values ($\overline{\dot{w}}_{CO_2}$, $\overline{\dot{w}}_{H_2O}$, $\tilde{T}$, $\overline{\rho}$, $\tilde{Y}_j$ where j=1,…,n, $j\neq$CO$_2$, H$_2$O) that enter into the CFD calculation.

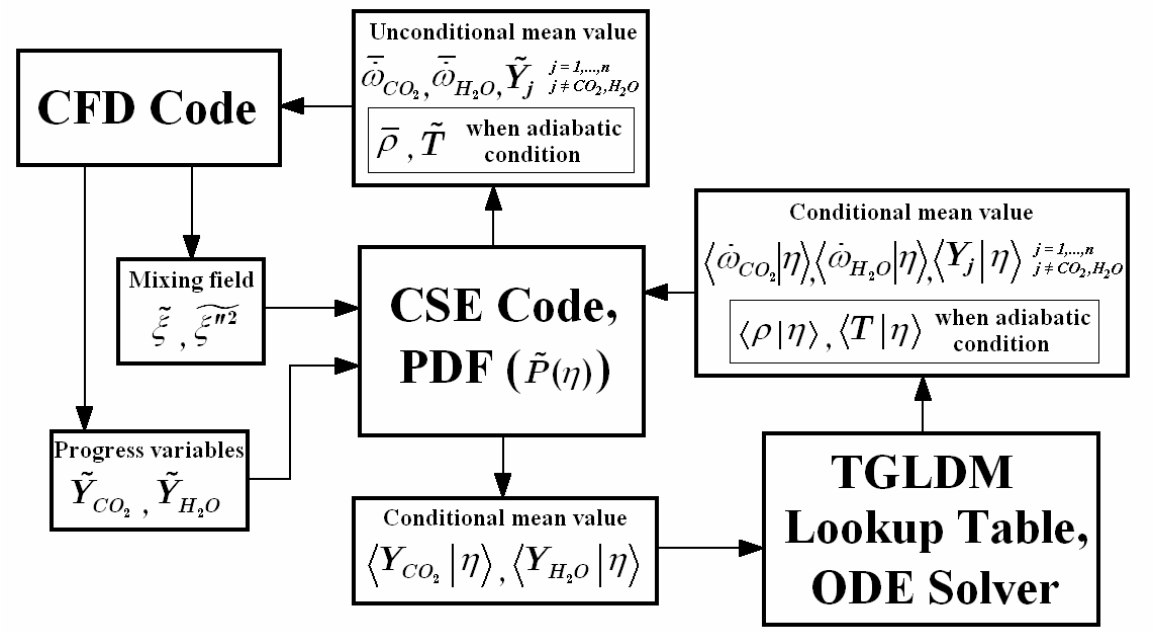

Figure 5.8. A schematic diagram of the interaction of CFD, CSE, and TGLDM lookup table.

5.3.2 Mathematical formulas for CSE method

As described in Chapter 2, in the CSE method a set of algebraic equations (inverse problem) is solved instead of a set of PDEs (Eq.(2.61)), to obtain the conditional mean scalar values ($\langle \phi|\eta\rangle$). The set of algebraic equations is formulated by using the integration technique of the β-PDF suggested by Liu *et al.* [74] and the regularization method with a proper stabilizing functional suggested by Huang and Bushe [89].

By using a trapezoidal quadrature and user-divided mixture fraction points the integral part in Eq.(2.67) can be approximated as

$$\int_{\varepsilon}^{1-\varepsilon} \phi(\eta) f_p(\eta,\alpha,\beta) d\eta \approx a\phi(0) + \sum_{j=1}^{n_{mf}} b_j \phi(\xi_j) + c\phi(1) \tag{5.1}$$

where n_{mf} is the number of the user-divided mixture fraction points. In this work, they were 83 mixture fraction points as described in section 4.3.1. Among them, 57 mixture fraction points correspond to the set of TGLDM lookup tables and the other 26 mixture fraction points, above 0.0800, correspond to their equilibrium state. The parameters a, b_j and c are quadrature coefficients. Note that more finely split mixture fractions are required for the appropriate evaluation of the β-PDF. Thus, we split the mixture fraction into about 600 points, and the quadrature coefficients corresponding to the user-dividing mixture fractions are obtained by using a linear interpolation between them. By substituting Eq.(5.1) into Eq.(2.67), a linear system of algebraic equations is obtained for the group (ensemble) sharing the same conditional mean scalar value:

$$\sum_{j=1}^{n_{mf}} \hat{b}_{kj} \phi(\xi_j) + \hat{a}_k \phi(0) + \hat{c}_k \phi(1) - \tilde{\phi}_k \approx 0, \quad k = 1,2,\ldots,n_c \tag{5.2}$$

$$\hat{a}_k = \left(\frac{\varepsilon^{\alpha}/\alpha + a}{beta(\alpha,\beta)} \right)_k, \quad \hat{c}_k = \left(\frac{\varepsilon^{\beta}/\beta + c}{beta(\alpha,\beta)} \right)_k \text{ and } \hat{b}_{kj} = \left(\frac{b_j}{beta(\alpha,\beta)} \right)_k$$

where n_c is the number of cells within the ensemble. This linear algebraic system is known as an ill-posed problem, called the inverse problem, and a regularization method is commonly used to solve it by adding *a priori* information. By letting $\sum_{k=1}^{n_c} \sum_{j=1}^{n_{mf}} \hat{b}_{kj} = \vec{\vec{B}}$, $\hat{a}_k \phi(0) + \hat{c}_k \phi(1) = \vec{d}$, $\tilde{\phi}_k = \vec{\tilde{\phi}}$ and $\phi(\xi_j) = \vec{\phi}(\xi)$, and applying *a priori* information, Eq.(5.2) can be transformed into a minimization problem:

$$\min \left\{ \left\| \vec{\vec{B}} \vec{\phi}(\xi) + \vec{d} - \vec{\tilde{\phi}} \right\|^2 + \lambda \left\| \vec{\phi}(\xi) - \vec{\phi}_*(\xi) \right\|^2 \right\} \tag{5.3}$$

where the second term is a stabilizing functional, $\vec{\phi}_*(\xi)$ is *a priori* information and λ is the regularization parameter determined from preliminary tests for a given problem. In this simulation, the regularization parameter was set as $\lambda = 5 \times Tr\left(\vec{\vec{B}}^T \vec{\vec{B}}\right) \Big/ Tr\left(\vec{\vec{I}}\right)$. Following the suggestion of Huang and Bushe [89], *a priori* information was obtained from a combination of the previous iteration step solution (or previous time step solution in an unsteady simulation) and the convection effect of the conditional mean scalar,

$$\vec{\phi}_*(\xi)^J = \vec{\phi}(\xi)^{J-1} - \Delta t\left(V_z \frac{\partial \vec{\phi}(\xi)}{\partial z}\right)^{J-1} \tag{5.4}$$

where J is the sequence number in the iteration steps (or time step in an unsteady simulation), V_z is a representative velocity in the main convection flow direction (jet flow direction), which can be expressed as $\iint \bar{\rho}\tilde{u}_z dxdy \Big/ \iint \bar{\rho} dxdy$, and Δt can be an arbitrary time value related to the retention time of cells in the CFD domain for steady-state simulation. Note that Δt would be just the consecutive time period for a transient simulation. In this case, Δt was set as the smallest retention time among the CFD cells.

By differentiating Eq.(5.3) in terms of the unknown conditional mean scalar variable, $\vec{\phi}(\xi)$, the minimization problem can be transformed into a linear algebraic system:

$$\left(\vec{\vec{B}}^T \vec{\vec{B}} + \lambda \vec{\vec{I}}\right)\vec{\phi}(\xi) = \vec{\vec{B}}^T\left(\vec{\tilde{\phi}} - \vec{d}\right) + \lambda \vec{\phi}_*(\xi) \tag{5.5}$$

This system was solved by Singular Value Decomposition (SVD) methods [87]. By applying Eq.(5.5) for the two progress variables ($\tilde{Y}_{CO_2}$, $\tilde{Y}_{H_2O}$), we can obtain the conditional mean mass fractions of the progress variables ($\vec{Y}_{CO_2}(\xi)$, $\vec{Y}_{H_2O}(\xi)$) at each ensemble that is divided along

with the jet flow direction. From them, we can obtain other necessary conditional mean scalar values such as the production/destruction rates of progress variables, mass fractions, temperature and density. The QSHEP2D algorithm was used for the interpolation of the set of TGLDM lookup tables.

5.3.3 Time-averaged production/destruction rate of progress variables

To prevent numerical overflow which frequently takes place in combustion calculations due to the stiffness of the chemical kinetic mechanism, the averaged production/destruction rate value over time is usually used instead of the instantaneous value, i.e.

$$\overline{\dot{w}_j} = \frac{1}{\tau}\int_0^{\tau} \overline{\dot{w}_j} dt = \frac{1}{\tau}\int_0^{\tau} \left\{ \bar{\rho} \int_0^1 \frac{\dot{w}_j(\eta)}{\rho(\eta)} \tilde{P}(\eta) d\eta \right\} dt \tag{5.6}$$

where τ is an arbitrary time value related to the retention time of cells for steady-state simulation or one step time period for transient simulation. Since the numerical evaluation of Eq.(5.6) is time-consuming, an alternate estimation was used:

$$\overline{\dot{w}_j} \approx \bar{\rho} \int_0^1 \left\{ \frac{1}{\tau}\int_0^{\tau} \frac{\dot{w}_j(\eta)}{\rho(\eta)} dt \right\} \tilde{P}(\eta) d\eta \tag{5.7}$$

In this RANS simulation the upper time limit in the integration, τ, was set as the smallest retention time among those of CFD cells like the time value in Eq.(5.4). The time integration of Eq.(5.7) was done along with the integration of the progress variables from their initial values obtained from Eq.(5.5). CVODE [102] was used for the integration. Note that other simpler stiff

ODE solvers, for instance the Rosenbrock method [87,92], would work properly because only two dependent variables are involved.

5.3.4 Favre-averaged mass fractions, temperature and time-averaged density

For the adiabatic simulation Favre-averaged mass fractions ($\tilde{Y}_i$, i=1,…,n, i≠CO_2, H_2O), temperature ($\tilde{T}$) and time-averaged density ($\overline{\rho}$) were directly calculated from the calculated coefficients ($\hat{a}_k$, $\hat{b}_{kj}$, $\hat{c}_k$) and the interpolated conditional mean values from the conditional mean mass fractions of the progress variables such as

$$\tilde{Y}_i = \int_0^1 Y_i(\eta)\tilde{P}(\eta)d\eta = \hat{a}\left(Y_i(0)\right) + \sum_{j=1}^{n_{mf}} \hat{b}_j\left(Y_i(\xi_j)\right) + \hat{c}\left(Y_i(1)\right)$$

$$\text{when } i = 1,...,n, \quad i \neq CO_2, H_2O \tag{5.8}$$

$$\tilde{T} = \int_0^1 T(\eta)\tilde{P}(\eta)d\eta = \hat{a}\left(T(0)\right) + \sum_{j=1}^{n_{mf}} \hat{b}_j\left(T(\xi_j)\right) + \hat{c}\left(T(1)\right) \tag{5.9}$$

$$\frac{1}{\overline{\rho}} = \int_0^1 \frac{1}{\rho(\eta)}\tilde{P}(\eta)d\eta = \hat{a}\left(\frac{1}{\rho(0)}\right) + \sum_{j=1}^{n_{mf}} \hat{b}_j\left(\frac{1}{\rho(\xi_j)}\right) + \hat{c}\left(\frac{1}{\rho(1)}\right) \tag{5.10}$$

Note that, unlike the case for the unconditional time-averaged production/destruction rates, these unconditional scalar values do not need the time integration procedure.

For non-adiabatic simulation, like Eq.(2.51), the Favre-averaged temperature ($\tilde{T}$) and the time-averaged density ($\overline{\rho}$) were calculated by solving the energy equation and the ideal gas law. The Favre-averaged mass fractions were first calculated from Eq.(5.8) by assuming that the mass

fractions for non-adiabatic conditions were similar to those for adiabatic conditions. The Favre-averaged temperature was then calculated by using these Favre-averaged mass fractions and Favre-averaged specific enthalpy from Eq.(2.38-b), i.e.

$$\int_{T_{ref}}^{\tilde{T}} \left(\sum_{j=1}^{n} \tilde{Y}_j c_{p,j} \right) dT + \sum_{j=1}^{n} \tilde{Y}_j h_j^o - \tilde{h} = 0 \tag{5.11}$$

The time-averaged density ($\overline{\rho}$) was calculated by using the Favre-averaged mass fractions and the Favre-averaged temperature, i.e.

$$\overline{\rho} = \frac{\overline{p}}{R\tilde{T} \sum_{j=1}^{n} \frac{\tilde{Y}_j}{W_j}} \tag{5.12}$$

Note that the meanings of the symbols can be found in Chapter 2.

5.3.5 Mesh and simulation setup for RANS simulation

For the RANS simulation, a wedge shape of meshing was applied to half of the SJ/WJ furnace as shown in Figure 5.9. This domain was split into 60 slices in z-direction and each slice had 2843 cells (when Case A and B in Table 5.1) or 2831 cells (when Case C and E in Table 5.1). This meshing scheme was carefully assessed by a preliminary grid independence test. The ensemble sharing the same conditional mean scalar values was set up as a rectangle with dimensions of 0.30 m in the x-direction, 0.15 m in the y-direction and each of the 60-slice elements for the z-direction, as shown in Figure 5.9 (b).

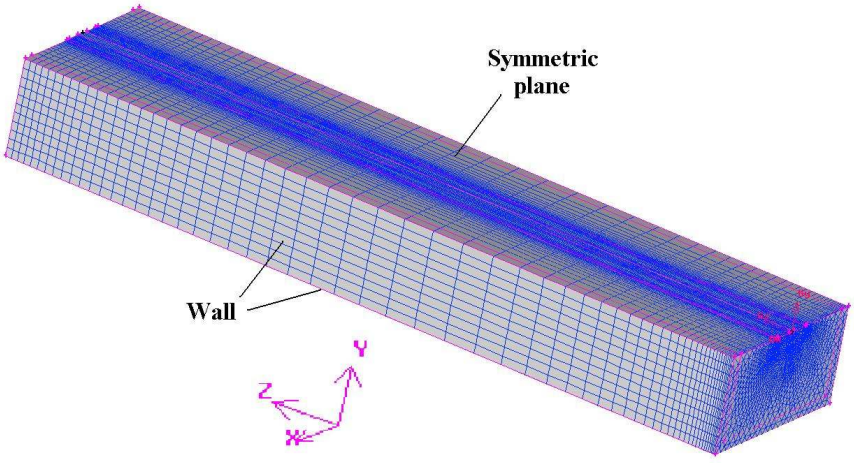

(a) 3-Dimensional view of the mesh

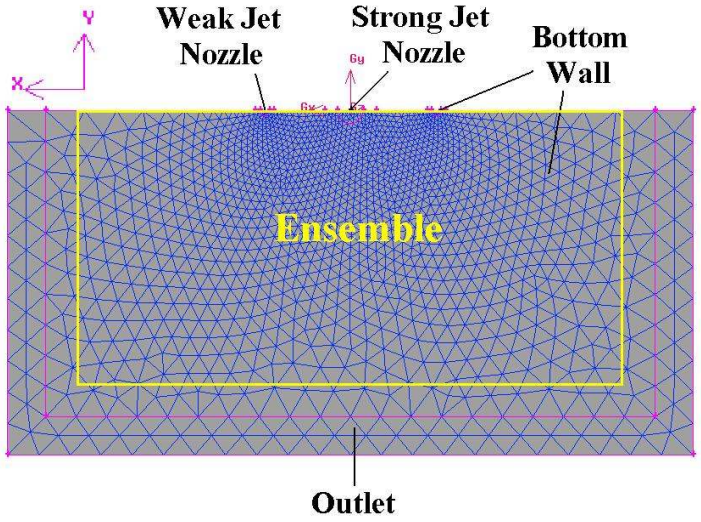

(b) Mesh and ensemble in the bottom view

Figure 5.9. Mesh and ensemble in the simulation domain of the SJ/WJ furnace.

All boundary conditions were set up to be consistent with the experimental conditions. For the non-adiabatic simulation, heat flux from a wall towards its surroundings was set as 2000 W/m^2. This estimate was based on the wall refractory (insulation board of 1 inch thickness) with thermal conductivity of ~0.05 W/mK, and the approximate temperature difference of ~1000 K.

For the selection of a radiation model, the optical thickness was first estimated as based on the characteristic length of this SJ/WJ furnace (0.4m) and a typical combustion product gas compositions (mass fractions of H_2O = 0.12, O_2 = 0.05, CO_2 = 0.11 and N_2 = 0.72). The DO radiation model was used for thermal radiation heat flux because this estimated value, ~0.15, indicated a very thin optical thickness and this RANS simulation was conducted in parallel computation environment. Also, the mean beam path length that was used to obtain the absorption coefficient of the gas medium from the weighted-sum-of-gray-gases model (WSGGM) was set as 0.4 m, based on the geometry of the SJ/WJ furnace. The internal emissivity of the walls was 0.8 and the refractive index was 1.0.

5.4 Results and discussion

In this section the RANS simulation results from the four combustion models (the adiabatic equilibrium chemistry, the adiabatic CSE-TGLDM, the non-adiabatic steady flamelet and the non-adiabatic CSE-TGLDM) for the four cases in Table 5.1 are presented and compared with experimental data.

In Figure 5.10 ~ Figure 5.13, contour maps of z-velocity, temperature, mass fractions of CO_2, H_2O, CO, OH on the symmetric and exit planes for the non-adiabatic CSE-TGLDM model are presented for the four cases. The fuel jet stream (WJ) impinged the furnace wall in Case B and D (Figure 5.11, Figure 5.13) while in Case A and C (Figure 5.10, Figure 5.12) the fuel jet stream was merged into the air jet stream (SJ). With the injection angle of 10°, the momentum flow ratios for Case B (0.0275) and Case D (0.0390) were too high for the fuel jet stream to merge into

the air jet stream before reaching the furnace wall. In addition, the reverse flow of the exhaust gases through the gap in the burner plate seems to have a somewhat negative influence on the merging of the fuel jet and air jet streams. An interesting phenomenon is displayed for the z-velocity contours in these figures. The darker blue shading represents a negative z-velocity, which corresponds to a reverse flow or a primary recirculation zone for the general flow pattern in the furnace. The formation of this recirculation zone was more evident on the fuel jet side of the furnace for Cases A and C (Figure 5.10(a) and Figure 5.12(a)) and on the opposite wall for Cases B and D (Figure 5.11(a) and Figure 5.13(a)).

The temperature contour maps show that the temperature field is quite uniform throughout the furnace except for high momentum regions of both the fuel and air jet streams. This uniformity characteristic can be also found in the contour maps of OH concentration. The OH concentration field is also uniformly distributed throughout the furnace because this radical is a representative intermediate reactive species produced by the principal combustion reactions. As expected, the CO concentration was high within the fuel jet stream because this is a major stable species under fuel-rich conditions. Contour maps from the other three combustion models were quite similar to these results.

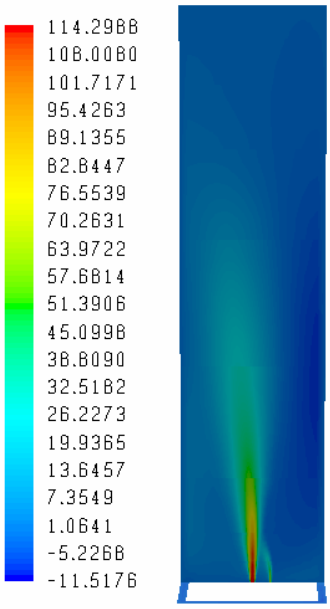

(a) z-velocity(m/s)

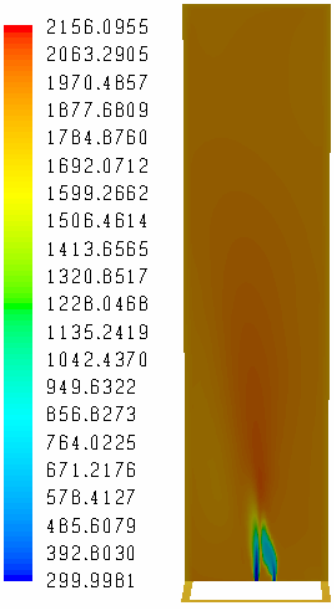

(b) Temperature(K)

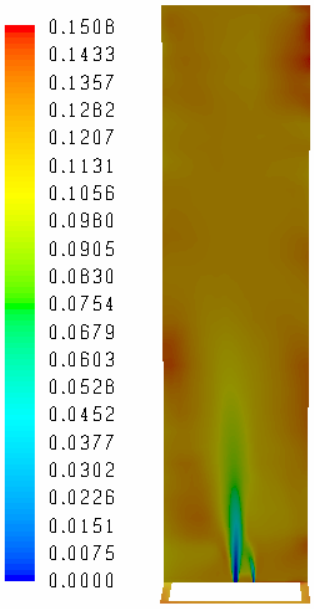

(c) Mass fraction of CO_2

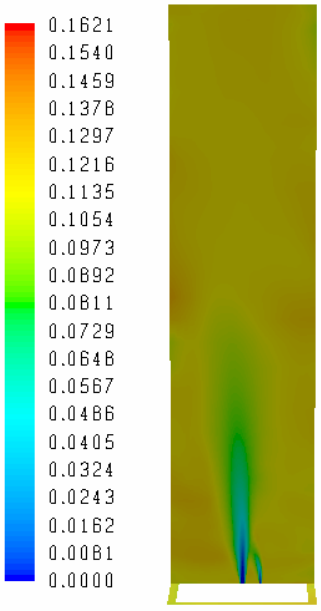

(d) Mass fraction of H_2O

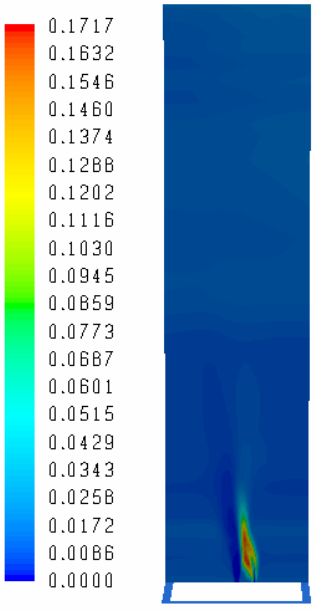

(e) Mass fraction of CO

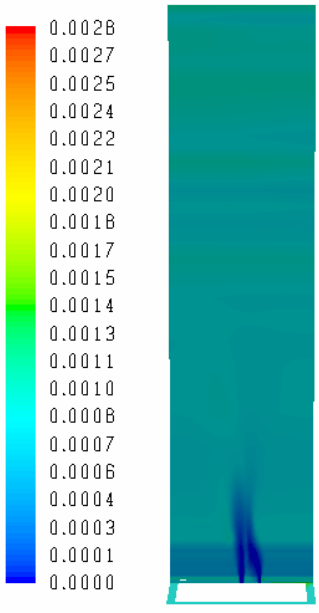

(f) Mass fraction of OH

Figure 5.10. Contour maps from the non-adiabatic CSE-TGLDM model for the Case A.

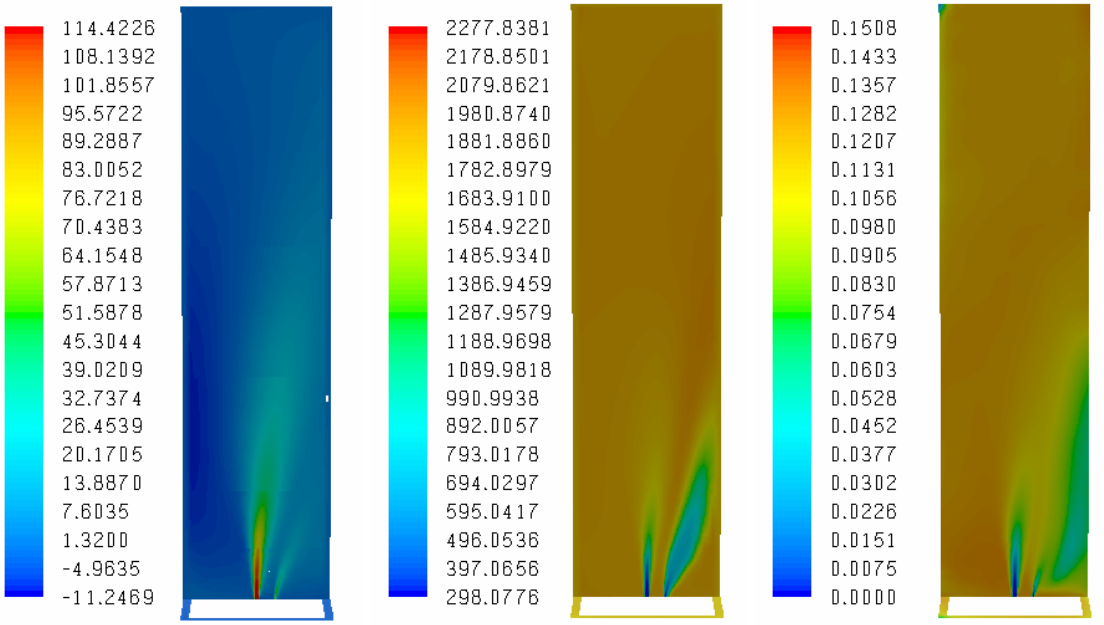

(a) z-velocity(m/s) (b) Temperature(K) (c) Mass fraction of CO_2

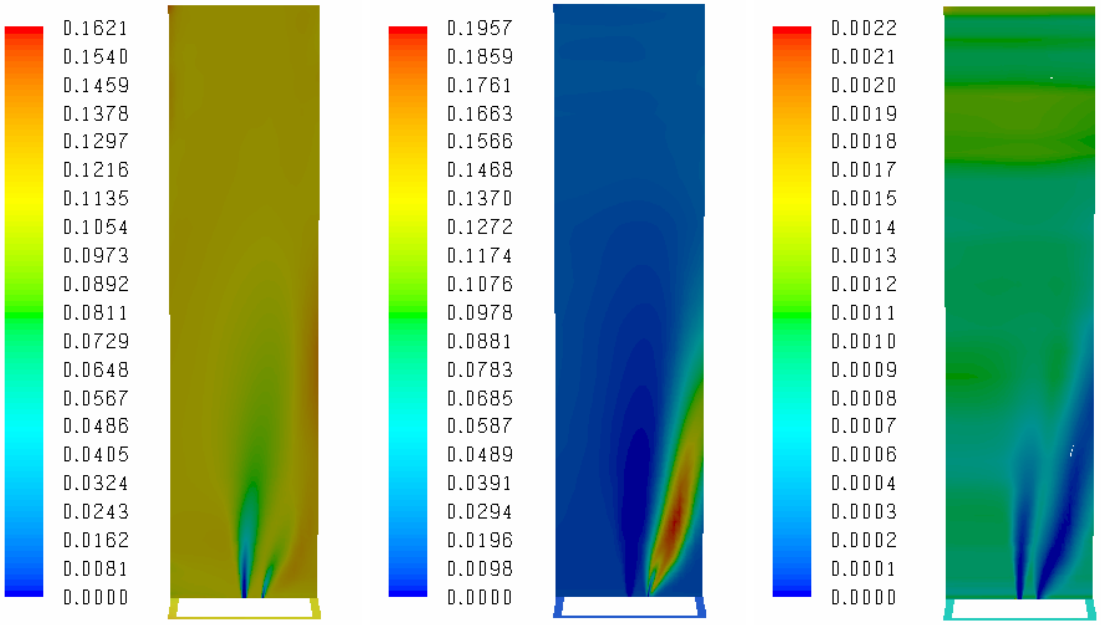

(d) Mass fraction of H_2O (e) Mass fraction of CO (f) Mass fraction of OH

Figure 5.11. Contour maps from the non-adiabatic CSE-TGLDM model for the Case B.

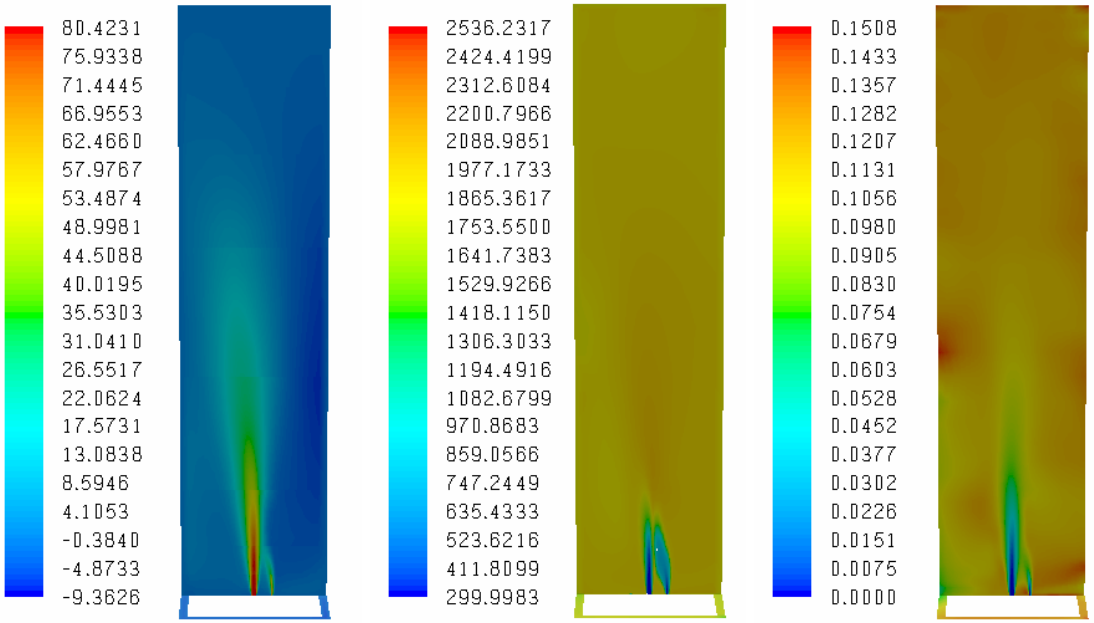

(a) z-velocity(m/s) (b) Temperature(K) (c) Mass fraction of CO_2

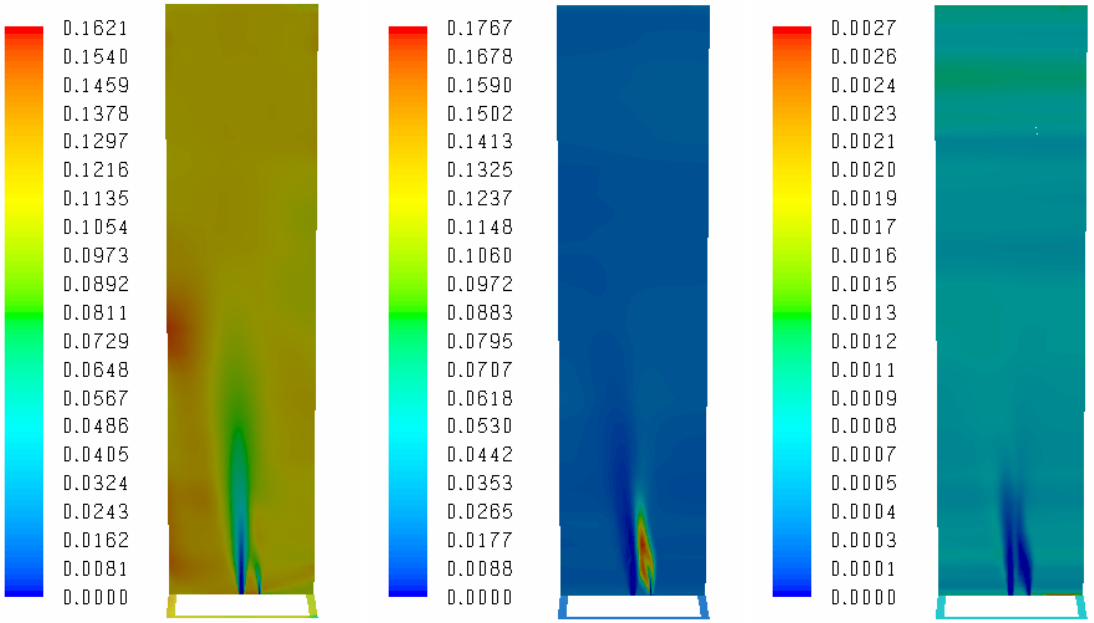

(d) Mass fraction of H_2O (e) Mass fraction of CO (f) Mass fraction of OH

Figure 5.12. Contour maps from the non-adiabatic CSE-TGLDM model for the Case C.

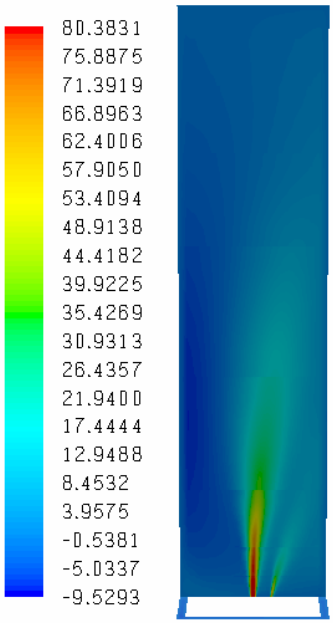

(a) z-velocity(m/s)

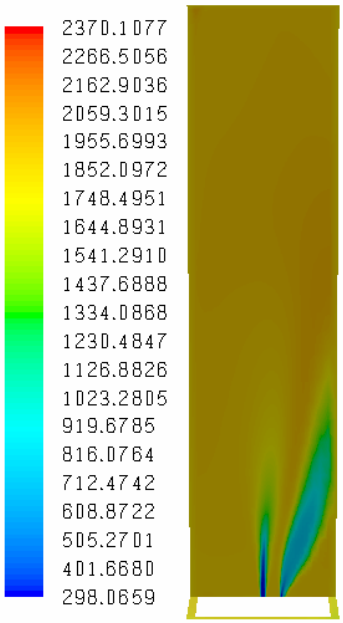

(b) Temperature(K)

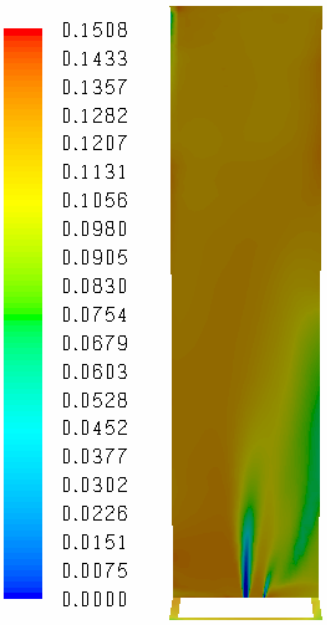

(c) Mass fraction of CO_2

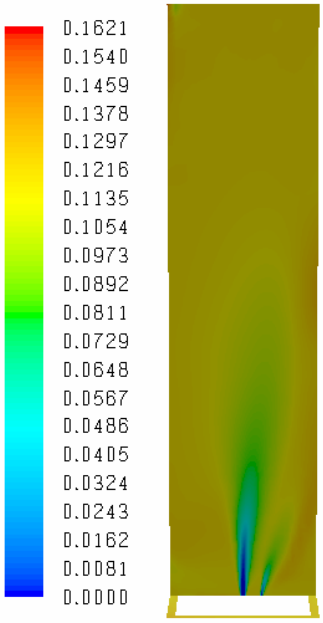

(d) Mass fraction of H_2O

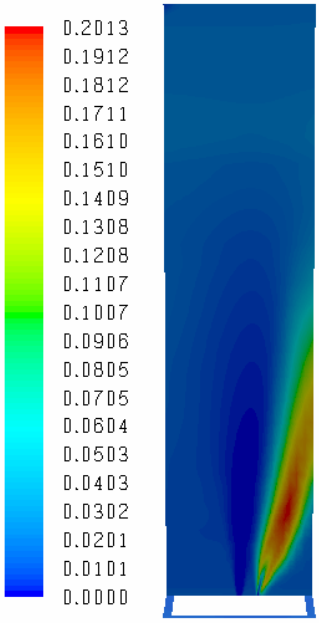

(e) Mass fraction of CO

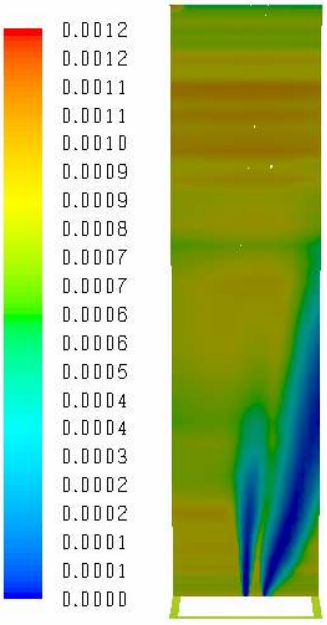

(f) Mass fraction of OH

Figure 5.13. Contour maps from the non-adiabatic CSE-TGLDM model for the Case D.

The temperature and concentration profiles for CO_2, O_2, CH_4 and CO based on the four combustion models are compared with experimental data for each sampling line and downstream position for the four cases in Figure 5.14 ~ Figure 5.25.

The temperature field for the recirculated combustion products was highly over-predicted with all four combustion models. This was also true for two non-adiabatic simulations, although there was less discrepancy for the non-adiabatic CSE-TGLDM model. A few of reasons for this discrepancy can be discussed. Firstly, the wall heat loss of 2000 W/m^2 used in the simulation might be poorly estimated, inconsistent with the experimental running condition. Secondly, it might be an over-simplified assumption that the non-adiabatic temperature in the CSE-TGLDM and flamelet models was estimated based on the adiabatic mixture composition, described in sections 2.4.2 and 5.3.4. In other words, the original statistical equation to estimate temperature in the non-adiabatic CSE-TGLDM model,

$$\tilde{T} = \int_{-\infty}^{\infty}\int_0^1\int_0^1\int_0^1 T(\eta, h, Y_{CO_2}, Y_{H_2O})\tilde{P}(\eta, h, Y_{CO_2}, Y_{H_2O})dY_{CO_2}dY_{H_2O}d\eta dh \tag{5.13}$$

was simplified into the working equations,

$$\begin{aligned} &\tilde{Y}_j = \int_0^1 Y_j(\eta, Y_{CO_2}, Y_{H_2O})\tilde{P}(\eta)d\eta,\ j = 1,\ldots,n, \\ &\tilde{T} = f_h(\overline{p}, \tilde{h}, \tilde{Y}_1, \tilde{Y}_2, \ldots, \tilde{Y}_n) \end{aligned}. \tag{5.14}$$

Lastly, it might be inappropriate that the equilibrium state be assigned, for the 26 mixture fraction points, above 0.0800 (see subsection 5.3.2) because there were no reliable TGLDM lookup tables for this fuel-rich range (see Chapter 4). That is, in Eq.(5.14),

$$Y_j(\eta, Y_{CO_2}, Y_{H_2O}) = Y_j^e(\eta) \quad \text{for } \eta > 0.0800 \tag{5.15}$$

The predicted CH_4 concentration profiles along sampling lines 1 and 3 show that the fuel jet stream for Case A and C has merged into the air jet stream before the downstream position z = 182 mm. This effect can also be observed in the contour plots, Figure 5.10 and Figure 5.12. However, at z = 182 mm, the experimental data show a distinct CH_4 peak indicating that the fuel jet is longer than the predicted results. These results also show that the non-adiabatic steady flamelet model predicted higher CH_4 concentrations than other the combustion models. This may be because the scalar dissipation that is used as important variable in the flamelet model was relatively high inside the jets, so a relatively incomplete combustion state was achieved.

The RANS simulations provided expected trends and reasonable predictions for the concentrations of the major species, CO_2, O_2 and CH_4. However, the predictions for the CO concentrations were much higher than the in-furnace measurement data.

The higher CO concentration predictions seem to arise from the nature of the PDF/Mixing approach where the mixture fraction is employed as an important progress variable. Usually, the mixture fraction in a certain fuel-rich range is connected to high CO concentration in most hydrocarbon combustion systems. For instance, the CO concentration profile obtained from the adiabatic equilibrium state of methane-air combustion was plotted in terms of mixture fraction in Figure 5.26. The CO concentration rapidly increases as soon as the mixture fraction passes the stoichiometric value (0.05516) and maintains a high concentration level over a wide range of rich-fuel mixture fractions (maximum CO mass fraction of about 0.225 at a mixture fraction of about 0.16). As mentioned earlier, in this study the equilibrium state was assumed as the conditional mean scalar values for the mixture fraction of above 0.08000. As another example, the 2-D TGLDM corresponding to the mixture fraction of 0.07789 (below 0.0800, but still in

fuel-rich range) is plotted showing the CO concentrations in Figure 5.27 – the CO concentration values in most regions are still high. This over-prediction of the CO concentration was not evident when the EDM with a global 2-step methane-air chemical kinetic model was applied for this flameless combustion simulation [15]. The global 2-step chemical kinetic model predicted the CO concentration within a similar order of magnitude as the experimental data but it failed to predict the trend of CO concentration profile.

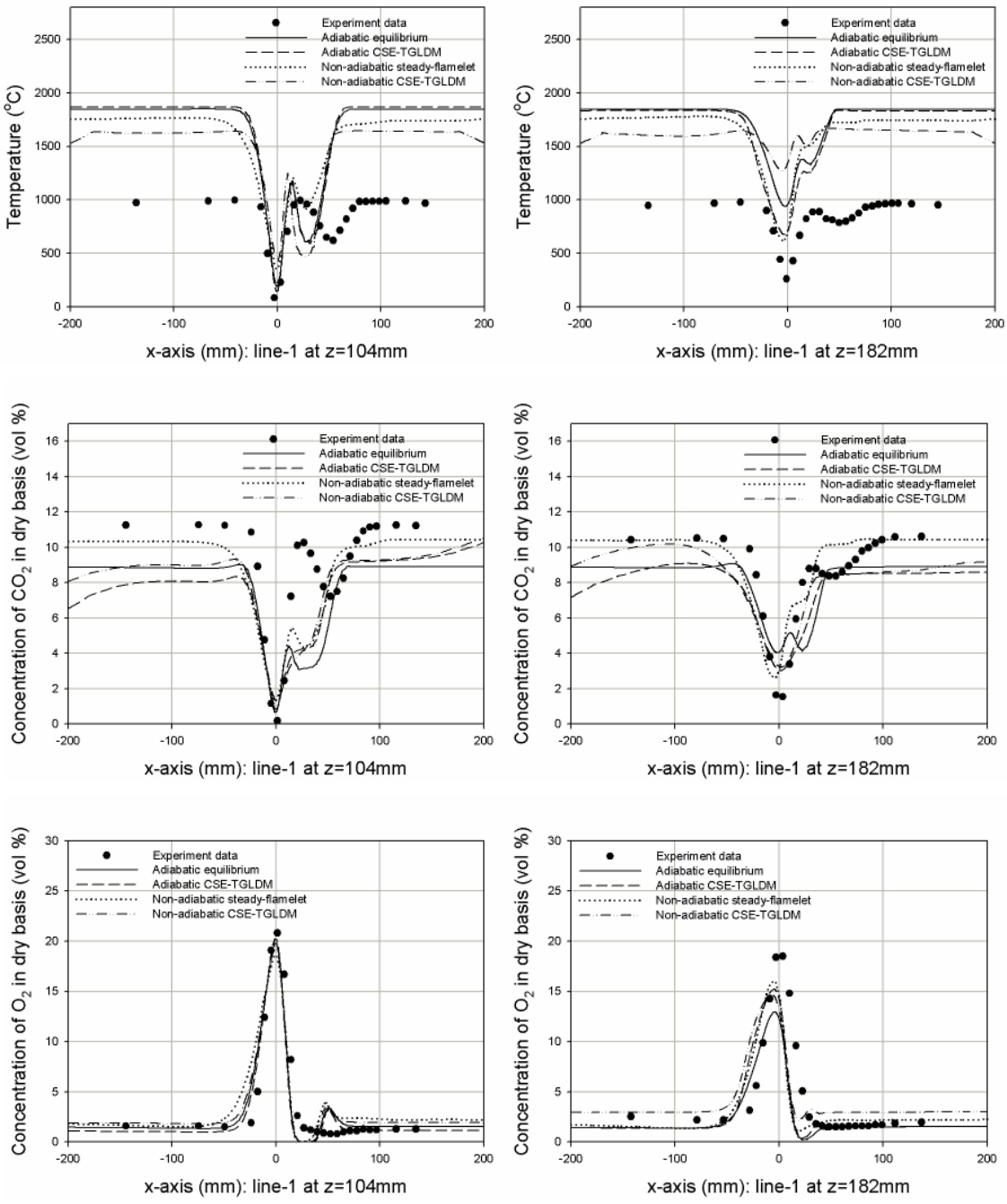
Experiment data
Adiabatic equilibrium
Adiabatic CSE-TGLDM
Non-adiabatic steady-flamelet
Non-adiabatic CSE-TGLDM
Temperature (°C)
Concentration of CO2 in dry basis (vol %)
Concentration of O2 in dry basis (vol %)
x-axis (mm): line-1 at z=104mm
x-axis (mm): line-1 at z=182mm

(continued)

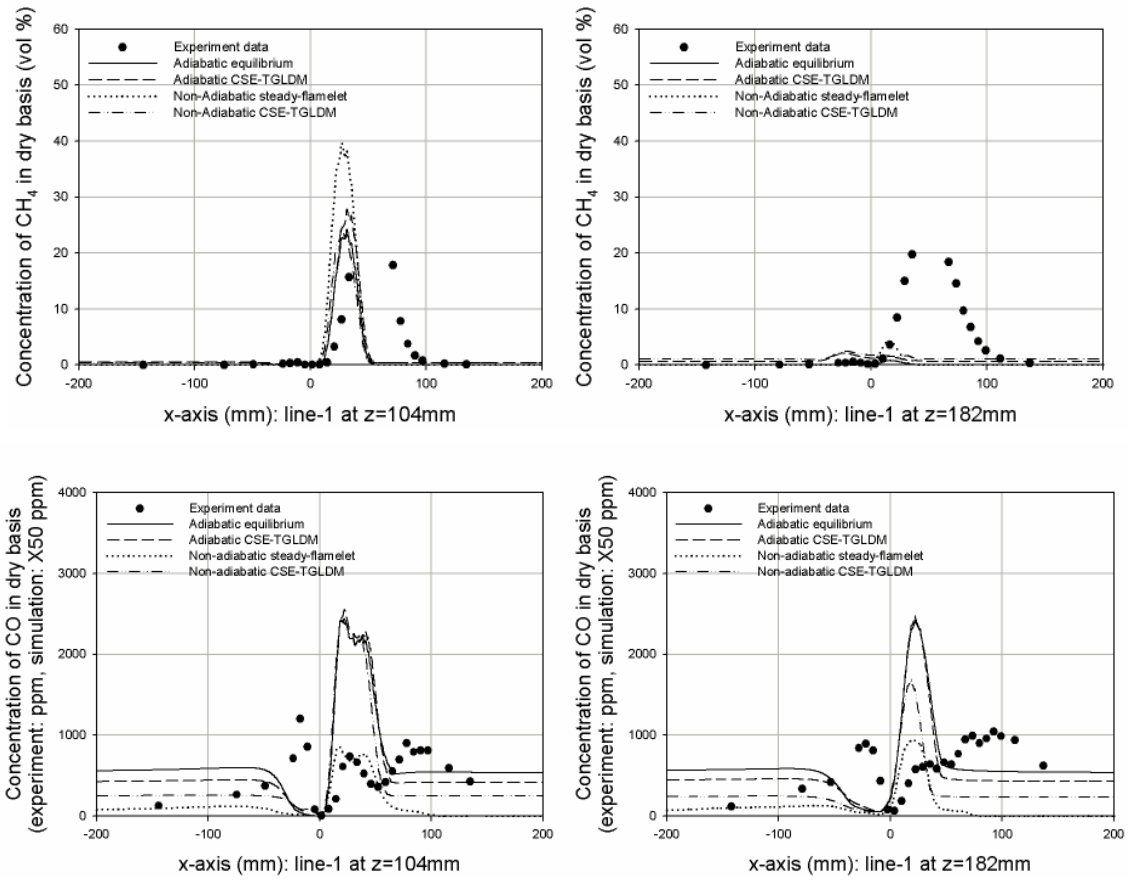

Figure 5.14. Comparisons of in-furnace measurements and RANS simulations at the sampling line 1 for Case A.

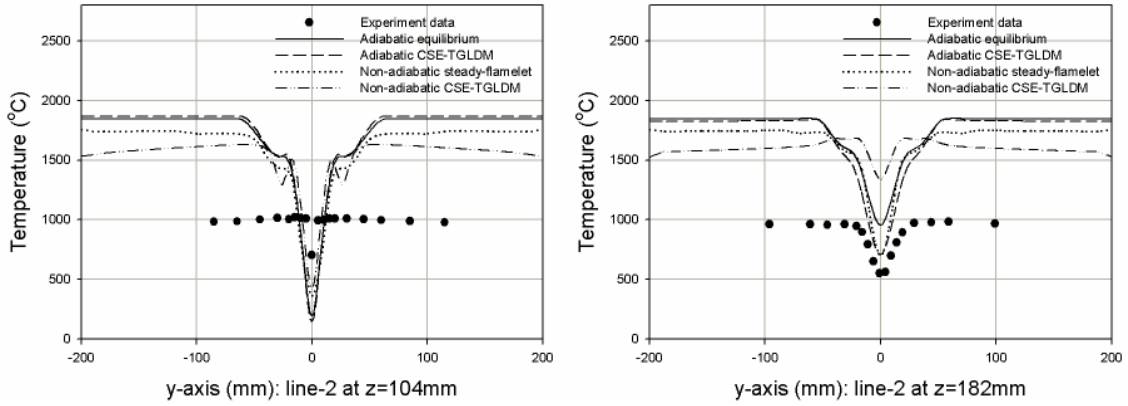

(continued)

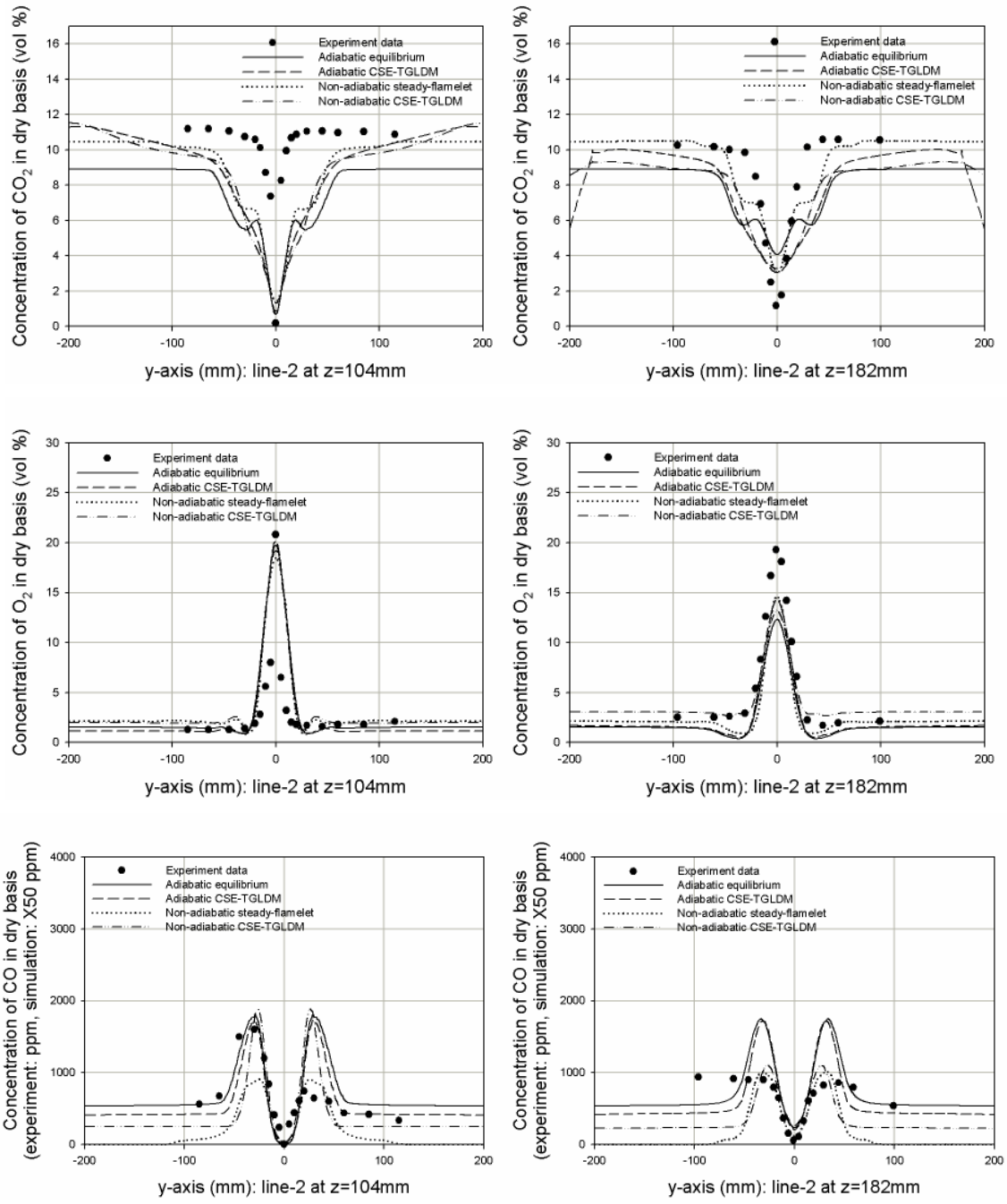

Figure 5.15. Comparisons of in-furnace measurements and RANS simulations at the sampling line 2 for Case A.

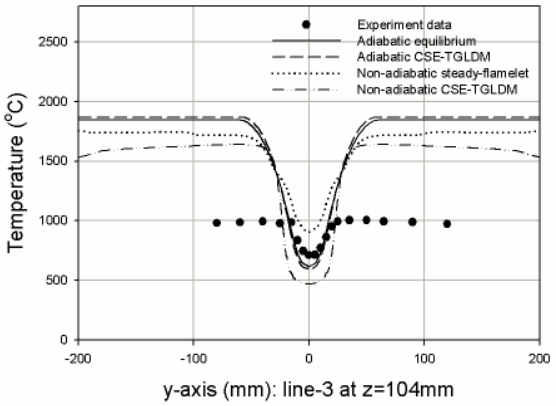
Experiment data
Adiabatic equilibrium
Adiabatic CSE-TGLDM
Non-adiabatic steady-flamelet
Non-adiabatic CSE-TGLDM
Temperature (°C)
y-axis (mm): line-3 at z=104mm

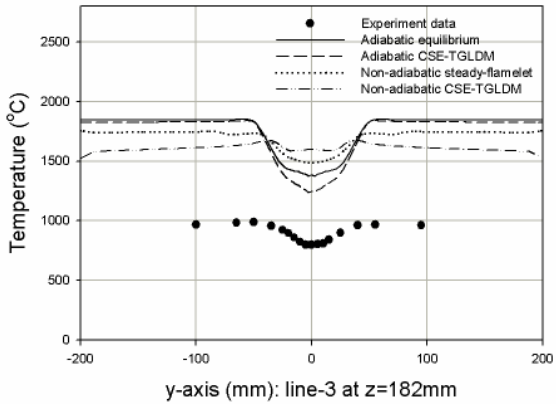
Experiment data
Adiabatic equilibrium
Adiabatic CSE-TGLDM
Non-adiabatic steady-flamelet
Non-adiabatic CSE-TGLDM
Temperature (°C)
y-axis (mm): line-3 at z=182mm

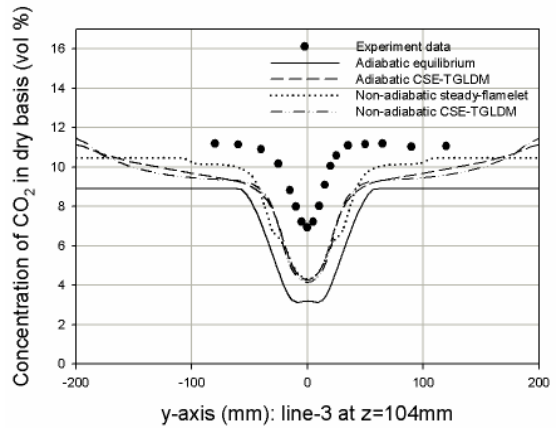
Experiment data
Adiabatic equilibrium
Adiabatic CSE-TGLDM
Non-adiabatic steady-flamelet
Non-adiabatic CSE-TGLDM
Concentration of CO2 in dry basis (vol %)
y-axis (mm): line-3 at z=104mm

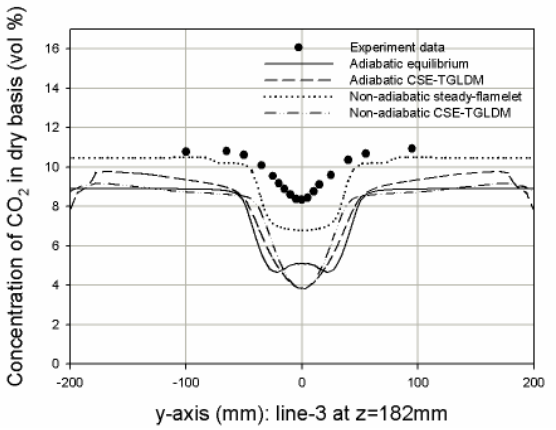
Experiment data
Adiabatic equilibrium
Adiabatic CSE-TGLDM
Non-adiabatic steady-flamelet
Non-adiabatic CSE-TGLDM
Concentration of CO2 in dry basis (vol %)
y-axis (mm): line-3 at z=182mm

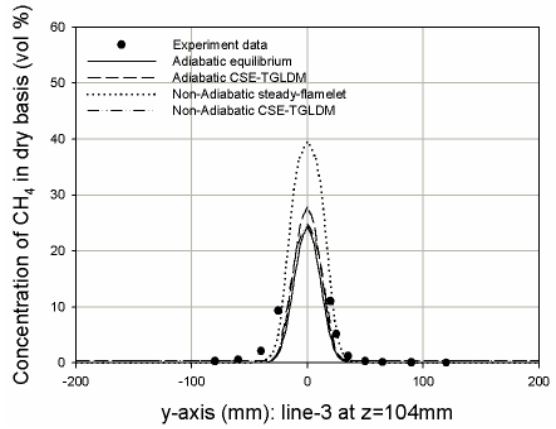
Experiment data
Adiabatic equilibrium
Adiabatic CSE-TGLDM
Non-Adiabatic steady-flamelet
Non-Adiabatic CSE-TGLDM
Concentration of CH4 in dry basis (vol %)
y-axis (mm): line-3 at z=104mm

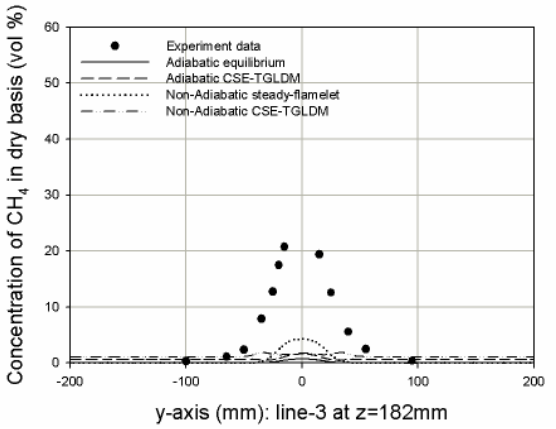
Experiment data
Adiabatic equilibrium
Adiabatic CSE-TGLDM
Non-Adiabatic steady-flamelet
Non-Adiabatic CSE-TGLDM
Concentration of CH4 in dry basis (vol %)
y-axis (mm): line-3 at z=182mm

(continued)

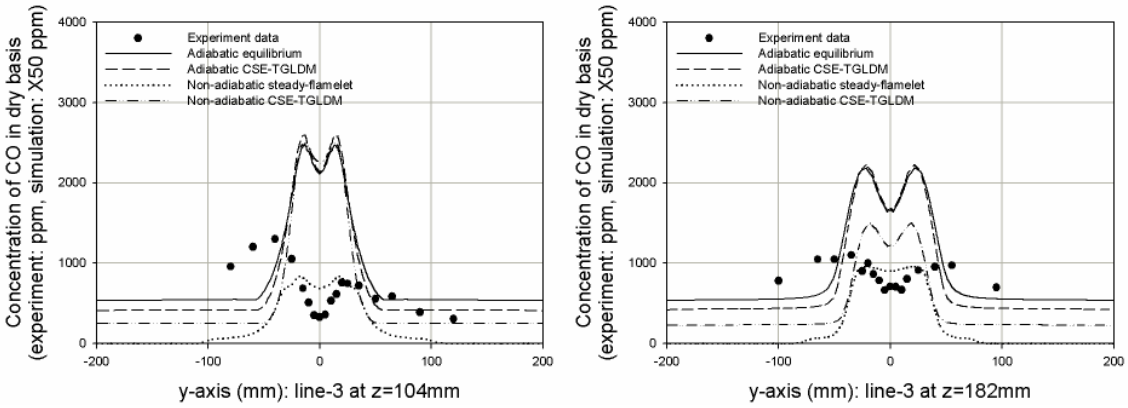

Figure 5.16. Comparisons of in-furnace measurements and RANS simulations at the sampling line 3 for Case A.

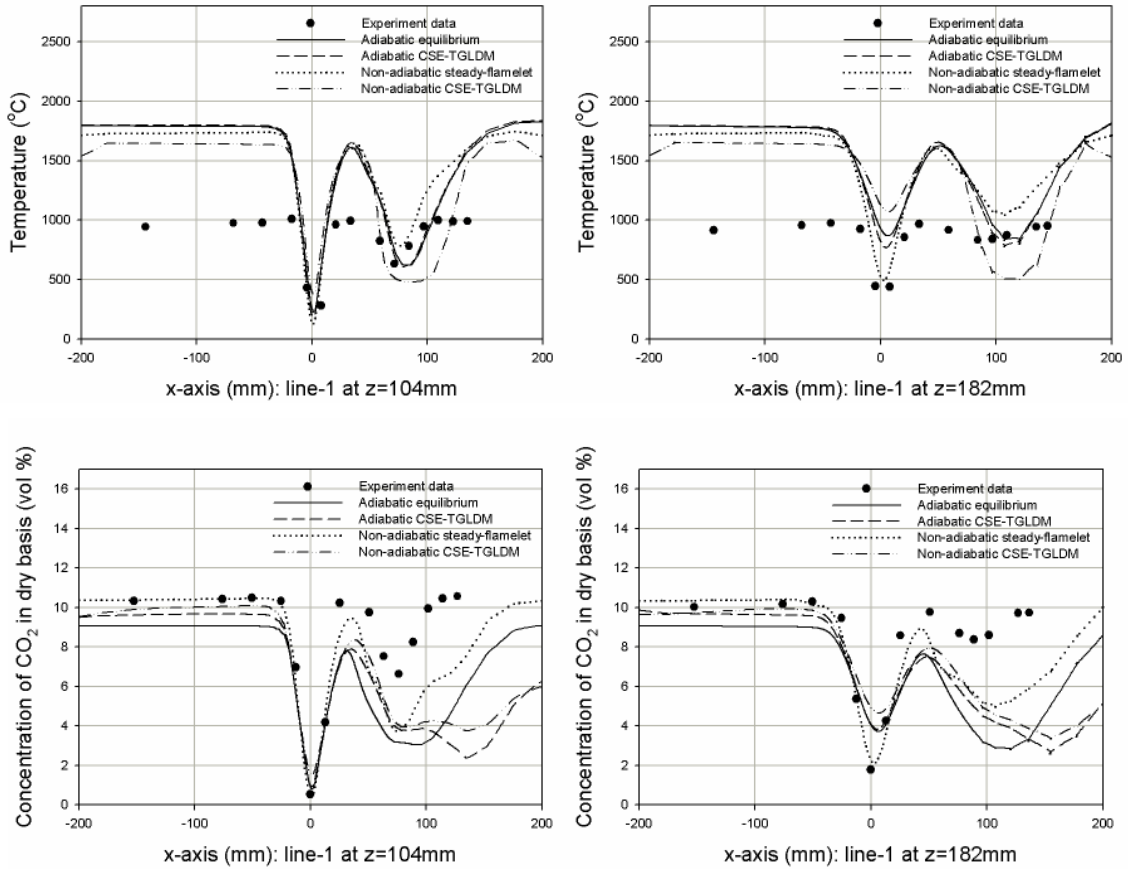

(continued)

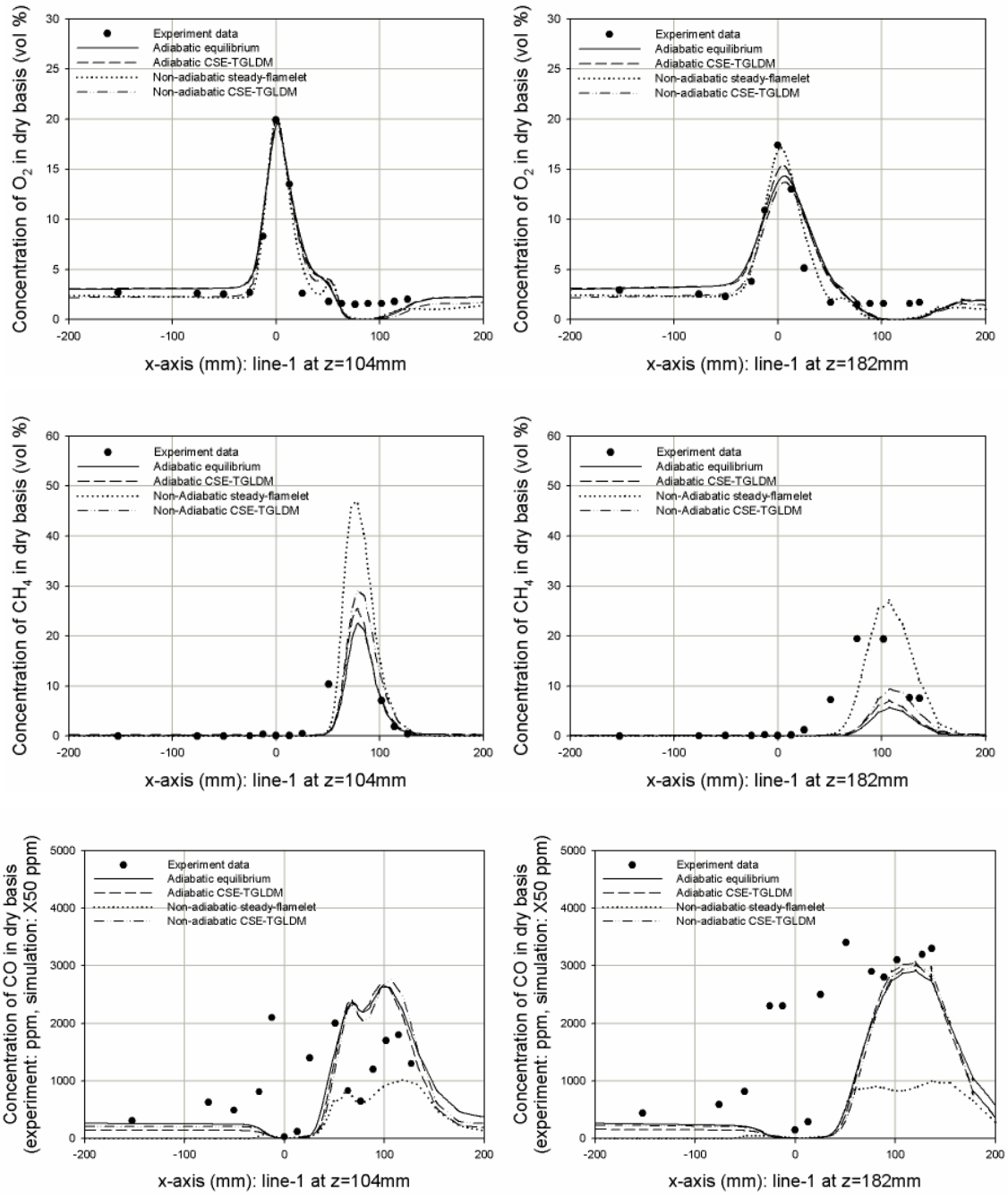

Figure 5.17. Comparisons of in-furnace measurements and RANS simulations at the sampling line 1 for Case B.

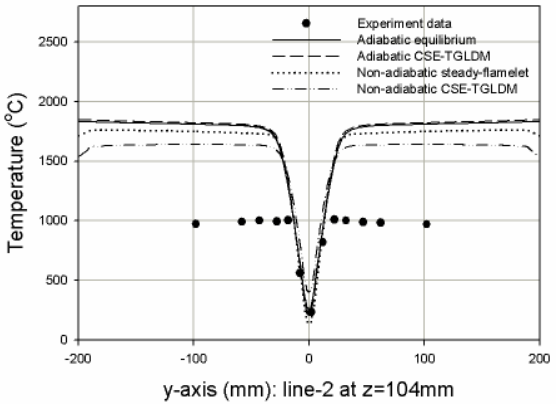
Experiment data
Adiabatic equilibrium
Adiabatic CSE-TGLDM
Non-adiabatic steady-flamelet
Non-adiabatic CSE-TGLDM
Temperature (°C)
y-axis (mm): line-2 at z=104mm

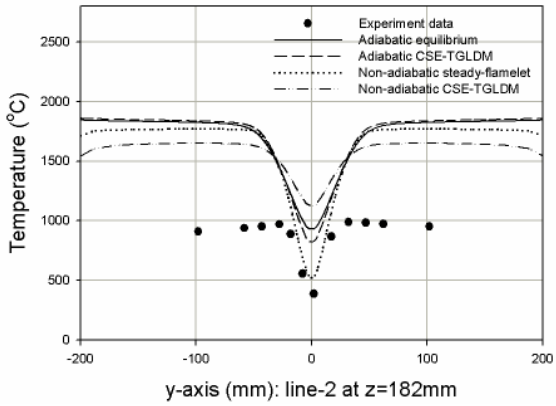
Experiment data
Adiabatic equilibrium
Adiabatic CSE-TGLDM
Non-adiabatic steady-flamelet
Non-adiabatic CSE-TGLDM
Temperature (°C)
y-axis (mm): line-2 at z=182mm

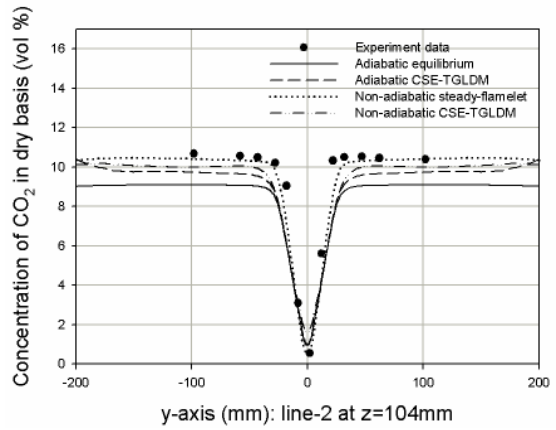
Experiment data
Adiabatic equilibrium
Adiabatic CSE-TGLDM
Non-adiabatic steady-flamelet
Non-adiabatic CSE-TGLDM
Concentration of CO2 in dry basis (vol %)
y-axis (mm): line-2 at z=104mm

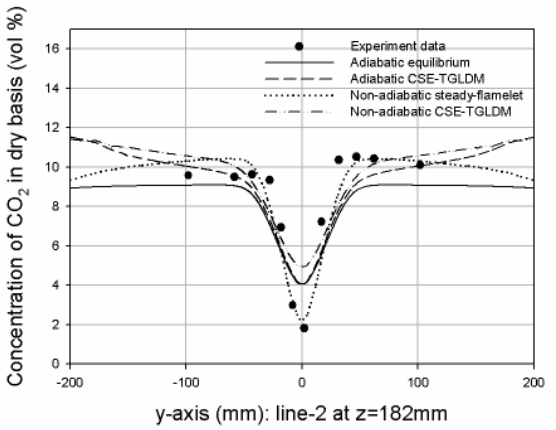
Experiment data
Adiabatic equilibrium
Adiabatic CSE-TGLDM
Non-adiabatic steady-flamelet
Non-adiabatic CSE-TGLDM
Concentration of CO2 in dry basis (vol %)
y-axis (mm): line-2 at z=182mm

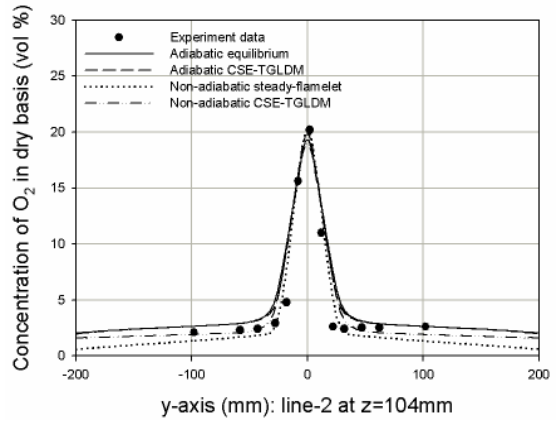
Experiment data
Adiabatic equilibrium
Adiabatic CSE-TGLDM
Non-adiabatic steady-flamelet
Non-adiabatic CSE-TGLDM
Concentration of O2 in dry basis (vol %)
y-axis (mm): line-2 at z=104mm

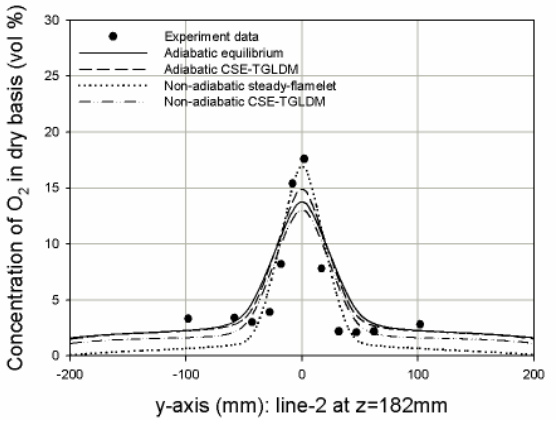
Experiment data
Adiabatic equilibrium
Adiabatic CSE-TGLDM
Non-adiabatic steady-flamelet
Non-adiabatic CSE-TGLDM
Concentration of O2 in dry basis (vol %)
y-axis (mm): line-2 at z=182mm

(continued)

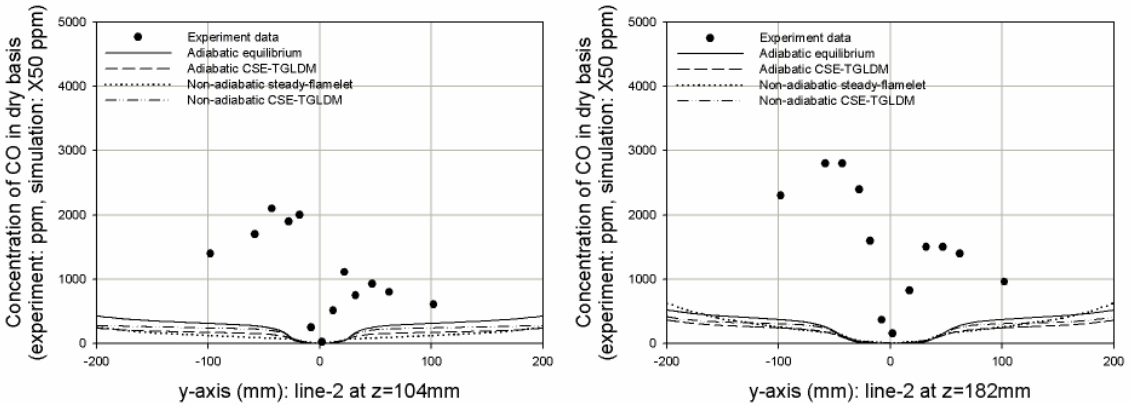

Figure 5.18. Comparisons of in-furnace measurements and RANS simulations at the sampling line 2 for Case B.

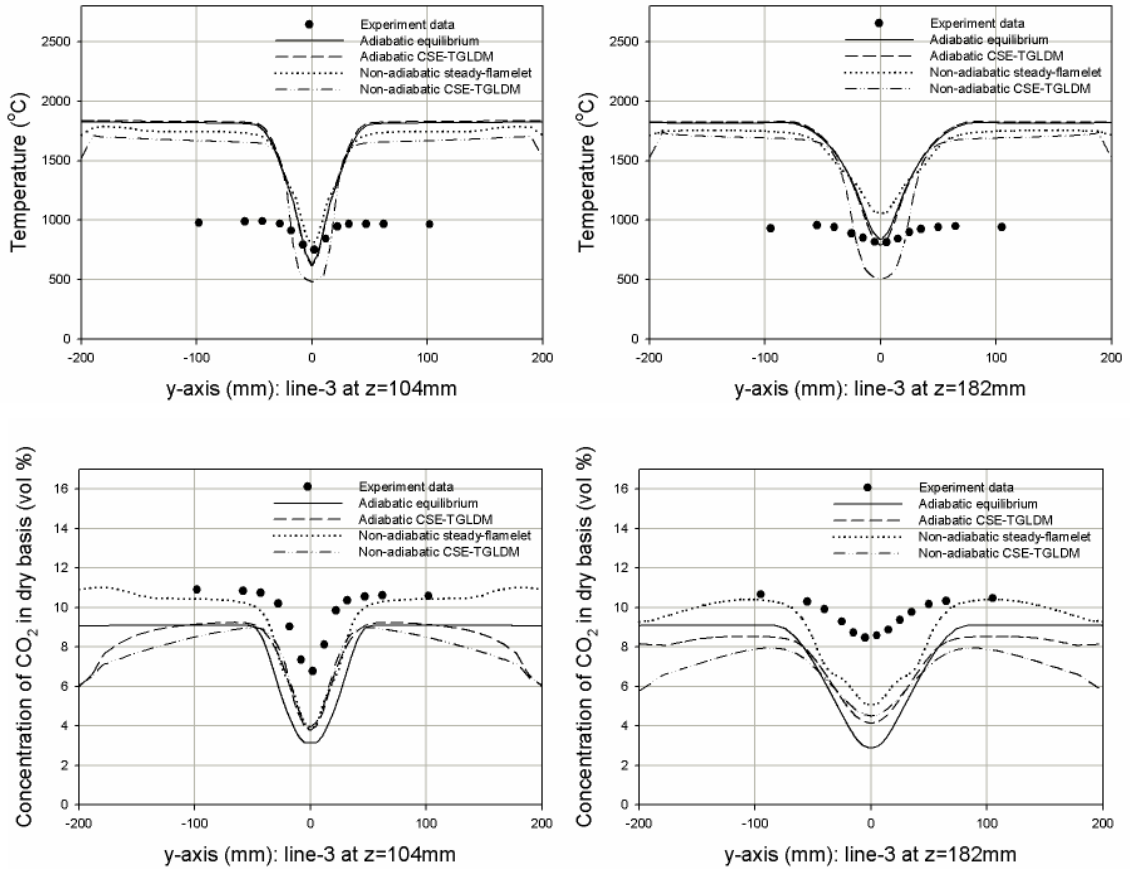

(continued)

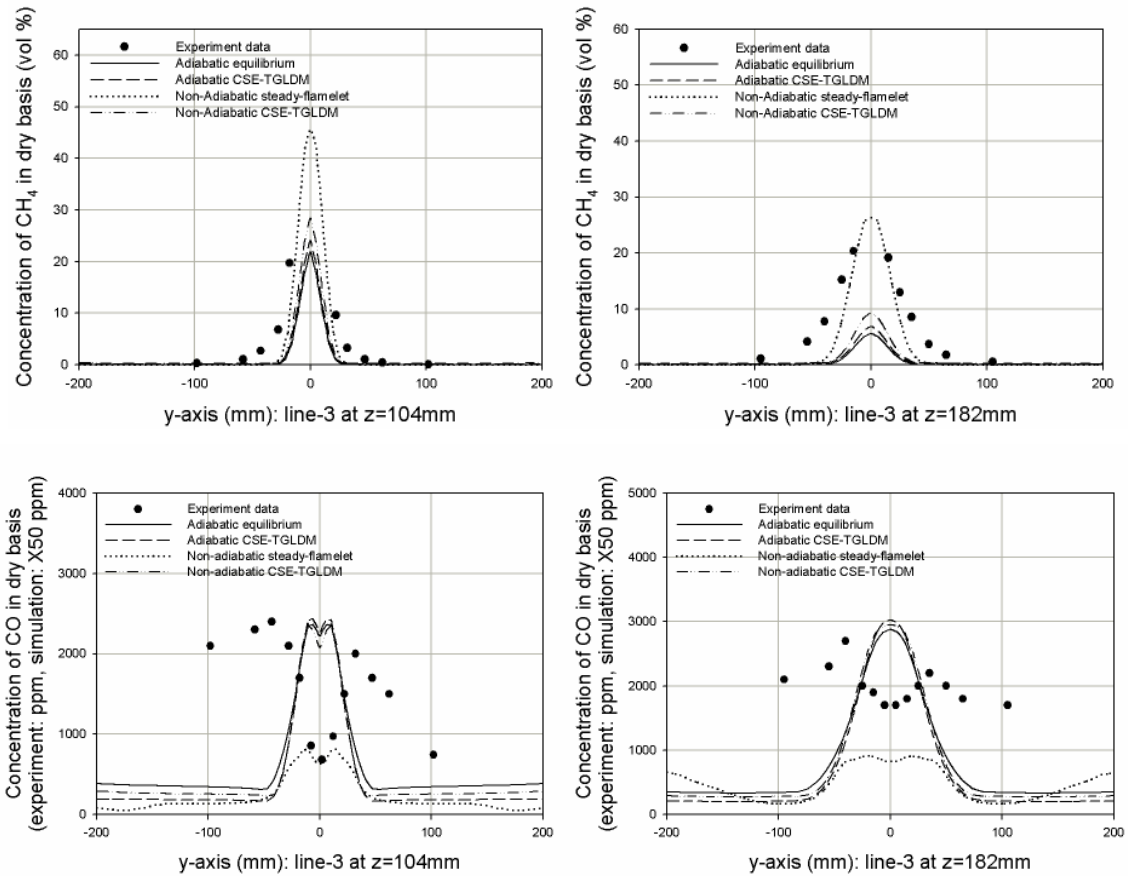

Figure 5.19. Comparisons of in-furnace measurements and RANS simulations at the sampling line 3 for Case B.

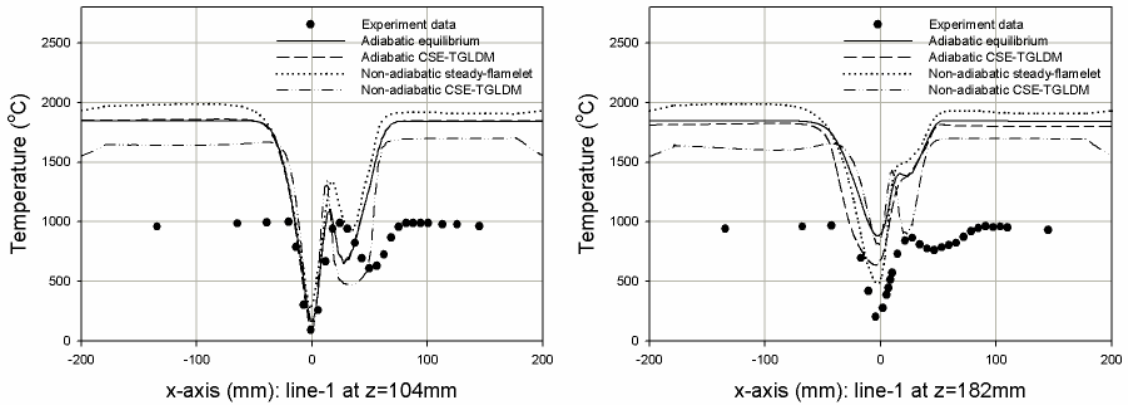

(continued)

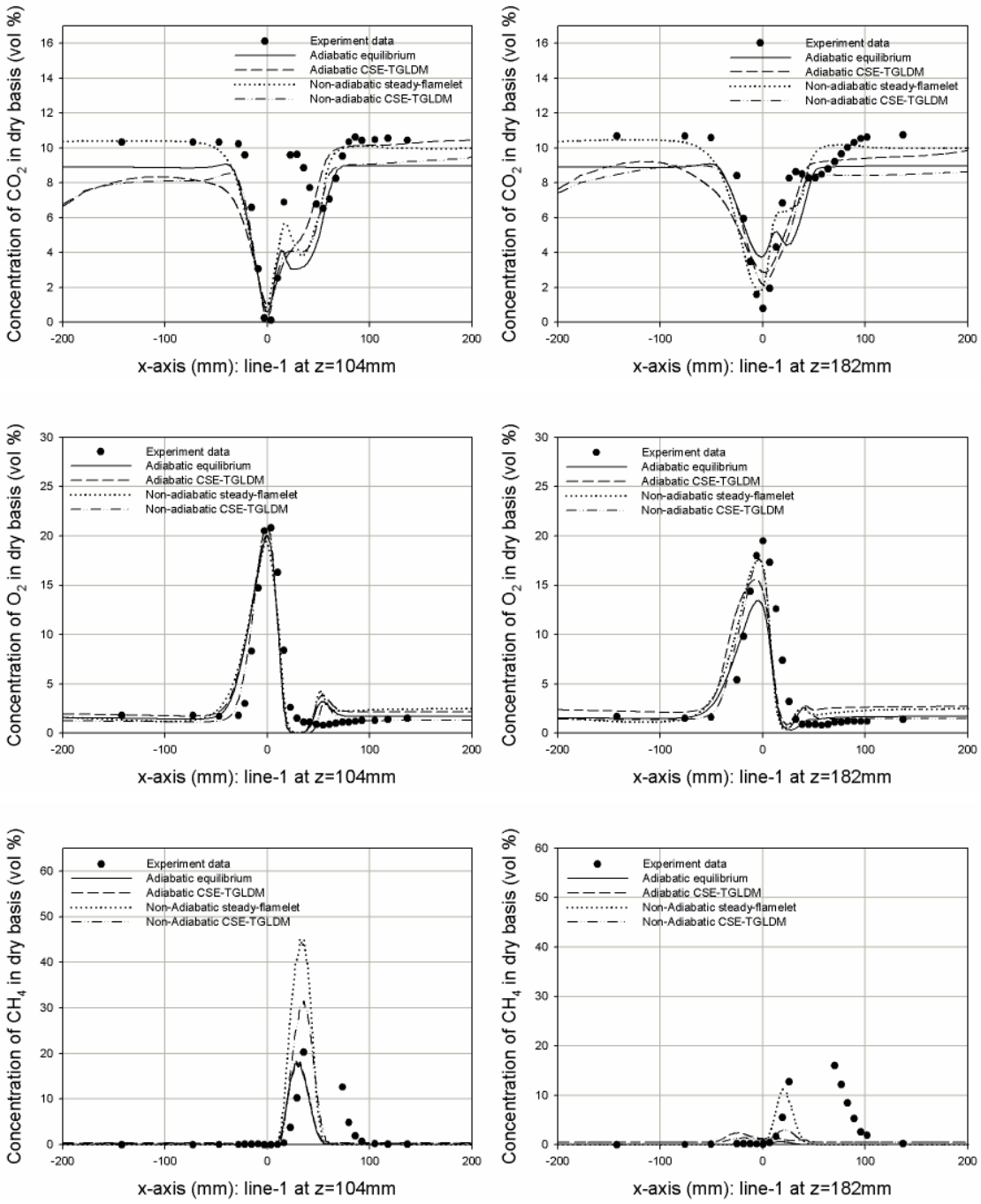
Concentration of CO_2 in dry basis (vol %)
Experiment data
Adiabatic equilibrium
Adiabatic CSE-TGLDM
Non-adiabatic steady-flamelet
Non-adiabatic CSE-TGLDM
x-axis (mm): line-1 at z=104mm
x-axis (mm): line-1 at z=182mm
Concentration of O_2 in dry basis (vol %)
Concentration of CH_4 in dry basis (vol %)
Non-Adiabatic steady-flamelet
Non-Adiabatic CSE-TGLDM

(continued)

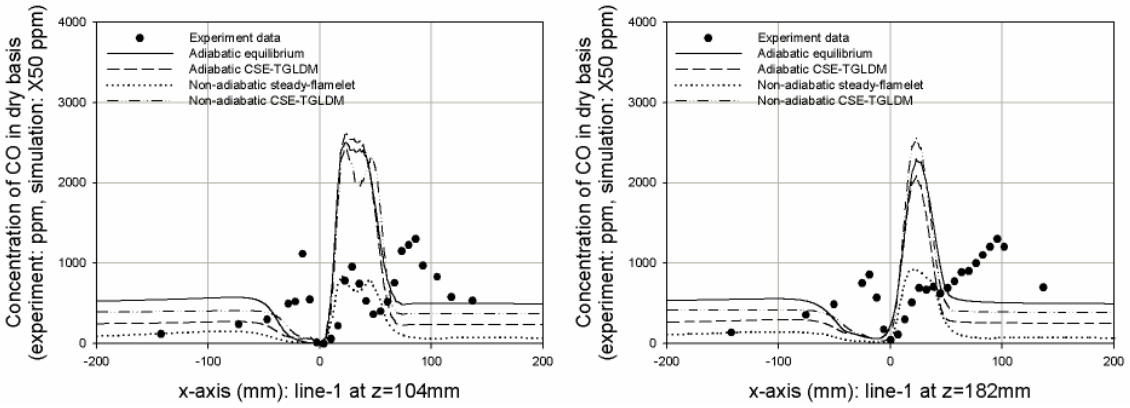

Figure 5.20. Comparisons of in-furnace measurements and RANS simulations at the sampling line 1 for Case C.

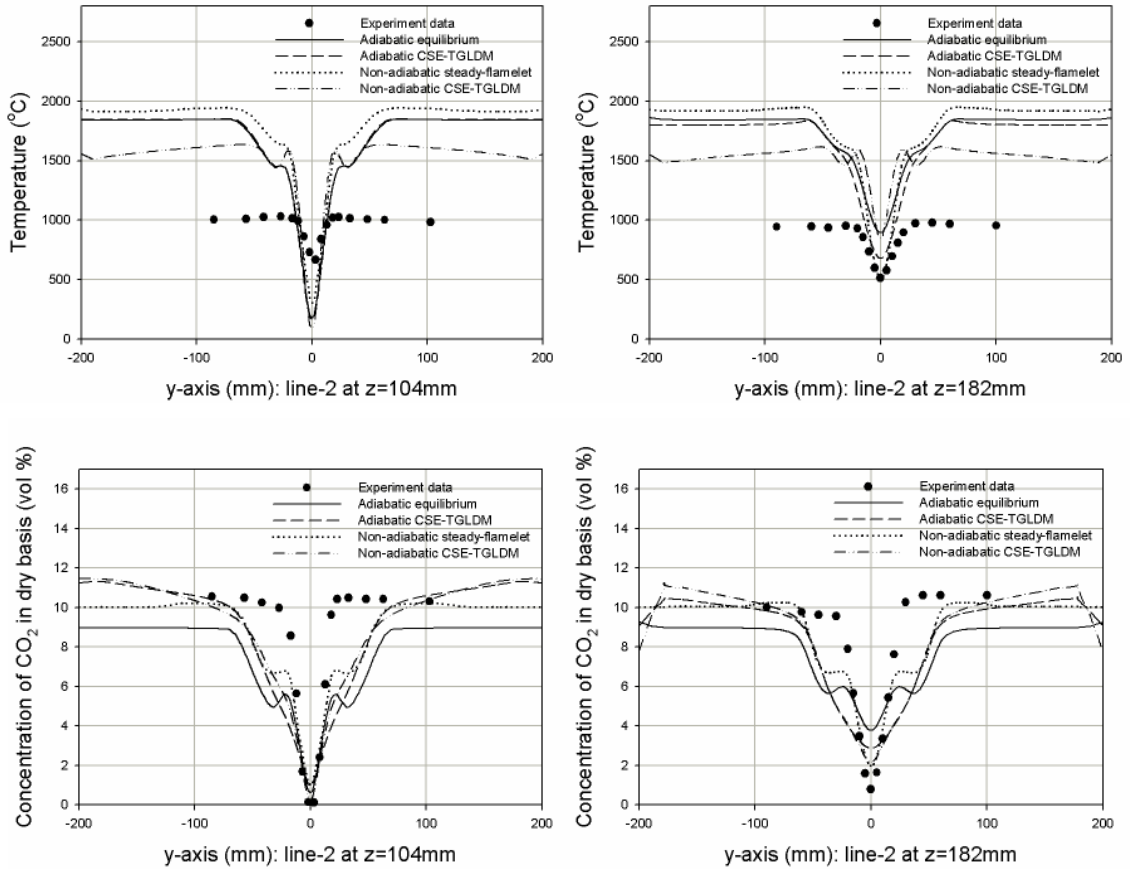

(continued)

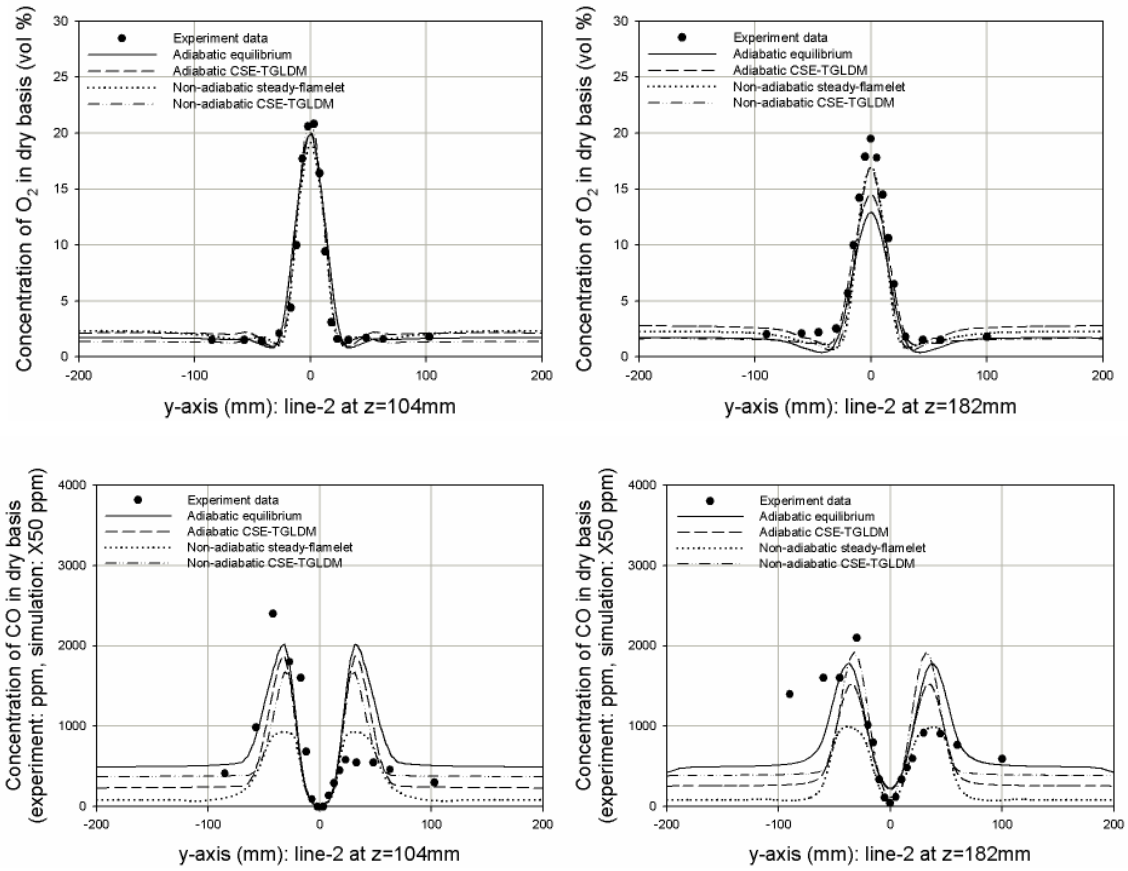

Figure 5.21. Comparisons of in-furnace measurements and RANS simulations at the sampling line 2 for Case C.

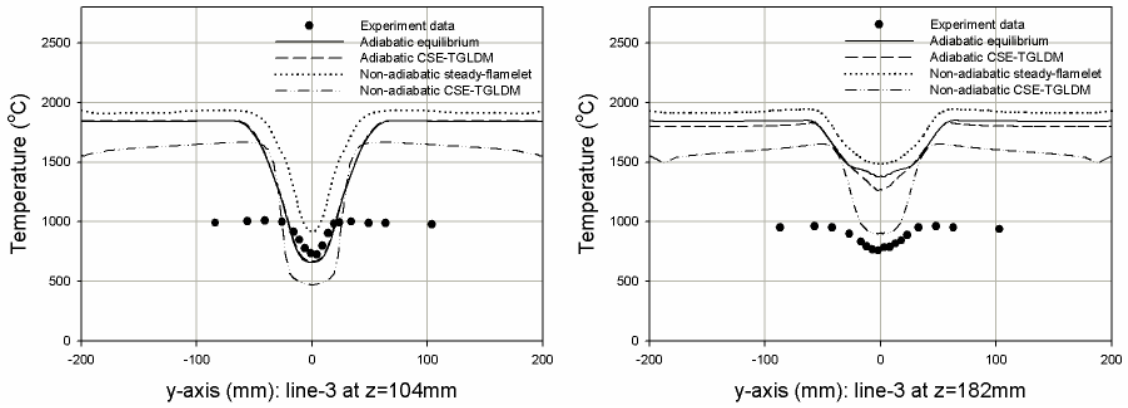

(continued)

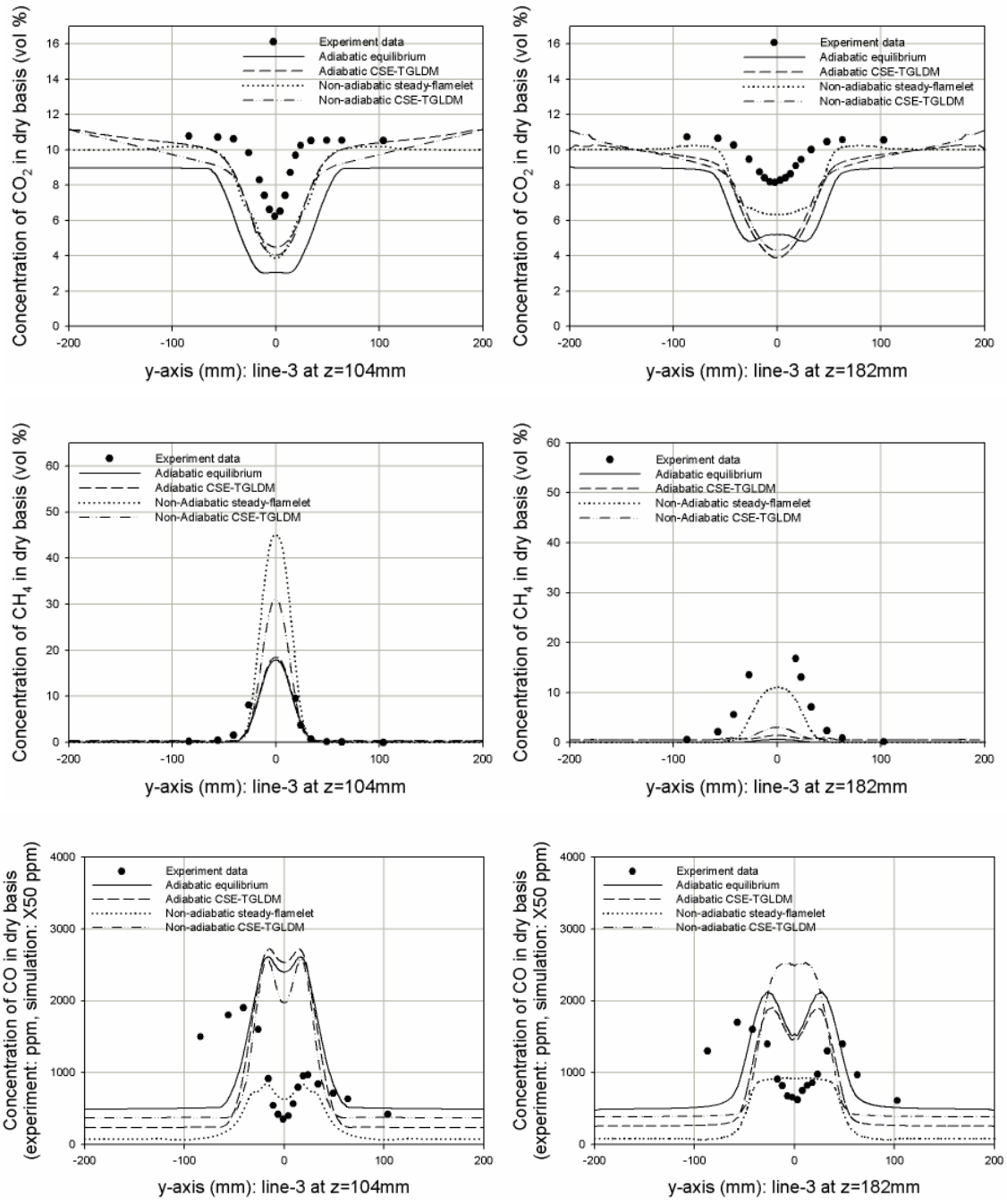

Figure 5.22. Comparisons of in-furnace measurements and RANS simulations at the sampling line 3 for Case C.

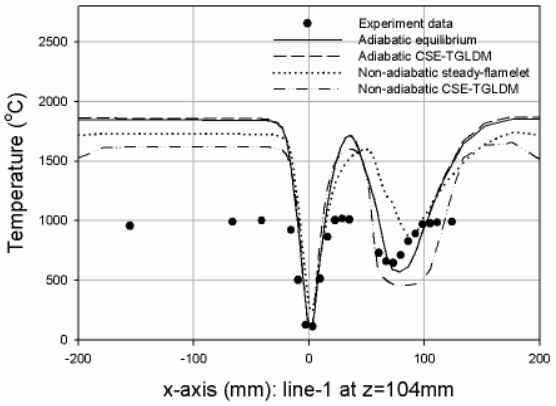
Experiment data
Adiabatic equilibrium
Adiabatic CSE-TGLDM
Non-adiabatic steady-flamelet
Non-adiabatic CSE-TGLDM
Temperature (°C)
x-axis (mm): line-1 at z=104mm

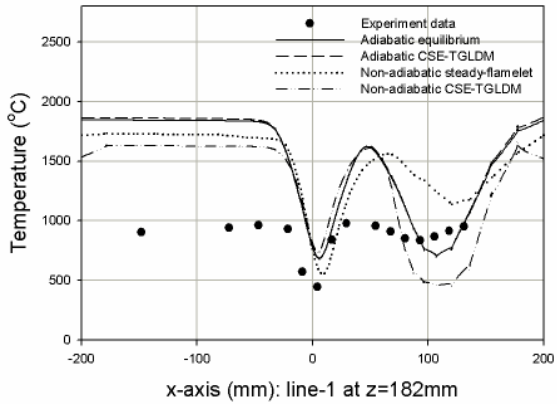
Experiment data
Adiabatic equilibrium
Adiabatic CSE-TGLDM
Non-adiabatic steady-flamelet
Non-adiabatic CSE-TGLDM
Temperature (°C)
x-axis (mm): line-1 at z=182mm

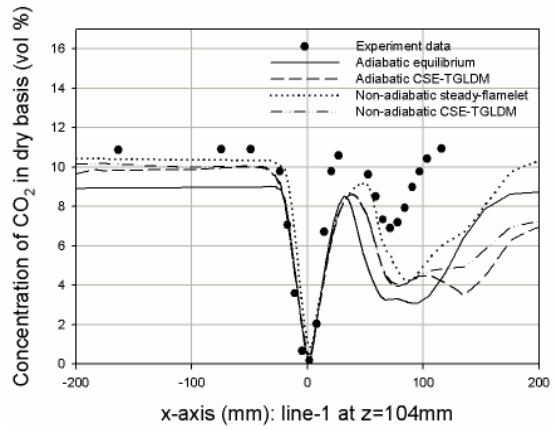
Experiment data
Adiabatic equilibrium
Adiabatic CSE-TGLDM
Non-adiabatic steady-flamelet
Non-adiabatic CSE-TGLDM
Concentration of CO2 in dry basis (vol %)
x-axis (mm): line-1 at z=104mm

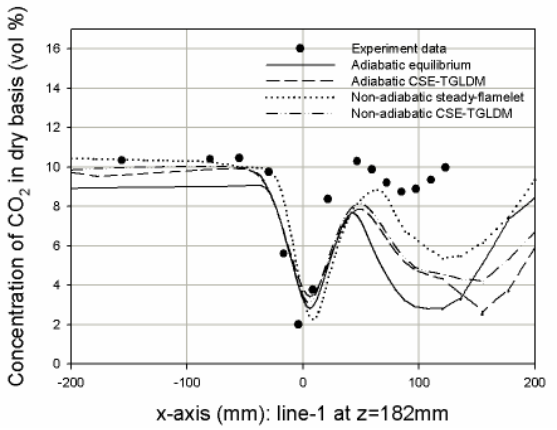
Experiment data
Adiabatic equilibrium
Adiabatic CSE-TGLDM
Non-adiabatic steady-flamelet
Non-adiabatic CSE-TGLDM
Concentration of CO2 in dry basis (vol %)
x-axis (mm): line-1 at z=182mm

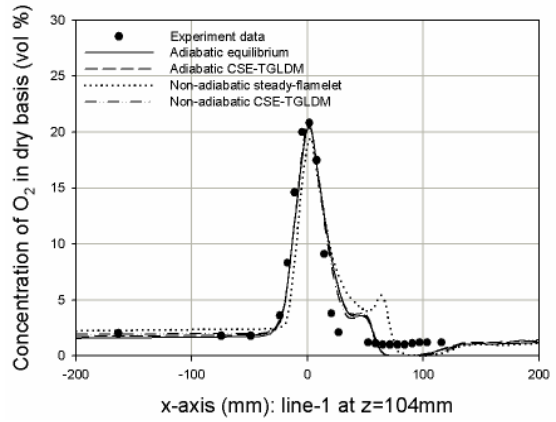
Experiment data
Adiabatic equilibrium
Adiabatic CSE-TGLDM
Non-adiabatic steady-flamelet
Non-adiabatic CSE-TGLDM
Concentration of O2 in dry basis (vol %)
x-axis (mm): line-1 at z=104mm

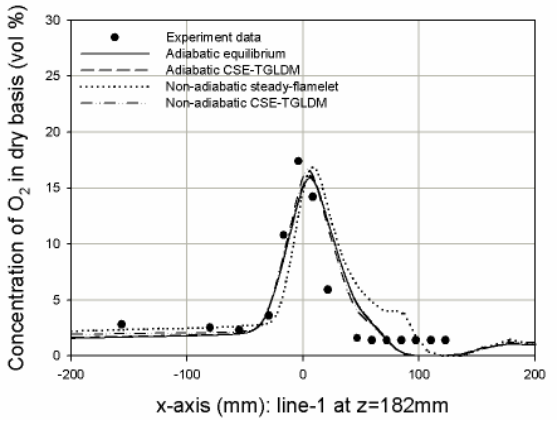
Experiment data
Adiabatic equilibrium
Adiabatic CSE-TGLDM
Non-adiabatic steady-flamelet
Non-adiabatic CSE-TGLDM
Concentration of O2 in dry basis (vol %)
x-axis (mm): line-1 at z=182mm

(continued)

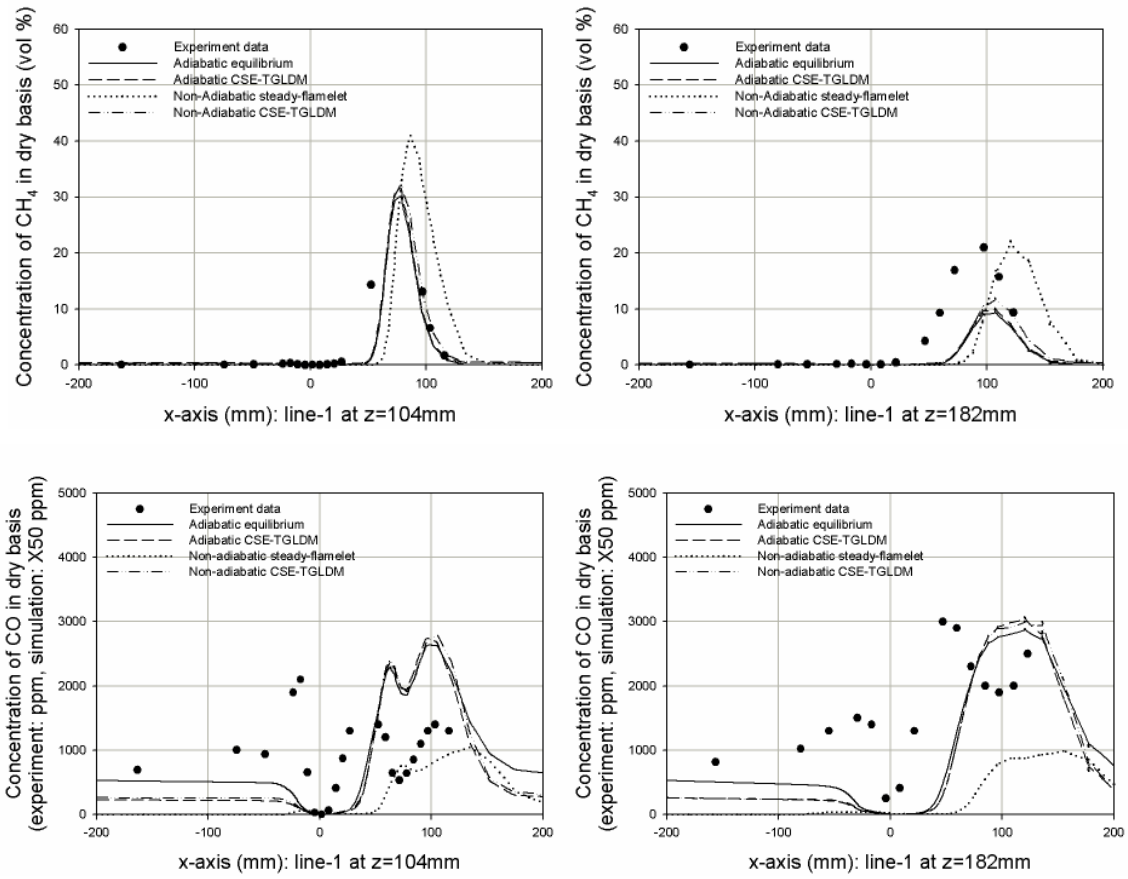

Figure 5.23. Comparisons of in-furnace measurements and RANS simulations at the sampling line 1 for Case D.

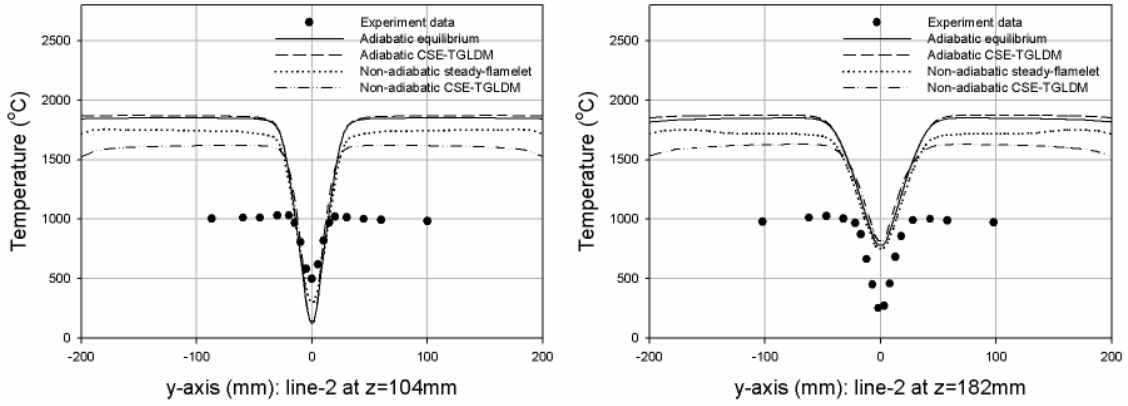

(continued)

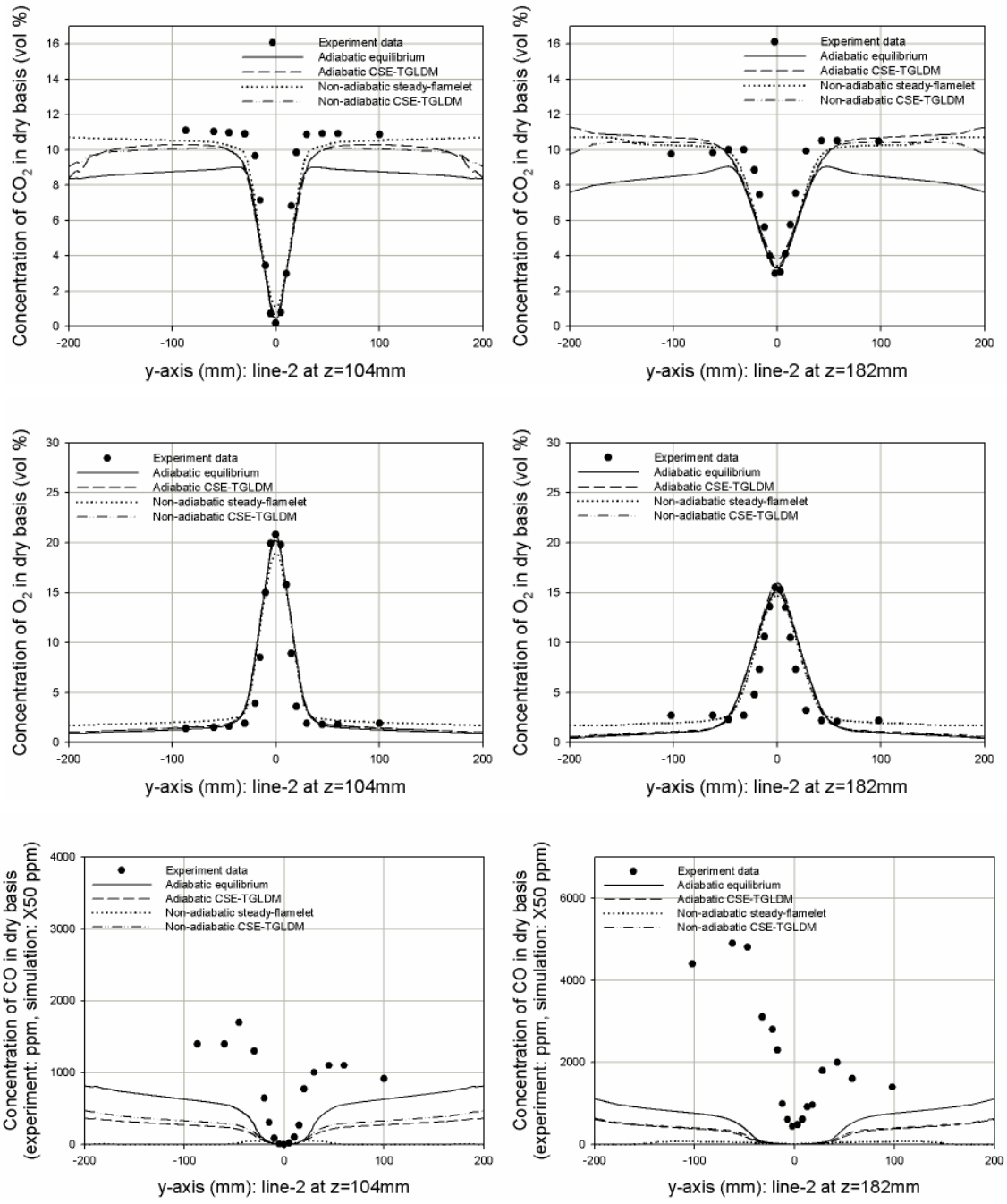

Figure 5.24. Comparisons of in-furnace measurements and RANS simulations at the sampling line 2 for Case D.

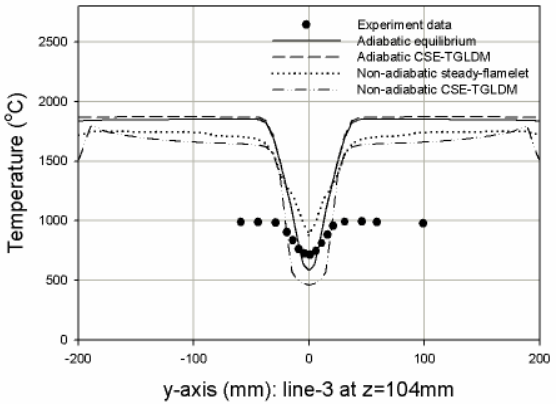
Experiment data
Adiabatic equilibrium
Adiabatic CSE-TGLDM
Non-adiabatic steady-flamelet
Non-adiabatic CSE-TGLDM
Temperature (°C)
y-axis (mm): line-3 at z=104mm

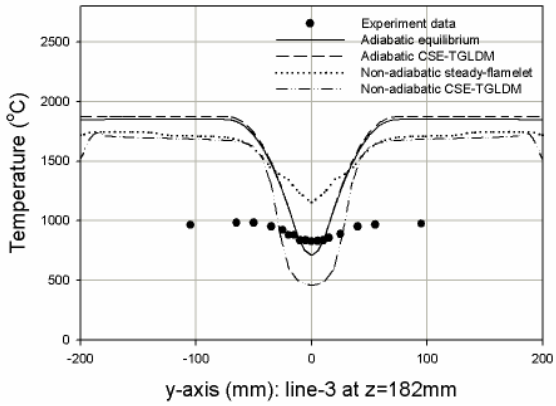
Experiment data
Adiabatic equilibrium
Adiabatic CSE-TGLDM
Non-adiabatic steady-flamelet
Non-adiabatic CSE-TGLDM
Temperature (°C)
y-axis (mm): line-3 at z=182mm

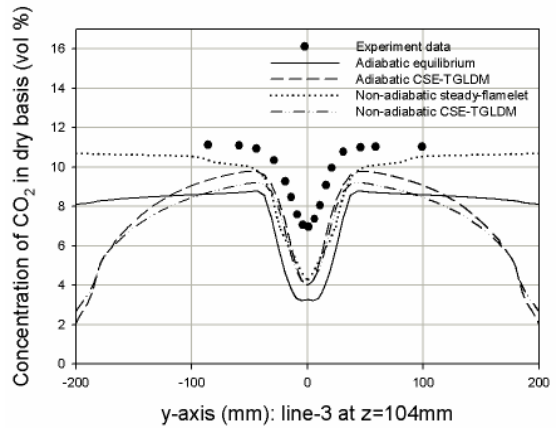
Experiment data
Adiabatic equilibrium
Adiabatic CSE-TGLDM
Non-adiabatic steady-flamelet
Non-adiabatic CSE-TGLDM
Concentration of CO2 in dry basis (vol %)
y-axis (mm): line-3 at z=104mm

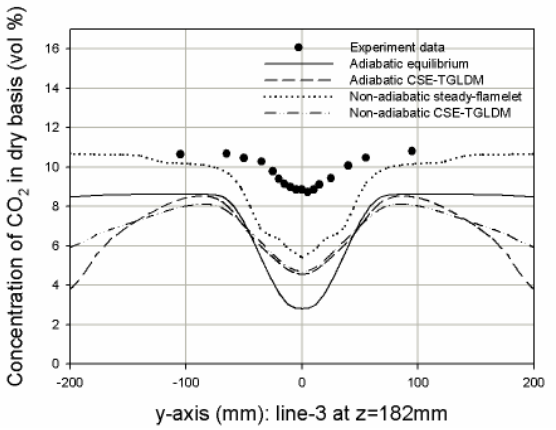
Experiment data
Adiabatic equilibrium
Adiabatic CSE-TGLDM
Non-adiabatic steady-flamelet
Non-adiabatic CSE-TGLDM
Concentration of CO2 in dry basis (vol %)
y-axis (mm): line-3 at z=182mm

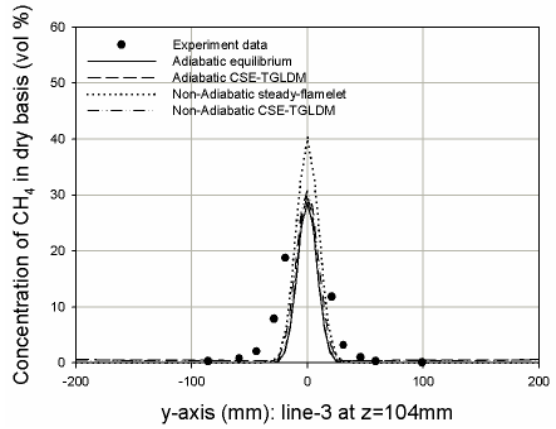
Experiment data
Adiabatic equilibrium
Adiabatic CSE-TGLDM
Non-Adiabatic steady-flamelet
Non-Adiabatic CSE-TGLDM
Concentration of CH4 in dry basis (vol %)
y-axis (mm): line-3 at z=104mm

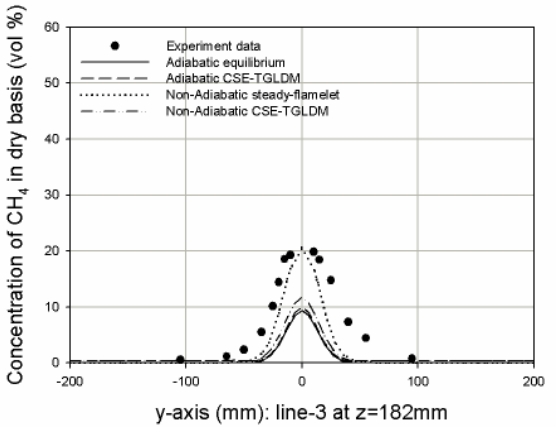
Experiment data
Adiabatic equilibrium
Adiabatic CSE-TGLDM
Non-Adiabatic steady-flamelet
Non-Adiabatic CSE-TGLDM
Concentration of CH4 in dry basis (vol %)
y-axis (mm): line-3 at z=182mm

(continued)

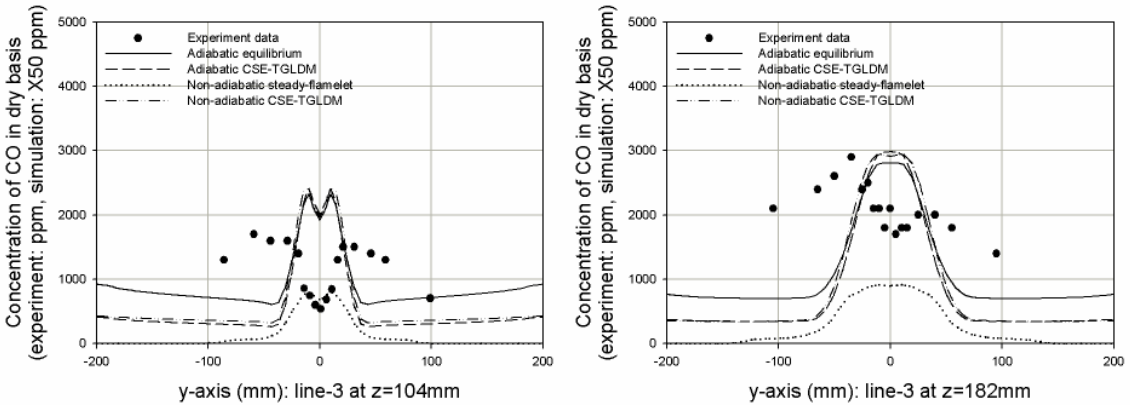

Figure 5.25. Comparisons of in-furnace measurements and RANS simulations at the sampling line 3 for Case D.

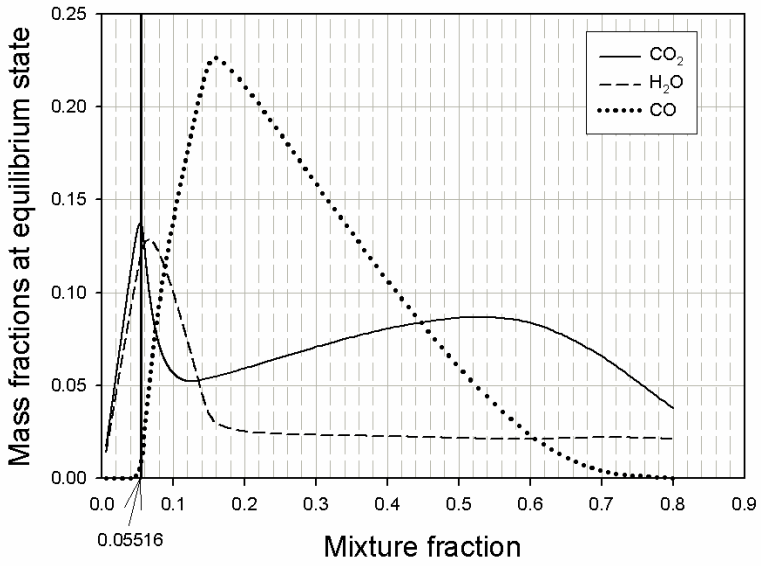

Figure 5.26. Mass fractions at equilibrium state with the mixture fraction from methane-air oxidation: stoichiometric mixture fraction is 0.05516.

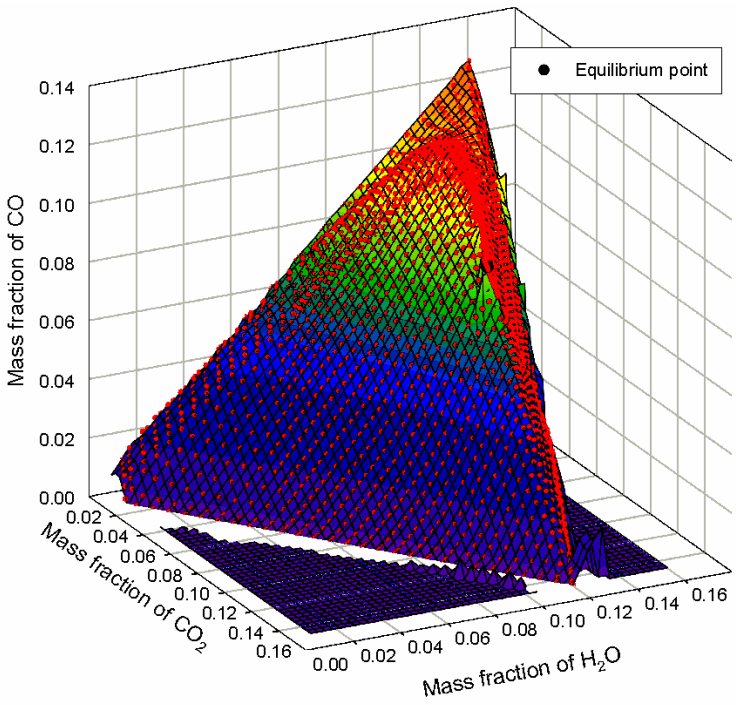

Figure 5.27. Mass fraction of CO at the mixture fraction of 0.07789. Red dot: data points of 2-D manifolds, mesh: interpolated value from the 2-D manifolds.

5.5 Conclusion

RANS simulation at steady-state was conducted for the flameless combustion of natural gas in the SJ/WJ furnace by using the novel CSE-TGLDM method, which enables us to include effects of detailed chemical reaction mechanism for combustion simulation. Other combustion models (the equilibrium chemistry model, the non-adiabatic steady flamelet model) were also used.

Experiments in the SJ/WJ furnace were conducted for flameless combustion with four different conditions. The experimental results confirmed the ultra-low NOx emission level achieved by the flameless combustion process.

All combustion models used in the RANS simulation provided good predictions of major species concentrations. However, the gas temperatures and CO concentrations were highly over-predicted. The reason may be related to the poor estimation of the wall heat loss, the over-simplified assumption for the non-adiabatic temperature, the assigned equilibrium state for the fuel-rich range and the nature of PDF/Mixing approach.

Chapter 6
Conclusion

6.1 Summary

The principal contributions of this study are

- development of the 3-D SJ/WJ physical model explaining the aerodynamic interaction of the SJ and the WJ and identifying the important design/operation factors of the 'Strong-Jet/Weak-Jet'(SJ/WJ) system,
- a significant simplification of the detailed chemical reaction mechanism (GRI-Mech 3.0) into the set of 2-D manifolds for the flameless combustion of natural gas, and
- the steady-state Reynolds-Averaged Navier-Stokes (RANS) simulation associated with the simplified flameless combustion kinetics in the SJ/WJ furnace.

Based on the results of this work the following conclusions can be made:

Development of the 3-D SJ/WJ physical model:

1. A general 3-D physical model was formulated for the isothermal, free, multiple-jet system by using the Lagrangian perspective.
2. The 3-D physical model was applied to the SJ/WJ configuration and validated by cold model experimentation.

3. From the 3-D SJ/WJ physical model, the WJ trajectory was predicted and four important design/operation factors were identified: the momentum flow ratio of the jets, the injection angle of the WJ, the nozzle separation distance, and the virtual origin of the SJ and the WJ.

4. The 3-D SJ/WJ physical model showed good agreement with experimental data while RANS simulation with standard k-ε model under-predicted the WJ trajectory. Thus, this physical model might be used to validate CFD models.

A simplification of the detailed chemical reaction mechanism into the set of 2-D manifolds:

1. A skeletal chemical reaction mechanism for flameless combustion of natural gas was reduced from GRI-Mech 3.0 by using Principal Component Analysis (PCA) combined with sensitivity analysis and reaction flow analysis.

2. The set of 2-D manifolds corresponding to 57 mixture fractions was constructed from the skeletal chemical reaction mechanism, and tested in Batch Reactor (BR) and Perfect Stirred Reactor (PSR) models.

3. For the treatment of the physical perturbation on the surface of the manifolds, the perpendicular projection assumption provided a reasonable prediction compared with the orthogonal projection. This also provided significant benefits for computational time and computer storage requirements.

4. The energy equation expressed in terms of specific enthalpy (implicit heat release rate term) may be preferable for CFD simulation rather than the energy equation expressed in terms of temperature or specific sensible enthalpy (explicit heat release rate term).

The steady-state RANS simulation associated with the simplified flameless combustion kinetics:

1. Based on experimental data, it was confirmed that the flameless combustion is a competitive technology to achieve ultra-low NOx emission levels in combustion facilities.
2. The CSE-TGLDM combustion model was used to simulate flameless combustion for the SJ/WJ furnace. These results were compared with other combustion models (the equilibrium chemistry model, the steady flamelet model) and experimental data.
3. All combustion models (PDF/Mixing approach) provided good predictions of major species concentrations. However the gas temperatures and CO concentrations were highly over-predicted.

6.2 Recommendations for future work

Based on the results of this study, the following recommendations are proposed for future work:

- An extension of the 3-D SJ/WJ physical model for a non-isothermal, confined SJ/WJ system can be developed so that the chemical kinetics can be linked together with the physical model. The extension of the current model will require a reliable relationship explaining the entrainment flow for the system.

- A higher-dimensional TGLDM may be necessary to minimize the overlapping problem and to weaken the effect of the physical perturbation. This will require strong computational resources.

- The steady-state RANS simulation of turbulent flameless combustion using the CSE-TGLDM model needs to be improved to show better agreement with the current set of experimental data. Some improvements can be achieved by employing additional independent variables such as the enthalpy and the scalar dissipation rate when estimating the conditional averaged value. This will also require strong computational resources.

Bibliography

1. Sobiesiak, A., Rahbar, S. and Becker, H., 1998, Performance Characteristics of the Novel Low-NO*x* CGRI Burner For Use with High Air Preheat, *Combustion and Flame*, Vol. 115, pp. 93-125.

2. Wuenning, J. A., Wuenning, J. G., 1997, Flameless Oxidation to Reduce Thermal NO-Formation, *Progress in Energy and Combustion Science*, Vol. 23, pp. 81-94.

3. Milani, A. and Saponaro, A., 2001, Diluted Combustion Technologies, *IFRF combustion Journal*, Article No. 200101.

4. Hasegawa, T., Tanaka, R. and Niioka T., 1997, High Temperature Air Combustion contributing to Energy Savings and Pollutant Reduction in Industrial Furnace, *Proceedings of International Joint Power Generation Conference*, Denver, Vol. 1, pp. 259-266.

5. Amiridis, M. D., Zhang, T. and Farrauto, R. J., 1996, Review: Selective Catalytic Reduction of Nitric Oxide by Hydrocarbons, *Applied Catalysis B: Environmental*, Vol. 10, pp. 203-227.

6. Javed, M. T., Irfan, N. and Gibbs, B.M., 2007, Review: Control of Combustion-Generated Nitrogen Oxides by Selective Non-Catalytic Reduction, *Journal of Environmental Management*, Vol. 83(3), pp. 251-289.

7. Gardiner, W. C., 2000, Gas-Phase Combustion Chemistry, Springer-Verlag, New York.

8. Poirier, D., Grandmaison, E.W., Lawrence, A.D., Matovic, M.D. and Boyd, E., 2004, Oxygen-Enriched Combustion Studies with the Low NOx CGRI Burner, *IFRF Combustion Journal*, Article No. 200404.

9. Yimer, I., Becker, H. A. and Grandmaison E. W., 1996, Development of Flow from Multiple-Jet Burners, *The Canadian Journal of Chemical Engineering*, Vol. 74, pp. 840-850.

10. Besik, F. K., Rahbar, S., Becker, H. A. and Sobiesiak, A., 1998, Low NOx Burner, United States Patent 5772421.

11. Fleck, B.A., Matovic, M.D., Grandmaison, E.W. and Sobiesiak, A., 2003, Modelling of the Near Field of a Multi-jet Burner, *IFRF Combustion Journal*, Article No. 200306.

12. Yimer, I., Becker, H. A. and Grandmaison, E. W., 2001, The Strong-jet/Weak-jet Problem: New Experiments and CFD, *Combustion and Flame*, Vol. 124, pp. 481-502.

13. Grandmaison, E. W., Yimer, I., Becker, H. A. and Sobiesiak, A., 1998, The Strong-Jet/Weak-Jet Problem and Aerodynamic Modeling of the CGRI Burner, *Combustion and Flame*, Vol. 114, pp. 381-396.

14. Gokulakrishnan, P., 2002, The Chemistry of Product-Gas Entrainment in Low-NOx Multi-Jet, Natural-gas Burners, Ph.D Thesis, Queen's University, Canada.

15. He, Y., 2008, Flameless Combustion of Natural Gas in the SJ/WJ Furnace, Ph.D Thesis, Queen's University, Canada.

16. Mancini, M., Weber, R. and Bollettini, U., 2002, Predicting NOx Emissions of a Burner Operated in Flameless Oxidation Mode, *Proceedings of the Combustion Institute*, Vol. 29, pp. 1155-1163.

17. Tabacco, D., Innarella, C. and Bruno, C., 2002, Theoretical and Numerical Investigation on Flameless Combustion, *Combustion Science and Technology*, Vol. 174(7), pp. 1-35.

18. Orsino, S., Weber, R. and Bollettini, U., 2001, Numerical Simulation of Combustion of Natural Gas with High-Temperature Air, *Combustion Science and Technology*, Vol. 170, pp. 1-34.

19. Mancini, M., Schwoppe, P., Weber, R. and Orsino, S., 2007, On mathematical modeling of flameless combustion, *Combustion and Flame*, Vol. 150, pp. 54-59.

20. Weber, R., Orsino, S., Lallemant, N. and Verlaan, Ad., 2000, Combustion of Natural Gas with High-Temperature Air and Large Quantities of Flue Gas, *Proceedings of the Combustion Institute*, Vol. 28, pp. 1315-1321.

21. Coelho, P.J. and Peters, N., 2001, Numerical Simulation of a Mild Combustion Burner, *Combustion and Flame*, Vol. 124, pp. 503-518.

22. Dally, B.B., Riesmeier, E. and Peters, N., 2004, Effect of fuel mixture on moderate and intense low oxygen dilution combustion, *Combustion and Flame*, Vol. 137, pp. 418-431.

23. Christo, F.C. and Dally, B.B., 2005, Modeling turbulent reacting jets issuing into a hot and diluted coflow, *Combustion and Flame*, Vol. 142, pp. 117-129.

24. Awosope, I.O., Kandamby, N.H. and Lockwood, F.C., 2006, Flameless oxidation modelling: on application to gas turbine combustors, *Journal of the Energy Institute*, Vol. 79(2), pp. 75-83.

25. Kim, S. H., Huh, K. Y. and Dally, B., 2005, Conditional Moment Closure Modeling of Turbulent Nonpremixed Combustion in Diluted Hot Coflow, *Proceedings of the Combustion Institute*, Vol. 30, pp. 751-757.

26. Bushe, W.K. and Steiner, H., 1999, Conditional Moment Closure for Large Eddy Simulation of Nonpremixed Turbulent Reacting Flow, *Physics of Fluids*, Vol.11(7), pp. 1896-1906.

27. Pope, S.B. and Maas, U., 1993, Simplifying Chemical Kinetics: Trajectory-Generated Low-Dimensional Manifolds, FDA 93-11.

28. Hussein, J.H., Capp, S.P. and George, W.K., 1994, Velocity measurements in a high-Reynolds-number, momentum-conserving, axisymmetric, turbulent jet, *Journal of Fluid Mechanics*, Vol. 258, pp. 31-75.

29. George, W.K. and Arndt, R., 1989, Advances in Turbulence, Hemisphere Publishing Co., pp. 52.

30. Ricou, F. P. and Spalding, D. B., 1961, Measurements of entrainment by axisymmetric jets, *Journal of Fluid Mechanics*, Vol. 11, pp. 21-32.

31. Malmstrom, T. G., Kirkpatrick, A. T., Christensen, B. and Knappmiller, K. D., 1997, Centreline velocity decay measurements in low-velocity axisymmetric jets, *Journal of Fluid Mechanics*, Vol. 246, pp. 363-377

32. Gregory P. Smith, David M. Golden, Michael Frenklach, Nigel W. Moriarty, Boris Eiteneer, Mikhail Goldenberg, C. Thomas Bowman, Ronald K. Hanson, Soonho Song, William C. Gardiner, Jr., Vitali V. Lissianski, and Zhiwei Qin, http://www.me.berkeley.edu/gri_mech/

33. Hilbert, R., Tap, F., El-Rabii, H. and Thevenin, D., 2004, Impact of detailed chemistry and transport models on turbulent combustion simulations, *Progress in Energy and Combustion Science*, Vol. 30, pp. 61-117.

34. Tsuji, H., Gupta, A.K., Hasegawa, T., Katsuki, M., Kishimoto, K. and Morita, M., 2003, High temperature air combustion: From Energy Conservation to Pollution Reduction, CRC press.

35. Linan, A., 1974, The asymptotic structure of counterflow diffusion flames for large activation energies, *Acta Astronautica*, Vol. 1, pp. 1007-1039.

36. Peters, N., 1985, Numerical and asymptotic analysis of systematically reduced reaction schemes for hydrocarbon flames; in Numerical simulation of combustion phenomena, Lecture notes in Physics 241, Springer-Verlag, Berlin.

37. Peters, N. and Kee, R. J., 1987, The computation of stretched laminar methane-air diffusion flames using a reduced four-step mechanism, *Combustion and Flame*, Vol. 68, pp. 17-29.

38. Bilger, R.W., Starner, S.H. and Kee, R.J., 1990, On reduced mechanisms for methane-air combustion in nonpremixed flames, *Combustion and Flame*, Vol. 80, pp. 135-149.

39. Peters, N. and Rogg, B., 1993, Reduced kinetic mechanisms for applications in combustion systems, Lecture notes in Physics, Springer-Verlag, Berlin.

40. Warnatz, J., Maas, U. and Dibble, R.W., 2006, Combustion: Physical and Chemical Fundamentals, Modeling and Simulation, Experiments, Pollutant Formation, 4th edition, Springer-Verlag, Berlin.

41. Dickinson, R.P. and Gelinas, R.J., 1976, Sensitivity analysis of ordinary differential equation systems - A direct method, *Journal of Computational Physics*, Vol. 21, pp. 123-143.

42. Warnatz, J., 1981, The structure of laminar alkane-, alkene-, and acetylene flames, *Eighteenth Symposium (International) on Combustion*, Vol. 18(1), pp. 369-384.

43. Jolliffe, I.T., 2002, Principal Component Analysis, 2nd edition, Springer-Verlag, Berlin.

44. Vajda, S., Valko, P. and Turanyi, T., 1985, Principal Component Analysis of Kinetics Models, *International Journal of Chemical Kinetics*, Vol. 17, pp. 55-81.

45. Brown, N.J., Li, G. and Koszykowski, M.L., 1997, Mechanism Reduction Via Principal Component Analysis, *International Journal of Chemical Kinetics*, Vol. 29, pp. 393-414.

46. Lam, S.H. and Goussis, D.A., Understanding Complex Chemical Kinetics with Computational Singular Perturbation, *Twenty-second Symposium (International) on Combustion*, Vol. 22, pp. 931-941.

47. Lam, S.H. and Goussis, D.A., 1991, Chapter 10 - Conventional Asymptotic and Computational Singular Perturbation for Simplified Kinetics Modelling; in Reduced Kinetic Mechanisms and Asymptotic Approximations for Methane-Air Flames, Lecture Notes in Physics 384, Springer-Verlag, Berlin.

48. Lam, S.H. and Goussis, D.A., 1992, A Study of Homogeneous Methanol Oxidation Kinetics Using CSP, *Twenty-fourth Symposium (International) on Combustion*, Vol. 24, pp. 113-120.

49. Lam, S.H., 1993, Using CSP to Understand Complex Chemical Kinetics, *Combustion Science and Technology*, Vol. 89(5-6), pp. 375-404.

50. Lam, S.H. and Goussis, D.A., 1994, The CSP Method for Simplifying Kinetics, *International Journal of Chemical Kinetics*, Vol. 26, pp. 461-486.

51. Maas, U. and Pope, S.B., 1992, Simplifying Chemical Kinetics: Intrinsic Low-Dimensional Manifolds in Composition Space, *Combustion and Flame*, Vol. 88, pp. 239-264.

52. Maas, U. and Pope, S.B., 1992, Implementation of Simplified Chemical Kinetics Based on Intrinsic Low-Dimensional Manifolds, *Twenty-Fourth Symposium (International) on Combustion/The Combustion Institute*, Vol. 24, pp. 103-112.

53. Maas, U. and Pope, S.B., 1994, Laminar Flame Calculations Using Simplified Chemical Kinetics Based on Intrinsic Low-Dimensional Manifolds, *Twenty-Fifth Symposium (International) on Combustion/The Combustion Institute*, Vol. 25, pp. 1349-1356.

54. Maas, U., 1998, Efficient Calculation of Intrinsic Low-Dimensional Manifolds for the Simplification of Chemical Kinetics, *Computing and Visualization in Science*, Vol. 1, pp. 69-81.

55. Keck, J.C. and Gillespie, D., 1971, Rate-Controlled Partial-Equilibrium Method for Treating Reacting Gas Mixtures, *Combustion and Flame*, Vol. 17, pp. 237-241.

56. Keck, J.C., 1990, Rate-Controlled Constrained-Equilibrium Theory of Chemical Reactions in Complex Systems, *Progress in Energy and Combustion Science*, Vol. 16, pp. 125-154.

57. Yousefian, V., 1998, A Rate-Controlled Constrained-Equilibrium Thermochemistry Algorithm for Complex Reacting Systems, *Combustion and Flame*, Vol. 115, pp.66-80.

58. Tang, Q. and Pope, S.B., 2002, Implementation of Combustion Chemistry by in situ Adaptive Tabulation of Rate-Controlled Constrained Equilibrium Manifolds, *Proceedings of the Combustion Institute*, Vol. 29, pp. 1411-1417.

59. Jones, W.P. and Rigopoulos, S., 2005, Rate-Controlled Constrained Equilibrium: Formulation and Application to Nonpremixed Laminar Flames, *Combustion and Flame*, Vol. 142, pp. 223-234.

60. Libby, P.A. and Williams, F.A., 1994, Turbulent Reacting Flows, Academic press.

61. Kuo K.K., 1986, Principles of Combustion, John Wiley & Sons Inc.

62. Schlichting, H., 1955, Boundary Layer Theory, 4th edition translated by Kestin, J., McGraw-Hill.

63. Launder, B. E. and Spalding, D. B., 1972, Lectures in Mathematical Models of Turbulence, Academic Press, London, England.

64. FLUENT Inc., 2006, FLUENT 6.3 User's Guide, FLUENT Inc., http://www.fluent.com/.

65. Siegel, R. and Howell, J.R., 1992, Thermal Radiation Heat Transfer, 3rd edition, Taylor & Francis.

66. Chui, E. H. and Raithby, G. D., 1993, Computation of Radiant Heat Transfer on a Non-Orthogonal Mesh Using the Finite-Volume Method, *Numerical Heat Transfer Part B*, Vol. 23, pp.269-288.

67. Raithby, G. D. and Chui, E. H., 1990, A Finite-Volume Method for Predicting a Radiant Heat Transfer in Enclosures with Participating Media, *Journal of Heat Transfer*, Vol. 112, pp. 415-423.

68. Murthy, J.Y. and Mathur, S.R., 1998, Finite Volume Method for Radiative Heat Transfer Using Unstructured Meshes, *Journal of Thermophysics and Heat Transfer*, Vol. 12(3), pp. 313-321.

69. Lockwood, F.C. and Shah, N.G., 1981, A New Radiation Solution Method for Incorporation in General Combustion Prediction Procedures, *Eighteenth Symposium (International) on Combustion*, Vol. 18(1), pp. 1405-1414.

70. Smith, T.F., Shen, Z.F. and Friedman, J.N., 1982, Evaluation of Coefficients for the Weighted Sum of Gray Gases Model, *Journal of Heat Transfer*, Vol. 104, pp.602-608.

71. Edwards, D. K. and Matavosian, R., 1984, Scaling Rules for Total Absorptivity and Emissivity of Gases, *Journal of Heat Transfer*, Vol. 106, pp.684-689.

72. Jones, W.P. and Whitelaw, J.H., 1982, Calculation Methods for Reacting Turbulent Flows: A Review, *Combustion and Flame*, Vol. 48, pp.1-26.

73. Bilger, R.W., 1976, Turbulent jet diffusion flames, *Progress in Energy and Combustion Science*, Vol. 1, pp. 87-109.

74. Liu, F., Guo, H., Smallwood, G.J., Gulder, O.L. and Matovic, M.D., 2002, A robust and accurate algorithm of the b-pdf integrating and its application to turbulent methane-air diffusion combustion in a gas turbine combustor simulator, *International Journal of Thermal Sciences*, Vol. 41, pp. 763-772.

75. Yun, S., Lightstone, M.F. and Thomson, M.J., 2005, An evaluation of beta PDF integration using the density-weighted PDF and the un-weighted PDF, *International Journal of Thermal Sciences*, Vol. 44, pp. 421-428.

76. Richardson, J.M., Howard, Jr. H.C., Smith, Jr. R.W., 1953, The relation between sampling-tube measurements and concentration fluctuations in a turbulent gas jet, *Fourth Symposium (International) on Combustion*, Massachusetts Institute of Technology, Cambridge, Massachusetts, Vol. 4(1), pp. 814-817.

77. Barths, H., Peters, N., Brehm, N., Mack, A., Pfitzner, M. and Smiljanovski, V., 1998, Simulation of pollutant formation in a gas-turbine combustor using unsteady flamelets, *Symposium (International) on Combustion*, Vol. 27(2), pp. 1841-1847.

78. Cuenot, B., Egolfopoulos, F. and Poinsot, T., 2000, An unsteady laminar flamelet model for non-premixed combustion, *Combustion Theory and Modelling*, Vol. 4(1), pp. 77-97.

79. Pitsch, H., 2000, Unsteady Flamelet Modeling of Differential Diffusion in Turbulent Jet Diffusion Flames, *Combustion and Flame*, Vol.123(3), pp.358-374.

80. Klimenko, A.Y. and Bilger, R.W., 1999, Conditional moment closure for turbulent combustion, *Progress in Energy and Combustion Science*, Vol. 25, pp. 595-687.

81. Klimenko, A.Y., 1990, Multicomponent diffusion of various admixtures in turbulent flow, *Fluid Dynamics*, Vol. 25, pp. 327-334.

82. Bilger, R.W., 1993, Conditional moment closure for turbulent reacting flow, *Physics of Fluids A*, Vol. 5(2), pp. 436-444.

83. Masri, A.R., Dibble, R.W. and Barlow, R.S., 1992, The structure of turbulent nonpremixed flames of methanol over a range of mixing rates, *Combustion and Flame*, Vol. 89, pp. 167-185.

84. Barlow, R.S. and Carter, C.D., 1994, Raman/Rayleigh/LIF measurements of nitric oxide formation in turbulent hydrogen jet flames, *Combustion and Flame*, Vol. 97, pp. 261-280.

85. Starner, S.H., Bilger, R.W., Lyons, K.M., Frank, J.H. and Long, M.B., 1994, Conserved scalar Measurements in turbulent diffusion flames by a Raman and Rayleigh ribbon imaging method, *Combustion and Flame*, Vol. 99, pp. 347-354.

86. Chen, Y.C. and Mansour, M.S., 1997, Measurements of scalar dissipation in turbulent hydrogen diffusion flames and some implications on combustion modeling, *Combustion Science and Technology*, Vol. 126, pp.291-313.

87. Press, W.H., Teukolsky, S.A., Vetterling, W.T. and Flannery, B.P., 1992, Numerical Recipes in Fortran, 2nd edition, Cambridge University Press.

88. Tikhonov, A.N. and Arsenin, V.Y., 1977, Solutions of ill-posed problems, V.H. Winston & Sons, Washington, D.C.

89. Huang, J. and Bushe, W.K., 2007, Simulation of transient turbulent methane jet ignition and combustion under engine-relevant conditions using conditional source-term estimation with detailed chemistry, *Combustion Theory and Modelling*, Vol. 11(6), pp. 977-1008.

90. Grout, R.W., Bushe, W.K and Blair, C., 2007, Predicting the ignition delay of turbulent methane jets using Conditional Source-term Estimation, *Combustion Theory and Modelling*, Vol. 11(6), pp. 1009-1028.

91. Becker, H.A., Hottel, H.C. and Williams, G.C., 1967, On the light-scatter technique for the study of turbulence and mixing, *Journal of Fluid Mechanics*, Vol. 30, pp. 259-284.

92. Rosenbrock, H.H., 1960, An automatic Method for finding the greatest or least Value of a Function, *Computer Journal*, Vol. 3, pp. 175-184.

93. Kee, R. J., Rupley, F. M. and Miller, J.A., 1990, Chemkin-II: A Fortran Chemical Kinetics Package for the Analysis of Gas-Phase Chemical Kinetics, Sandia National Laboratories, Report SAND89-8009.

94. Renka, R.J., 1988, QSHEP2D: Quadratic Shepard Method for Bivariate Interpolation of Scattered Data, Algorithm 660, *ACM Transaction on Mathematical Software*, Vol. 14(2), pp. 149-150.

95. Renka, R.J., 1996, TRIPACK: A Constrained Two-Dimensional Delaunay Triangulation Package, Algorithm 751, *ACM Transaction on Mathematical Software*, Vol. 22(1), pp. 1-8.

96. Renka, R.J., 1996, SRFPACK: Software for Scattered Data Fitting with a Constrained Surface under Tension, Algorithm 752, *ACM Transaction on Mathematical Software*, Vol. 22(1), pp. 9-17.

97. Brown, P.N., Byrne, G.D. and Hindmarsh, A.C., 1989, VODE: A Variable Coefficient ODE Solver, *SIAM Journal on Scientific and Statistical Computing*, Vol. 10(5), pp. 1038-1051.

98. Magnussen, B.F. and Hjertager, B.H., 1977, On Mathematical Modeling of Turbulent Combustion with Special Emphasis on Soot Formation and Combustion, *16th Symposium (International) on Combustion*, Vol. 16(1), pp. 719-729.

99. Cavigiolo, A., Galbiati, M.A., Effuggi, A., Gelosa, D. and Rota, R., 2003, Mild combustion in a laboratory-scale apparatus, *Combustion Science and Technology*, Vol. 175, pp. 1347-1367.

100. Canadian Council of Ministers of the Environment, March 1998, National Emission Guideline for Commercial/Industrial Boilers and Heaters, Initiative N306, PN 1286.

101. http://www.hpcvl.org/

102. Cohen S.D. and Hindmarsh, A.C., 1996, CVODE, A Stiff/Nonstiff ODE Solver in C, *Computers in Physics*, Vol. 10(2), pp. 138-143.

Appendix A

Reduced Mechanism-3 (Skeletal chemical reaction mechanism)

Table A1. List of species and elements in the reduced mechanism-3.

Species	H2, H, O, O2, OH, H2O, HO2, H2O2, CH2, CH2(S), CH3, CH4, CO, CO2, HCO, CH2O, CH3O, C2H3, C2H4, C2H5, C2H6, HCCO, CH2CO, CH2CHO, N2
Elements	H, C, O, N

Table A2. List of reactions of the reduced mechanism-3 in the CHEMKIN format.

$k = AT^b \exp\left(\frac{-E_a}{RT}\right)$, Units: mole-cm-sec-K, and cal/mole

No.	Reaction	A	b	Ea
1.	O+H2<=>H+OH	3.87E+04	2.7	6260.0
2.	O+HO2<=>OH+O2	2.00E+13	0.0	0.0
3.	O+CH3<=>H+CH2O	5.06E+13	0.0	0.0
4.	O+CH4<=>OH+CH3	1.02E+09	1.5	8600.0
5.	O+CH2O<=>OH+HCO	3.90E+13	0.0	3540.0
6.	O+C2H4<=>CH3+HCO	1.25E+07	1.8	220.0
7.	O+C2H6<=>OH+C2H5	8.98E+07	1.9	5690.0
8.	O2+CH2O<=>HO2+HCO	1.00E+14	0.0	40000.0
9.	H+O2+M<=>HO2+M	2.80E+18	-0.9	0.0
	O2 Enhanced by 0.000E+00			
	H2O Enhanced by 0.000E+00			
	CO Enhanced by 7.500E-01			
	CO2 Enhanced by 1.500E+00			
	C2H6 Enhanced by 1.500E+00			
	N2 Enhanced by 0.000E+00			
10.	H+O2+H2O<=>HO2+H2O	1.13E+19	-0.8	0.0

11.	H+O2+N2<=>HO2+N2	2.60E+19	-1.2	0.0
12.	H+O2<=>O+OH	2.65E+16	-0.7	17041.0
13.	H+OH+M<=>H2O+M	2.20E+22	-2.0	0.0
	H2 Enhanced by 7.300E-01			
	H2O Enhanced by 3.650E+00			
	CH4 Enhanced by 2.000E+00			
	C2H6 Enhanced by 3.000E+00			
14.	H+HO2<=>O2+H2	4.48E+13	0.0	1068.0
15.	H+HO2<=>2OH	8.40E+13	0.0	635.0
16.	H+CH3(+M)<=>CH4(+M)	1.39E+16	-0.5	536.0
	Low pressure limit: 0.26200E+34 -0.47600E+01 0.24400E+04			
	TROE centering: 0.78300E+00 0.74000E+02 0.29410E+04 0.69640E+04			
	H2 Enhanced by 2.000E+00			
	H2O Enhanced by 6.000E+00			
	CH4 Enhanced by 3.000E+00			
	CO Enhanced by 1.500E+00			
	CO2 Enhanced by 2.000E+00			
	C2H6 Enhanced by 3.000E+00			
17.	H+CH4<=>CH3+H2	6.60E+08	1.6	10840.0
18.	H+CH2O(+M)<=>CH3O(+M)	5.40E+11	0.5	2600.0
	Low pressure limit: 0.22000E+31 -0.48000E+01 0.55600E+04			
	TROE centering: 0.75800E+00 0.94000E+02 0.15550E+04 0.42000E+04			
	H2 Enhanced by 2.000E+00			
	H2O Enhanced by 6.000E+00			
	CH4 Enhanced by 2.000E+00			
	CO Enhanced by 1.500E+00			
	CO2 Enhanced by 2.000E+00			
	C2H6 Enhanced by 3.000E+00			
19.	H+CH2O<=>HCO+H2	5.74E+07	1.9	2742.0
20.	H+C2H4(+M)<=>C2H5(+M)	5.40E+11	0.5	1820.0

Low pressure limit: 0.60000E+42 -0.76200E+01 0.69700E+04

TROE centering: 0.97530E+00 0.21000E+03 0.98400E+03 0.43740E+04

H2 Enhanced by 2.000E+00

H2O Enhanced by 6.000E+00

CH4 Enhanced by 2.000E+00

CO Enhanced by 1.500E+00

CO2 Enhanced by 2.000E+00

C2H6 Enhanced by 3.000E+00

21.	H+C2H4<=>C2H3+H2	1.32E+06	2.5	12240.0
22.	H+C2H6<=>C2H5+H2	1.15E+08	1.9	7530.0
23.	H+CH2CO<=>HCCO+H2	5.00E+13	0.0	8000.0
24.	H+CH2CO<=>CH3+CO	1.13E+13	0.0	3428.0
25.	OH+H2<=>H+H2O	2.16E+08	1.5	3430.0
26.	2OH(+M)<=>H2O2(+M)	7.40E+13	-0.4	0.0

Low pressure limit: 0.23000E+19 -0.90000E+00 -0.17000E+04

TROE centering: 0.73460E+00 0.94000E+02 0.17560E+04 0.51820E+04

H2 Enhanced by 2.000E+00

H2O Enhanced by 6.000E+00

CH4 Enhanced by 2.000E+00

CO Enhanced by 1.500E+00

CO2 Enhanced by 2.000E+00

C2H6 Enhanced by 3.000E+00

27.	2OH<=>O+H2O	3.57E+04	2.4	-2110.0
28.	OH+HO2<=>O2+H2O Declared duplicate reaction	1.45E+13	0.0	-500.0
29.	OH+H2O2<=>HO2+H2O	1.70E+18	0.0	29410.0
30.	OH+CH3<=>CH2(S)+H2O	6.44E+17	-1.3	1417.0
31.	OH+CH4<=>CH3+H2O	1.00E+08	1.6	3120.0
32.	OH+CO<=>H+CO2	4.76E+07	1.2	70.0
33.	OH+CH2O<=>HCO+H2O	3.43E+09	1.2	-447.0
34.	OH+C2H4<=>C2H3+H2O	3.60E+06	2.0	2500.0

35.	OH+C2H6<=>C2H5+H2O	3.54E+06	2.1	870.0
36.	OH+CH2CO<=>HCCO+H2O	7.50E+12	0.0	2000.0
37.	2HO2<=>O2+H2O2	4.20E+14	0.0	12000.0
38.	HO2+CH3<=>O2+CH4	1.00E+12	0.0	0.0
39.	HO2+CH3<=>OH+CH3O	3.78E+13	0.0	0.0
40.	HO2+CH2O<=>HCO+H2O2	5.60E+06	2.0	12000.0
41.	CH2+O2=>OH+H+CO	5.00E+12	0.0	1500.0
42.	CH2(S)+N2<=>CH2+N2	1.50E+13	0.0	600.0
43.	CH3+O2<=>O+CH3O	3.56E+13	0.0	30480.0
44.	CH3+O2<=>OH+CH2O	2.31E+12	0.0	20315.0
45.	2CH3(+M)<=>C2H6(+M)	6.77E+16	-1.2	654.0
	Low pressure limit: 0.34000E+42 -0.70300E+01 0.27620E+04			
	TROE centering: 0.61900E+00 0.73200E+02 0.11800E+04 0.99990E+04			
	H2 Enhanced by 2.000E+00			
	H2O Enhanced by 6.000E+00			
	CH4 Enhanced by 2.000E+00			
	CO Enhanced by 1.500E+00			
	CO2 Enhanced by 2.000E+00			
	C2H6 Enhanced by 3.000E+00			
46.	2CH3<=>H+C2H5	6.84E+12	0.1	10600.0
47.	CH3+CH2O<=>HCO+CH4	3.32E+03	2.8	5860.0
48.	CH3+C2H6<=>C2H5+CH4	6.14E+06	1.7	10450.0
49.	HCO+H2O<=>H+CO+H2O	1.50E+18	-1.0	17000.0
50.	HCO+M<=>H+CO+M	1.87E+17	-1.0	17000.0
	H2 Enhanced by 2.000E+00			
	H2O Enhanced by 0.000E+00			
	CH4 Enhanced by 2.000E+00			
	CO Enhanced by 1.500E+00			
	CO2 Enhanced by 2.000E+00			
	C2H6 Enhanced by 3.000E+00			
51.	HCO+O2<=>HO2+CO	1.34E+13	0.0	400.0

52.	CH3O+O2<=>HO2+CH2O	4.28E-13	7.6	-3530.0
53.	C2H3+O2<=>HCO+CH2O	4.58E+16	-1.4	1015.0
54.	C2H5+O2<=>HO2+C2H4	8.40E+11	0.0	3875.0
55.	HCCO+O2<=>OH+2CO	3.20E+12	0.0	854.0
56.	O+CH3=>H+H2+CO	3.37E+13	0.0	0.0
57.	O+C2H4<=>H+CH2CHO	6.70E+06	1.8	220.0
58.	OH+HO2<=>O2+H2O Declared duplicate reaction	5.00E+15	0.0	17330.0
59.	CH2+O2=>2H+CO2	5.80E+12	0.0	1500.0
60.	C2H3+O2<=>O+CH2CHO	3.03E+11	0.3	11.0
61.	H+CH2CO(+M)<=>CH2CHO(+M)	4.86E+11	0.4	-1755.0

Low pressure limit: 0.10120E+43 -0.76300E+01 0.38540E+04

TROE centering: 0.46500E+00 0.20100E+03 0.17730E+04 0.53330E+04

H2	Enhanced by	2.000E+00
H2O	Enhanced by	6.000E+00
CH4	Enhanced by	2.000E+00
CO	Enhanced by	1.500E+00
CO2	Enhanced by	2.000E+00
C2H6	Enhanced by	3.000E+00